Sill emplacement and contact metamorphism in sedimentary basins

Local processes with global implications

by

Ingrid Aarnes

Thesis submitted for the degree of

Philosophiae Doctor

Faculty of Mathematics and Natural Sciences
University of Oslo

June 2010

Series of dissertations submitted to the
Faculty of Mathematics and Natural Sciences, University of Oslo
No. 967

ISSN 1501-7710

Cover: Inger Sandved Anfinsen.
Printed in Norway: AiT e-dit AS.

Produced in co-operation with Unipub.
The thesis is produced by Unipub merely in connection with the
thesis defence. Kindly direct all inquiries regarding the thesis to the copyright
holder or the unit which grants the doctorate.

Principal supervisor:
Dr. Henrik Svensen
Subsidiary supervisor:
Professor Yuri Y. Podladchikov

When you are face to face with a difficulty, you are up against a discovery. - lord Kelvin

Contents

Preface

The Earth is a dynamic planet. Every day throughout its history there have been processes working in, on and around it, from atomic scale to astronomical scale. And every process contributes to a change. Sometimes this change can be minor, for example when a water molecule trapped in a mineral decides to leave; or the change can be major, for example when large volumes of the Earths crust are filled up with glowing hot magma in a relatively short period of time. While studying the Earth in detail we realize that in most cases, several of these processes work together. Sometimes the result can be disastrous.

Climate changes. You have probably read it in the news, heard about it on the TV and discussed it over dinner with friends and family. And you notice it, because you still have a vague childhood memory that the climate was not that extreme before. But then we quickly adapt, we forget and loose interest. Who does not want a few degrees warming when the polar wind strikes through your body with its ice needles. Although feeling a little annoyed by the outlook of having to pay more to keep our lifestyle, we happily separate paper from plastic while clapping our own shoulders 'we did what we could'. Still, we have no real intentions to stop exploiting our nature and the gift of convertible energy. We remind ourselves that it cannot be that dangerous, because global warming has happened before when there were no humans around.

And yes, we have seen it happen before; the Earth has experienced global warming. Interestingly enough, we never follow up our reassuring statement with: yes, but several of these warming events were also followed by mass extinctions. And if that was not enough to make you worried, these warming and mass extinction events also correlate in time with what is interpreted to be related to a massive release of greenhouse gases to the atmosphere. By the Earth itself! In 2004 a potential link interlacing these events was discovered by Svensen and his co-workers. They showed how the emplacement of large volumes magma into what in the oil industry is referring to as good source-rocks for oil and gas would result in massive generation of, yes exactly, oil and gas. Never has the ill breath of the Earths catastrophic past been able to touch us more directly. Every year we pump up massive amounts of the fossil fuel stored in the ground before we release it to the atmosphere though our increasing energy consumption. The analogy to what could happen to us in the future is thus stored in the past geological record. This thesis is another piece in the jigsaw puzzle portraying the many coincidental events that led to such disastrous impacts on the Earths global cycles. The major focus of this work has been what happens with the rocks that are subjected to the heat from the igneous intrusions, in terms of organic and inorganic reactions, gas volumes, pressure evolution, and potential processes for the gas to reach the atmosphere.

The work would not have been done without my main supervisor Henrik Svensen. From the times of hiring until the delivery of this thesis and beyond, he has been in continuous support of me and my work. I am grateful for the conferences, field trips, and the stay abroad at ETH Zürich he has allowed me to go to, all of which I benefited a lot from. His many ideas, subtle humor and organized way of doing science have brought me inspiration and great help during this work. His talent in choosing catching titles is still unmatched. A million thanks goes to my co-supervisor Yuri Podladchikov for whom I have great respect for both as mentor and untraditional scientist. From our first discussion one winter night in 2005 until the final thesis-delivery I have had the privilege of working with this free-thinker, who uses his world of simple logic, excellent argumentation skills and ”high-school” knowledge intermixed with psychological entertainments to explore and simplify the world around and below him. I have gained a lot of inspiration, knowledge and scientific courage by working with such a devoted person as him. In this context I would also like to acknowledge Jamie Connolly, who was my caretaker and host-supervisor during my visit at ETH. He is an ingenious person, with first-class observational capacity and entertaining linguistic skills. He showed remarkable patience with my many questions, and I enjoyed a lot all the stories and digressions, especially the one about reversible heat transfer.

I am very thankful for all my friends and colleagues at PGP throughout my time here who taught me new things, took part in social activities and made lunch-break a highlight in the day. I have enjoyed greatly your company of contrasting background leading to new insights in everything from science to culture, and I admit it was fun assigning animals to the PGP zoo! Karin Brastad will always be the Mother Hen of PGP, and I am very thankful for all the nice times I spent in her office; she brings warmth and care for all of us. Bjørn Jamtveit is the natural leader of our group, and without his vision of synergy none of this would have been possible. I am thankful for the field-trips he brought me to, with sand-dune jumping and informative plane-rides. Hans Vrijmoed and Marta Adamuszek were always there to listen, laugh, play pool, discuss life and other ongoing projects. My office-mates Kirsten Fristad and Filip Nicolaisen have contributed with native English and music. Thanks go to Sverre Planke, Stephane Polteau and Christophe Galerne for exchange of ideas and data; Dag Karlsen, Marcin Dabrowski and Viktoriya Yarushina for educational discussions; Muriel Erambert and Berit Løken Berg for technical assistance during analysis, and Jacqueline for Swiss influence. I am happy for meeting all of the people at ETH Zürich; the ex-Hönggerberg group for skiing and discussions, friday-beer people, and everyone at IMP anno 2008 who brought about many life-time memories.

My friends and family outside PGP deserve a place in this acknowledgement for always being there with me during my studies. I would like to thank my family for showing real interest and support in my choice of subject. My dad gave me a lot of good advices, where the one where I should quit if it stopped being fun was the one I appreciated the most. I am also (weirdly enough) thankful for my friends who would groan painfully whenever I brought up the subject of rocks. Many waffles have been consumed during relaxing breaks at my Grandmothers place throughout the PhD.

My dearest acknowledgement goes to Maarten, lieve mijn. I came into his life and his apartment half-way through my studies, and he took very good care of me ever since. With his love ispedd a lot of ”ta vare” he brought everyday laughter, and motivation when times where a little rougher on the edges. Ik zie ernaar uit het fantastisch leven door te brengen met jou, met veel gelach, kos en reizen rond de wereld. Du er best en ik houd van jou.

During the PhD studies I participated in what we called the ”Wednesday Club”, and that I thought was fun to acknowledge by the following:

One day there went out a PGP call
a marvelous chance to solve it all.
”What is the meaning of life?”
asked the razor-sharp knife.
Wednesday evenings provided the frame
and we lurched out of our office like moths to the flame
Hans brought drive and silent passion
Vika knew sponges and latest fashion
Timm came with shades of blue and of green
Jenya & Chris made a dream of a team.
Magnus found a term that was lost
Nina looked for sun to outlive the frost.
Discussions were many on Martas mixing
the Marcins joined for model fixing
while Julia worked on solid confusion.
Could there really be a solution?
The years went by and we kept on going
Sure the answer in the wind was blowing
After all the brains and workforce spent
you may wonder where it all went.
Did we learn how to solve life and the rest
or did we merely embark on our quest?

Chapter 1

Introduction

1.1 Do you believe in coincidences?

Large Igneous Provinces (LIPs) have coincided with major climatic and environmental perturbations since the Palaeozoic (Fig. 1.1) (e.g. Rampino & Stothers, 1988; Stothers, 1993; Palfy & Smith, 2000; Wignall, 2001; Benton & Twitchett, 2003; Courtillot & Renne, 2003; Jenkyns, 2003; Webb *et al.*, 2009). The synchronous timing of global warming and mass extinction with the LIPs outlines a gigantic scientific puzzle, where the arrangement of the individual pieces of data is subjected to continuing debates. The proxy data from the same time-periods typically reveal global warming of about 4-6 °C or more (Koch *et al.*, 1992; Zachos *et al.*, 1993; Thomas & Shackleton, 1996; McElwain *et al.*, 1999; Bailey *et al.*, 2003), ocean anoxia with increased organic burial (Jenkyns, 1988; Arthur *et al.*, 1988; Sliter, 1989; Jenkyns & Clayton, 1997; Jenkyns *et al.*, 2001; Méhay *et al.*, 2009; Tejada *et al.*, 2009), and carbon cycle perturbations generally attributed to the release of greenhouse gases such as methane (CH_4) and CO_2 to the atmosphere (e.g. Norris & Röhl, 1999; Krull & Retallack, 2000; Hesselbo *et al.*, 2002; Svensen *et al.*, 2004; Cohen *et al.*, 2007; Hesselbo *et al.*, 2007a).

Many hypotheses explaining these events are provided in the literature, ranging from a complete detachment of the processes, like gas release owing to astronomical forcing (Kemp *et al.*, 2005), to the gas being generated by the LIP intrusive events themselves through contact metamorphism of organic material (Svensen *et al.*, 2004; McElwain *et al.*, 2005; Svensen *et al.*, 2007, 2009). Other studies invoke a combination of LIP formation with other events, such as discharge of methane clathrate from the seafloor as a response to warming associated with volcanic or thermogenic gas release (Dickens *et al.*, 1995; Hesselbo *et al.*, 2000, 2002; Cohen *et al.*, 2007). There is also a considerable attention on resolving the issues linked to the mass extinction events (e.g. Raup & Sepkoski, 1984; Little & Benton, 1995; McElwain *et al.*, 1999; Berner, 2002; Benton & Twitchett, 2003; Visscher *et al.*, 2004), as these also correlate with LIPs (Wignall, 2001; Courtillot & Renne, 2003).

Our understanding concerning the causal effects of global warming and its associated mass extinctions is of principal importance for how Earths history can be applied to understand future challenges. If we are able to unravel the processes behind such catastrophic events in the Earths history, we can use this knowledge to predict future scenarios related to increasing anthropogenic gas release and environmental disturbances (cf. Broecker, 1975; IPCC, 2007).

The background for this thesis is to evaluate the hypothesis of thermogenic gas release during contact metamorphism of organic-rich sedimentary rocks, as first proposed by Svensen *et al.* (2004). This is a recently proposed hypothesis which need further testing and evaluation. Relatively little is known about the details of contact metamorphism of organic-rich shales intruded by large magma volumes. Moreover, the amount of generated gases during metamorphism is poorly constrained, as is the actual release mechanisms from the aureole to the atmosphere. An improved understanding of these aspects is needed for establishing the hypothesis as a theory for past environmental changes, and is critical when testing the aureole-hypothesis against the plethora of other hypotheses (gas hydrate dissociation, changes in oceanic circulation, meteorite impact, oceanic degassing, to mention a few). This thesis is aiming at addressing these and other unsolved challenges related to sill emplacement and contact metamorphism in sedimentary basins.

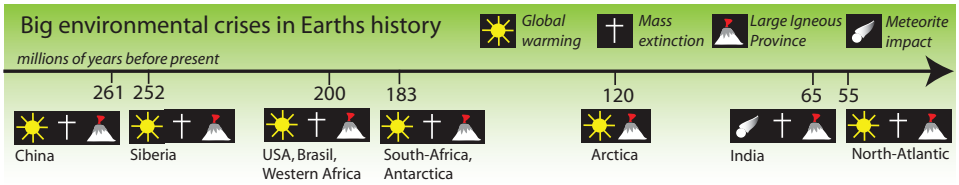

Figure 1.1: Large Igneous Provinces, global warming and mass extinction are temporally associated since the Palaeozoic.

1.2 Volcanic basins

Sedimentary basins intruded by large volumes of magma are referred to as volcanic basins. The magmas are mostly of basaltic composition, and often associated with LIP-formation. When the magma reaches the surface it can create kilometer thick piles of lava, referred to as flood-basalts. Below the surface, the igneous intrusions are emplaced both as sub-horizontal (sills) and sub-vertical (dikes) sheets within the sedimentary formations. The heat transfer from the hot intrusions to the surrounding host-rocks is the driving force of contact metamorphism in these basins. Because sedimentary basins represent one of the Earth's largest carbon reservoirs (Falkowski *et al.*, 2000), there is a huge potential of liberation of carbon gases such as CH_4 and CO_2 from the sediments in a volcanic basin during contact metamorphism.

In 2004 a potential link between volcanic basins and the well established environmental perturbations recorded at ∼55 Ma (the Paleocene-Eocene Thermal Maximum; PETM) was discovered on the basis of detailed seismic imaging and borehole studies in the Vøring and Møre basins, offshore Norway (Svensen *et al.*, 2004). The principal idea is rapid generation of large volumes of greenhouse gases during contact metamorphism that were released efficiently to the atmosphere triggering global warming. This idea was later followed up to encompass other coinciding LIPs and climate perturbations, among others the Karoo volcanic basin intruded during the Toarcian (∼183 Ma), the Siberian Traps during the end-Permian (∼252 Ma) and the Emeishan volcanic province during the end-Guadalupian (∼261 Ma) (e.g. McElwain *et al.*, 2005; Beerling *et al.*, 2007; Svensen *et al.*, 2007; Retallack & Jahren, 2008; Svensen *et al.*, 2009; Ganino & Arndt, 2009).

There is some controversy whether the Toarcian carbon isotope perturbation was a global or local event (van de Schootbrugge *et al.*, 2005; Wignall *et al.*, 2006; McArthur, 2007; Hesselbo *et al.*, 2007b; McArthur *et al.*, 2008). One argument against the Toarcian excursion being a global event is the absence of the $\delta^{13}C$ excursion in belemnites in a secion on the coast of Yorkshire, UK (van de Schootbrugge *et al.*, 2005). An alternative model for the negative excursions is the Küspert's model (1982) referring to advection of isotopically light, organic matter-derived CO_2 from anoxic bottom waters associated with the anoxic event (Schouten *et al.*, 2000).

The key to further constraints on the mechanisms related to the negative carbon isotope spikes may lie in volcanic basins, where enormous volumes of magma were rapidly emplaced synchronously with the excursion events. The Karoo Basin is particular well-exposed volcanic basin covering nearly two-thirds of South Africa (Chevallier & Woodford, 1999). It is basically undisturbed by tectonic forces since the time of emplacement of the Karoo-Ferrar Volcanic Province at ~183 Ma (Duncan *et al.*, 1997; Jourdan *et al.*, 2008). From field work, satelite images and borehole cores from the Karoo Basin, we can study processes that happened in the past. This involves processes related to the emplacement and differentiation of the magma (Marsh & Eales, 1984; Marsh *et al.*, 1997; Galerne *et al.*, 2008; Polteau *et al.*, 2008a,b; Galerne *et al.*, 2010, Chapter 6, this thesis), the effects of contact metamorphism and fluid generation in the intruded sedimentary formations (Svensen *et al.*, 2007; Polteau *et al.*, in prep., Chapters 2 and 3, this thesis), or processes related to sediment deformation and fluid expulsion (Jamtveit *et al.*, 2004; Svensen *et al.*, 2006, 2007, 2008, Chapters 4 and 5, this thesis).

There is still limited data and modeling on the actual fluxes of carbon gases to the atmosphere. Due to the existence of vertical cylindrical conduits referred to as vents, we know that there must have been a release of the aureole fluids some time during or after the sill emplacement (cf. Jamtveit *et al.*, 2004; Svensen *et al.*, 2006, 2007, Chapter 4). However, the relative importance of gas release through venting or through seepage is unconstrained by our current data set. If our estimates are correct, which shows that there has been a massive fluid generation throughout the Karoo basin (Svensen *et al.*, 2007, Chapters 2 and 3), and that most of these gases were efficiently released to the atmosphere through the vents, it implies that also the lower Toarcian carbon isotope perturbation can be related to a global event arising from the massive release of carbon gases.

1.3 Organic matter in shales

This section is an introduction to relevant aspects of organic matter in marine shales and their formation. The shales considered in this thesis is of marine origin, emplaced in front of the Cape Fold Belt forming the Karoo Basin (Lock, 1980; Smith, 1990; Cole, 1992; Catuneanu *et al.*, 1998).

1.3.1 Formation of shales

Primary production of organic matter starts with photosynthesis where water and CO_2 react to produce carbohydrates, water and oxygen with the use of solar energy. The carbon in the oxygen is thus reduced with the help of living organisms. The photosynthesis needs sunlight, chlorophyll and nutrients. The main sources for production of organic matter are phytoplankton using the photosynthesis, and

zooplankton living on the phytoplankton in the photic zone of the oceans, and to some degree lakes. Algae growth in lakes may cause perfect conditions for accumulation of organic-rich sediments. Organic matter can also accumulate from spores and pollen, woody fragments or other types of life.

The accumulation of organic matter in sediments requires that it is not eaten on its way down to the bottom and it is not oxidized back to CO_2. Commonly, less than 0.1% of the produced organic matter gets preserved in the sediments. Favorable conditions for accumulation of organic matter in a basin is thus anoxic conditions, i.e. no free O_2 available. Rocks rich in organic matter such as shales and coals are accumulated under such conditions, and are source-rocks for oil and gas. The more hydrogen in the organic matter, the more petroleum can be generated.

During burial, or diagenesis, the biopolymers such as lipids, carbohydrates and proteins are reduced to biomonomers by bacterial degradation up to about 60 °C . The biomonomers have 'glue' electrons and can combine to form geopolymers. The resulting complex combination of different building blocks of geopolymers and undegraded biopolymers become the precursor of kerogen. During diagenesis they undergo a whole series of low-temperature reactions such as decarboxylation, polymerization and reduction forming the kerogen in lithified sediments. Kerogen is defined as the organic matter insoluble in organic solvents (Durand, 1980).

When the temperature reaches above at least 60 °C , the kerogen breaks down to non-volatile organic matter called bitumen, which is the organic matter soluble in organic solvents (Hunt, 1996). The bitumen can decompose further by a process called organic cracking to oil, gas and carbonaceous residue (graphite). The cracking involves breaking of carbon bonds to form smaller compounds. During decomposition of kerogen there is a loss of functional groups and increasing aromatization of the residue. The long chains of carbon with hydrogens attached (C_{15+}) called *n*-alkanes are the constituents of oil, while the short compounds (C_{1-3}) make up the gas fraction of the generated hydrocarbons.

The difference in kerogen types determines the amount of oil and gas that can be generated. There are three main types: Type I kerogen is a uniform type of materials with a very high hydrogen fraction. This gives a very good potential for oil and gas generation, and due to the high hydrogen-content almost all of the organic matter ($\sim$90%) can crack into hydrocarbons (Ungerer & Pelet, 1987). Type II kerogen has a more diverse composition with a higher oxygen to hydrogen ratio, but is still a very good source for oil and gas. About 60% of the kerogen can crack into hydrocarbons (Ungerer & Pelet, 1987). Organic rich shales have commonly a mixture of Type I and Type II kerogen. Type III kerogen is a very diverse mixture of organic matter, usually with woody fragments with a high oxygen to hydrogen ratio. Hence, this kerogen type is mostly a source of carbon gases, such as CO_2 and CH_4. It is a common constituent in coals, and typically around $\sim$25% of the kerogen is available for hydrocarbon generation (Ungerer & Pelet, 1987). Upon heating above $\sim$130 °C , oil can be converted into gas in a process called secondary cracking (Hunt, 1996).

Coals are composed of macerals in a similar way as rocks are composed of minerals. The three main maceral groups are liptinite, vitrinite and inertinite. These macerals are also constituents in shales. Vitrinite is particularly useful maceral due to its qualities as a maturation index. Vitrinite is composed of aromatic rings stacked on top of each other and linked with longer chains. Upon maturation, i.e. generation of hydrocarbons, the longer chains break off and increase the aromaticity of the vitrinite (Dow, 1977; Behar & Vandenbroucke, 1987). This increases the reflectivity of the vitrinite.

The reflectivity measurements are made with a reflecting microscope, and if one uses oil-immersion objectives to enhance the reflectivity the value is reported in %Ro ('o' for oil), which is the percentage of incident light that is reflected back through the microscope.

Heat is the major factor in cracking of organic matter to hydrocarbons which initiates at about 90 °C (Dieckmann *et al.*, 1998), where the rate depends exponentially on the temperature (e.g. Burnham & Sweeney, 1989; Sweeney & Burnham, 1990; Ungerer, 1990; Behar *et al.*, 1992; Seewald *et al.*, 1998). Furthermore, at about 130-150 °C oil cracks further into gas (Hunt, 1996; Dieckmann *et al.*, 1998). Changes in heating rates can shift these temperatures with about 15 °C increase per order of magnitude increase in heating rate (Pepper & Corvi, 1995). In a contact metamorphic setting where the temperatures reach up to several hundred degrees (∼600 °C), the conditions are prosperous for generation of gaseous hydrocarbons.

1.3.2 Contact metamorphism of organic material

Tholeiitic sills, such as the ones intruded into the Karoo Basin holds temperatures between about 1100 °C and 1200 °C . The sharp thermal gradients developing to the relatively cold (30-100 °C) host-rocks cause rapid heat transfer from the intrusion into the surroundings.

When organic matter stored in sedimentary rocks are subjected to heating above ∼85 °C it will decompose into hydrocarbons such as oil and gas (Tissot & Welte, 1984). Thus, the temperatures during contact metamorphism are favorable for rapid maturation of organic material. The generation of hydrocarbons during contact metamorphism is recorded as a progressive loss of total organic matter (TOC) towards the intrusive contact and an corresponding increase in the vitrinite reflectance (%Ro), i.e. increased organic maturation (Fig. 1.2). The intrusive heat can also cause dehydration of hydrous minerals generating H_2O in the contact zone. This is confirmed through several studies of intrusions emplaced in both shales and coals (e.g. Simoneit *et al.*, 1978; Peters *et al.*, 1983; Bostick & Pawlewicz, 1984; Raymond & Murchison, 1988; Gurba & Weber, 2001; Drits *et al.*, 2007, Chapter 3). Contact metamorphism of organic material is discussed in more detail in Chapters 2 and 4.

1.3.3 Carbon isotopes

Organic matter contains less of the carbon isotope ^{13}C relative to ^{12}C than the average atmospheric composition due to fractionation during photosynthesis, where ^{12}C is preferred over ^{13}C because of the slight differences in weight. This difference can be expressed through $\delta^{13}C$ in ‰ by the formula:

$$\delta^{13}C = \frac{\left(^{13}C/^{12}C\right)_{\text{sample}} - \left(^{13}C/^{12}C\right)_{\text{standard}}}{\left(^{13}C/^{12}C\right)_{\text{standard}}} \times 1000. \tag{1.3.1}$$

A common standard used to express the carbon ratio is the Vienna PeeDee Belemnite (VPDB) which consequently has a $\delta^{13}C$ of 0 ‰. In the case of organic material, this ratio is much lower than that of the VPDB, and the $\delta^{13}C$ is a negative value, commonly between -15 and -25 ‰ (Whiticar, 1996).

When carbon is released during contact metamorphism, the bonds between $^{12}C - {}^{12}C$ breaks more easily than ^{12}C-^{13}C bonds, and the result is hydrocarbons with even more negative $\delta^{13}C$ values than the precursor kerogen (Clayton & Bostick, 1986; Lorant *et al.*, 1998). Because of this fractionation,

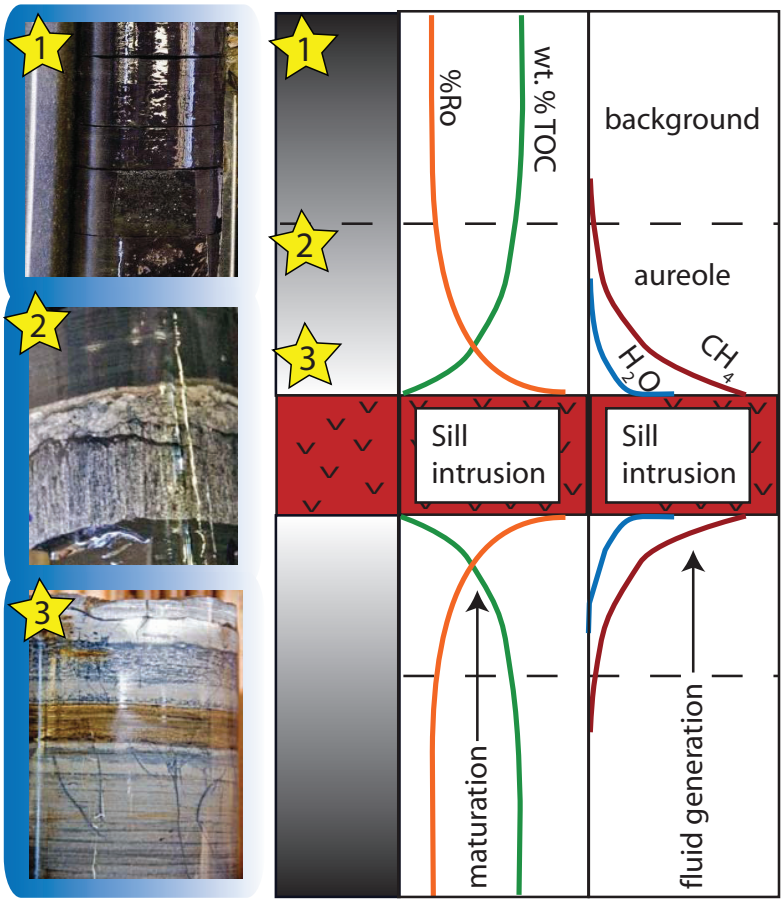

Figure 1.2: Schematic model of contact metamorphism of shales. The intrusive heating causes organic maturation seen as increased vitrinite reflectance (%Ro) and decreasing total organic carbon (TOC) towards the contacts. As a result hydrocarbons, such as methane (CH_4) is generated. The sediment heating also initiates inorganic reactions of hydrous minerals liberating H_2O.

methane has isotopic compositions ($\delta^{13}C$) ranging between -20 and -50 ‰ (Andresen *et al.*, 1995; Whiticar, 1996; Cramer *et al.*, 1998). When large amounts of ^{13}C depleted gases are released rapidly to the atmosphere, it has the potential to perturb the average isotopic carbon composition of the exogenic cycle (including the carbonate and the organic carbon cycles).

1.4 Rapid release from vast carbon reservoirs

1.4.1 The proxy records

The negative carbon-isotope excursions ($\delta^{13}C$) on the order of -2 to -8 ‰ (depending on the material analyzed and the sampling location) found in both the marine and terrestrial reservoirs characterize the

global events of LIPs and mass extinctions (Thomas & Shackleton, 1996; Jenkyns & Clayton, 1997; Gröcke *et al.*, 1999; Jenkyns *et al.*, 2001; Palfy *et al.*, 2001; Ward *et al.*, 2001; Jenkyns, 2003; Hesselbo *et al.*, 2007a). The causal process for such excursions must be fast enough and large enough to explain the carbon isotopic records (Norris & Röhl, 1999; Röhl *et al.*, 2000). This requirement can be illustrated from a simple mass balance expression for the change in $\delta^{13}C$ of the exogenic carbon cycle through time ($\Delta\delta_{Ex}/\Delta t$) (e.g. Kump & Arthur, 1999; Dickens, 2001),

$$\frac{\Delta\delta_{Ex}}{\Delta t} = \frac{F_{add}}{M_{Ex}}(\delta_{add} - \delta_{Ex}) + \frac{F_{in}}{M_{Ex}}(\delta_{in} - \delta_{Ex}) - kf \tag{1.4.1}$$

where F_{add} is the flux of added carbon (Gt C per year) with isotopic composition δ_{add} of -35‰, F_{in} is the background flux of carbon into the cycle (0.8) with a flux-weighted isotopic composition $\delta_{in} = -5$‰ (Dickens, 2001), M_{Ex} is the total mass (42 529 Gt C) in the exogenic carbon cycle (atmosphere, biosphere and oceans), k is the residence time of carbon in the system (1/100 000 years), and f is the isotopic fractionation relative to organic and carbonate carbon with a value kept constant at -9‰. The initial value for the carbon isotope composition of the total system before release δ^0_{Ex} is 0.18‰. The values are taken from Beerling *et al.* (2002) and are representative for the Early Toarcian.

We can solve for δ_{Ex} explicitly as a function of release time t by intergrating Eq. 1.4.1 with respect to time,

$$\begin{aligned}\delta_{Ex}(t) = &-\frac{\left(F_{add}\left(\delta_{add} - \delta^0_{Ex}\right) + F_{in}\left(\delta_{in} - \delta^0_{Ex}\right) - M_{Ex}kf\right)e^{\left(-\frac{(F_{add}+F_{in})t}{M_{Ex}}\right)}}{F_{add}+F_{in}} \\ &+ \frac{F_{add}\delta_{add} + F_{in}\delta_{in} - M_{Ex}kf}{F_{add}+F_{in}}\end{aligned} \tag{1.4.2}$$

Figure 1.3 shows the solution to Eq. 1.4.2 for continuous gas release (in the Toarcian) as a function of the relased mass of carbon (C) and total release time. By using this figure as a proxy for the Toarcian isotopic excursion, we can infer that in order to get isotopic excursions of -5 to -6 ‰ observed in the geological record of the Toarcian event (Hesselbo *et al.*, 2000; Beerling & Brentnall, 2007; Cohen *et al.*, 2007), the release must have occurred within maximum 200 ky.

To assume a regular, continuous release of carbon to the atmosphere might be too simplified. Indeed, the proxy records indicate that the release occurred in pulses (Kemp *et al.*, 2005). In Figure 1.4 I illustrate how the carbon excursion becomes more negative when the release occurs in pulses rather than being continuous. If the total release occurs in periods of extreme fluxes into the atmosphere, the total mass needed to generate a particular excursion decreases.

1.4.2 Thermogenic gas versus methane clathrates

There are two leading hypotheses that can explain the proxy data from among others the PETM and the Toarcian; release of methane clathrates and thermogenic gas release through pipes (Beerling & Brentnall, 2007). Methane clathrates are crystalline substances of CH_4 molecules trapped within water cages, with stabilities dependent on temperature, pressure and salinity (Kvenvolden, 1993).

An initial warming from the release of volcanic gases, potentially aided by tectonic activities or

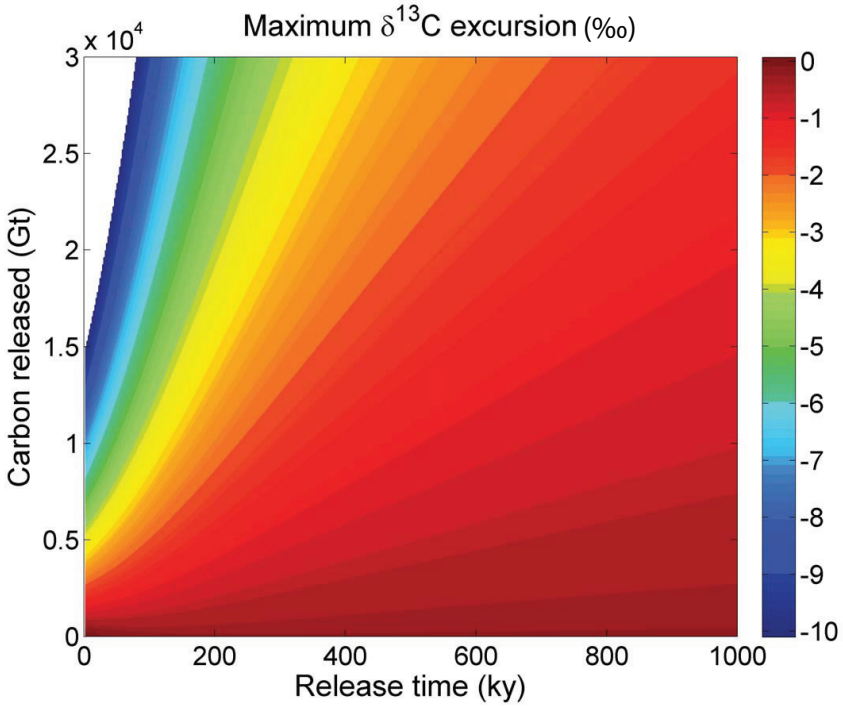

Figure 1.3: $\delta^{13}C$ excursion as function of release time (continuous) and amount of carbon released. The figure is calculated for carbon released with a $\delta^{13}C$ of -35 ‰. Other values are representative for the Toarcian global cycle, and are taken from Beerling *et al.* (2002).

sea level drop, could therefore result in clathrate instability with positive feedback to the climate (e.g. Dickens *et al.*, 1995, 1997; Hesselbo *et al.*, 2000; Beerling & Berner, 2002). This hypothesis is popular among many scientists because of: 1) the very negative isotopic signature of clathrates (average $\delta^{13}C$ of ~ -60‰), which requires much less gas mass to explain the excursions. 2) The feedback of the methane release can rise the global temperatures, causing instabilities of further clathrate packages. This will result in a pulsed release, thus reducing the required gas mass (Fig. 1.4). 3) The sizes of past clathrate reservoirs are ambiguous, but are generally thought to comprise a sufficient volume to cause the global carbon cycle perturbations.

The major dilemma or blessing with this hypothesis is that there are limited methods available to prove - or disprove - methane clathrate gas release, as it would leave few traces in the geological record other than the isotopic signature. Moreover, the model requires a triggering mechanism which is a weakness of this hypothesis.

The hypothesis of thermogenic gas release during contact metamorphism as a consequence of LIP formation was developed on the basis of seismic data showing disrupted hydrothermal vent complexes and breccia pipes originating from sill intrusions (Svensen *et al.*, 2004). Breccia pipes are cylindrical pipe-structures, generally between 20 and 150 m in diameter, formed in the contact aureoles of sills that

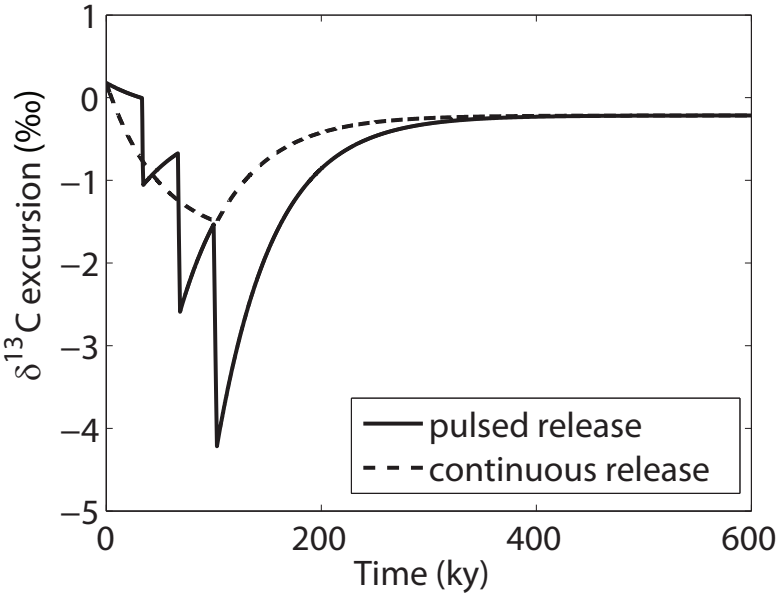

Figure 1.4: Illustration of negative carbon excursions as a result of continuous and pulsed release of methane. A total mass of 5000 Gt is released over 100 000 years into the Toarcian exogenic carbon cycle. The continuous release yields a maximum excursion of -1.5 ‰, while a release of three 1000 years pulses over the same interval results in a -4.2 ‰ excursion.

intruded organic-rich sedimentary formations (e.g. Svensen *et al.*, 2007, 2008, 2009). Hydrothermal vent complexes are used to denote less than 1 km deep pipes related to boiling and expansion of pore-fluids (Jamtveit *et al.*, 2004; Svensen *et al.*, 2006).

Such pipes, or vents, must be the result of local pressure build-up (Jamtveit *et al.*, 2004; Svensen *et al.*, 2006; Rozhko *et al.*, 2007). An effective way of generating overpressures deeper than 1 km is to break down organic material stored in the sedimentary rocks into mobile hydrocarbons. There will be sufficient heat for the devolatilization reactions to occur as the melts are protruding sideways and upwards throughout the sedimentary basin. The hydrocarbons would then be pulsed out to the atmospheric cycle over a relatively short time-span through the breccia pipes. Furthermore, it is likely that an initial warming by thermogenic gas release could trigger further destabilization of methane clathrates by a positive feedback-mechanism (Svensen *et al.*, 2004; Cohen *et al.*, 2007).

This model provides the background skeleton to some of the problems addressed in this thesis. The pipe-structures are observed and mapped, the loss of organic content towards intrusion contacts are well documented and the timing of the intrusive events are within the same time-frame as the negative carbon excursions. Now remain the questions of 1) how much gas can be generated from sill intrusions, 2) what is the nature of the contact metamorphism of shales in a volcanic basin, and 3) what is the magnitude of the pressure building up from devolatilization? Further physical and chemical implications of the pressure anomalies developing in and around the intrusions during contact metamorphism are explored in the two last chapters of this thesis.

1.5 Modeling of contact metamorphism

All of the chapters in this thesis include numerical modeling. This section gives a brief introduction to modeling of heat transfer coupled to organic maturation, which is a key topic in Chapters 2 and 3. More detailed modeling descriptions are given in the relevant chapters.

Cooling of a sheet intrusion is a well known process studied by both numerical and analytical methods (e.g. Jaeger & Cook, 1979; Turcotte & Schubert, 2002). The basic equation for conductive heat transfer is called Fourier's law and can be written

$$q_T = -\lambda \nabla T \tag{1.5.1}$$

which states that the heat flux q_T is proportional to the thermal gradient ∇T with a constant of proportionality λ i.e. the heat conductivity coefficient. The negative sign arises because the heat flux goes from hot to cold areas, i.e. down along the thermal gradient.

The heat flow equation describes the temporal evolution of the temperature,

$$\rho Cp \frac{\partial T}{\partial t} = \nabla (\lambda \nabla T) \tag{1.5.2}$$

where Cp is specific heat capacity and ρ is density, stating that the rate of temperature change is proportional to the difference between heat flux in and out of the system (i.e. the gradient of the thermal flux).

The equation describes a continuous temperature field, while in a numerical model the system is divided into tiny fractions in space (Δx, i.e. x-direction only assuming a 1D model) and time (Δxt). Hence, the equation is discretized in order to solve it numerically,

$$\frac{T^{\text{new}} - T^{\text{old}}}{\Delta t} = \frac{\lambda}{\rho Cp} \left(\frac{T_{i+1}^{\text{old}} - 2T_i^{\text{old}} + T_{i-1}^{\text{old}}}{\Delta x^2} \right) \tag{1.5.3}$$

where i defines the position on the regular numerical grid, $\Delta x = x_i - x_{i-1} = x_{i+1} - x_i$. There are several methods available for discretization of such a partial differential equation, and this method is usually referred to as finite difference explicit model. Explicit refers to the fact that the temperature on the right hand side of Eq. 1.5.3 is the old temperature. Both explicit finite difference and implicit finite element methods are utilized in this thesis.

The details of organic maturation and kerogen cracking is poorly understood due to the complex nature of precursor material (i.e. life) (Peters *et al.*, 2006). Luckily, it has been shown that for a wide range of geological processes the organic reactions can be approximated by a first order reaction kinetics following the Arrhenius law,

$$k = A \exp(-E/RT) \tag{1.5.4}$$

(Burnham & Sweeney, 1989; Sweeney & Burnham, 1990), where k is the reaction rate, A is the prefactor, E is the activation energy and R is the universal gas constant. One can think of the kinetic system as balls rolling back and forth in a half-cylinder, and that A is the total number of rolling balls, $\exp(-E/RT)$ is the hight of the cylinder wall and k is the rate of balls rolling out of the half-cylinder (i.e. reactions

occurring). The rate of change in organic material W converted into hydrocarbons is,

$$\frac{\partial W}{\partial t} = kW. \tag{1.5.5}$$

Implicit discretization of this equation (Eq. 1.5.5) gives,

$$W^{\text{new}} = \frac{W^{\text{old}}}{(1-k\Delta t)}, \tag{1.5.6}$$

where W^{new} is the amount of convertible organic matter left after a given time. Eq. 1.5.5 is coupled to Eq. 1.5.3 through temperature T.

1.6 Equilibrium thermodynamics

Thermodynamic relations are utilized in Chapter 4. Here we present a brief overview of some key thermodynamic concepts, such as the first and second law of thermodynamics, and local thermodynamic equilibrium.

The first law of thermodynamics is a statement based on conservation of energy. There are all sorts of mechanisms by which energy can be put into or taken out of a system. In thermodynamics, these mechanisms are usually classified under two categories, heat (Q) and work (W). Heat is defined as any spontaneous flow of energy from one object to another caused by a temperature difference. Work in thermodynamics is defined as any other transfer of energy into or out of a system. The first law of thermodynamics states that there exists a quantity called internal energy (U) that changes both due to work done on the system and the heat transfer in the system,

$$dU = dQ + dW. \tag{1.6.1}$$

If the only work that is done on the system is compression-work in a quasi-static system, we can rewrite the work term by considering work = force$\times$distance = pressure (P) $\times$ volume change (dV), i.e.

$$dW = -PdV. \tag{1.6.2}$$

The negative sign comes from the convention that work done on the system should be positive, although positive work gives a negative volume change (i.e. volume decrease). The system is quasistatic in the sense that the process is slow enough for the system to continuously equilibrate to the changing conditions.

The second law of thermodynamics states the change in a quantity called entropy (S) can be related to the amount of heat transferred between a system and its surroundings. For a system undergoing a reversible process the second law can be written

$$dS = dQ/T. \tag{1.6.3}$$

Reversible processes are defined as continuous successions of equilibrium states, which means that a

system changes from one equilibrium state to another, without ever leaving equilibrium. The reversible process can be described as an imaginary path between two states that are used for calculation of the energy difference between those states.

There are many formulations of the second law, and another part of this law is that the entropy will never decrease, but can remain constant (for reversible processes) or increase (for irreversible processes). Irreversible processes are referring to systems going from a higher energy state to a lower energy state. It does not mean that the system cannot revert back to a higher energy state, but that it will not be a spontaneous process. Because energy is conserved, this energy loss is actually an entropy gain. Thus, for any process we can write,

$$dS \geq 0 \tag{1.6.4}$$

Considering only reversible processes, the first and second laws of thermodynamics can be combined to give

$$dU = TdS - PdV. \tag{1.6.5}$$

This is the fundamental equation that relates energy changes to the state variables S, T, V and P for a closed system. This equation can be extended to include other types of work such as chemical work relating chemical potential and concentration, and mechanical work relating deviatoric strain and changes in volume fractions (i.e. porosity).

Eq. 1.6.5 is defined for a total system in equilibrium. It means that there are no gradients in temperature, pressure or composition. This is an unlikely state for geological systems almost constantly in some kind of flux of e.g. heat and matter. We still want to apply thermodynamics to these systems. We can divide our system into parts that are small enough and where the changes are slow enough that we can assume equilibrium in that local fraction of the system. This local equilibrium is not part of the thermodynamics, but a concept we apply in order to solve our system.

Our system should not depend on the amount of mass in our system, i.e. the variables we use for local equilibrium should be intensive. We can make the extensive variables in Eq. 1.6.5 intensive by normalizing them by unit mass,

$$du = Tds - Pd(1/\rho), \tag{1.6.6}$$

where u is specific internal energy, s is specific entropy and $1/\rho$ is specific volume. Hence we can apply our assumption of local thermodynamic equilibrium to all the variables in our system. This makes it possible to solve systems that are not in global equilibrium, i.e. systems in which transport processes such as heat and fluid flow occur.

1.7 Unresolved questions

Geologists recognized more than a century ago that rocks lose volatile compounds such as H_2O and CO_2 during metamorphism (Dana, 1863). However there are still many unresolved questions linked to prograde metamorphism and emplacement of igneous intrusions in sedimentary basins.

First of all there is a general deficiency in integrated studies concentrating on both organic and inorganic effects of the intrusions, with only a few good examples (e.g. Finkelman *et al.*, 1998; Drits

et al., 2007). The major focus is commonly localized effects of single, relatively thin intrusions on organic matter (e.g. Bostick, 1979; Simoneit *et al.*, 1978; Perregaard & Schiener, 1979; Bostick & Pawlewicz, 1984; Clayton & Bostick, 1986; Saxby & Stephenson, 1987; Bishop & Abbott, 1995). The extent of the thermal aureoles is commonly discussed in the papers, and conclusions vary significantly for the different study areas. Systematic evaluations of aureole development are surprisingly rare, with only a few exceptions (e.g. Raymond & Murchison, 1988; Barker *et al.*, 1998). In order to make a global statement of the thermal aureoles, we need to identify the major processes influencing the aureole thicknesses.

Thermal modeling is a common method to quantify the extent of contact metamorphism around intrusions (e.g. Jaeger, 1959; Delaney, 1982; Barker & Bone, 1995; Bishop & Abbott, 1995; Barker *et al.*, 1998; Dutrow *et al.*, 2001). It is however less common to couple the thermal evolution with kinetic modeling of organic reactions to estimate the actual effect on organic maturation (Braun & Burnham, 1987; Sweeney & Burnham, 1990; Galushkin, 1997; Kjeldstad *et al.*, 2003; Fjeldskaar *et al.*, 2008). None of the aureole models have been used to quantify the organic and inorganic devolatilization reactions on a larger scale, and only limited estimates of how much gas can actually be released from shales due to sill intrusions exist (e.g. Svensen *et al.*, 2004, 2007).

In a volcanic basin multiple intrusions could significantly alter the thermal regime (e.g. Hanson & Barton, 1989). Further quantification of the effect of multiple sills on the total organic maturation in a volcanic basin, such as the Karoo Basin, is therefore needed.

Although we know that fluid overpressure can be generated in a contact aureole from for example the presence of fractures, there are limited studies quantifying the pressure buildup in the contact aureoles (e.g. Litvinovski *et al.*, 1990; Hanson, 1995; Jamtveit *et al.*, 2004). It is however well recognized that devolatilization reactions can induce overpressure during regional metamorphism (e.g. Walther & Orville, 1982; Connolly, 1997; Osborne & Swarbrick, 1997; Ague *et al.*, 1998; Balashov & Yardley, 1998).

One feature related to overpressure in the aureole is the formation of sandstone dikes intruding into the igneous sills (Walton & O'Sullivan, 1950; Van Biljon & Smitter, 1956). Although overpressure can be explained by e.g. boiling and expansion of porefluids (e.g. Delaney, 1982; Kokelaar, 1982), there are no explanation why sandstone dikes should preferentially intrude into the sill from both above and below, irrespective of gravity.

Zooming in from the global effects of contact metamorphic gas generation to the aureole processes and further into interaction between the aureole and the sill, we arrive at the processes occurring within the cooling sill. For a long time the question of reversed geochemical differentiation (D-shaped profiles) within tholeiitic intrusions have been a question of continued debate (Latypov, 2003, , and references therein). Proposed mechanisms range from crystal settling (Simkin, 1967) and multiple intrusions (Gibb & Henderson, 1992) to a combination of thermal and compositional convection (Kerr & Tait, 1986; Tait & Jaupart, 1992; Jaupart & Tait, 1995). The latter model suggests an important contribution of melt-movement to the differentiation process. If we know that there are pressure anomalies in the aureole we could potentially think of pressure anomalies also existing within the sill. To our knowledge no-one has investigated the generation of pressure anomalies within a sill, and the influence of pressures on the melt flow. Such pressure-induced flow can have important implications for our interpretation of geochemical

differentiation.

1.8 Introduction to the chapters

This thesis is a collection of papers, either accepted (Chapter 2), submitted (Chapter 3), ready for submission (Chapter 4), in press (Chapter 5) or published (Chapter 6). The chapters are arranged from global impacts and basin-scale considerations to local aureole and sill processes, where Chapters 2 and 3 encompass contact metamorphism of shales in sedimentary basins, Chapter 4 couples contact metamorphism to pressure, and Chapters 5 and 6 consider some implications of the pressure anomalies.

The first paper in this thesis entitled '*How contact metamorphism can trigger global climate changes: Modeling gas generation around igneous sills in sedimentary basins*' explores the nature of contact metamorphism in shales by compiling previous studies, and by developing a numerical model to describe organic and inorganic reactions during contact metamorphism (Chapter 2). The model is applied to calculate gas generation on a basin scale, and to discuss the potential global implications.

This paper aligns itself in the debate regarding global climate changes associated with LIPs, with the major focus on the Karoo Basin ($\sim$183 Ma) and the Vøring and Møre basins ($\sim$55 Ma). From upscaling of gas generation around one intrusion to basin scale, we show that the amount of carbon gas that can be generated is on the order of 10^3 to 10^4 Gt methane (CH_4), depending on the initial organic content in the sediment and the size of the basin. The magnitudes are compatible with the proxy data from each time period, and thus conclude in favor of thermogenic gas release as an important mechanism inducing global climate change. Such estimates based on actual calculations are not available in the existing literature.

Before drawing this conclusion we go through a large set of published studies related to sill intrusions into organic-rich sediments to look for systematic characteristics of aureoles. From this compilation we can make global statements about fluid production in the sedimentary basin, and compare the model with the existing data. By first sight it seems to be no 'rule of thumb' between the sill thickness and aureole thickness. However, from several numerical calculations we discover that the lack of clear correlations are due to the fact that the aureole thickness also has a strong dependence on initial temperature of the host-rock, and to some degree the temperature of the intrusion. The nature of this relationship is deduced from linear regression of $\sim$1500 model runs.

In addition to the kinetic modeling of organic reactions we use mineral equilibria calculated using Perple_X (Connolly, 2005) to model dehydration reactions, and compare the relative amounts. We use these results in combination with fluid-fluid equilibrium calculations to show that the expected fluid composition will tend towards a CH_4-dominated fluid and a H_2O-dominated fluid.

The second paper entitled '*Contact metamorphic devolatilization of shales in the Karoo Basin, South Africa, and the effects of multiple sill intrusions*' investigates the details of contact metamorphism by presenting two case studies from the organic-rich shale formations in the Karoo Basin, South Africa (Chapter 3). The first case study is used to constrain the model introduced in the first paper. The model is also extended to encompass multiple (2-5) sills, backed up by data from the second case study. The

main aim is to establish the effects of multiple intrusions on the organic maturation and devolatilization in the basin.

This paper backs up on the conclusions from the first paper, by showing that the numerical model explains well data from organic-rich Jurassic shales affected by the Karoo-Ferrar LIP about 183 Ma. Furthermore, it suggest that the gas generation potential based on one sill in the first paper could be a lower estimate, as multiple levels of sill intrusions cause elevated hydrocarbon generation throughout the intruded formations. The effects of multiple sills on the fluid production potential have to our knowledge not been constrained before.

We show that two simultaneously emplaced sills can generate up to 35% more CH_4 than two single sills. One implication of this is that in a sedimentary basin intruded by a LIP, metamorphism is no longer localized at the sill contacts, but can extend over the whole basin. Multiple intrusions are equivalent of having a higher background temperature in the host-rock, which from the first paper is shown to be an important factor determining the extent of the aureole.

We have less data to constrain the dehydration modeling, but the presence of metamorphic minerals such as biotite and epidote and the decreasing clay content towards the contact suggest dehydration of even more hydrous minerals within 1-2 meters away from a 10 meter thick intrusion. This is supported by the numerical model, where we show that the generation of H_2O from mineral dehydration is more localized to the aureoles than the CH_4-generation from breakdown of organic matter.

The presence of an extensive fracture network and breccia pipes originating in the aureoles of the shale formations supports devolatilization and generation of overpressure.

The third paper entitled '*Fluid overpressure and rate of devolatilization during metamorphism*' couples the devolatilization reactions in shales with pressure generation in the aureole by the usage of analytical and numerical methods (Chapter 4). The main aim is to establish a new analytical solution coupling reaction induced overpressure generation and fluid flow. The model is applied to evaluate the feedback of overpressure on the reactions, and to find conditions for aureole fracturing and vent-formation related to massive degassing of the aureole.

The first and second paper concluded on extensive devolatilization of the contact metamorphic shales. This paper deals with the effect of such devolatilization on the fluid pressure and the related escape of the fluids to the atmosphere. The analytical solutions show that for generation of low-density CH_4 gas in low-permeable systems such as shales, fracturing and venting are likely to occur. This is important for the thermogenic gas model, as the proxy data is best explained by a rapid release.

The derivations presented in this paper are based on very few assumptions, and the basic equations of temperature, pressure and fluid flow are derived from conservation of mass, momentum and energy, and are thermodynamically admissible. The equations are consistent with the equations used in this thesis, and thus this paper provides a theoretical basis for the whole study.

This paper uses a known analytical solution for the diffusion-equations to solve for the temperature evolution of a sill intrusion with latent heat of crystallization. The novel thing in the analytical solutions is coupling of a temperature driven reaction front with a net volume change with fluid pressure evolution and fluid flow. We thus obtain an exact solution for the overpressure at the front. The efficiency of the volume changing reaction building up the overpressure relative to the efficiency of the fluid flow

reducing the overpressure determines the overpressure at the reaction front.

The dynamics of the reaction front are determined by the degree of host-rock heating before the reaction occurs, the pressure-dependency of the reaction and the magnitude of the overpressure. If the overpressure is large enough, the equilibrium conditions for the reactions are shifted towards higher reaction temperatures, and thus more heating is required for the reaction to proceed. This may ultimately terminate the reaction.

The fourth paper entitled '*Sandstone dikes in dolerite sills: Evidence for high pressure gradients and sediment mobilization during solidification of magmatic sheet intrusions in sedimentary basins*' examines the interaction between the overpressure in the heated aureole and the corresponding underpressure in the cooling sill through sandstone dike injections into the sill (Chapter 5). The paper integrates field work, geochemical data, mineral equilibria calculations and numerical modeling of thermal stresses related to sill cooling and aureole heating to investigate the intrusion mechanism of the sandstone dikes.

This paper focuses on local processes related to pressure anomalies generated during sill cooling and the implications for sediment and fluid transport. The main concepts utilized in this paper are the interaction between overpressure in the aureole described in the third paper (Chapter 4) and the underpressure in the crystallizing sill introduced in the fifth paper (Chapter 6). We show that the down-pressure gradients going from the aureole and into the sill cause a favorable directional pathway for sandstone dikes to intrude into the sill, both from above and below. This is a novel idea which can have further implications for the interactions between magmatic and aureole processes. This study provides further evidence for generation of aureole overpressure. The overpressure generation causing sandstone fluidization is most likely governed by boiling and expansion of existing pore-fluids rather than devolatilization reaction. However, it is the same basic physics of a fluid pressure source related to the positive net volume change of a reaction.

Furthermore, we calculate the phase equilibria similar to those introduced in the first paper and compare it to the mineral assemblages of the presented sandstone dikes to constrain the peak metamorphic conditions. We use the peak metamorphic condition to constrain the timing of sediment dyke intrusions.

The fifth paper entitled '*Post-emplacement melt flow induced by thermal stresses: Implications for differentiation in sills*' delves into the processes within the sill itself and presents a new mechanism for magmatic differentiation related to thermal stresses and underpressure within the sill (Chapter 6). It is an integrated study of geochemical analyses, modeling of thermal stresses and the model is applied to deduce geochemical changes arising from underpressure-driven melt flow within the crystal network.

This paper deals with processes within the crystallizing sill. The model is based on the same governing principles applied in Chapter 4 and 5, i.e. temperature-driven pressure anomalies and the implications for chemical reactions. Using the same physical laws as with the well established overpressure generation, we show that for reactions with a net negative volume change the result is a fluid underpressure. The preferred injection of overpressurized sandstone dikes into the sills, regardless of the direction of gravitational force, supports the existence of underpressure in the sills (Chapter 5).

The net negative volume change within the sill relates to the phase transition of melt to crystals upon magma cooling. When melt crystallizes the density increases. However, if crystallization occurs within a strong crystal network, the rigid crystals provide a strong surrounding frame that cannot contract enough to adjust to the volume decrease associated with the density increase. The result is a fluid underpressure. The crystal network thus plays a similar role as the host-rock sediment matrix for the limited accommodation of the volume change of the reactions.

The result will be a a sucking force, promoting porous flow of melt towards within the zone of crystallization. Segregation of crystals from its equilibrium melt is a well known phenomenon that creates magmatic differentiation. Traditionally this transport is attributed to the crystals moving away from the melt, while we propose that this transport might as well go the other way around. The movement of more primitive melt from the center and into the sill margins successfully explains why the composition at the margins is more primitive at exactly the margins relative to the center, i.e. reversed differentiation.

1.9 Outlook

- There is still a long way to go before getting good flux estimates of the carbon gases to the atmosphere. Combining the reactions solved in the two first papers with the solutions in the third paper will put further constraints on the release mechanisms and fluxes.
- Another angle of approach that could help estimating the carbon flux is to constrain the effect of melt emplacement rates on gas generation and shale maturation.
- A quantification of the effects of relative emplacement timing between intrusions is the next step in the evaluation of the implications of multiple intrusions.
- We assume that the data collected in the Karoo Basin is representative for the sill intrusion event. However, we have little constrain on what happened in the 180 Ma after the volcanic event. This could be investigated by making a full basin model. Such model could help constrain further the paleodepth, as this is difficult to do with traditional methods such as vitrinite reflectance, due to the overall elevated organic maturation in the basin.
- The analytical solutions can be expanded to include a finite sill length, which could then account for longer term effects also after crystallization of the sill. Alternatively, this can easily be done numerically.
- There are some processes that are not considered and that may play a role on a longer time scale, such as compaction driven flow, and advective processes related to for example the breccia-pipes. Advective processes can be important when convective systems develop and the host-rock permeabilities are high. It would be interesting to investigate the effect of extensive fluid flow by coupling of the fluid pressure and flow to temperature and contact metamorphism.
- The analytical model developed in Chapter 4 could be expanded to also include underpressure development in the intrusion. Such extension will be valuable in constraining interactions between

the intrusion and the host-sediment, and evaluate the potential for magma contamination. Such model will be the next logical step in developing the melt-flow differentiation model further.

- A more close coupling between chemical reactions in general and the processes already considered in Chapter 4 will give a powerful tool that can be applied to investigate an array of geological processes.

REFERENCES

AGUE J.J., PARK J. & RYE D.M. (1998) Regional Metamorphic Dehydration and Seismic Hazard. *Geophysical Research Letters*, **25**.

ANDRESEN B., THRONDSEN T., RÅHEIM A. & BOLSTAD J. (1995) A comparison of pyrolysis products with models for natural gas generation. *Chemical Geology*, **126**, 261–280.

ARTHUR M.A., DEAN W.E. & PRATT L.M. (1988) Geochemical and Climatic Effects of Increased Marine Organic-Carbon Burial at the Cenomanian Turonian Boundary. *Nature*, **335**, 714–717.

BAILEY T.R., ROSENTHAL Y., MCARTHUR J.M., VAN DE SCHOOTBRUGGE B. & THIRLWALL M.F. (2003) Paleoceanographic changes of the Late Pliensbachian-Early Toarcian interval: a possible link to the genesis of an Oceanic Anoxic Event. *Earth and Planetary Science Letters*, **212**, 307–320.

BALASHOV V.N. & YARDLEY B.W.D. (1998) Modeling metamorphic fluid flow with reaction-compaction-permeability feedbacks. *American Journal of Science*, **298**, 441–470.

BARKER C.E. & BONE Y. (1995) The minimal response to contact metamorphism by the Devonian Buchan Caves Limestone, Buchan Rift, Victoria, Australia. *Organic Geochemistry*, **22**, 151–164.

BARKER C.E., BONE Y. & LEWAN M.D. (1998) Fluid inclusion and vitrinite-reflectance geothermometry compared to heat-flow models of maximum paleotemperature next to dikes, western onshore Gippsland Basin, Australia. *International Journal of Coal Geology*, **37**, 73–111.

BEERLING D.J. & BERNER R.A. (2002) Biogeochemical constraints on the Triassic-Jurassic boundary carbon cycle event. *Global Biogeochemical Cycles*, **16**.

BEERLING D.J. & BRENTNALL S.J. (2007) Numerical evaluation of mechanisms driving Early Jurassic changes in global carbon cycling. *Geology*, **35**, 247–250.

BEERLING D.J., HARFOOT M., LOMAX B. & PYLE J.A. (2007) The stability of the stratospheric ozone layer during the end-Permian eruption of the Siberian Traps. *Philosophical Transactions of the Royal Society A: Mathematical, Physical and Engineering Sciences*, **365**, 1843–1866.

BEERLING D.J., LOMAS M.R. & GROCKE D.R. (2002) On the nature of methane gas-hydrate dissociation during the Toarcian and Aptian Oceanic anoxic events. *American Journal of Science*, **302**, 28–49.

BEHAR F., KRESSMANN S., RUDKIEWICZ J.L. & VANDENBROUCKE M. (1992) Experimental Simulation in a Confined System and Kinetic Modeling of Kerogen and Oil Cracking. *Organic Geochemistry*, **19**, 173–189.

BEHAR F. & VANDENBROUCKE M. (1987) Chemical Modeling of Kerogens. *Organic Geochemistry*, **11**, 15–24.

BENTON M.J. & TWITCHETT R.J. (2003) How to kill (almost) all life: the end-Permian extinction event. *Trends in Ecology & Evolution*, **18**, 358–365.

BERNER R.A. (2002) Examination of hypotheses for the Permo-Triassic boundary extinction by carbon cycle modeling. *Proceedings of the National Academy of Sciences*, **99**, 4172–4177.

BISHOP A.N. & ABBOTT G.D. (1995) Vitrinite Reflectance and Molecular Geochemistry of Jurassic Sediments - the Influence of Heating by Tertiary Dykes (Northwest Scotland). *Organic Geochemistry*, **22**, 165–177.

BOSTICK N.H. (1979) Microscopic measurement of the level of catagenesis of solid organic matter in sedimentary rocks to aid exploration for petroleum and to determine former burial temperatures – a review. In: *Aspects of Diagenesis, S.E.P.M Special Publication* (Ed. P.A. Scholle & P.R. Schluger), vol. 26, 17–43.

BOSTICK N.H. & PAWLEWICZ M.J. (1984) Paleotemperatures based on vitrinite reflectance of shales and limestones in igneous dike aureoles in the Upper Cretaceous Pierre Shale, Walsenburg, Colorado. In: *Hydrocarbon Source Rocks of the Greater Rocky Mountain Region* (Ed. J.G. Woodward, F.F. Meissner & C.J. Clayton), 387–392. Rocky Mountain Association of Geologists.

BRAUN R.L. & BURNHAM A.K. (1987) Analysis of Chemical-Reaction Kinetics Using a Distribution of Activation-Energies and Simpler Models. *Energy & Fuels*, **1**, 153–161.

BROECKER W.S. (1975) Climatic Change: Are We on the Brink of a Pronounced Global Warming? *Science*, **189**, 460–463.

BURNHAM A.K. & SWEENEY J.J. (1989) A Chemical Kinetic-Model of Vitrinite Maturation and Reflectance. *Geochimica Et Cosmochimica Acta*, **53**, 2649–2657.

CATUNEANU O., HANCOX P.J. & RUBIDGE B.S. (1998) Reciprocal flexural behaviour and contrasting stratigraphies: a new basin development model for the Karoo retroarc foreland system, South Africa. *Basin Research*, **10**, 417–439.

CHEVALLIER L. & WOODFORD A. (1999) Morpho-tectonics and mechanism of emplacement of the dolerite rings and sills of the Western Karoo, South Africa. *South African Journal of Geology*, **102**, 43–54.

CLAYTON J.L. & BOSTICK N.H. (1986) Temperature effects on kerogen and on molecular and isotopic composition of organic matter in Pierre Shale near an igneous dike. *Organic Geochemistry*, **10**, 135–143.

COHEN A.S., COE A.L. & KEMP D.B. (2007) The Late Palaeocene Early Eocene and Toarcian (Early Jurassic) carbon isotope excursions: a comparison of their time scales, associated environmental changes, causes and consequences. *Journal of the Geological Society*, **164**, 1093–1108.

COLE D.I. (1992) Evolution and Development of the Karoo Basin. *Inversion Tectonics of the Cape Fold Belt, Karoo and Cretaceous Basins of Southern Africa*, 87–99.

CONNOLLY J.A.D. (1997) Devolatilization-generated fluid pressure and deformation-propagated fluid flow during prograde regional metamorphism. *Journal of Geophysical Research-Solid Earth*, **102**, 18149–18173.

CONNOLLY J.A.D. (2005) Computation of phase equilibria by linear programming: A tool for geodynamic modeling and its application to subduction zone decarbonation. *Earth and Planetary Science Letters*, **236**, 524–541.

COURTILLOT V.E. & RENNE P.R. (2003) On the ages of flood basalt events. *Comptes Rendus Geosciences*, **335**, 113–140.

CRAMER B., KROOSS B.M. & LITTKE R. (1998) Modelling isotope fractionation during primary cracking of natural gas: a reaction kinetic approach. *Chemical Geology*, **149**, 235–250.

DANA J.D. (1863) *Manual of Geology*. Theodore Bliss, Philadelphia.

DELANEY P.T. (1982) Rapid Intrusion of Magma into Wet Rock - Groundwater-Flow Due to Pore Pressure Increases. *Journal of Geophysical Research*, **87**, 7739–756.

DICKENS G.R. (2001) Carbon addition and removal during the Late Palaeocene Thermal Maximum: basic theory with a preliminary treatment of the isotope record at ODP Site 1051, Blake Nose. *Geological Society, London, Special Publications*, **183**, 293–305.

DICKENS G.R., CASTILLO M.M. & WALKER J.C.G. (1997) A blast of gas in the latest Paleocene: Simulating first-order effects of massive dissociation of oceanic methane hydrate. *Geology*, **25**, 259–262.

DICKENS G.R., ONEIL J.R., REA D.K. & OWEN R.M. (1995) Dissociation of Oceanic Methane Hydrate as a Cause of the Carbon-Isotope Excursion at the End of the Paleocene. *Paleoceanography*, **10**, 965–971.

DIECKMANN V., SCHENK H.J., HORSFIELD B. & WELTE D.H. (1998) Kinetics of petroleum generation and cracking by programmed-temperature closed-system pyrolysis of Toarcian Shales. *Fuel*, **77**, 23–31.

DOW W.G. (1977) Kerogen studies and geological interpretations. *Journal of Geochemical Exploration*, **7**, 79–99.

DRITS V.A., LINDGREEN H., SAKHAROV B.A., JAKOBSEN H.J., FALLICK A.E., SALYN A.L., DAINYAK L.G., ZVIAGINA B.B. & BARFOD D.N. (2007) Formation and transformation of mixed-layer minerals by tertiary intrusives in cretaceous mudstones, West Greenland. *Clays and Clay Minerals*, **55**, 260–283.

DUNCAN R., HOOPER P., REHACEK J., MARSH J. & DUNCAN A. (1997) The timing and duration of the Karoo igneous event, southern Gondwana. *Journal of Geophysical Research*, **102, B8**, 18127–18138.

DURAND B. (1980) *Kerogen: insoluble organic matter from sedimentary rocks*. Editions Technip.

DUTROW B.L., TRAVIS B.J., GABLE C.W. & HENRY D.J. (2001) Coupled heat and silica transport associated with dike intrusion into sedimentary rock: effects on isotherm location and permeability evolution. *Geochimica et Cosmochimica Acta*, **65**, 3749–3767.

FALKOWSKI P., SCHOLES R.J., BOYLE E., CANADELL J., CANFIELD D., ELSER J., GRUBER N., HIBBARD K., HOGBERG P., LINDER S., MACKENZIE F.T., MOORE B. I., PEDERSEN T., ROSENTHAL Y., SEITZINGER S., SMETACEK V. & STEFFEN W. (2000) The Global Carbon Cycle: A Test of Our Knowledge of Earth as a System. *Science*, **290**, 291–296.

FINKELMAN R.B., BOSTICK N.H., DULONG F.T., SENFTLE F.E. & THORPE A.N. (1998) Influence of an igneous intrusion on the inorganic geochemistry of a bituminous coal from Pitkin County, Colorado. *International Journal of Coal Geology*, **36**, 223–241.

FJELDSKAAR W., HELSET H.M., JOHANSEN H., GRUNNALEITEN I. & HORSTAD I. (2008) Thermal modelling of magmatic intrusions in the Gjallar Ridge, Norwegian Sea: implications for vitrinite reflectance and hydrocarbon maturation. *Basin Research*, **20**, 143–159.

GALERNE C.Y., NEUMANN E.R., AARNES I. & PLANKE S. (2010) Magmatic differentiation processes in saucer-shaped sills: Evidence from the Golden Valley Sill in the Karoo Basin, South Africa. *Geosphere*, **in press**.

GALERNE C.Y., NEUMANN E.R. & PLANKE S. (2008) Emplacement mechanisms of sill complexes: Information from the geochemical architecture of the Golden Valley Sill Complex, South Africa. *Journal of Volcanology and Geothermal Research*, **177**, 425–440.

GALUSHKIN Y.I. (1997) Thermal effects of igneous intrusions on maturity of organic matter: A possible mechanism of intrusion. *Organic Geochemistry*, **26**, 645–658.

GANINO C. & ARNDT N.T. (2009) Climate changes caused by degassing of sediments during the emplacement of large igneous provinces. *Geology*, **37**, 323–326.

GIBB F. & HENDERSON C. (1992) Convection and crystal settling in sills. *Contributions to Mineralogy and Petrology*, **109**, 538–545.

GRÖCKE D.R., HESSELBO S.P. & JENKYNS H.C. (1999) Carbon-isotope composition of Lower Cretaceous fossil wood: Ocean-atmosphere chemistry and relation to sea-level change. *Geology*, **27**, 155–158.

GURBA L.W. & WEBER C.R. (2001) Effects of igneous intrusions on coalbed methane potential, Gunnedah Basin, Australia. *International Journal of Coal Geology*, **46**, 113–131.

HANSON R.B. (1995) The hydrodynamics of contact-metamorphism. *Geological Society of America Bulletin*, **107**, 595–611.

HANSON R.B. & BARTON M.D. (1989) Thermal Development of Low-Pressure Metamorphic Belts - Results from Two-Dimensional Numerical-Models. *Journal of Geophysical Research-Solid Earth and Planets*, **94**, 10363–10377.

HESSELBO S.P., GROCKE D.R., JENKYNS H.C., BJERRUM C.J., FARRIMOND P., BELL H.S.M. & GREEN O.R. (2000) Massive dissociation of gas hydrate during a Jurassic oceanic anoxic event. *Nature*, **406**, 392–395.

HESSELBO S.P., JENKYNS H.C., DUARTE L.V. & OLIVEIRA L.C.V. (2007a) Carbon-isotope record of the Early Jurassic (Toarcian) Oceanic Anoxic Event from fossil wood and marine carbonate (Lusitanian Basin, Portugal). *Earth and Planetary Science Letters*, **253**, 455–470.

HESSELBO S.P., JENKYNS H.C., DUARTE L.V. & OLIVEIRA L.C.V. (2007b) Reply to comment on "Carbon-isotope record of the Early Jurassic (Toarcian) oceanic anoxic event from fossil wood and marine carbonate (Lusitanian Basin, Portugal)". *Earth and Planetary Science Letters*, **259**, 640–641.

HESSELBO S.P., ROBINSON S.A., SURLYK F. & PIASECKI S. (2002) Terrestrial and marine extinction at the Triassic-Jurassic boundary synchronized with major carbon-cycle perturbation: A link to initiation of massive volcanism? *Geology*, **30**, 251–254.

HUNT J.M. (1996) *Petroleum Geochemistry and Geology (Second Edition)*. W.H. Freeman and Company, 2nd edn.

IPCC (2007) *Climate Change 2007 - The Physical Science Basis, Contribution of Working Group I to the Fourth Assessment Report of the IPCC*. Cambridge University Press.

JAEGER J. (1959) Temperatures outside a cooling intrusive sheet. *American Journal of Science*, **257**, 44–54.

JAEGER J.C. & COOK N.G.W. (1979) *Fundamentals of rock mechanics*. Chapman and Hall, New York.

JAMTVEIT B., SVENSEN H. & PODLADCHIKOV Y.Y. (2004) Hydrothermal vent complexes associated with sill intrusions in sedimentary basins. In: *Physical Geology of High-Level Magmatic Systems* (Ed. C. Breitkreuz & N. Petford), vol. 234. Geological Society, London, Special Publications.

JAUPART C. & TAIT S. (1995) Dynamics of Differentiation in Magma Reservoirs. *Journal of Geophysical Research-Solid Earth*, **100**, 17615–17636.

JENKYNS H.C. (1988) The early Toarcian (Jurassic) anoxic event; stratigraphic, sedimentary and geochemical evidence. *American Journal of Science*, **288**, 101–151.

JENKYNS H.C. (2003) Evidence for rapid climate change in the Mesozoic-Palaeogene greenhouse world. *Philosophical Transactions of the Royal Society a-Mathematical Physical and Engineering Sciences*, **361**, 1885–1916.

JENKYNS H.C. & CLAYTON C.J. (1997) Lower Jurassic epicontinental carbonates and mudstones from England and Wales: chemostratigraphic signals and the early Toarcian anoxic event. *Sedimentology*, **44**, 687–706.

JENKYNS H.C., GROCKE D.R. & HESSELBO S.P. (2001) Nitrogen isotope evidence for water mass denitrification during the early Toarcian (Jurassic) oceanic anoxic event. *Paleoceanography*, **16**, 593–603.

JOURDAN F., FERAUD G., BERTRAND H., WATKEYS M.K. & RENNE P.R. (2008) The Ar-40/Ar-39 ages of the sill complex of the Karoo large igneous province: Implications for the Pliensbachian-Toarcian climate change. *Geochemistry Geophysics Geosystems*, **9**.

KEMP D.B., COE A.L., COHEN A.S. & SCHWARK L. (2005) Astronomical pacing of methane release in the Early Jurassic period. *Nature*, **437**, 396–399.

KERR R.C. & TAIT S.R. (1986) Crystallization and Compositional Convection in a Porous-Medium with Application to Layered Igneous Intrusions. *Journal of Geophysical Research-Solid Earth and Planets*, **91**, 3591–3608.

KJELDSTAD A., LANGTANGEN H.P., SKOGSEID J. & BJØRLYKKE K. (2003) Simulation of sedimentary basins. In: *Advanced Topics in Computational Partial Differential Equations - Numerical Methods and Diffpack Programming* (Ed. H.P. Langtangen & A. Tveito), vol. 33, 611–658. Springer Verlag.

KOCH P.L., ZACHOS J.C. & GINGERICH P.D. (1992) Correlation between Isotope Records in Marine and Continental Carbon Reservoirs near the Paleocene Eocene Boundary. *Nature*, **358**, 319–322.

KOKELAAR B.P. (1982) Fluidization of Wet Sediments During the Emplacement and Cooling of Various Igneous Bodies. *Journal of the Geological Society*, **139**, 21–33.

KRULL E.S. & RETALLACK G.J. (2000) δ^{13}C depth profiles from paleosols across the Permian-Triassic boundary: Evidence for methane release. *Geological Society of America Bulletin*, **112**, 1459–1472.

KÜSPERT W. (1982) Environmental changes during oil shale deposition as deduced from stable isotope ratios. In: *Cyclic and Event Stratification* (Ed. G. Einsele & A. Seilacher). Springer, Berlin.

KUMP L.R. & ARTHUR M.A. (1999) Interpreting carbon-isotope excursions: carbonates and organic matter. *Chemical Geology*, **161**, 181–198.

KVENVOLDEN K.A. (1993) Gas Hydrates - Geological Perspective and Global Change. *Reviews of Geophysics*, **31**, 173–187.

LATYPOV R. (2003) The origin of basic-ultrabasic sills with S-, D- and I-shaped compositional profiles by in situ crystallization of a single input of phenocryst-poor parental magma. *Journal of Petrology*, **44**, 1619–1656.

LITTLE C.T.S. & BENTON M.J. (1995) Early Jurassic Mass Extinction - a Global Long-Term Event. *Geology*, **23**, 495–498.

LITVINOVSKI B.A., PODLADCHIKOV Y.Y., ZANVILEVITCH A.N. & DUNITCHEV V.M. (1990) On the melting of acidic volcanites in the contact of basic magma at shallow depth. *Geochimya*, **6**, 807–814.

LOCK B.E. (1980) Flat-Plate Subduction and the Cape Fold Belt of South-Africa. *Geology*, **8**, 35–39.

LORANT F., PRINZHOFER A., BEHAR F. & HUC A.Y. (1998) Carbon isotopic and molecular constraints on the formation and the expulsion of thermogenic hydrocarbon gases. *Chemical Geology*, **147**, 249–264.

MARSH J., HOOPER P., REHACEK J., DUNCAN R. & DUNCAN A. (1997) Stratigraphy and age of Karoo basalts of Lesotho and implications for correlations within the Karoo igneous province. In: *Large Provinces: continental, oceanic and planetary flood volcanism* (Ed. J. Mahoney & M. Coffin), vol. 100, 247–272. Geophysical Monograph.

MARSH J.S. & EALES H.V. (1984) The chemistry and petrogenesis of igneous rocks of the Karoo Central Area, Southern Africa. In: *Petrogenesis of the Volcanic Rocks of the Karoo Province. Geological Society of South Africa Special Publication* (Ed. A.J. Erlank), vol. 13, 27–67.

MCARTHUR J.M. (2007) Comment on "Carbon-isotope record of the Early Jurassic (Toarcian) Oceanic Anoxic Event from fossil wood and marine carbonate (Lusitanian Basin, Portugal)" by Hesselbo S., Jenkyns H.C., Duarte L.V. and Oliveira L.C.V. *Earth and Planetary Science Letters*, **259**, 634–639.

MCARTHUR J.M., ALGEO T.J., VAN DE SCHOOTBRUGGE B., LI Q. & HOWARTH R.J. (2008) Basinal restriction, black shales, Re-Os dating, and the Early Toarcian (Jurassic) oceanic anoxic event. *Paleoceanography*, **23**, PA4217.

MCELWAIN J.C., BEERLING D.J. & WOODWARD F.I. (1999) Fossil Plants and Global Warming at the Triassic-Jurassic Boundary. *Science*, **285**, 1386–1390.

MCELWAIN J.C., WADE-MURPHY J. & HESSELBO S.P. (2005) Changes in carbon dioxide during an oceanic anoxic event linked to intrusion into Gondwana coals. *Nature*, **435**, 479–482.

MÉHAY S., KELLER C.E., BERNASCONI S.M., WEISSERT H., ERBA E., BOTTINI C. & HOCHULI P.A. (2009) A volcanic CO_2 pulse triggered the Cretaceous Oceanic Anoxic Event 1a and a biocalcification crisis. *Geology*, **37**, 819–822.

NORRIS R.D. & RÖHL U. (1999) Carbon cycling and chronology of climate warming during the Palaeocene/Eocene transition. *Nature*, **401**, 775–778.

OSBORNE M.J. & SWARBRICK R.E. (1997) Mechanisms for generating overpressure in sedimentary basins: A reevaluation. *AAPG Bulletin*, **81**, 1023–1041.

PALFY J., DEMENY A., HAAS J., HETENYI M., ORCHARD M.J. & VETO I. (2001) Carbon isotope anomaly and other geochemical changes at the Triassic-Jurassic boundary from a marine section in Hungary. *Geology*, **29**, 1047–1050.

PALFY J. & SMITH P.L. (2000) Synchrony between Early Jurassic extinction, oceanic anoxic event, and the Karoo-Ferrar flood basalt volcanism. *Geology*, **28**, 747–750.

PEPPER A.S. & CORVI P.J. (1995) Simple kinetic models of petroleum formation. Part I: oil and gas generation from kerogen. *Marine and Petroleum Geology*, **12**, 291–319.

PERREGAARD J. & SCHIENER E.J. (1979) Thermal alteration of sedimentary organic matter by a basalt intrusive (Kimmeridgian Shales, Milne Land, East Greenland). *Chemical Geology*, **26**, 331–343.

PETERS K.E., WALTERS C.C. & MANKIEWICZ P.J. (2006) Evaluation of kinetic uncertainty in numerical models of petroleum generation. *AAPG Bulletin*, **90**, 387–403.

PETERS K.E., WHELAN J.K., HUNT J.M. & TARAFA M.E. (1983) Programmed pyrolysis of organic matter from thermally altered Cretaceous black shales. *AAPG Bulletin*, **67**, 2137–2146.

POLTEAU S., FERRE E.C., PLANKE S., NEUMANN E.R. & CHEVALLIER L. (2008a) How are saucer-shaped sills emplaced? Constraints from the Golden Valley Sill, South Africa. *Journal of Geophysical Research-Solid Earth*, **113, B12**, B12104.

POLTEAU S., MAZZINI A., GALLAND O., PLANKE S. & MALTHE-SØRENSSEN A. (2008b) Saucer-shaped intrusions: Occurrences, emplacement and implications. *Earth and Planetary Science Letters*, **266**, 195–204.

POLTEAU S., SVENSEN H., PLANKE S. & AARNES I. (in prep.) Geochemistry of contact metamorphic black shale around sill intrusions in the Karoo Basin and the implication for the Toarcian carbon isotope excursion.

RAMPINO M.R. & STOTHERS R.B. (1988) Flood-Basalt Volcanism During the Past 250 Million Years. *Science*, **241**, 663–668.

RAUP D.M. & SEPKOSKI J.J. (1984) Periodicity of Extinctions in the Geologic Past. *Proceedings of the National Academy of Sciences of the United States of America-Biological Sciences*, **81**, 801–805.

RAYMOND A.C. & MURCHISON D.G. (1988) Development of Organic Maturation in the Thermal Aureoles of Sills and Its Relation to Sediment Compaction. *Fuel*, **67**, 1599–1608.

RETALLACK G.J. & JAHREN A.H. (2008) Methane Release from Igneous Intrusion of Coal during Late Permian Extinction Events. *The Journal of Geology*, **116**, 1–20.

RÖHL U., BRALOWER T.J., NORRIS R.D. & WEFER G. (2000) New chronology for the late Paleocene thermal maximum and its environmental implications. *Geology*, **28**, 927–930.

ROZHKO A.Y., PODLADCHIKOV Y.Y. & RENARD F. (2007) Failure patterns caused by localized rise in pore-fluid overpressure and effective strength of rocks. *Geophysical Research Letters*, **34**, L22304.

SAXBY J.D. & STEPHENSON L.C. (1987) Effect of anigneous intrusion on oil shale at Rundle (Australia). *Chemical Geology*, **63**, 1–16.

SCHOUTEN S., VAN KAAM-PETERS H.M.E., RIJPSTRA W.I.C., SCHOELL M. & DAMSTE J.S.S. (2000) Effects of an oceanic anoxic event on the stable carbon isotopic composition of Early Toarcian carbon. *American Journal of Science*, **300**, 1–22.

SEEWALD J.S., BENITEZ-NELSON B.C. & WHELAN J.K. (1998) Laboratory and theoretical constraints on the generation and composition of natural gas. *Geochimica Et Cosmochimica Acta*, **62**, 1599–1617.

SIMKIN T. (1967) Flow differentiation in the picritic sills of north Skye. In: *Ultramafic and Related Rocks* (Ed. P. Wyllie), 64–49. Wiley, New York.

SIMONEIT B.R.T., BRENNER S., PETERS K.E. & KAPLAN I.R. (1978) Thermal Alteration of Cretaceous Black Shale by Basaltic Intrusions in Eastern Atlantic. *Nature*, **273**, 501–504.

SLITER W.V. (1989) Aptian Anoxia in the Pacific Basin. *Geology*, **17**, 909–912.

SMITH R.M.H. (1990) A review of stratigraphy and sedimentary environments of the Karoo Basin of South Africa. *Journal of African Earth Sciences*, **10**, 117–137.

STOTHERS R.B. (1993) Flood Basalts and Extinction Events. *Geophysical Research Letters*, **20**, 1399–1402.

SVENSEN H., BEBOUT G., KRONZ A., LI L., PLANKE S., CHEVALLIER L. & JAMTVEIT B. (2008) Nitrogen geochemistry as a tracer of fluid flow in a hydrothermal vent complex in the Karoo Basin, South Africa. *Geochimica et Cosmochimica Acta*, **72**, 4929–4947.

SVENSEN H., JAMTVEIT B., PLANKE S. & CHEVALLIER L. (2006) Structure and evolution of hydrothermal vent complexes in the Karoo Basin, South Africa. *Journal of the Geological Society*, **163**, 671–682.

SVENSEN H., PLANKE S., CHEVALLIER L., MALTHE-SØRENSSEN A., CORFU F. & JAMTVEIT B. (2007) Hydrothermal venting of greenhouse gases triggering Early Jurassic global warming. *Earth and Planetary Science Letters*, **256**, 554–566.

SVENSEN H., PLANKE S., MALTHE-SORENSSEN A., JAMTVEIT B., MYKLEBUST R., EIDEM T.R. & REY S.S. (2004) Release of methane from a volcanic basin as a mechanism for initial Eocene global warming. *Nature*, **429**, 542–545.

SVENSEN H., PLANKE S., POLOZOV A.G., SCHMIDBAUER N., CORFU F., PODLADCHIKOV Y.Y. & JAMTVEIT B. (2009) Siberian gas venting and the end-Permian environmental crisis. *Earth and Planetary Science Letters*, **277**, 490–500.

SWEENEY J. & BURNHAM .K. (1990) Evaluation of a simple model of vitrinite reflectance based on chemical kinetics. *AAPG Bulletin*, **74**, 1559–1570.

TAIT S. & JAUPART C. (1992) Compositional Convection in a Reactive Crystalline Mush and Melt Differentiation. *Journal of Geophysical Research-Solid Earth*, **97**, 6735–6756.

TEJADA M.L.G., SUZUKI K., KURODA J., COCCIONI R., MAHONEY J.J., OHKOUCHI N., SAKAMOTO T. & TATSUMI Y. (2009) Ontong Java Plateau eruption as a trigger for the early Aptian oceanic anoxic event. *Geology*, **37**, 855–858.

THOMAS E. & SHACKLETON N.J. (1996) The Paleocene-Eocene benthic foraminiferal extinction and stable isotope anomalies. *Geological Society, London, Special Publications*, **101**, 401–441.

TISSOT B. & WELTE D.H. (1984) *Petroleum Formation and Occurrence*. Springer Verlag, Berlin, 2nd edn.

TURCOTTE D.L. & SCHUBERT G. (2002) *Geodynamics*. Cambridge, 2nd edn.

UNGERER P. (1990) State-of-the-Art of Research in Kinetic Modeling of Oil Formation and Expulsion. *Organic Geochemistry*, **16**, 1–25.

UNGERER P. & PELET R. (1987) Extrapolation of the Kinetics of Oil and Gas-Formation from Laboratory Experiments to Sedimentary Basins. *Nature*, **327**, 52–54.

VAN BILJON W.J. & SMITTER Y.H. (1956) A note on the occurrence of two sandstone dykes in a Karoo dolerite sill near Devon, South-Eastern Transvaal. *Transactions of the Geological Society of South Africa*, **59**, 135–139.

VAN DE SCHOOTBRUGGE B., MCARTHUR J.M., BAILEY T.R., ROSENTHAL Y., WRIGHT J.D. & MILLER K.G. (2005) Toarcian oceanic anoxic event: An assessment of global causes using belemnite C isotope records. *Paleoceanography*, **20**, PA3008.

VISSCHER H., LOOY C.V., COLLINSON M.E., BRINKHUIS H., VAN KONIJNENBURG-VAN CITTERT J.H.A., KÄRSCHNER W.M. & SEPHTON M.A. (2004) Environmental mutagenesis during the end-Permian ecological crisis. *Proceedings of the National Academy of Sciences of the United States of America*, **101**, 12952–12956.

WALTHER J.V. & ORVILLE P.M. (1982) Volatile Production and Transport in Regional Metamorphism. *Contributions to Mineralogy and Petrology*, **79**, 252–257.

WALTON M.S. & O'SULLIVAN R.B. (1950) The intrusive mechanics of a clastic dike (Connecticut). *American Journal of Science*, **248**, 1–21.

WARD P.D., HAGGART J.W., CARTER E.S., WILBUR D., TIPPER H.W. & EVANS T. (2001) Sudden productivity collapse associated with the Triassic-Jurassic boundary mass extinction. *Science*, **292**, 1148–1151.

WEBB A.E., LEIGHTON L.R., SCHELLENBERG S.A., LANDAU E.A. & THOMAS E. (2009) Impact of the Paleocene-Eocene thermal maximum on deep-ocean microbenthic community structure: Using rank-abundance curves to quantify paleoecological response. *Geology*, **37**, 783–786.

WHITICAR M.J. (1996) Stable isotope geochemistry of coals, humic kerogens and related natural gases. *International Journal of Coal Geology*, **32**, 191–215.

WIGNALL P.B. (2001) Large igneous provinces and mass extinctions. *Earth-Science Reviews*, **53**, 1–33.

WIGNALL P.B., MCARTHUR J.M., LITTLE C.T.S. & HALLAM A. (2006) Palaeoceanography - Methane release in the Early Jurassic period. *Nature*, **441**, E5–E5.

ZACHOS J.C., LOHMANN K.C., WALKER J.C.G. & WISE S.W. (1993) Abrupt Climate Change and Transient Climates During the Paleogene - a Marine Perspective. *Journal of Geology*, **101**, 191–213.

Chapter 2

How contact metamorphism can trigger global climate changes: Modeling gas generation around igneous sills in sedimentary basins

by
Ingrid Aarnes*, Henrik Svensen*, James A. D. Connolly† and Yuri Y. Podladchikov*
Manuscript accepted in Geochimica et Cosmochimica Acta‡

2.1 Abstract

Large volumes of greenhouse gases such as CH_4 and CO_2 form by contact metamorphism of organic-rich sediments in aureoles around sill intrusions in sedimentary basins. Thermogenic gas generation and dehydration reactions in shale are treated numerically in order to quantify basin-scale devolatilization. We show that elevated organic maturation occurs within 30-250% of sill thickness, depending on host-rock temperature and intrusion temperature. In contact metamorphism of shales with total organic carbon (TOC) content of $>$5 wt%, CH_4 is the dominant volatile generated through organic cracking, with 85-135 kg CH_4 being generated per cubic meter of aureole, while H_2O generation from dehydration reactions is 30-110 kg/m^3-aureole. Even using conservative estimates of melt volumes, extrapolation of our results to the scale of sill complexes in a sedimentary basin indicates that the devolatilization released $\sim$2700-16200 Gigaton (Gt) CH_4 in the Karoo Basin (South Africa), and $\sim$600-3500 Gt CH_4 in the Vøring and Møre basins (offshore Norway). The generation of volatiles is occurring on a time-scale of 10-1000 years within an aureole, which makes the tempo of sill emplacement in organic-bearing lithologies the time-constraining factor on a basin scale.

*Physics of Geological Processes, University of Oslo, P.box 1048 Blindern, 0316 Oslo, Norway.
†Institut für Mineralogie und Petrographie ETH-Zentrum, Claussiusstrasse 25 CH-8092, Zürich, Switzerland
‡Manuscript accepted with revisions not included here

2.2 Introduction

The emplacement of Large Igneous Provinces (LIPs) were synchronous with major climatic and environmental perturbations since the Paleozoic (e.g. Stothers, 1993; Wignall, 2001; Courtillot & Renne, 2003). Pronounced negative carbon-isotope ($\delta^{13}C$) excursions are identified from proxy data records covering these events, suggesting a release of ^{12}C-enriched carbon gases to the atmosphere (e.g. Jenkyns, 1988; Dickens *et al.*, 1995; Hesselbo *et al.*, 2000). The sources of these gases are debated, and both gas hydrate dissociation and lava degassing have been suggested. Svensen *et al.* (2004) suggested that the source of carbon could be contact metamorphism of organic-rich shale around intrusive sills during LIP emplacement, and that the generated gases subsequently vented to the atmosphere. This hypothesis is supported by the presence of degassing pipes associated with the sills, and is now adopted to explain the end-Guadalupian (261 Ma), the end-Permian (252 Ma), the end-Triassic (200 Ma), the Toarcian (183 Ma), and the PETM (55 Ma) (McElwain *et al.*, 2005; Payne & Kump, 2007; Svensen *et al.*, 2007; Retallack & Jahren, 2008; Ganino & Arndt, 2009; Svensen *et al.*, 2009). The key process of this hypothesis, gas generation during contact metamorphism of organic matter, remains poorly constrained.

Organic matter stored in sedimentary rocks (e.g. black shale) represents one of the Earth's largest carbon reservoirs (Falkowski *et al.*, 2000). This reservoir is tapped during contact metamorphism of organic material (e.g. Perregaard & Schiener, 1979; Saxby & Stephenson, 1987; Raymond & Murchison, 1988; Barker *et al.*, 1998; Gurba & Weber, 2001; Othman *et al.*, 2001). Carbon loss in aureoles is manifest by a decreasing total organic carbon (TOC) content and increasing vitrinite reflectance (%Ro) towards the contact with the sill intrusions.

A large fraction of the carbon gases are released from the aureoles to the atmosphere through the formation of hydrothermal vent complexes and evidence of aureole degassing through these vents has been reported from many volcanic sedimentary basins related to LIP formation, such as the Karoo Basin, (South Africa), the Tunguska Basin (Russia) and in sedimentary basins offshore Norway (Planke *et al.*, 2005; Svensen *et al.*, 2006, 2007, 2009). These vents were formed by pressure-buildup due to devolatilization and phase transitions in the fluid (e.g. Jamtveit *et al.*, 2004).

The aim of this study is to quantify gas formation by cracking of organic material and devolatilization of minerals in contact aureoles by numerical modeling (Fig. 2.1b). We quantify aureole thickness on the basis of vitrinite reflectance profiles and obtain the mass and composition of devolatilization products as a function of sill volume and TOC content (Fig. 2.1c). The composition and fate of the generated fluids are discussed. We extrapolate our results from aureole scale (10-100 meters) to basin-scale ($> 70\,000$ km^2) to evaluate the causal connection between contact metamorphism during LIP formation and global carbon cycle perturbations.

2.3 Aureole processes

2.3.1 Contact metamorphism of organic material

Maturation of organic material in contact with igneous intrusions is thoroughly documented in the literature using several methods, including vitrinite reflectance measurements, Rock-Eval pyrolysis, gas chromatography, and stable isotope analysis (e.g. Powers & Clapp, 1932; Simoneit *et al.*, 1978;

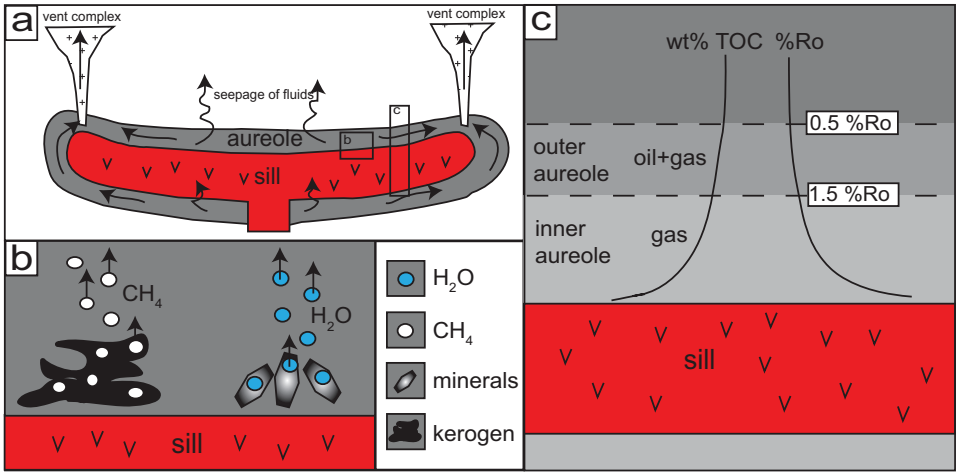

Figure 2.1: **(a)** Schematic model of a contact aureole around a sill intrusion emplaced into sedimentary rocks. Overpressure in the aureole may ultimately cause venting of fluids to the atmosphere. **(b)** Schematic details of the two main fluid-producing processing occurring together in an aureole; kerogen cracks to methane, and hydrous minerals release H_2O during prograde metamorphic reactions. **(c)** The final aureole is consisting of an inner aureole defined by vitrinite reflectance >1.5 %Ro where only gas is generated and an outer aureole defined by >0.5 %Ro, where gas and potentially oil can be generated. The TOC content decreases and the %Ro increases towards the contact.

Bostick, 1979; Simoneit *et al.*, 1981; Saxby & Stephenson, 1987; George, 1992; Bishop & Abbott, 1995; Zhu *et al.*, 2007; Mastalerz *et al.*, 2009). Contact metamorphism of organic material leads to elevated vitrinite reflectance (%Ro), loss of TOC, increased aromatization and changes in carbon isotope compositions ($\delta^{13}C$) of the residual organic material towards the contact (e.g. Peters *et al.*, 1983; Clayton & Bostick, 1986; Barker & Bone, 1995; Meyers & Simoneit, 1999; Cooper *et al.*, 2007). Sill intrusions are accordingly important in many sedimentary basins for maturing source rocks and producing methane-rich gases.

Many studies focus on local contact metamorphic effects and seldom present complete sets of the key analyses needed to quantify organic and inorganic devolatilization reactions. In addition, sill thicknesses, host-rock compositions, and depth of emplacement vary considerably. We have summarized 39 aureole case studies around sheet intrusions published since 1959 (Table 2.1) to get an overview of published data and aureole processes that have been considered in the literature. Only 5 of these studies include modeling of vitrinite (Sweeney & Burnham, 1990; Brown *et al.*, 1994; Galushkin, 1997; Fjeldskaar *et al.*, 2008; Rodriguez Monreal *et al.*, 2009). Most numerical models are restricted to calculations of the temperature profile around intrusions, which is not sufficient when trying to estimate the amount and composition of fluids that can be generated.

A key issue discussed in the literature is the estimation of contact aureole thickness. A common method is based on vitrinite reflectance profiles, and aureole thicknesses usually vary between 30-200% of the intrusion thickness (Table 2.1). The great span in this parameter in published aureole data suggests an influence of several factors, for example degree of background maturation, varying temperature of

Table 2.1: List of studies dealing with contact metamorphism from sill intrusions.

References	Modeling provided	Data provided	Intrusion thickness	Normalized aureole	Lithology of host-rock
Barker & Bone (1995)		V_b-Da	2.2 m	∼5% D	high grade limestone
Barker *et al.* (1998)	T-F-L_C	V	0.06-40 m	30-150%[a] D	clay/sediments
Bishop & Abbott (1995)	T	V-TOC.RE-GC	0.3-3.0 m	30-70%[a] D	shale/silty shale
Bostick (1979)		V	0.5-9.2 m	50-75%[a] D	coal/oranic matter
Bostick & Pawlewicz (1984)		V	3.6-10.4 m	75-100%[a] D	shale/limestone
Brown *et al.* (1994)	T-Ro	V	40-80 m	150%[a] S	
Clayton & Bostick (1986)		V-RE-GC-Da	1.3 m	∼50%[a] D	siltstone
Cooper *et al.* (2007)		V-TOC-Da	0.15-1.8 m	75-110%[a] S/D	coal/black shale
Delaney (1982)	T-F-Me				
Dow (1977)		V	∼180 m	200%[a] S	
Drits *et al.* (2007)		Mi	0.5-80 m	∼75%[a] S	mudstone
Dutrow *et al.* (2001)	T-F-R	TOC-Da	11 m	35-55%[b] D	carbonate/siltstone
Finkelman *et al.* (1998)		V-RE-EL-Mi	1.5 m	∼35%[a] D	coal/coke
Fjeldskaar *et al.* (2008)	T-Ro	V	118.5 m	∼150%[c] S	silt/shale/sandstone
Galushkin (1997)	T-F-L_C-L_D-Ro	V	0.9-118.5 m	55-170%[a] S/D	black shale/silt
George (1992)		V-RE-GC-Da	.5 m	∼70%[a] D	silt/oil shale
Golab *et al.* (2007)		Mi-El-Da	∼0.1-3 m	∼200%[a] D	coal
Gröcke *et al.* (2009)		V-Da	1.2-1.5 m	∼100%[a] D	coal
Gurba & Weber (2001)		V	20.8-39.3 m	30-90%[a] S	coal
Hanson & Barton (1989)	T-L_C-L_D			D	
Jaeger (1959)	T-F-L_V			100%[c]	
Kjeldstad *et al.* (2003)	T-F-P-Ro				
Litvinovski *et al.* (1990)	T-L_M-P		500 m	>>10%[b] D	clay/pumice
Mastalerz *et al.* (2009)		V-Da	>1.2 m	∼50%[a] D	coal
Meyers & Simoneit (1999)		TOC-RE-Da	1.5 m	∼60%[b] S	coal
Othman *et al.* (2001)		V-RE-GC	0.4-15.7 m	S	mudstone
Perregaard & Schiener (1979)		V-GC	4.5 m	∼50%[a] D	shale
Peters *et al.* (1983)		V-RE-GC	0.2-15 m	50%-70%[a] S	black shale
Polyansky & Reverdatto (2006)	T-L_M-F-R		280 m	10-70%[c] S	sand/siltstone
Raymond & Murchison (1988)		V	50-118.5 m	∼100-200%[a] S	shale/silt/limestone
Rodriguez Monreal *et al.* (2009)	T-Ro-HC	V-RE-GC	110-600 m	50-100%[a] S	black shale
Saghafi *et al.* (2008)		V-Da	∼2.4 m	∼400%[a] D	coal
Santos *et al.* (2009)	T	Mi-El	13 m	∼90%[b] S	carbonate/black shale
Saxby & Stephenson (1987)		TOC-GC-Da	3 m	∼50%[b] S	oil shale
Simoneit *et al.* (1978, 1981)		V-TOC-GC-Da	0.2-15 m	40-50%[a] S	black shale
Snyman & Barclay (1989)		V		50-1400%[a] D/S	coal
Svensen *et al.* (2007)		V-TOC-Re	80 m	∼30%[a] S	clack shale/shale
Sweeney & Burnham (1990)	T-Ro	V	10.4 m	∼100%[a/c] D	shale
Zhu *et al.* (2007)		V-GC-Da	50 m	∼20%[a] S	black mudstone

[a]Calculated from elevated vitrinite profiles. [b]Based on other measurement techniques. [c]Based on modeling results.

Modeling: T- Thermal modeling; F- Effect of fluids; L_C - Latent heat of cystallization; L_D - Latent heat of dehydration; L_M - Latent heat of host-rock melting; L_V - Latent heat of vaporization; Me - Mechanical failure;

Data: V - Vitrinite; Vb - Bitumen reflectance; TOC - Total organic carbon; RE - Rock-Eval analysis; GC - Gas chromatography; Da - Additional data; Mi - Mineralogical data; El - Elemental Data.

Aureole: D - Dike; S - Sill;

intrusion contact, different fluid systems, or multiple intrusions (Raymond & Murchison, 1988; Hanson & Barton, 1989; Galushkin, 1997; Barker *et al.*, 1998; Kjeldstad *et al.*, 2003; Fjeldskaar *et al.*, 2008). To constrain some of these variations and how they influence the aureole processes, we test how key parameters (intrusion temperature, host-rock temperature and sill thickness) affect both the aureole thickness and the mass of generated gases during heating. Through numerical modeling we are able to cover the whole range of natural variations and simulate the response of the host shale.

2.3.2 Modeling of aureoles

Numerical modeling of aureole-processes has several approaches, including pure heat conduction, heat conduction with latent heat of crystallization, dehydration and contact melting, inclusion of heat advection by fluids with or without pore-pressure buildup (e.g. Jaeger, 1959; Delaney, 1982; Hanson & Barton, 1989; Litvinovski *et al.*, 1990; Barker *et al.*, 1998; Dutrow *et al.*, 2001; Annen & Sparks, 2002; Kjeldstad *et al.*, 2003). Some common modeling approaches are presented in Table 2.1. Studies of mixed inorganic and organic reactions in shale and coal during contact metamorphism are less common (e.g. Finkelman *et al.*, 1998; Golab *et al.*, 2007; Santos *et al.*, 2009). Contact metamorphism processes such as mineral dehydration, decarbonation and host-rock melting reactions are commonly done in aureoles of large plutons (e.g. Jamtveit *et al.*, 1992; Svensen & Jamtveit, 1998; Holness & Isherwood, 2003; Polyansky & Reverdatto, 2006; Nabelek, 2007). Mineral reactions in sedimentary host-rocks around sheet intrusions are comparatively poorly documented (Holness & Watt, 2002; Haave, 2005; Drits *et al.*, 2007; Henry *et al.*, 2007; Ganino *et al.*, 2008).

2.4 Methods

We use a 2D finite element model for conductive heat-flow around a sill intrusion with latent heat of crystallization, latent heat of kerogen cracking and latent heat of dehydration reactions. The model accounts for vitrinite maturation and kerogen cracking by kinetic modeling using Easy%Ro (Sweeney & Burnham, 1990) and mineral dehydration as predicted by phase equilibria (Connolly, 2005). We focus on first-order effects and do not involve fluid flow and heat advection. This simplification is justified by an analytical solution showing that advective heating has little effect on intrusive cooling for low-permeability systems (Podladchikov & Wickham, 1994). In addition, we avoid making global assumptions about the permeability and amount of pre-existing fluids in the basin host-rocks. Despite the common use of Easy%Ro to estimate vitrinite profiles around sill intrusions, there has been little focus on the sensitivity of the model to varying initial parameters. We therefore conducted a series of simulations calculating vitrinite reflectance profiles to study the response of the model to the key parameters influencing the thermal input: sill thickness; intrusion temperature; and host-rock temperature.

2.4.1 Thermal modeling

We have developed a numerical model solving the thermal evolution of sill cooling using 2D finite element and 1D finite difference method. The thermal solver is shown in Fig. 2.2.

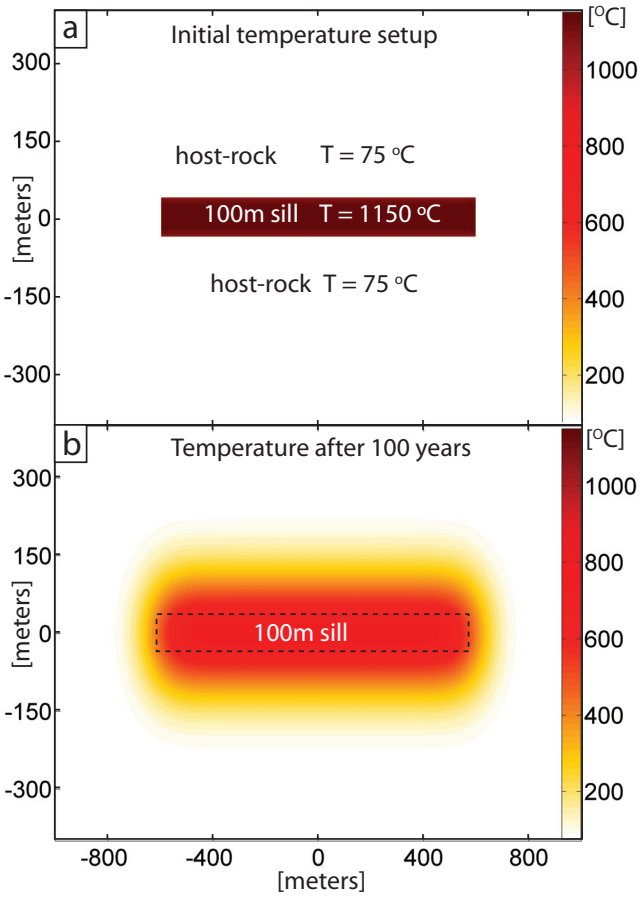

Figure 2.2: Setup of the numerical model for a 100 meter thick sill. **(a)** Initial conditions. An instantaneous emplacement of a 1150 °C sill in a host-rock of 100 °C. **(b)** The sill is cooling by conduction with time. Parameters used in the modeling are given in Table 2.2.

We assume instantaneous igneous emplacement and no post-emplacement flow. The physical parameters used in the modeling are given in Table 2.2. We use the 1D model to calculate a series of aureole thicknesses by systematically varying the intrusion temperature from 900 to 1300 °C, the host-rock temperature from 10 to 110 °C, and the sill thickness from 1-150 m. The 1D model gives similar results to the 2D model, but is far more time-efficient for the array of runs conducted. We solve the heat conduction equation with latent heat,

$$\frac{\partial T}{\partial t} = \frac{k}{\rho C_P^{\text{eff}}}\left(\frac{\partial^2 T}{\partial x} + \frac{\partial^2 T}{\partial z}\right) - \frac{L_{OM} R_{OM}}{\rho C_P} - \frac{L_D R_D}{\rho C_P}, \tag{2.4.1}$$

where T is temperature, ρ is density, k is thermal conductivity, C_P is heat capacity, t is time, x is horizontal direction, z is vertical direction, L is latent heat of devolatilization reactions, and R is rate

of devolatilization reactions. An effective heat capacity, ρC_P^{eff} , accounts for the latent heat of fusion in the crystallizing parts of the sill,

$$\begin{aligned} C_P^{\text{eff}} &= C_p(1+Ste) \quad for \quad (T_S < T < T_L) \\ C_P^{\text{eff}} &= C_p \qquad\quad for \quad (T_S > T). \end{aligned} \tag{2.4.2}$$

The Stefan number, C_P^{eff}, is quantifying the effect of the latent heat by

$$Ste = \frac{L_C}{(T_L - T_S)C_P}, \tag{2.4.3}$$

where L_C is latent heat of crystallization, T_L is liquidus temperature and T_S is solidus temperature of the melt. Effects of latent heat of mineral dehydration and organic cracking are accounted for by the enthalpy method. Reaction rates are coupled directly to the devolatilization reactions. We have fixed the boundary conditions to the host-rock temperature at the top and bottom of the domain, while the boundary conditions at the sides are free. The boundaries do not influence the developing thermal field. We assume that the host-rock temperature above and below the intrusion are equal.

2.4.2 Organic maturation

The individual chemical steps during kerogen cracking are complex and to a large degree unknown (e.g. Beardsmore & Cull, 2001). However, it has been shown for a bulk organic system that the kinetics can be satisfactorily approached by the Arrhenius equation using a set of parallel first order reactions,

$$k = A\exp(-E_i/RT), \tag{2.4.4}$$

where A is the frequency factor, R is the gas constant and E_i is the activation energy for the i^{th} reaction (e.g. Tissot *et al.*, 1987; Ungerer & Pelet, 1987). The parallel reactions (i) represent different kinetics of the kerogen bonds. We utilize the model Easy%Ro developed by Sweeney & Burnham (1990) for consistent modeling of vitrinite reflectance and organic cracking reactions. It is based on an average set of kerogen kinetics and conveniently implemented using the following approach. The Arrhenius equation is integrated over time,

$$I_t = \int_0^t A\exp(-E/RT)dt, \tag{2.4.5}$$

in order to calculate the decrease in the initial amount of convertible material (W_{i0}),

$$W_{it} = W_{i0}\exp(-I_{it}), \tag{2.4.6}$$

where W_{it} is the fraction of convertible material at time t (g_{HC}/kg_{TOC}). The total amount of product released at time t, Q_t , is

$$Q_t = \sum_i W_{i0} - W_{it}. \tag{2.4.7}$$

Table 2.2: Parameters used in the thermal modeling.

Symbol	Description	Value	Unit
T_m	Initial temperature of melt	1423*	K
T_{hr}	Initial temperature of host-rock	348*	K
T_L	Liquidus temperature	1423[a]	K
T_S	Solidus temperature	1223[a/*]	K
K_T	Thermal diffusivity $(k/\rho/C_P)$	10^{-6}[b/c]	m^2/s
ρ_m	Density melt	2600[b]	kg/m^3
C_{Pm}	Heat capacity melt	820[b]	J/kg/K
ρ_{hr}	Density host-rock	2400[d]	kg/m^3
C_{Phr}	Heat capacity host-rock	850[e]	J/kg/K
k	Thermal conductivity	2.1[b/f]	$J/K/m^3$
L_C	Latent heat of crystallization	320[g]	kJ/kg
L_D	Enthalpy of mineral dehydration	2800[h]	kJ/kg_{H_2O}
L_{OM}	Enthalpy of organic cracking	375[i]	kJ/kg_{TOC}
R	Gas constant	8.31	J/K/mol
A	Frequency factor	10^{13}[j]	1/s
E	Activation energy	142-301	kJ/mol
d	Aureole thickness		m
h	sill thickness	1-150*	m
W	fraction of convertible organic matter pr TOC	850[j]	g/kg
R_{OM}	rate of kerogen conversion into hydrocarbons		$kg_{TOC}/m^3/s$
R_D	rate of mineral dehydration reaction		$kg_{HC}/m^3/s$
X_O	atomic fraction of n_O relative to $n_H + n_O$		-
n_O	number of moles of oxygen per mole fluid		-
n_H	number of moles of hydrogen per mole fluid		-

*This study approximations; [a]Métrich & Rutherford (1998); [b]Barker *et al.* (1998); [c]Delaney (1982); [d]Storvoll *et al.* (2005); [e]Berkovich *et al.* (2000); [f]Reiter & Tovar (1982), for shale; [g]Turcotte & Schubert (2002); [h]Trommsdorff & Connolly (1996), average dehydration; [i]Shih & Sohn (1978); [j]Sweeney & Burnham (1990).

Vitrinite reflectance is calculated by

$$\%\mathrm{Ro} = \exp(-1.6 + 3.7F), \tag{2.4.8}$$

where $F = \sum_i f_i \left(1 - \frac{W_i}{W_{i0}}\right)$ and f_i is the weighting factor for the i^{th} reaction. Values for E and f can be found in Sweeney & Burnham (1990). From this model it becomes apparent that the minimum value of %Ro is $\exp(-1.6) = 0.2$ when $F = 0$, and oppositely, at maximum conversion $F = 0.85$, the value of %Ro is $0.2 \times \exp(3.7 \times 0.85) = 4.6$.

We assume that all hydrocarbons are converted into methane (CH_4), because the kinetic conditions for transformation of organic matter at high temperatures favor gaseous products over liquid petroleum (e.g. Reverdatto & Melenevskii, 1983; Tissot & Welte, 1984; Karlsen & Skeie, 2006). Secondary cracking of oil to gas is expected to initiate around 180 °C (Schenk *et al.*, 1997), which is reached even in the outer aureole, supporting our assumption.

The CH_4 yield (kg_{CH_4}/m^3_{rock}) is calculated from the relation

$$Q_{CH_4} = Q_t \times \tau \times M_f \times \rho_{hr}, \tag{2.4.9}$$

where Q_t is hydrocarbon yield ($g_{HC}/kg_{TOC}/1000$), τ is kg carbon per kg shale (wt% TOC/100), M_f is conversion factor from C to CH_4 (1.34), and ρ_{hr} is density of the host-rock (2400 kg/m^3) which corresponds to an average density of sediments at ∼3 km depth in a basin (Storvoll *et al.*, 2005). We use this depth as an analog to the paleo-depth of the deep organic-rich shale formations in the Karoo Basin (Catuneanu *et al.*, 2005).

We extrapolate the calculations of gas quantities generated in one aureole to basin-scale gas generation by assuming a cumulative sill thickness of 100 meter intruding into organic formations in a basin. The amount of CH_4 generated per unit area of sill (kg m^{-2}) is determined by summing up a 1D section above and below the 100 m thick sill.

2.4.3 Mineral dehydration modeling

Mineral dehydration reactions are modeled to estimate the relative amounts of CH_4 and H_2O generated in aureoles for different initial wt% TOC and sill thicknesses. The thermal solver is coupled to mineralogy by phase equilibrium modeling (Connolly, 2005). We use an average pelitic sediment composition after Caddick & Thompson (2008), with SiO_2 = 59.80 %, Al_2O_3 = 16.57 %, MgO = 2.62 %, Na_2O = 1.73 %, CaO = 1.09 %, FeO = 5.81 %, H_2O = 5.00 %, by weight. Fig. 2.3a shows the calculated equilibrium mineral assemblages of the pelite, and Fig. 2.3b displays the bulk water content of the mineral assemblage as a function of temperature and pressure. We fix the thermodynamic pressure at 100 MPa, and use the transient thermal solver to extract contact aureole temperatures (along the dashed line). The discrepancy between the H_2O content in the mineral assemblage of the initial host-rock (5 wt% H_2O) and the transient H_2O content equals the amount of H_2O released as a free fluid phase. The total amount of H_2O generated is thus directly linked to the maximum temperature obtained in the aureole.

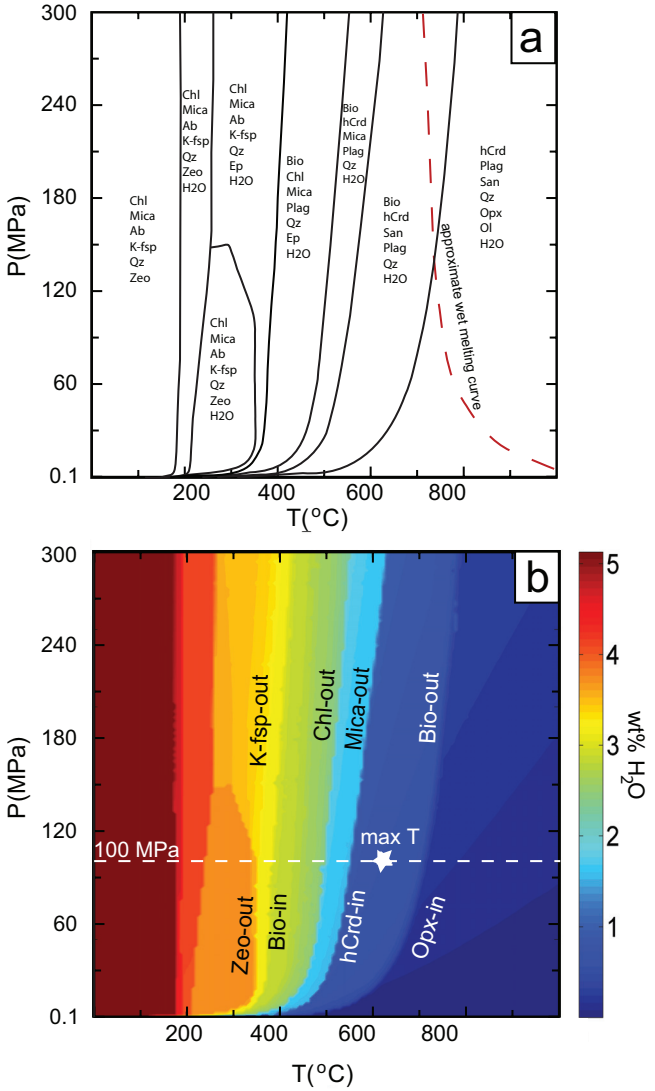

Figure 2.3: **(a)** Stable mineral assemblages calculated from Perple_X (Connolly, 2005) for an average pelite (Caddick & Thompson, 2008). The assemblages are simplified from original calculations to consider major dehydration reactions. Wet melting may occur above ∼750 °C as indicated by the dashed line (Nichols *et al.*, 1994; Grant, 2004). **(b)** Calculated bulk maximum H_2O content as a function of pressure and temperature. The dashed line indicates where the calculations in our model are done. Maximum temperature obtained in the aureoles in this study is indicated by the star at ∼600 °C. Mineral abbreviations: Ab - albite; Bio - biotite; Chl - chlorite; Ep - epidote; hCrd - hydrous cordierite; K-fsp - alkali-feldspar; Mica - white mica; Ol - olivine; Opx - orthopyroxene; Plag - plagioclase; Qz - quartz; San - sanidine; Zeo - zeolite;

2.4.4 Linear regression analysis

We apply linear regression analysis to our set of 1D calculations of aureole thicknesses. The parameters and results are assembled in matrices which are solved for the unknown coefficients C:

$$\left[\frac{d^1}{h^1} \cdot\cdot \frac{d^n}{h^n}\right] = \begin{bmatrix} C_{T_{host-rock}} \\ C_{T_{intrusion}} \\ C_{ln(h)} \\ C_1 \end{bmatrix} \begin{bmatrix} T^1_{host-rock} & T^1_{intrusion} & \ln(h)^1 & 1^1 \\ : & : & : & : \\ T^n_{host-rock} & T^n_{intrusion} & \ln(h)^n & 1^n \end{bmatrix}, \tag{2.4.10}$$

where d is the aureole thickness, h is the sill thickness and n is the number of calculations in this study ($\sim$1500). The coefficients are used to construct a simple formula predicting the normalized aureole thickness. To evaluate the accuracy of the regression model we find the coefficient of determination R^2 from

$$R^2 \equiv 1 - \frac{S_{err}}{S_{tot}}, \tag{2.4.11}$$

where S_{tot} is the total sum of squares, $S_{tot} = \sum_{i=1}^{n} (y_i - \bar{y}_i)^2$, where $y = (d/h)_{calculated}$ is the calculated aureole thicknesses (d) normalized over sill thickness (h) and $\bar{y} = \frac{1}{n}\sum_{i=1}^{n} y_i$ is the grand mean of the normalized aureole thickness; $S_{err} = \sum_{i=1}^{n} (y_i - z_i)^2$ is the total sum of squared errors, where $z = (d/h)_{fitted}$ for the fitted aureole thicknesses normalized over sill thickness.

2.4.5 Fluid composition

Fluid speciation calculations are conducted in order to find the phase relation between the generated H_2O and CH_4. We calculate carbon saturated fluid phase equilibria in Perple_X as a function of temperature using the equation of state from Connolly & Cesare (1993). Carbon-saturated fluids have only one compositional degree of freedom (X_O) which is specified by

$$X_O = \frac{n_O}{n_O + n_H}, \tag{2.4.12}$$

where n_O and n_H are number of moles of O and H per mole of fluid (Connolly, 1995). A pure CH_4-fluid has $X_O = 0$, and a pure H_2O-fluid has $X_O = 1/3$. For the bulk fluid composition in the aureoles we use the calculations of H_2O and CH_4 generated in the inner aureole. Preexisting pore-fluids are not considered.

2.5 Results

2.5.1 Devolatilization reactions

Fig. 2.4 shows the results of the final reaction stages of fluid generation as a function of TOC content (1 and 5 wt%) of the host-rocks. We define the inner aureole as vitrinite reflectance larger than 1.5 %Ro marking the metagenetic maturation level (gas only), and outer aureole as %Ro between 0.5 and

1.5 marking the catagenetic maturation (oil+gas) (e.g. Dow, 1977; Hunt, 1996). The aureole thickness is defined from the 1%Ro contour, and is ∼150 meter for the 100 meter thick sill (Fig. 2.4d). The amount of CH_4 generated during heating varies greatly with the initial total organic carbon. The amount of H_2O generated in the inner aureole ranges from 30 to 110 kg/m^3, decreasing to 0 kg/m^3 in the outer aureole (Fig. 2.4a). The CH_4 generation in a shale of 1 wt% TOC is ∼20-30 kg/m^3 in the inner aureole, decreasing to 10 kg/m^3 in the outer aureole (Fig. 2.4b). For 5 wt% TOC the CH_4 generation is 85-135 kg/m^3 in the inner aureole, decreasing to 40 kg/m^3 in the outer aureole (Fig. 2.4c). This implies that in the case of 1 wt% TOC the mass of generated CH_4 is 2-4 times less than the amount of H_2O. For 5 wt% TOC the amount of generated CH_4 is up to twice the amount of H_2O. The mass per volume of generated fluids is unaffected by the sill thickness. However, a lager sill will affect a larger total volume of rocks and hence generate a larger total mass of CH_4 and H_2O. The total masses of fluids summed up for the 2D sections are for the 100×1200 meter case 20100 ton/m H_2O, 10400 ton/m CH_4 for 1 wt% TOC, and 51200 ton/m CH_4 for 5 wt% TOC. The devolatilization reactions are completed within ten to several hundreds of years, depending on sill thickness.

2.5.2 Aureole thickness

To compare published data from different geological settings we have normalized the aureole thicknesses d to the intrusion thickness h (Fig. 2.5a). The assembled data from Table 2.1 show that most of the aureole thicknesses fall between 30-200% of the sill thickness (Fig. 2.5b). There is a tendency for the thinner intrusions to have smaller aureoles than thicker intrusions, although no clear distinction can be made. The distribution of observed aureole thicknesses is within the same range as the calculated distribution of aureole thicknesses shown in Figure 2.5c, resulting from systematic variations of sill thickness (1-150m), intrusion temperature (900-1300°C) and host-rock temperature (10-110°C).

Applying linear regression analysis (Eq. 2.4.10) to the series of runs conducted results in the following fitting formula

$$\frac{d}{h} \approx 0.0102 \cdot T_{\text{host - rock}} + 0.0029 \cdot T_{\text{intrusion}} + 0.1936 \cdot \ln(h) - 6.8611, \tag{2.5.1}$$

where d is the aureole thickness and h is the sill thickness. Figure 2.6a shows a plot of the values obtained from this formula against calculated values. Most of the calculated aureoles are reproduced by the fitting formula to within a factor 2 (Fig. 2.6)b). The fit is most accurate for sills of 5 to 20 meters, with less accuracy for higher sill thicknesses. From Eq. 2.4.11 the coefficient of determination is $R^2 = 0.89$, which indicates that we capture about 90% of the response of d/h in the calculations by our approximated formula based on our three key variables (Eq. 2.5.1). This simple relationship originates from vitrinite calculations using an equation with a total of three exponents (Eq. 2.4.8). From the formula we see that changing the host-rock temperature by 50 °C has a larger influence on the aureole thickness than changing the intrusion temperature by 50 °C. Changing the sill thickness by 50 meters will have an intermediate influence. Hence, host-rock temperature is the most sensitive parameter, while sill thickness will be most important for the non-normalized aureole thickness. This suggests that the depth of sill emplacement and the geothermal gradient in the basin are important factors in determining the volume of heated sediments, and hence the total mass of generated gas.

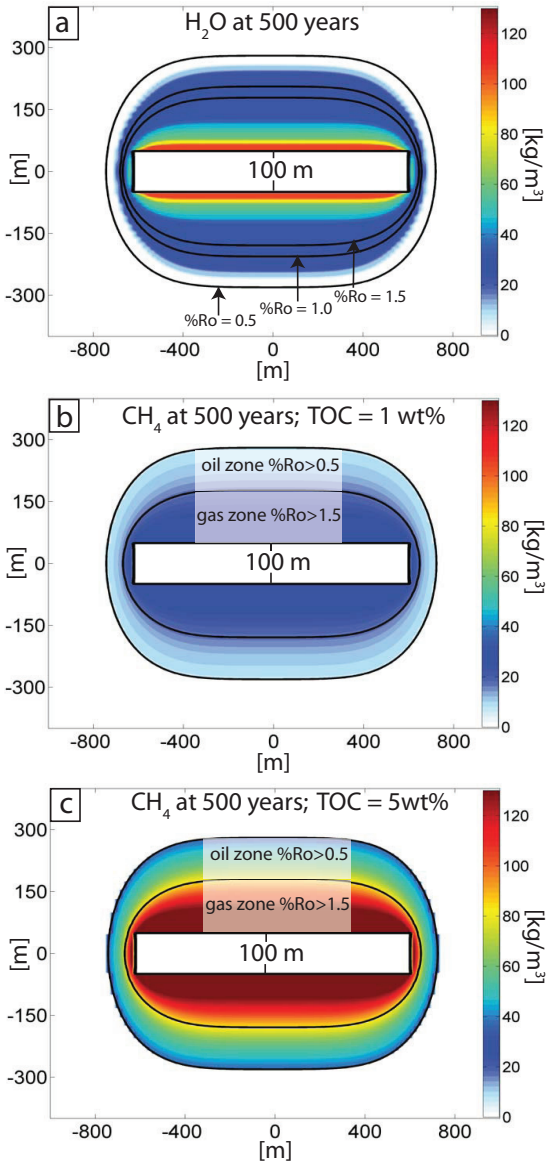

Figure 2.4: Calculation of **(a)** H_2O, **(b)** CH_4 for 1 wt % TOC and **(c)** 5 wt% TOC for a 100 m thick sill emplaced at ∼3 km depth with intrusion temperature of 1150 °C and host-rock temperature of 75 °C. Generated amounts are given in kg m^{-3}. The figure shows the final aureole at 500 years.

2.5.3 Latent heat

Calculations with and without latent heat of crystallization and devolatilization reactions on the vitrinite profiles are compared with normalized data from a 10.4 meter thick sill (Bostick & Pawlewicz, 1984).

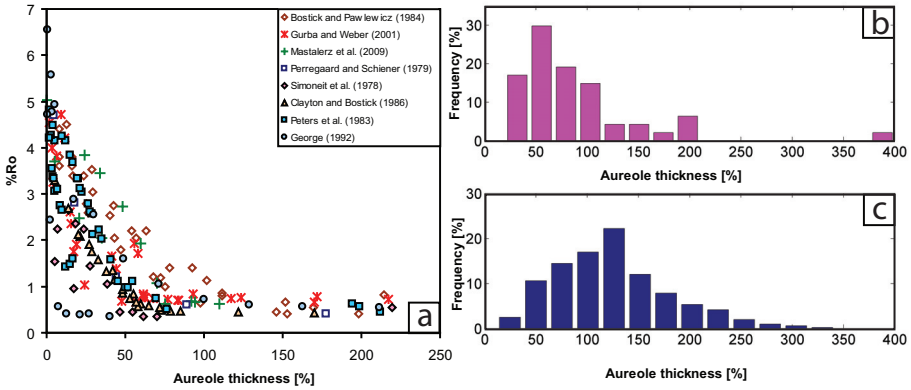

Figure 2.5: (a) Vitrinite profiles from several sill intrusions of various thicknesses plotted as a function of normalized aureole thicknesses. There is a large diversity in the profiles, although all profiles show an increase from ∼0.5-1 %Ro up to ∼5 %Ro at the contact. **(b)** Relative aureole thicknesses based on elevated vitrinite reflectance varying from ∼30 to 400 % sill thickness (Table 2.1). **(c)** Calculated relative aureole thicknesses based on %Ro >1, for varying sill thickness and temperature of intrusion and host-rock.

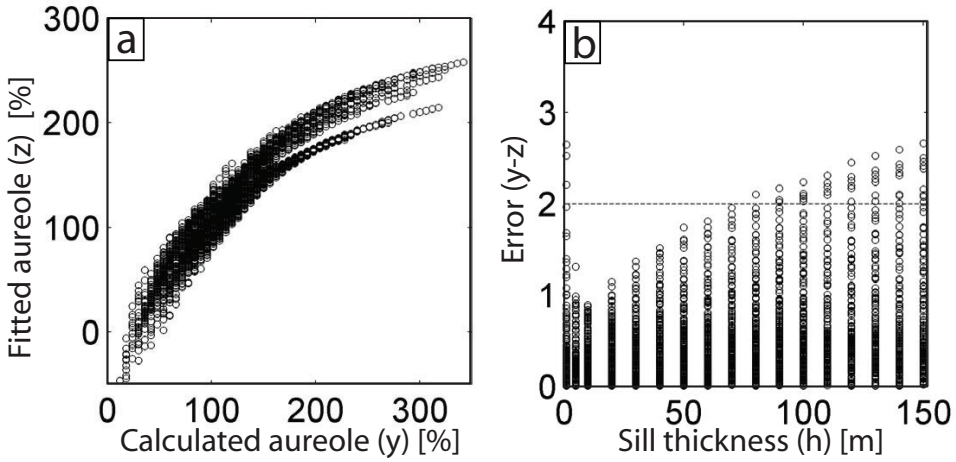

Figure 2.6: **(a)** Calculated aureole thicknesses (y) plotted versus fitted aureole thicknesses (z) (Eq. 2.5.1). About 90% of the data can be reproduced by a plane involving intrusion and host-rock temperature, as well as the natural logarithm of the sill thickness. **(b)** Differences between calculated and fitted aureole thicknesses (error) are approximately within a factor 2 (dashed line), i.e. the fitting formula (Eq. 2.5.1) gives a good indication of expected aureole thickness arising from heat conduction within a factor 2 error. The fitting formula is most accurate for sills around 5-20 meters, with progressive less accuracy with increasing (and decreasing) sill thickness.

It is approximately 20% difference in the aureole thickness between latent heat of crystallization, dehydration and cracking and no latent heat, and about 28% difference with latent heat of crystallization

only (Fig. 2.7). The spreading of the data points is by comparison 10-20%. The calculation without latent heat fits with the lower end of the data, while the calculated lines with latent heat fit the upper end of the data. We have used initial thermal values reported by Bostick & Pawlewicz (1984) with a host-rock temperature of 30 °C and an intrusion temperature of 1240 °C for the calculated lines in Fig. 2.7. By using a lower intrusion temperature, all three calculations fit better to the data points closest to the intrusion, suggesting that the reported intrusion temperature is overestimated.

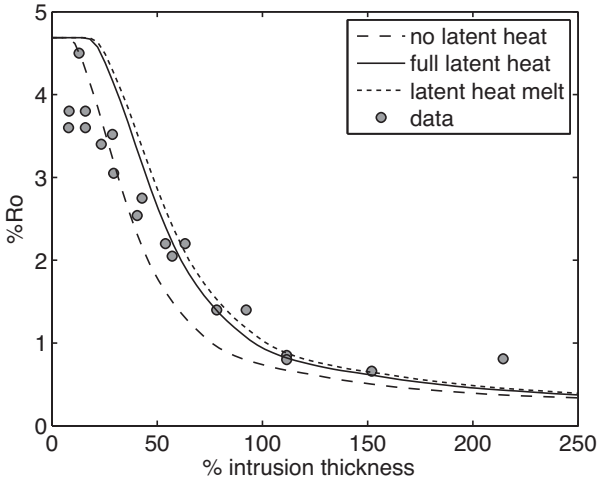

Figure 2.7: Comparison of numerical calculations without (long dashed line) latent heat, with latent heat of crystallization and devolatilization (solid line) and latent heat of crystallization only (short dashed line) with data (circles) from aureoles around a 10.4 m dike (Bostick & Pawlewicz, 1984), normalized over intrusion thickness. Host-rock temperature is 30 °C and intrusion temperature is 1240 °C (Bostick & Pawlewicz, 1984), the other values used are given in Table 2.2.

2.5.4 Fluid composition

The results of fluid speciation calculations are plotted in Figure 2.8a, contoured for pressures ranging from 100 MPa to 500 MPa. Fig. 2.8b shows densities at 100 MPa calculated using the equation of state from Connolly & Cesare (1993). The compositions of the fluids generated are calculated from average aureole values. In the case of 1 wt% TOC we use 20 kg/m^3 (1259 mol/m^3) CH_4 and 90 kg/m^3 (5000 mol/m^3) H_2O, which gives a mole fraction of oxygen of $n_O = 0.40$ and a mole fraction of hydrogen of $n_H = 1.20$. For the 5 wt% case we use 120 kg/m^3 (7500 mol/m^3) and the same H_2O, resulting in $n_O = 0.29$ and $n_O = 2.29$. Substituting these numbers into Eq. 2.4.12 yields $X_O^{1\text{wt\%}} = 0.25$ and $X_O^{5\text{wt\%}} = 0.11$, indicated by stars in Fig. 2.8a.

The density of the fluid generated from a shale with 1 wt% TOC will be 350 kg/m^3 at time of high-temperature generation (450 °C and 100 MPa) (Fig. 2.8b). At 375 °C the fluid will exsolve into a CH_4-dominated phase and a H_2O-dominated phase. The density of the CH_4-dominated phase will decrease from 300 kg/m^3 to 180 kg/m^3 down-temperature (375-200 °C) due to exsolution of progressively more

H_2O. The density of the H_2O-dominated fluid will increase from 700 kg/m^3 at 375 °C to 900 kg/m^3 at 200 °C. For a shale with 5 wt% TOC, the relatively lower amount of H_2O (∼90 kg/m^3) will be miscible with the generated CH_4 (∼120 kg/m^3) down to temperatures of 275 °C at 100 MPa. Then the fluid will unmix into a CH_4-dominated fluid with a density of 140-180 kg/m^3 (450-200 °C) and a H_2O-dominated fluid with a density of 800-900 kg/m^3.

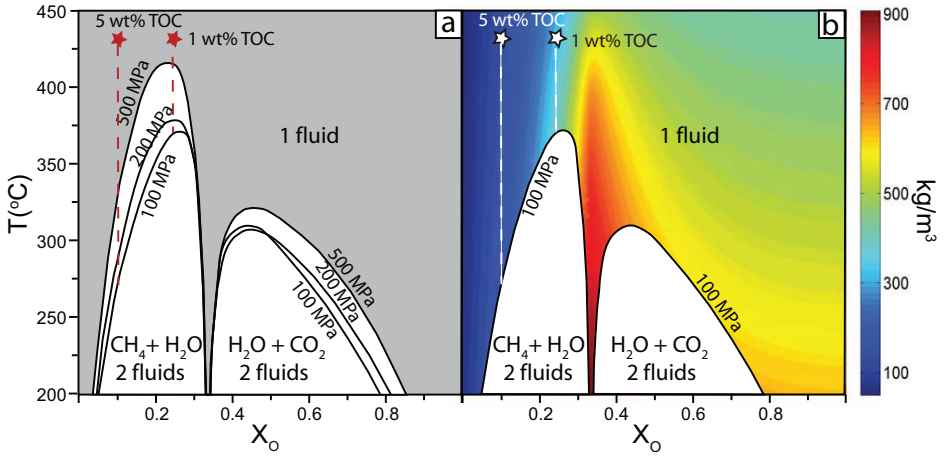

Figure 2.8: **(a)** Fluid speciation phase diagram calculated from Perple_X, using the equation of state from Connolly & Cesare (1993) contoured for pressures ranging from 100 - 500 MPa. For 1 wt% TOC there will be miscibility between water and methane at ∼375 °C, while fluids in rocks of 5 wt% TOC are miscible at ∼275 °C , for thermodynamic pressures of 100-200 MPa. **(b)** Calculated densities of the fluid(s) at 100 MPa. At this pressure the CH_4-dominated phase will have a relatively low density of ∼200 kg/m^3, while the H_2O-dominated phase will have a relatively much higher density of ∼900 kg/m^3.

2.5.5 Basin-scale gas generation

Figure 2.9 shows the extrapolation of CH_4 generated in the aureole to basin scale sill complexes emplaced in shale as a function of function of TOC content from 0.5-10 wt% and area covered by a cumulative sill thickness of 100 meter. This is relevant to understand gas generation in sedimentary basins affected by LIPs, like the Vøring and Møre basins (offshore Norway), the Karoo Basin (South Africa), and the Tunguska Basin (Russia). The total area estimated to be covered by sills in the Vøring and Møre basins is 85 000 km^2 (Svensen *et al.*, 2004). However, the Vøring and Møre basins belong to the North Atlantic Volcanic Province, which is probably at least 5 times as large (Svensen *et al.*, 2004). The extent of sills intruding into the Western Karoo Basin is ∼50 000 km^2 based on the mapped area of vent structures (Svensen *et al.*, 2007). For the total Karoo Basin we use an area of 390 000 km^2 as an estimate for area of sills intruded into carbon-rich sediments (Svensen *et al.*, 2007). For the Siberian Traps we use an area of 1.6 million km^2 based on outcropping sill intrusions (Svensen *et al.*, 2009). For a 1-6 wt% TOC background shale, the CH_4 generation potential from sill intrusions for the

Vøring and Møre basins is calculated to be ∼600-3500 Gt (Fig. 2.9). The total production potential in the Karoo Basin ranges from ∼2700 to ∼16200 Gt of CH_4 (for 1-6 wt% TOC). The source of carbon from the Karoo Basin is mainly the organic rich Ecca Group, including the black shale of the Whitehill Formation of 2-8 wt% TOC and the Prince Albert Formation of 0.5-4 wt% TOC (Svensen *et al.*, 2007). With an average TOC content of 2-4 wt%, a conservative estimate of the methane produced in the Karoo Basin is ∼5400-10700 Gt CH_4. The formation of the Siberian Traps are responsible for massive contact metamorphism and enhanced maturation in the Tunguska Basin, Russia (e.g. Kontorovich *et al.*, 1997). We estimate that at least ∼12000-66000 Gt of CH_4 (for 1-6 wt% TOC) could have been generated through contact metamorphism of organic material in the Tunguska Basin, using the same upscaling approach as for the other basins.

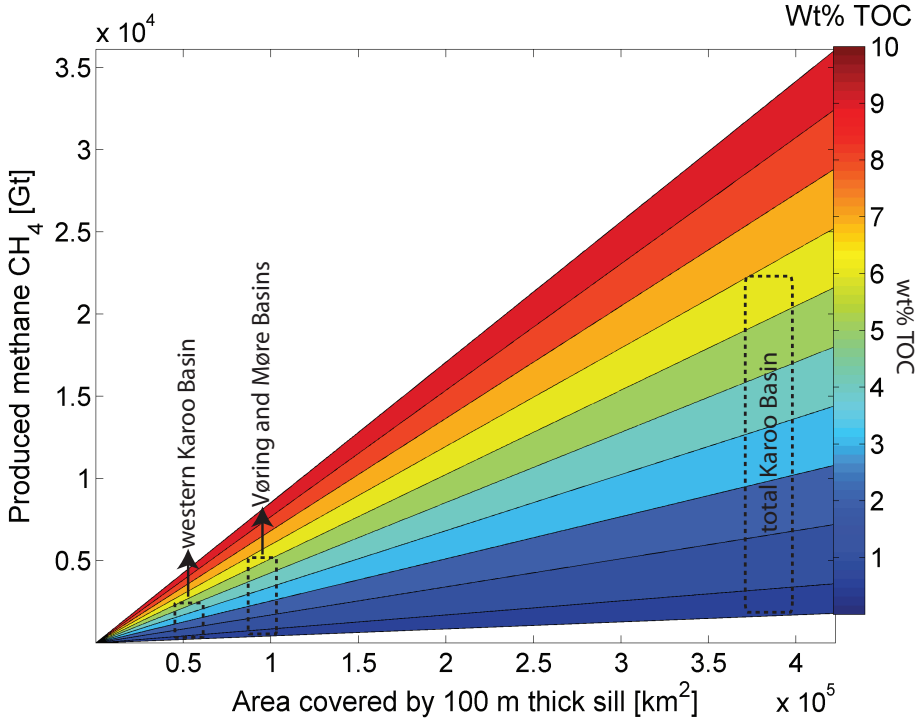

Figure 2.9: Calculated total methane potential in Gigatonnes (Gt) as a function of area covered by a cumulative intrusion thickness of 100 meter continuous sill. The generation potentials are for the Western Karoo Basin (50 000 km^2) ∼400-2100 Gt CH_4, the Vøring and Møre basins (85 000 km^2) ∼600-3500 Gt CH_4 and the total Karoo Basin (390 000 km^2) ∼2700-16200 Gt CH_4, for values of reacted shales from 1 to 6 wt% TOC.

2.6 Discussion

2.6.1 Modeling of contact metamorphism in shales

Heat flow model

We have used a heat conduction model with latent heat of crystallization and devolatilization reactions to estimate volatile production around igneous sills in sedimentary basins. We included latent heat of crystallization as it is considered a first order effect in cooling and crystallization of melts (e.g. Jaeger, 1957; Spohn *et al.*, 1988; Barker *et al.*, 1998). Conversely, the effect of latent heat consumed in dehydration reactions is believed to have minor influence on the thermal profile (e.g. Walther & Wood, 1984; Hanson & Barton, 1989; Galushkin, 1997). However, latent heat of organic cracking indicate measurable quantities of latent heat consumed in the organic cracking (Berkovich *et al.*, 1997). Combining latent heats of crystallization in the sill and devolatilization in the aureole gives an approximate 20% correction to the aureole thickness, which is similar to the variations within vitrinite reflectance measurements itself (10-20%). Misfits between data and calculated profiles can be compensated by varying thermal properties of the sill and the host-rock. Hence, effects of latent heat on calculated vitrinite reflectance profiles are only of major importance when all other thermal properties in the aureole are well constrained.

Latent heat of vaporization may also be a heat sink in shallow intrusions, but because we consider deeply buried shales ($\sim$3 km) with low porosity we do not incorporate this effect, as vaporization of pure H_2O is confined to the upper $\sim$1 km of a sedimentary basin (Kokelaar, 1982; Wagner & Pruss, 2002).

We have assumed no additional heat transport by fluid flow (i.e. a Peclet number of zero) because of the large uncertainties associated with effect of heat advection on thermal profiles on a basin scale. Although not shown here, there is a tendency of larger aureoles above than below sill intrusions (e.g. Simoneit *et al.*, 1978; Peters *et al.*, 1983; Gurba & Weber, 2001), which can result from vertical heat transport by fluids or incremental emplacement history (e.g. Kjeldstad *et al.*, 2003; Annen, 2009). However, conduction is the main heat-transfer process in low-permeable shale sequences due to limited pore-water convection (Bjørlykke *et al.*, 1988; Raymond & Murchison, 1988; Connolly & Thompson, 1989; Podladchikov & Wickham, 1994). Organic cracking by conductive heat has not been fully explored by numerical modeling, which makes it an important task to complete before more complexity is added.

Gas generation

Using default kinetic parameters from Easy%Ro determined from a wide range of source rocks is ideal for our generalised numerical approach to basin-scale aureole processes. The total generation potential W used in Easy%Ro adds up to 850 g_{HC}/kg_{rock}, similar to Type I kerogen, while the broad distribution of activation energies (142-301 kJ/mol) resembles the behaviour of Type III kerogen (Ungerer & Pelet, 1987). Thus, the overall behaviour of kerogen kinetics in shale source-rocks in our model is maintained. Note that the usage of default kinetics implies that our model cannot explain all case studies, due to a vast array of kinetic responses in different rock types (e.g. Snowdon, 1979; Holness & Watt, 2002;

Peters *et al.*, 2006).

Organic cracking reactions have multiple-order kinetics (Price, 1983). However, the simple first order Arrhenius equation provides sufficient coverage of the bulk kerogen kinetics due to its flexibility, i.e. it has a temperature dependence in both the frequency factor (A) and the activation energies E. Indeed, the vitrinite model Easy%Ro by Sweeney & Burnham (1990) is demonstrated to fit well with measured vitrinite profiles in many geological settings (e.g. Sweeney & Burnham, 1990; Fjeldskaar *et al.*, 2008), including this study.

The type of kerogen in the heated sediments dictates how much gas can be generated. Humic coals are mainly composed of Type III kerogen from which 10-25% of the carbon mass can be converted into gas (e.g. Hunt, 1996). In contrast, Type I and II kerogen commonly found in organic rich shales have the potential of converting up to 95% of the TOC to hydrocarbons (e.g. Ungerer & Pelet, 1987; Behar & Vandenbroucke, 1988). Because we use a conversion factor of 85% by weight, our approach will lead to an overestimation of gas generated from coal source rocks. Moreover, a considerable proportion of the carbon gases generated in coals can be retained due to a high trapping efficiency within the structural network of coals (Behar & Vandenbroucke, 1988; Hunt, 1996; Saghafi *et al.*, 2007, 2008). Also precipitation of carbonates derived from coal decomposition and CO_2 can cause further retention of the carbon gases (Finkelman *et al.*, 1998; Golab & Carr, 2004). Coals are therefore less important for generating and releasing large volumes of CH_4 gases relative to black shales. Still, there are several case studies demonstrating considerable gas generation in coal experiencing contact metamorphism (Snyman & Barclay, 1989; Gurba & Weber, 2001; Cooper *et al.*, 2007; Gröcke *et al.*, 2009). Hence, it is reasonable to assume that coal-derived carbon gases may play an important role during large scale contact metamorphism in sedimentary basins (McElwain *et al.*, 2005).

Isotope fractionation during gas generation

A recent study by Gröcke *et al.* (2009) suggesting that the generation potential of isotopically depleted carbon gases from coals is low based on lack of carbon-isotope ($\delta^{13}C$) enrichment in residual kerogen towards the intrusion contact. The fractionation of CH_4 relative to total kerogen is -1.4‰ to -12‰ for coals and -17.5‰ to -15‰ for shales (e.g. Clayton, 1991; Andresen *et al.*, 1995), which is commonly believed to cause a corresponding enrichment in $\delta^{13}C$ in the residual kerogen. However, care should be taken when using carbon-isotope composition of residual kerogen to infer the mass and composition of thermogenic gas released, as experiments show that there is no simple relationship between residual kerogen and the gas generated (Andresen *et al.*, 1995; Lorant *et al.*, 1998). For example, CO_2 has a positive fractionation of about 1‰ to 3‰ for coals, and 3‰ to 5‰ for shales (Andresen *et al.*, 1995). Hence, we expect that a large generation of CO_2 can contribute to the small lowering of $\delta^{13}C$ values in the residual carbon. Indeed, some coals have a correlation between higher maturity and more negative kerogen $\delta^{13}C$ (Andresen *et al.*, 1995; Cooper *et al.*, 2007; Schimmelmann *et al.*, 2009). More commonly, studies report no significant shift in $\delta^{13}C$ of the residual kerogen with increasing coal maturity (e.g. Faure, 1986; Ripley & Taib, 1989; Whiticar, 1996), even when methane with $\delta^{13}C$ values from -50 ‰ to -25‰ is released (Cramer *et al.*, 1998). Due to the lack of response in residual kerogen in addition to several factors influencing the $\delta^{13}C$ values, it is speculative to use kerogen $\delta^{13}C$ values as proxy for the

generation of isotopically light carbon gases (cf. Gröcke *et al.*, 2009).

Dehydration of minerals

We assume that the dehydration reactions occur at thermodynamic equilibrium. The advantage of this approach compared to kinetic modeling is that kinetics of mineral reactions are often poorly constrained, and rely on overstepping for reactions to occur (e.g. Nabelek, 2007). The overstepping temperature needed for dehydration reactions are rarely more than a few degrees, with a maximum of 40 °C (Walther & Wood, 1984), and would only lead to a minor shift of the equilibrium reaction conditions (Fig. 2.3).

The rate of dehydration reactions depends primarily on the rate of heat input (e.g. Walther & Orville, 1982). Dehydration reactions at contact aureole temperatures (∼500 °C) are estimated to go to completion after ∼200 years (Walther & Wood, 1984). This is well within the cooling time of thicker sills of 100 meters (∼500-1000 years). For thinner sills of 10 meters, the time of elevated temperature in the aureole may be too short for the minerals to reach equilibrium (∼10-50 years). Heating experiments on oil shales show a water loss of ∼40 kg_{H_2O}/m^3, using the reported density of 2200 kg/m^3 (Gregg *et al.*, 1981). This is in agreement with the lower range predicted by our numerical model.

2.6.2 Aureole thickness

We have shown that the existing 'rule of thumb' predicting aureole thicknesses of about 100% of the sill thickness can be improved to involve temperature of host-rock and intrusion, in addition to sill thickness (Eq. 2.5.1). The derived relationship is consistent with a large diversity in the data (Fig. 2.5a,b), and with the compilation of Raymond and Murchison (1988) showing a relation between the logarithm of intrusion thickness and the aureole thickness. However, there is a consistent tendency for the numerical modeling to over-estimate the vitrinite profile relative to observed profile data. This indicates that there are some local processes which are not considered in our generalized model. A non-instantaneous emplacement model could potentially account for some of these discrepancies (Galushkin, 1997).

An important implication of the relationship in Eq. 2.5.1 is that we expect larger aureoles to occur when sills intrude into host-rocks of relatively high background temperatures, as long as the temperature is within the field of normal organic maturation. Thus thicker aureoles will develop in basins with high geothermal gradients or around deeply emplaced sills. This is illustrated in Figure 2.10a using Eq. 2.5.1, showing aureole thicknesses as a function of different geothermal gradients. The figure is calculated using a sill thickness of 50 meters and a constant intrusion temperature of 1150 °C. Figure 2.10b illustrates how sill thicknesses influence the aureole thicknesses with depth. The geothermal gradient is fixed at 20 °C/km, with a constant intrusion temperature of 1150 °C. Due to the natural logarithm of the sill thickness in Eq. 2.5.1, the increase in aureole thickness between a 10 and a 50 meter thick sill is larger than the increase between a 50 and a 100 meter thick sill. In a volcanic basin, multiple sill intrusions can cause larger aureoles due to elevated background temperatures (Hanson & Barton, 1989; Deyoreo *et al.*, 1991).

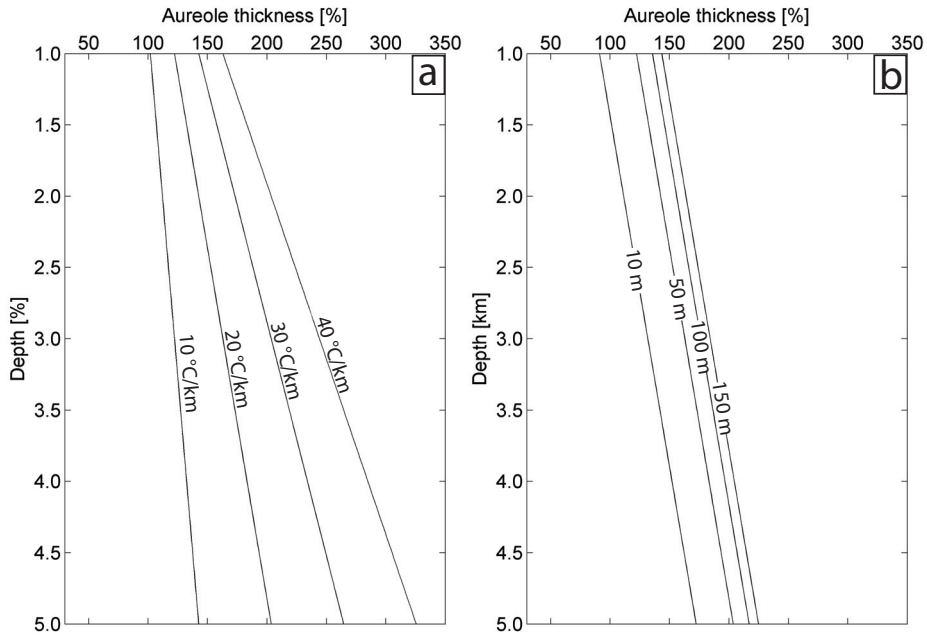

Figure 2.10: Calculated aureole thicknesses as a function of geothermal gradient **(a)** and sill thickness **(b)** using Eq. 2.5.1. In Figure (a) the sill thickness is set to 50 meters, whereas the geothermal gradient is fixed at 20 °C/km in Figure (b). A sill temperature of 1150 °C is applied in both cases.

2.6.3 Composition and fate of fluids

The fluid speciation suggests the presence of a fully miscible fluid in the sediments in the early stages of cooling, while at lower temperature (<300 °C) the fluid will unmix into a low density CH_4-phase and a more dense H_2O-phase (Fig. 2.8). At 100 MPa the solubility of CH_4 in H_2O is 0.4-10 wt% for the temperature range 100-350 °C (Bonham, 1978). This implies that for an aureole of 5 wt% TOC, a maximum of $\sim$20 kg/m^3 CH_4 can be retained in the denser, less mobile H_2O-dominated phase (10% of 120 kg/m^3 CH_4 + 90 kg/m^3 H_2O). Contact aureoles in shales will be dominated by CH_4-H_2O fluids rather than H_2O-CO_2 fluids, because of low oxygen fugacity resulting from a lack of oxygen sources (Connolly & Cesare, 1993). This fits well with our assumption of kerogen converting mainly into CH_4, rather than CO_2. Substantial addition of CO_2 from decarbonation or kerogen Type III rich sources can lead to a shift towards H_2O-CO_2 fluids (e.g. Gregg *et al.*, 1981; Hunt, 1996; Finkelman *et al.*, 1998; Santos *et al.*, 2009). Also, H_2O can react with residual graphite to produce CH_4-CO_2 fluids, with composition depending on the redox conditions (e.g. Pattison, 2006; Boiron *et al.*, 2007).

The fates of the generated fluids will depend on relative densities, capillary pressures and over-pressure buildup, among others (e.g. England *et al.*, 1987; Jamtveit & Yardley, 1997). A fluid-pressure buildup in the aureole will promote fluid flow out of the aureole either by seepage through

microfractures, or by explosive venting. Fluid-expansion resulting from kerogen cracking to gas is a well established source of overpressure in shales (e.g. Osborne & Swarbrick, 1997; Tingay *et al.*, 2009). There is a large density decrease going from CH_4 incorporated in kerogen matter ($\sim$1000 kg/m^3) and H_2O stored in hydrous minerals (2400 kg/m^3) to volatile CH_4 and H_2O ($\sim$200 and $\sim$800 kg/m^3), supporting pressure buildup and vertical fluid flow. The extra porosity generated from devolatilization can cause compaction and initiation of porosity-waves, which provides an effective transport mechanism to the atmosphere (e.g. Connolly, 1997; Connolly & Podladchikov, 1998; Appold & Nunn, 2002).

If a large volume of rock is undergoing contact-metamorphic devolatilization-reactions more rapidly than the fluids can escape, the building up of overpressure may eventually be released through extensive brecciation of the rock. Pipe-like flow structures originating from contact aureoles are evidence of such overpressures (e.g. Skinner & Marsh, 2004; Oliver *et al.*, 2006; Svensen *et al.*, 2006, 2009). An overpressurized aureole can arise from boiling and expansion of pore-fluids down to depths of $\sim$1 km (Delaney, 1982; Kokelaar, 1982; Manning & Bird, 1991; Jamtveit *et al.*, 2004). At larger depths, enhanced compaction reduces the amount of pore-fluids available, while higher pressures will reduce thermal expansion of the fluids. Pipe-structures rooted down to 4 km are thus more likely to form due to generation of substantial masses of CH_4 and H_2O in aureoles (Svensen *et al.*, 2006, 2007). Depending on the time-scale and extent of fluid generation, such explosive release of over-pressure through brecciated vents will rapidly transport the aureole fluids to the atmosphere (Svensen *et al.*, 2006). Vents are observed to commonly originate at sill tips (Planke *et al.*, 2005). Thus, vents can drain aureole fluids from both upper and lower aureoles through lateral flow (cf. England *et al.*, 1987). A typical pipe source region can be on the order of 5 km^3, effectively draining the aureole systems for the generated fluids (Svensen *et al.*, 2009).

2.6.4 Climate implication of basin-scale gas generation

Throughout geologic history, formation of Large Igneous Provinces in sedimentary basins has coincided with episodes of global warming and mass extinctions (e.g. Wignall, 2001; Svensen *et al.*, 2004). The Emeishan volcanic province ($\sim$260 Ma) is related to the end-Guadalupian extinction and warming event (e.g. Zhou *et al.*, 2002; Retallack *et al.*, 2006; Ganino & Arndt, 2009), the Siberian Traps ($\sim$252 Ma) coincides with the end-Permian extinction and warming event (e.g. Visscher *et al.*, 2004; Retallack & Jahren, 2008; Svensen *et al.*, 2009), the Central Atlantic magmatic province ($\sim$200 Ma) is related to the Triassic-Jurassic extinction and warming event (e.g. McElwain *et al.*, 1999; Courtillot & Renne, 2003), the Karoo igneous province ($\sim$183 Ma) is related to a global warming and minor extinction event (e.g. Jenkyns & Clayton, 1997; Svensen *et al.*, 2007, 2008) and the North Atlantic igneous province ($\sim$55 Ma) is related to the global warming and minor extinction event at the Palaeocene-Eocene boundary (e.g. Svensen *et al.*, 2004; Storey *et al.*, 2007). All these events can be explained by large scale contact metamorphism of organic material, with subsequent gas generation and release to the atmosphere through vents. In addition, large-scale extinctions related to the end-Permian (Siberian Traps) and the end- Guadalupian (Emeishan Igneous Province) can be enhanced by the release of ozone-depleting halogens formed by contact metamorphism of evaporite horizons (Visscher *et al.*, 2004; Beerling *et al.*, 2007; Svensen *et al.*, 2009).

Commonly, thick sills (>100 m) covering several square kilometers are found in deep levels of many sedimentary basins (e.g. Mjelde *et al.*, 1998; Chevallier & Woodford, 1999; Planke *et al.*, 2005; Polteau *et al.*, 2008). This implies a relatively high host-rock temperature (∼75-100 °C) and potentially elevated background maturation at the time of the LIP formations. In our model, these conditions support the formation of thick aureoles (Eq. 2.5.1). If the intruded shale is mature, the original source-rock potential is decreased and the kinetic behavior of the kerogen will be dictated by higher activation energies as the most labile bonds break off in the initial maturation. This is not accounted for in our modeling, but can be approached by using a TOC content that corresponds to the level of background maturation in the basin. We therefore assume that the host-rocks have a maximum average of 6 wt% TOC on the basin scale, although individual shale-formations can have initial TOC contents of at least 10 wt%.

The calculated amounts of CH_4 generated in the Vøring and Møre basins in Fig. 2.9 are similar to the ∼1340 Gt CH_4 that was estimated for a 200 meter thick aureole (i.e. 100 meter thick sill) at 2 wt% TOC by Svensen *et al.* (2004). This is a conservative value as the cumulative sill thickness in the basins can reach at least 300 meters, giving values three times higher than presented in Figure 2.9. Release of these gases has been linked to the Paleocene-Eocene Thermal Maximum (PETM) occurring at ∼55 Ma. A -2 to -3 ‰ drop in $\delta^{13}C$ values recorded at the PETM can be explained by release of about 1600-3100 Gt isotopically depleted methane (Dickens *et al.*, 1995; Higgins & Schrag, 2006). Pagani *et al.* (2006) estimate a larger negative drop of -3 to -5 ‰. Comparing our estimate of 3500 Gt CH_4 to calculations of Pagani *et al.* (2006) give a -2.5 to -3.5 ‰ negative shift of $\delta^{13}C$ depending on the isotopic composition of the released methane (i.e. $\delta^{13}C$ of -35 to -50 ‰). For the conservative value of 2000 Gt CH_4 the drop is -1.5 to -2 ‰ for the same $\delta^{13}C$ range of methane released. For our least conservative estimate using 300 meters of cumulative sill thickness in the Vøring and Møre basins, ∼4000 Gt C (5250 Gt CH_4) can be generated to match the higher estimates (4000 Gt C with $\delta^{13}C$ of -35 ‰) required by the study of Panchuk *et al.* (2008).

The values calculated for the Western Karoo Basin (Fig. 2.9) coincide well with the values 394-675 Gt CH_4 estimated by Svensen *et al.* (2007) based on actual aureole measurements. Similarly, the calculated methane generation potential for the total Karoo Basin corresponds well with the estimates ranging from 2505 to 10037 Gt CH_4 for a TOC-interval of 2-5 wt% and cumulative sill thickness of 100-200 meters (Svensen *et al.*, 2007).

Rapid production (i.e. 10-1000 years) of large amounts of isotopically light carbon gas is compatible with the proxy data suggesting rapid release of huge amount of $\delta^{13}C$-depleted gases to the atmosphere (e.g. Hesselbo *et al.*, 2000; Kemp *et al.*, 2005; McElwain *et al.*, 2005). The rate-limiting process will mainly be the duration of sill-emplacement in organic-rich formations, as both cracking and subsequent venting are relatively rapid processes. A massive release of methane from contact aureoles can trigger positive feedback mechanisms, such as release of methane from gas hydrates (e.g. Dickens *et al.*, 1995; Hesselbo *et al.*, 2000; Berner, 2002) and decreased overall storage capacity of carbon in the Earth system (e.g. Cox *et al.*, 2000; Friedlingstein *et al.*, 2006). The advantages of the thermogenic gas release over the methane hydrate mechanism are: 1) no requirement of any pre-warming episode; 2) the existence of geological evidences that hydrocarbons were generated, and released, from basin-wide occurring contact aureoles; 3) the generation potential of methane is in the same magnitude required to explain the proxy data, which may not be the case for the methane hydrate source (Higgins & Schrag, 2006;

Panchuk *et al.*, 2008); 4) a coherent explanation of the coincidental timing of LIP formation and global carbon-cycle perturbations.

2.7 Conclusions

We have developed a numerical model that predicts aureole thicknesses, gas generation and mineral dehydration for a wide range of intrusion thicknesses, intrusion temperatures and host-rock temperatures. By extrapolating our model to basin-scales, we are able to estimate information about aureoles that are directly observable. Our key conclusions are:

- Aureole thicknesses can vary from ∼30-200% of the sill thickness, depending on host-rock temperature, sill thickness and intrusion temperature. Effects of latent heat can give up to 20% correction to the calculated vitrinite profiles relative to calculations with no latent heat. Vitrinite data itself may vary up to 10-20%. A formula to estimate aureole thicknesses was developed to include temperature of host-rock and intrusion as well as sill thickness:

$$\frac{d}{h} \approx 0.0102 \cdot T_{\text{host-rock}} + 0.0029 \cdot T_{\text{intrusion}} + 0.1936 \cdot \ln(h) - 6.8611$$

- CH_4-H_2O fluids will be the dominating product from contact metamorphism of shale, while H_2O-CO_2 fluids can form in the presence of carbonate or humic host-rocks. CH_4 will dominate for TOC contents of >5 wt%, while H_2O will dominate for TOC contents of <1 wt%.

- Conversion of organic material to hydrocarbons in contact aureoles is a rapid process (10-1000 years) depending on intrusion thickness. The rate-limiting factor for hydrocarbon generation is the duration of sill emplacement.

- We estimate that the generation potential of CH_4 is ∼600-3500 Gt from the Vøring and Møre basins, ∼2700-16200 Gt from the Karoo Basin and ∼12000-66000 Gt from the Tunguska Basin. The key parameters are sill volume and TOC content of the intruded shale formations.

- Density change and pore-pressure build-up associated with the kerogen decomposition promotes overpressure and venting of CH_4 to the atmosphere through pipe-structures and seepage.

- Thermogenic gas generation related to LIP formations in sedimentary basins, with subsequent release of these gases to the atmosphere provides a causal connection for triggering global carbon cycle and environmental perturbations in times of LIP formation, like the end-Permian (∼252 Ma), the Toarcian (∼183 Ma) and the Paleocene-Eocene (∼55 Ma).

Acknowledgements

This study is supported by Grant 169457/S30 from the Norwegian Research Council. We would like to thank B. Jamtveit and S. Planke for important ideas, discussion and initiation of this project. We would like to thank D. A. Karlsen and M. Dabrowski for important input and discussions. M. Aerts, and G. Gisler are thanked for improving the manuscript.

REFERENCES

ANDRESEN B., THRONDSEN T., RÅHEIM A. & BOLSTAD J. (1995) A comparison of pyrolysis products with models for natural gas generation. *Chemical Geology*, **126**, 261–280.

ANNEN C. (2009) Implications of incremental emplacement of magma bodies for magma differentiation, thermal aureole dimensions and plutonism-volcanism relationships. *Tectonophysics*, **In Press, Corrected Proof**.

ANNEN C. & SPARKS R.S.J. (2002) Effects of repetitive emplacement of basaltic intrusions on thermal evolution and melt generation in the crust. *Earth and Planetary Science Letters*, **203**, 937–955.

APPOLD M.S. & NUNN J.A. (2002) Numerical models of petroleum migration via buoyancy-driven porosity waves in viscously deformable sediments. *Geofluids*, **2**, 233–247.

BARKER C.E. & BONE Y. (1995) The minimal response to contact metamorphism by the Devonian Buchan Caves Limestone, Buchan Rift, Victoria, Australia. *Organic Geochemistry*, **22**, 151–164.

BARKER C.E., BONE Y. & LEWAN M.D. (1998) Fluid inclusion and vitrinite-reflectance geothermometry compared to heat-flow models of maximum paleotemperature next to dikes, western onshore Gippsland Basin, Australia. *International Journal of Coal Geology*, **37**, 73–111.

BEARDSMORE G. & CULL J. (2001) *Crustal heat flow*. Cambridge University Press.

BEERLING D.J., HARFOOT M., LOMAX B. & PYLE J.A. (2007) The stability of the stratospheric ozone layer during the end-Permian eruption of the Siberian Traps. *Philosophical Transactions of the Royal Society A: Mathematical, Physical and Engineering Sciences*, **365**, 1843–1866.

BEHAR F. & VANDENBROUCKE M. (1988) Characterization and Quantification of Saturates Trapped inside Kerogen - Implications for Pyrolysate Composition. *Organic Geochemistry*, **13**, 927–938.

BERKOVICH A.J., LEVY J.H., SCHMIDT S.J. & YOUNG B.R. (2000) Heat capacities and enthalpies for some Australian oil shales from non-isothermal modulated DSC. *Thermochimica Acta*, **357-358**, 41–45.

BERKOVICH A.J., YOUNG B.R., LEVY J.H., SCHMIDT S.J. & RAY A. (1997) Thermal characterisation of Australian oil shales. *Journal of Thermal Analysis*, **49**, 737–743.

BERNER R.A. (2002) Examination of hypotheses for the Permo-Triassic boundary extinction by carbon cycle modeling. *Proceedings of the National Academy of Sciences*, **99**, 4172–4177.

BISHOP A.N. & ABBOTT G.D. (1995) Vitrinite Reflectance and Molecular Geochemistry of Jurassic Sediments - the Influence of Heating by Tertiary Dykes (Northwest Scotland). *Organic Geochemistry*, **22**, 165–177.

BJØRLYKKE K., MO A. & PALM E. (1988) Modelling of thermal convection in sedimentary basins and its relevance to diagenetic reactions. *Marine and Petroleum Geology*, **5**, 338–351.

BOIRON M.C., CATHELINEAU M., RUGGIERI G., JEANNINGROS A., GIANELLI G. & BANKS D.A. (2007) Active contact metamorphism and CO_2-CH_4 fluid production in the Larderello geothermal field (Italy) at depths between 2.3 and 4 km. *Chemical Geology*, **237**, 303–328.

BOSTICK N.H. (1979) Microscopic measurement of the level of catagenesis of solid organic matter in sedimentary rocks to aid exploration for petroleum and to determine former burial temperatures – a review. In: *Aspects of Diagenesis, S.E.P.M Special Publication* (Ed. P.A. Scholle & P.R. Schluger), vol. 26, 17–43.

BOSTICK N.H. & PAWLEWICZ M.J. (1984) Paleotemperatures based on vitrinite reflectance of shales and limestones in igneous dike aureoles in the Upper Cretaceous Pierre Shale, Walsenburg, Colorado. In: *Hydrocarbon Source Rocks of the Greater Rocky Mountain Region* (Ed. J.G. Woodward, F.F. Meissner & C.J. Clayton), 387–392. Rocky Mountain Association of Geologists.

BROWN R., GALLAGHER K. & DUANE M. (1994) A quantitative assessment of the effects of magmatism on the thermal history of the Karoo sedimentary sequence. *Journal of African Earth Sciences*, **18**, 227–243.

CADDICK M.J. & THOMPSON A.B. (2008) Quantifying the tectono-metamorphic evolution of pelitic rocks from a wide range of tectonic settings: mineral compositions in equilibrium. *Contributions to Mineralogy and Petrology*, **156**, 177–195.

CATUNEANU O., WOPFNER H., ERIKSSON P.G., CAIRNCROSS B., RUBIDGE B.S., SMITH R.M.H. & HANCOX P.J. (2005) The Karoo basins of south-central Africa. *Journal of African Earth Sciences*, **43**, 211–253.

CHEVALLIER L. & WOODFORD A. (1999) Morpho-tectonics and mechanism of emplacement of the dolerite rings and sills of the Western Karoo, South Africa. *South African Journal of Geology*, **102**, 43–54.

CLAYTON C. (1991) Carbon isotope fractionation during natural gas generation from kerogen. *Marine and Petroleum Geology*, **8**, 232–240.

CLAYTON J.L. & BOSTICK N.H. (1986) Temperature effects on kerogen and on molecular and isotopic composition of organic matter in Pierre Shale near an igneous dike. *Organic Geochemistry*, **10**, 135–143.

CONNOLLY J.A.D. (1995) Phase-Diagram Methods for Graphitic Rocks and Application to the System C-O-H-FeO-TiO_2-SiO_2. *Contributions to Mineralogy and Petrology*, **119**, 94–116.

CONNOLLY J.A.D. (1997) Devolatilization-generated fluid pressure and deformation-propagated fluid flow during prograde regional metamorphism. *Journal of Geophysical Research-Solid Earth*, **102**, 18149–18173.

CONNOLLY J.A.D. (2005) Computation of phase equilibria by linear programming: A tool for geodynamic modeling and its application to subduction zone decarbonation. *Earth and Planetary Science Letters*, **236**, 524–541.

CONNOLLY J.A.D. & CESARE B. (1993) C-O-H-S Fluid Composition and Oxygen Fugacity in Graphitic Metapelites. *Journal of Metamorphic Geology*, **11**, 379–388.

CONNOLLY J.A.D. & PODLADCHIKOV Y.Y. (1998) Compaction-driven fluid flow in viscoelastic rock. *Geodinamica Acta*, **11**, 55–84.

CONNOLLY J.A.D. & THOMPSON A.B. (1989) Fluid and enthalpy production during regional metamorphism. *Contributions to Mineralogy and Petrology*, **102**, 347–366.

COOPER J.R., CRELLING J.C., RIMMER S.M. & WHITTINGTON A.G. (2007) Coal metamorphism by igneous intrusion in the Raton Basin, CO and NM: Implications for generation of volatiles. *International Journal of Coal Geology*, **71**, 15–27.

COURTILLOT V.E. & RENNE P.R. (2003) On the ages of flood basalt events. *Comptes Rendus Geosciences*, **335**, 113–140.

COX P.M., BETTS R.A., JONES C.D., SPALL S.A. & TOTTERDELL I.J. (2000) Acceleration of global warming due to carbon-cycle feedbacks in a coupled climate model. *Nature*, **408**, 184–187.

CRAMER B., KROOSS B.M. & LITTKE R. (1998) Modelling isotope fractionation during primary cracking of natural gas: a reaction kinetic approach. *Chemical Geology*, **149**, 235–250.

DELANEY P.T. (1982) Rapid Intrusion of Magma into Wet Rock - Groundwater-Flow Due to Pore Pressure Increases. *Journal of Geophysical Research*, **87**, 7739–756.

DEYOREO J.J., LUX D.R. & GUIDOTTI C.V. (1991) Thermal Modeling in Low-Pressure High-Temperature Metamorphic Belts. *Tectonophysics*, **188**, 209–238.

DICKENS G.R., ONEIL J.R., REA D.K. & OWEN R.M. (1995) Dissociation of Oceanic Methane Hydrate as a Cause of the Carbon-Isotope Excursion at the End of the Paleocene. *Paleoceanography*, **10**, 965–971.

DOW W.G. (1977) Kerogen studies and geological interpretations. *Journal of Geochemical Exploration*, **7**, 79–99.

DRITS V.A., LINDGREEN H., SAKHAROV B.A., JAKOBSEN H.J., FALLICK A.E., SALYN A.L., DAINYAK L.G., ZVIAGINA B.B. & BARFOD D.N. (2007) Formation and transformation of mixed-layer minerals by tertiary intrusives in cretaceous mudstones, West Greenland. *Clays and Clay Minerals*, **55**, 260–283.

DUTROW B.L., TRAVIS B.J., GABLE C.W. & HENRY D.J. (2001) Coupled heat and silica transport associated with dike intrusion into sedimentary rock: effects on isotherm location and permeability evolution. *Geochimica et Cosmochimica Acta*, **65**, 3749–3767.

ENGLAND W.A., MACKENZIE A.S., MANN D.M. & QUIGLEY T.M. (1987) The Movement and Entrapment of Petroleum Fluids in the Subsurface. *Journal of the Geological Society*, **144**, 327–347.

FALKOWSKI P., SCHOLES R.J., BOYLE E., CANADELL J., CANFIELD D., ELSER J., GRUBER N., HIBBARD K., HOGBERG P., LINDER S., MACKENZIE F.T., MOORE B. I., PEDERSEN T., ROSENTHAL Y., SEITZINGER S., SMETACEK V. & STEFFEN W. (2000) The Global Carbon Cycle: A Test of Our Knowledge of Earth as a System. *Science*, **290**, 291–296.

FAURE G. (1986) *Principles of isotope geology*. John Wiley and Sons, New York.

FINKELMAN R.B., BOSTICK N.H., DULONG F.T., SENFTLE F.E. & THORPE A.N. (1998) Influence of an igneous intrusion on the inorganic geochemistry of a bituminous coal from Pitkin County, Colorado. *International Journal of Coal Geology*, **36**, 223–241.

FJELDSKAAR W., HELSET H.M., JOHANSEN H., GRUNNALEITEN I. & HORSTAD I. (2008) Thermal modelling of magmatic intrusions in the Gjallar Ridge, Norwegian Sea: implications for vitrinite reflectance and hydrocarbon maturation. *Basin Research*, **20**, 143–159.

FRIEDLINGSTEIN P., COX P., BETTS R., BOPP L., VON BLOH W., BROVKIN V., CADULE P., DONEY S., EBY M., FUNG I., BALA G., JOHN J., JONES C., JOOS F., KATO T., KAWAMIYA M., KNORR W., LINDSAY K., MATTHEWS H.D., RADDATZ T., RAYNER P., REICK C., ROECKNER E., SCHNITZLER K.G., SCHNUR R., STRASSMANN K., WEAVER A.J., YOSHIKAWA C. & ZENG N. (2006) Climate-carbon cycle feedback analysis: Results from the (CMIP)-M-4 model intercomparison. *Journal of Climate*, **19**, 3337–3353.

GALUSHKIN Y.I. (1997) Thermal effects of igneous intrusions on maturity of organic matter: A possible mechanism of intrusion. *Organic Geochemistry*, **26**, 645–658.

GANINO C. & ARNDT N.T. (2009) Climate changes caused by degassing of sediments during the emplacement of large igneous provinces. *Geology*, **37**, 323–326.

GANINO C., ARNDT N.T., ZHOU M.F., GAILLARD F. & CHAUVEL C. (2008) Interaction of magma with sedimentary wall rock and magnetite ore genesis in the Panzhihua mafic intrusion, SW China. *Mineralium Deposita*, **43**, 677–694.

GEORGE S.C. (1992) Effect of igneous intrusion on the organic geochemistry of a siltstone and an oil shale horizon in the Midland Valley of Scotland. *Organic Geochemistry*, **18**, 705–723.

GOLAB A.N. & CARR P.F. (2004) Changes in geochemistry and mineralogy of thermally altered coal, Upper Hunter Valley, Australia. *International Journal of Coal Geology*, **57**, 197–210.

GOLAB A.N., HUTTON A.C. & FRENCH D. (2007) Petrography, carbonate mineralogy and geochemistry of thermally altered coal in Permian coal measures, Hunter Valley, Australia. *International Journal of Coal Geology*, **70**, 150–165.

GRANT J.A. (2004) Liquid compositions from low-pressure experimental melting of pelitic rock from Morton Pass, Wyoming, USA. *Journal of Metamorphic Geology*, **22**, 65–78.

GREGG M.L., CAMPBELL J.H. & TAYLOR J.R. (1981) Laboratory and Modeling Investigation of a Colorado Oil-Shale Block Heated to 900 °C. *Fuel*, **60**, 179–188.

GRÖCKE D.R., RIMMER S.M., YOKSOULIAN L.E., CAIRNCROSS B., TSIKOS H. & VAN HUNEN J. (2009) No evidence for thermogenic methane release in coal from the Karoo-Ferrar large igneous province. *Earth and Planetary Science Letters*, **277**, 204–212.

GURBA L.W. & WEBER C.R. (2001) Effects of igneous intrusions on coalbed methane potential, Gunnedah Basin, Australia. *International Journal of Coal Geology*, **46**, 113–131.

HAAVE C. (2005) *Metamorphic and petrophysical effects of sill intrusions in sedimentary strata: The Karoo basin, South Africa*. Ph.D. Dissertation, University of Oslo.

HANSON R.B. & BARTON M.D. (1989) Thermal Development of Low-Pressure Metamorphic Belts - Results from Two-Dimensional Numerical-Models. *Journal of Geophysical Research-Solid Earth and Planets*, **94**, 10363–10377.

HENRY C., BOISSON J.Y., BOUCHET A. & MEUNIER A. (2007) Thermally induced mineral and chemical transformations in calcareous mudstones around a basaltic dyke (Perthus Pass, southern Massif Central, France). Possible implications as a natural analogue of nuclear waste disposal. *Clay Minerals*, **42**, 213–231.

HESSELBO S.P., GROCKE D.R., JENKYNS H.C., BJERRUM C.J., FARRIMOND P., BELL H.S.M. & GREEN O.R. (2000) Massive dissociation of gas hydrate during a Jurassic oceanic anoxic event. *Nature*, **406**, 392–395.

HIGGINS J.A. & SCHRAG D.P. (2006) Beyond methane: Towards a theory for the Paleocene-Eocene Thermal Maximum. *Earth and Planetary Science Letters*, **245**, 523–537.

HOLNESS M.B. & ISHERWOOD C.E. (2003) The aureole of the Rum Tertiary Igneous Complex, Scotland. *Journal of the Geological Society*, **160**, 15–27.

HOLNESS M.B. & WATT G.R. (2002) The Aureole of the Traigh Bhan na Sgurra Sill, Isle of Mull: Reaction-Driven Microcracking During Pyrometamorphism. *Journal of Petrology*, **43**, 511–534.

HUNT J.M. (1996) *Petroleum Geochemistry and Geology (Second Edition)*. W.H. Freeman and Company, 2nd edn.

JAEGER J. (1959) Temperatures outside a cooling intrusive sheet. *American Journal of Science*, **257**, 44–54.

JAEGER J.C. (1957) The temperature in the neighborhood of a cooling intrusive sheet. *American Journal of Science*, **255**, 306–318.

JAMTVEIT B., GRORUD H.F. & BUCHER-NURMINEN K. (1992) Contact metamorphism of layered carbonate-shale sequences in the Oslo Rift. II: Migration of isotopic and reaction fronts around cooling plutons. *Earth and Planetary Science Letters*, **114**, 131–148.

JAMTVEIT B., SVENSEN H. & PODLADCHIKOV Y.Y. (2004) Hydrothermal vent complexes associated with sill intrusions in sedimentary basins. In: *Physical Geology of High-Level Magmatic Systems* (Ed. C. Breitkreuz & N. Petford), vol. 234. Geological Society, London, Special Publications.

JAMTVEIT B. & YARDLEY B. (1997) *Fluid flow and transport in rocks. Mechanisms and effects*. Chapman and Hall.

JENKYNS H.C. (1988) The early Toarcian (Jurassic) anoxic event; stratigraphic, sedimentary and geochemical evidence. *American Journal of Science*, **288**, 101–151.

JENKYNS H.C. & CLAYTON C.J. (1997) Lower Jurassic epicontinental carbonates and mudstones from England and Wales: chemostratigraphic signals and the early Toarcian anoxic event. *Sedimentology*, **44**, 687–706.

KARLSEN D.A. & SKEIE J.E. (2006) Petroleum migration, faults and overpressure, Part I: Calibrating basin modelling using petroleum in traps - A review. *Journal of Petroleum Geology*, **29**, 227–255.

KEMP D.B., COE A.L., COHEN A.S. & SCHWARK L. (2005) Astronomical pacing of methane release in the Early Jurassic period. *Nature*, **437**, 396–399.

KJELDSTAD A., LANGTANGEN H.P., SKOGSEID J. & BJØRLYKKE K. (2003) Simulation of sedimentary basins. In: *Advanced Topics in Computational Partial Differential Equations - Numerical Methods and Diffpack Programming* (Ed. H.P. Langtangen & A. Tveito), vol. 33, 611–658. Springer Verlag.

KOKELAAR B.P. (1982) Fluidization of Wet Sediments During the Emplacement and Cooling of Various Igneous Bodies. *Journal of the Geological Society*, **139**, 21–33.

KONTOROVICH A.E., KHOMENKO A.V., BURSHTEIN L.M., LIKHANOV I.I., PAVLOV A.L., STAROSELTSEV V.S. & TEN A.A. (1997) Intense basic magmatism in the Tunguska petroleum basin, eastern Siberia, Russia. *Petroleum Geoscience*, **3**, 359–369.

LITVINOVSKI B.A., PODLADCHIKOV Y.Y., ZANVILEVITCH A.N. & DUNITCHEV V.M. (1990) On the melting of acidic volcanites in the contact of basic magma at shallow depth. *Geochimya*, **6**, 807–814.

LORANT F., PRINZHOFER A., BEHAR F. & HUC A.Y. (1998) Carbon isotopic and molecular constraints on the formation and the expulsion of thermogenic hydrocarbon gases. *Chemical Geology*, **147**, 249–264.

MANNING C.E. & BIRD D.K. (1991) Porosity Evolution and Fluid-Flow in the Basalts of the Skaergaard Magma-Hydrothermal System, East Greenland. *American Journal of Science*, **291**, 201–257.

MASTALERZ M., DROBNIAK A. & SCHIMMELMANN A. (2009) Changes in optical properties, chemistry, and micropore and mesopore characteristics of bituminous coal at the contact with dikes in the Illinois Basin. *International Journal of Coal Geology*, **77**, 310–319.

MCELWAIN J.C., BEERLING D.J. & WOODWARD F.I. (1999) Fossil Plants and Global Warming at the Triassic-Jurassic Boundary. *Science*, **285**, 1386–1390.

MCELWAIN J.C., WADE-MURPHY J. & HESSELBO S.P. (2005) Changes in carbon dioxide during an oceanic anoxic event linked to intrusion into Gondwana coals. *Nature*, **435**, 479–482.

MÉTRICH N. & RUTHERFORD M.J. (1998) Low pressure crystallization paths of H_2O-saturated basaltic-hawaiitic melts from Mt Etna: Implications for open-system degassing of basaltic volcanoes. *Geochimica et Cosmochimica Acta*, **62**, 1195–1205.

MEYERS P.A. & SIMONEIT B.R.T. (1999) Effects of extreme heating on the elemental and isotopic compositions of an Upper Cretaceous coal. *Organic Geochemistry*, **30**, 299–305.

MJELDE R., DIGRANES P., SHIMAMURA H., SHIOBARA H., KODAIRA S., BREKKE H., EGEBJERG T., SØRENES N. & THORBJØRNSEN S. (1998) Crustal structure of the northern part of the Vøring Basin, mid-Norway margin, from wide-angle seismic and gravity data. *Tectonophysics*, **293**, 175–205.

NABELEK P.I. (2007) Fluid evolution and kinetics of metamorphic reactions in calc-silicate contact aureoles - From H_2O to CO_2 and back. *Geology*, **35**, 927–930.

NICHOLS G.T., WYLLIE P.J. & STERN C.R. (1994) Subduction zone melting of pelagic sediments constrained by melting experiments. *Nature*, **371**, 785–788.

OLIVER N.H.S., RUBENACH M.J., FU B., BAKER T., BLENKINSOP T.G., CLEVERLEY J.S., MARSHALL L.J. & RIDD P.J. (2006) Granite-related overpressure and volatile release in the mid crust: fluidized breccias from the Cloncurry District, Australia. *Geofluids*, **6**, 346–358.

OSBORNE M.J. & SWARBRICK R.E. (1997) Mechanisms for generating overpressure in sedimentary basins: A reevaluation. *AAPG Bulletin*, **81**, 1023–1041.

OTHMAN R., AROURI K.R., WARD C.R. & MCKIRDY D.M. (2001) Oil generation by igneous intrusions in the northern Gunnedah Basin, Australia. *Organic Geochemistry*, **32**, 1219–1232.

PAGANI M., CALDEIRA K., ARCHER D. & ZACHOS J.C. (2006) Atmosphere: An Ancient Carbon Mystery. *Science*, **314**, 1556–1557.

PANCHUK K., RIDGWELL A. & KUMP L.R. (2008) Sedimentary response to Paleocene-Eocene Thermal Maximum carbon release: A model-data comparison. *Geology*, **36**, 315–318.

PATTISON D.R.M. (2006) The fate of graphite in prograde metamorphism of pelites: An example from the Ballachulish aureole, Scotland. *Lithos*, **88**, 85–99.

PAYNE J.L. & KUMP L.R. (2007) Evidence for recurrent Early Triassic massive volcanism from quantitative interpretation of carbon isotope fluctuations. *Earth and Planetary Science Letters*, **256**, 264–277.

PERREGAARD J. & SCHIENER E.J. (1979) Thermal alteration of sedimentary organic matter by a basalt intrusive (Kimmeridgian Shales, Milne Land, East Greenland). *Chemical Geology*, **26**, 331–343.

PETERS K.E., WALTERS C.C. & MANKIEWICZ P.J. (2006) Evaluation of kinetic uncertainty in numerical models of petroleum generation. *AAPG Bulletin*, **90**, 387–403.

PETERS K.E., WHELAN J.K., HUNT J.M. & TARAFA M.E. (1983) Programmed pyrolysis of organic matter from thermally altered Cretaceous black shales. *AAPG Bulletin*, **67**, 2137–2146.

PLANKE S., RASMUSSEN T., REY S.S. & MYKLEBUST R. (2005) Seismic characteristics and distribution of volcanic intrusions and hydrothermal vent complexes in the Vøring and Møre basins. In: *Petroleum Geology: North-West Europe and Global Perspectives & Proceedings of the 6th Petroleum Geology Conference. Geological Society, London*, 833–844.

PODLADCHIKOV Y.Y. & WICKHAM S.M. (1994) Crystallization of Hydrous Magmas - Calculation of Associated Thermal Effects, Volatile Fluxes, and Isotopic Alteration. *Journal of Geology*, **102**, 25–45.

POLTEAU S., MAZZINI A., GALLAND O., PLANKE S. & MALTHE-SØRENSSEN A. (2008) Saucer-shaped intrusions: Occurrences, emplacement and implications. *Earth and Planetary Science Letters*, **266**, 195–204.

POLYANSKY O.P. & REVERDATTO V.V. (2006) Contact metamorphism and metasomatism near the Talnakh intrusion: Fluid convection and heat transfer modeling on the basis of the Finite-Difference method. *Doklady Earth Sciences*, **114**, 803–807.

POWERS S. & CLAPP F.G. (1932) Nature and origin of occurrences of oil, gas, and bitumen in igneous and metamorphic rocks. *AAPG Bulletin*, **16**, 719–726.

PRICE L.C. (1983) Geologic time as a parameter in organic metamorphism and vitrinite reflectance as an absolute paleogeothermometer. *Journal of Petroleum Geology*, **6**, 5–37.

RAYMOND A.C. & MURCHISON D.G. (1988) Development of Organic Maturation in the Thermal Aureoles of Sills and Its Relation to Sediment Compaction. *Fuel*, **67**, 1599–1608.

REITER M. & TOVAR R.J.C. (1982) Estimates of Terrestrial Heat-Flow in Northern Chihuahua, Mexico, Based Upon Petroleum Bottom-Hole Temperatures. *Geological Society of America Bulletin*, **93**, 613–624.

RETALLACK G.J. & JAHREN A.H. (2008) Methane Release from Igneous Intrusion of Coal during Late Permian Extinction Events. *The Journal of Geology*, **116**, 1–20.

RETALLACK G.J., METZGER C.A., GREAVER T., JAHREN A.H., SMITH R.M.H. & SHELDON N.D. (2006) Middle-Late Permian mass extinction on land. *Geological Society of America Bulletin*, **118**, 1398–1411.

REVERDATTO V.V. & MELENEVSKII V.N. (1983) Magmatic heat as a factor in generation of hydrocarbons: the case of basalt sills. *Geologiya i Geofizika*, **24**, 15–23.

RIPLEY E.M. & TAIB N.I. (1989) Carbon isotopic studies of metasedimentary and igneous rocks at the Babbitt Cu—Ni deposit, Duluth complex, Minnesota, U.S.A. *Chemical Geology: Isotope Geoscience section*, **73**, 319–342.

RODRIGUEZ MONREAL F., VILLAR H.J., BAUDINO R., DELPINO D. & ZENCICH S. (2009) Modeling an atypical petroleum system: A case study of hydrocarbon generation, migration and accumulation related to igneous intrusions in the Neuquen Basin, Argentina. *Marine and Petroleum Geology*, **26**, 590–605.

SAGHAFI A., FAIZ M. & ROBERTS D. (2007) CO_2 storage and gas diffusivity properties of coals from Sydney Basin, Australia. *International Journal of Coal Geology*, **70**, 240–254.

SAGHAFI A., PINETOWN K.L., GROBLER P.G. & VAN HEERDEN J.H.P. (2008) CO_2 storage potential of South African coals and gas entrapment enhancement due to igneous intrusions. *International Journal of Coal Geology*, **73**, 74–87.

SANTOS R.V., DANTAS E.L., DE OLIVEIRA C.G., DE ALVARENGA C.J.S., DOS ANJOS C.W.D., GUIMARÃES E.M. & OLIVEIRA F.B. (2009) Geochemical and thermal effects of a basic sill on black shales and limestones of the Permian Irati Formation. *Journal of South American Earth Sciences*, **28**, 14–24.

SAXBY J.D. & STEPHENSON L.C. (1987) Effect of anigneous intrusion on oil shale at Rundle (Australia). *Chemical Geology*, **63**, 1–16.

SCHENK H.J., DIPRIMIO R. & HORSFIELD B. (1997) The conversion of oil into gas in petroleum reservoirs .1. Comparative kinetic investigation of gas generation from crude oils of lacustrine, marine and fluviodeltaic origin by programmed-temperature closed-system pyrolysis. *Organic Geochemistry*, **26**, 467–481.

SCHIMMELMANN A., MASTALERZ M., GAO L., SAUER P.E. & TOPALOV K. (2009) Dike intrusions into bituminous coal, Illinois Basin: H, C, N, O isotopic responses to rapid and brief heating. *Geochimica et Cosmochimica Acta*, **73**, 6264–6281.

SHIH S.M. & SOHN H.Y. (1978) A mathematical model for the retorting of a large block of oil shale: effect of the internal temperature gradient. *Fuel*, **57**, 622–630.

SIMONEIT B.R.T., BRENNER S., PETERS K.E. & KAPLAN I.R. (1978) Thermal Alteration of Cretaceous Black Shale by Basaltic Intrusions in Eastern Atlantic. *Nature*, **273**, 501–504.

SIMONEIT B.R.T., BRENNER S., PETERS K.E. & KAPLAN I.R. (1981) Thermal Alteration of Cretaceous Black Shale by Diabase Intrusions in the Eastern Atlantic .2. Effects on Bitumen and Kerogen. *Geochimica Et Cosmochimica Acta*, **45**, 1581–1602.

SKINNER E.M.W. & MARSH J.S. (2004) Distinct kimberlite pipe classes with contrasting eruption processes. *Lithos*, **76**, 183–200.

SNOWDON L.R. (1979) Errors in extrapolation of experimental kinetic parameters to organic geochemical systems. *AAPG Bulletin*, **63**, 1128–1134.

SNYMAN C.P. & BARCLAY J. (1989) The Coalification of South-African Coal. *International Journal of Coal Geology*, **13**, 375–390.

SPOHN T., HORT M. & FISCHER H. (1988) Numerical-Simulation of the Crystallization of Multicomponent Melts in Thin Dikes or Sills .1. the Liquidus Phase. *Journal of Geophysical Research-Solid Earth and Planets*, **93**, 4880–4894.

STOREY M., DUNCAN R.A. & SWISHER C. C. I. (2007) Paleocene-Eocene Thermal Maximum and the Opening of the Northeast Atlantic. *Science*, **316**, 587–589.

STORVOLL V., BJORLYKKE K. & MONDOL N.H. (2005) Velocity-depth trends in mesozoic and cenozoic sediments from the Norwegian shelf. *AAPG Bulletin*, **89**, 359–381.

STOTHERS R.B. (1993) Flood Basalts and Extinction Events. *Geophysical Research Letters*, **20**, 1399–1402.

SVENSEN H., BEBOUT G., KRONZ A., LI L., PLANKE S., CHEVALLIER L. & JAMTVEIT B. (2008) Nitrogen geochemistry as a tracer of fluid flow in a hydrothermal vent complex in the Karoo Basin, South Africa. *Geochimica et Cosmochimica Acta*, **72**, 4929–4947.

SVENSEN H. & JAMTVEIT B. (1998) Contact metamorphism of shales and limestones from the Grua area, the Oslo Rift, Norway: a phase-petrological study. *Norsk Geologisk Tidsskrift*, **78**, 81–98.

SVENSEN H., JAMTVEIT B., PLANKE S. & CHEVALLIER L. (2006) Structure and evolution of hydrothermal vent complexes in the Karoo Basin, South Africa. *Journal of the Geological Society*, **163**, 671–682.

SVENSEN H., PLANKE S., CHEVALLIER L., MALTHE-SØRENSSEN A., CORFU F. & JAMTVEIT B. (2007) Hydrothermal venting of greenhouse gases triggering Early Jurassic global warming. *Earth and Planetary Science Letters*, **256**, 554–566.

SVENSEN H., PLANKE S., MALTHE-SORENSSEN A., JAMTVEIT B., MYKLEBUST R., EIDEM T.R. & REY S.S. (2004) Release of methane from a volcanic basin as a mechanism for initial Eocene global warming. *Nature*, **429**, 542–545.

SVENSEN H., PLANKE S., POLOZOV A.G., SCHMIDBAUER N., CORFU F., PODLADCHIKOV Y.Y. & JAMTVEIT B. (2009) Siberian gas venting and the end-Permian environmental crisis. *Earth and Planetary Science Letters*, **277**, 490–500.

SWEENEY J. & BURNHAM .K. (1990) Evaluation of a simple model of vitrinite reflectance based on chemical kinetics. *AAPG Bulletin*, **74**, 1559–1570.

TINGAY M.R.P., HILLIS R.R., SWARBRICK R.E., MORLEY C.K. & DAMIT A.R. (2009) Origin of overpressure and pore-pressure prediction in the Baram province, Brunei. *AAPG Bulletin*, **93**, 51–74.

TISSOT B. & WELTE D.H. (1984) *Petroleum Formation and Occurrence*. Springer Verlag, Berlin, 2nd edn.

TISSOT B.P., PELET R. & UNGERER P. (1987) Thermal History of Sedimentary Basins, Maturation Indexes, and Kinetics of Oil and Gas Generation. *AAPG Bulletin*, **71**, 1445–1466.

TROMMSDORFF V. & CONNOLLY J.A.D. (1996) The ultramafic contact aureole about the Bregaglia (Bergell) tonalite: Isograds and a thermal model. *Schweizerische Mineralogische Und Petrographische Mitteilungen*, **76**, 537–547.

TURCOTTE D.L. & SCHUBERT G. (2002) *Geodynamics*. Cambridge, 2nd edn.

UNGERER P. & PELET R. (1987) Extrapolation of the Kinetics of Oil and Gas-Formation from Laboratory Experiments to Sedimentary Basins. *Nature*, **327**, 52–54.

VISSCHER H., LOOY C.V., COLLINSON M.E., BRINKHUIS H., VAN KONIJNENBURG-VAN CITTERT J.H.A., KÄRSCHNER W.M. & SEPHTON M.A. (2004) Environmental mutagenesis during the end-Permian ecological crisis. *Proceedings of the National Academy of Sciences of the United States of America*, **101**, 12952–12956.

WAGNER W. & PRUSS A. (2002) The IAPWS formulation 1995 for the thermodynamic properties of ordinary water substance for general and scientific use. *Journal of Physical and Chemical Reference Data*, **31**, 387–535.

WALTHER J.V. & ORVILLE P.M. (1982) Volatile Production and Transport in Regional Metamorphism. *Contributions to Mineralogy and Petrology*, **79**, 252–257.

WALTHER J.V. & WOOD B.J. (1984) Rate and Mechanism in Prograde Metamorphism. *Contributions to Mineralogy and Petrology*, **88**, 246–259.

WHITICAR M.J. (1996) Stable isotope geochemistry of coals, humic kerogens and related natural gases. *International Journal of Coal Geology*, **32**, 191–215.

WIGNALL P.B. (2001) Large igneous provinces and mass extinctions. *Earth-Science Reviews*, **53**, 1–33.

ZHOU M.F., MALPAS J., SONG X.Y., ROBINSON P.T., SUN M., KENNEDY A.K., LESHER C.M. & KEAYS R.R. (2002) A temporal link between the Emeishan large igneous province (SW China) and the end-Guadalupian mass extinction. *Earth and Planetary Science Letters*, **196**, 113–122.

ZHU D., JIN Z., HU W., SONG Y. & GAO X. (2007) Effect of igneous activity on hydrocarbon source rocks in Jiyang sub-basin, eastern China. *Journal of Petroleum Science and Engineering*, **59**, 309–320.

Chapter 3

Contact metamorphic devolatilization of shales in the Karoo Basin, South Africa, and the effects of multiple sill intrusions

by Ingrid Aarnes*, Henrik Svensen*, Stephane Polteau*† and Sverre Planke*†
Manuscript submitted to Chemical Geology

.

3.1 Abstract

Quantification of fluid generation during contact metamorphism of shale is important for the understanding of metamorphic processes, fluid flow in sedimentary basins and perturbations of the global carbon cycle. In this study we provide geochemical and numerical analyses from the organic-rich Ecca Group in the Karoo Basin, South Africa, which was affected by contact metamorphism from multiple sill intrusions in the Early Jurassic. Organic matter was efficiently converted to hydrocarbons during contact metamorphism, and complete loss of organic carbon in the innermost aureole is common. Mineral dehydration reactions are evident from the occurrence of metamorphic minerals like biotite and loss of the clay fraction towards the intrusive contact. We have developed a numerical model in order to quantify fluid production from both inorganic and organic reactions during contact metamorphism. The modelling results are constrained by data from two case studies in the Karoo Basin in order to obtain reliable estimates of the carbon loss from metamorphism of shale. We show that single, thin ($\sim$15 meter thick) sills have a gas production potential of several gigatons of methane (CH_4) if emplaced over a $>$1000 km^2 area. Furthermore, the vertical spacing between simultaneously emplaced sills has an important influence on the gas generation potential. When two sills are emplaced with a vertical spacing of $\sim$7 times the intrusion thickness, the total CH_4 generation is up to $\sim$35 % more than for two separate sills. Data and modelling from five sills emplaced within the Ecca Group show hydrocarbon generation

*Physics of Geological Processes, University of Oslo, P.box 1048 Blindern, 0316 Oslo, Norway.
†VBPR, Oslo Innovation Center, Gaustadalléen 21, N-0349 Oslo, Norway

throughout the organic-rich section, with total carbon loss next to the sills. This has implications for the fluid production and metamorphism in volcanic basins where multiple sills are common.

3.2 Introduction

Large Igneous Provinces (LIPs), such as the Karoo-Ferrar province, are characterized by the presence of an extensive network of sills and dykes emplaced in sedimentary rocks (Du Toit, 1920; Walker & Poldervaart, 1949; Marsh *et al.*, 1997; Chevallier & Woodford, 1999; Galerne *et al.*, 2008; Polteau *et al.*, 2008). An important consequence of the intrusive activity is rapid heating of the host sediments, causing devolatilization of organic matter and hydrous minerals. Modelling and field data show that several thousand gigatons of methane (CH_4) can be generated during basin-scale contact metamorphism, subsequently released to the atmosphere through breccia pipes and hydrothermal vent complexes (Svensen *et al.*, 2004, 2006, 2007; Polteau *et al.*, in prep.; Aarnes *et al.*, accepted). Such voluminous release of methane will perturb the global carbon cycle if generated and released on a short timescale.

There are several examples of concurrent global climatic perturbations and emplacement of LIPs into sedimentary basins, such as in the North Atlantic Province ($\sim$55 Ma), the Karoo-Ferrar Province ($\sim$183 Ma), the Siberian Traps ($\sim$252 Ma) and the Emeshian Volcanic Province ($\sim$260 Ma) (Rampino & Stothers, 1988; Palfy & Smith, 2000; Wignall, 2001; Courtillot & Renne, 2003; Svensen *et al.*, 2004, 2007; Ganino & Arndt, 2009; Svensen *et al.*, 2009). Indeed, the isotopic records associated with several LIP emplacement events show sharp negative carbon excursions which are best explained by a massive and rapid release of ^{13}C depleted carbon gases, e.g. methane, to the atmosphere (Dickens *et al.*, 1997; Jenkyns & Clayton, 1997; Hesselbo *et al.*, 2000; Kemp *et al.*, 2005; McElwain *et al.*, 2005; Suan *et al.*, 2008). Although basin scale estimates of thermogenic gas generation from contact metamorphism shows that the potential gas generation is sufficient to explain the proxy record (Svensen *et al.*, 2004, 2007, 2009; Aarnes *et al.*, accepted), there is a need for complementary studies that investigate how multiple sills within organic-rich strata affect the gas generation potential.

There are several studies documenting hydrocarbon generation during contact metamorphism of organic matter around single sheet intrusions (Simoneit *et al.*, 1978; Perregaard & Schiener, 1979; Clayton & Bostick, 1986; Raymond & Murchison, 1988). They conclude that these single intrusions had only localized effects on the organic maturation in the host sediments, mainly because the studies were made on thin intrusions, often dikes. In a volcanic basin such as the Karoo Basin, several levels sill intrusions of 10 to over 100 meter vertical thickness are common. Multiple intrusion levels will rise the temperature over much larger rock volumes than single intrusions (Hanson & Barton, 1989), leading to enhanced hydrocarbon generation on a basin scale (Price, 1983). The coupling between thermal evolution of sills and the organic maturation and devolatilization reactions occurring in the host-rocks has been modelled by Aarnes *et al.* (accepted), and enables quantification of methane generation during contact metamorphism.

This study focuses on integrating field data and numerical modelling of single and multiple intrusions emplaced into the organic-rich Ecca Group in the Karoo Basin, South Africa. The aim is to quantify the degree of organic maturation and extent of fluid production based on geological data. We provide two case studies, one near Hopetown in the northern Karoo Basin, and one in

Calvinia in the western Karoo Basin. In the Hopetown case study we compare data from one contact metamorphic borehole section with its unmetamorphosed equivalent, and use the information to constrain the numerical modelling. In the Calvinia case study we present data from the whole Ecca Group intruded by five sills emplaced at different levels. We apply the developed model to quantify the combined thermal effects of the multiple sills on the intruded shales. Moreover, we identify the sill spacing as an important factor that enhances the maximum gas generation. The effects of multiple sills and sill spacing are relevant for other geological systems where large volumes of magma intrude into sedimentary formations.

3.3 Geological setting

The Karoo Basin covers nearly two thirds of South Africa (Fig. 3.1). The basin accommodates a >5 kilometers thick sedimentary sequence of Late Carboniferous to Early Jurassic age deposited in the foreland basin of the Cape Fold Belt (Lock, 1980; Cole, 1992; Catuneanu *et al.*, 1998). The depositional environments range from partly marine (Dwyka and Ecca groups) to fluvial and aeolian in the Beaufort and Stormberg groups (Smith, 1990; Catuneanu *et al.*, 1998). The sedimentation was terminated by the extensive volcanism in the early Jurassic (183 $\pm$ 1 Ma; Duncan *et al.*, 1997).

The organic-rich shale formations of the Karoo Basin are located within the Ecca Group, and include the Prince Albert, the Whitehill, and the Tierberg formations. The Prince Albert Fm. is dominated by dark greenish-grey shale deposited in a deep water environment (Catuneanu *et al.*, 1998). The total organic carbon (TOC) content of the Prince Alberg Fm. varies considerably, with up to 12 wt. % TOC locally (Faure & Cole, 1999). The Whitehill Fm. is a black shale unit consisting of carbonaceous pyritic shale, with overall high TOC contents of up to 15 wt. % (Faure and Cole, 1999; Branch et al., 2007). The hydrogen and oxygen indexes from the Whitehill Fm. indicate a mixture of Type I and Type II kerogen (Faure & Cole, 1999). The depositional environment ranges from brackish to deep marine deposits (Smith, 1990; Visser, 1992; Catuneanu *et al.*, 2005). The Whitehill Fm. reaches a maximum thickness of about 80 meters in the Loeriesfontein area (Visser, 1992). The Tierberg Fm. is a grey shale with an upward transition from deep-water submarine to shallow-water deltaic deposits and finally terrestrial facies (Faure & Cole, 1999). The average TOC contents in the Tierberg Fm. are 1-2 wt. % (Svensen *et al.*, 2007).

Lower Jurassic sills and dikes are present throughout the Karoo sedimentary sequence, with the most extensive and thickest sills located within the Ecca Group (Du Toit, 1920; Chevallier & Woodford, 1999). Because of the overall high TOC contents in the Ecca Group, these shales represent a potentially significant source of methane-rich fluids when heated during contact metamorphism.

3.4 Methods

3.4.1 Borehole sampling

In this study we present two case studies from 1) Calvinia and 2) Hopetown locations (Fig. 3.1). Near Calvinia in the western Karoo Basin two fully cored boreholes were drilled trough breccia

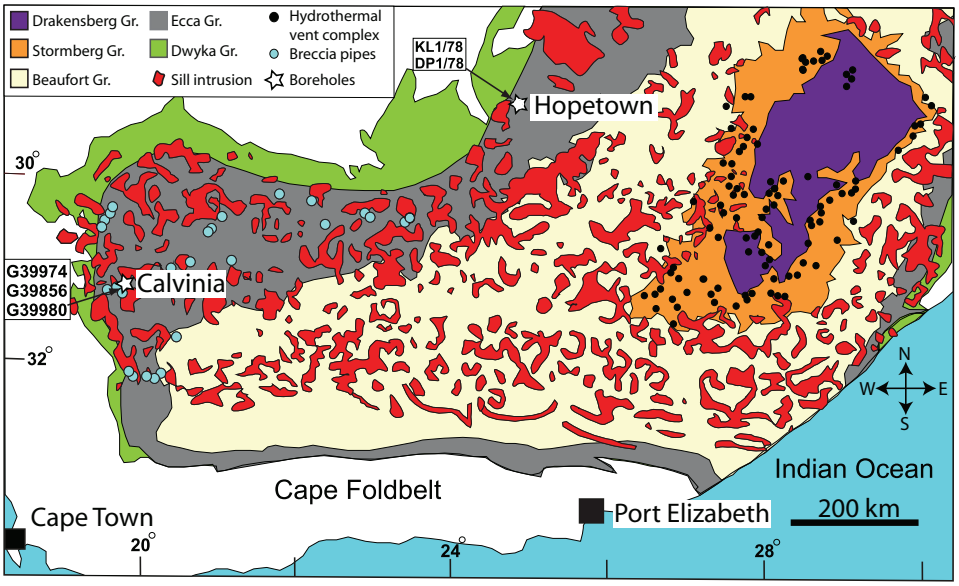

Figure 3.1: Simplified geological map of the Karoo Basin, South Africa after Svensen *et al.* (2008). The borehole locations used in this study are indicated with stars. The green Dwyka Group sediments define the basement of the basin, followed by the Ecca Group, the Beaufort Group, the Stormberg Group with the extrusive lavas of the Drakensberg Group stratigraphically on top. Outcropping sills are marked in red. Inferred deep-rooted breccia pipes are located in the Ecca Group, while the hydrothermal vent complexes are found in the Stormberg Group (Svensen *et al.*, 2007). Note that the circles indicate pipe clusters and not individual pipes

pipes (G39980 and G39856) and one was drilled through an undisrupted reference borehole (G39974). Samples were collected in 2007 at the core library of the Council for Geoscience in Pretoria, South Africa. Based on outcropping geology and the logs from these Calvinia cores (Svensen *et al.*, 2007) we constructed a simplified cross-section (Fig. 3.2). 13 samples were collected in 2007 and additional data were compiled from Svensen *et al.* (2007). The G39974 borehole was drilled to 1016 meters. The sampling was focused around a 10 meter thick sill located between the Whitehill and the Tierberg formations.

There are two cored boreholes in the Hopetown location in the northern Karoo Basin; the KL 1/78 and DP 1/78 drilled 3 km apart. Figure 3.3 shows a simplified cross-section from Hopetown. The KL 1/78 core was drilled through a 15.5 meter thick sill intruded into the Whitehill Fm., while this sill is not present in the DP 1/78. Since there are only two thin sills (1-2 m thick) intruded into the DP 1/78 section, we use this borehole as a reference of background maturation. The presented data from 31 samples from the KL 1/78 and 13 samples from the DP 1/78 are compiled from Polteau *et al.* (in prep.).

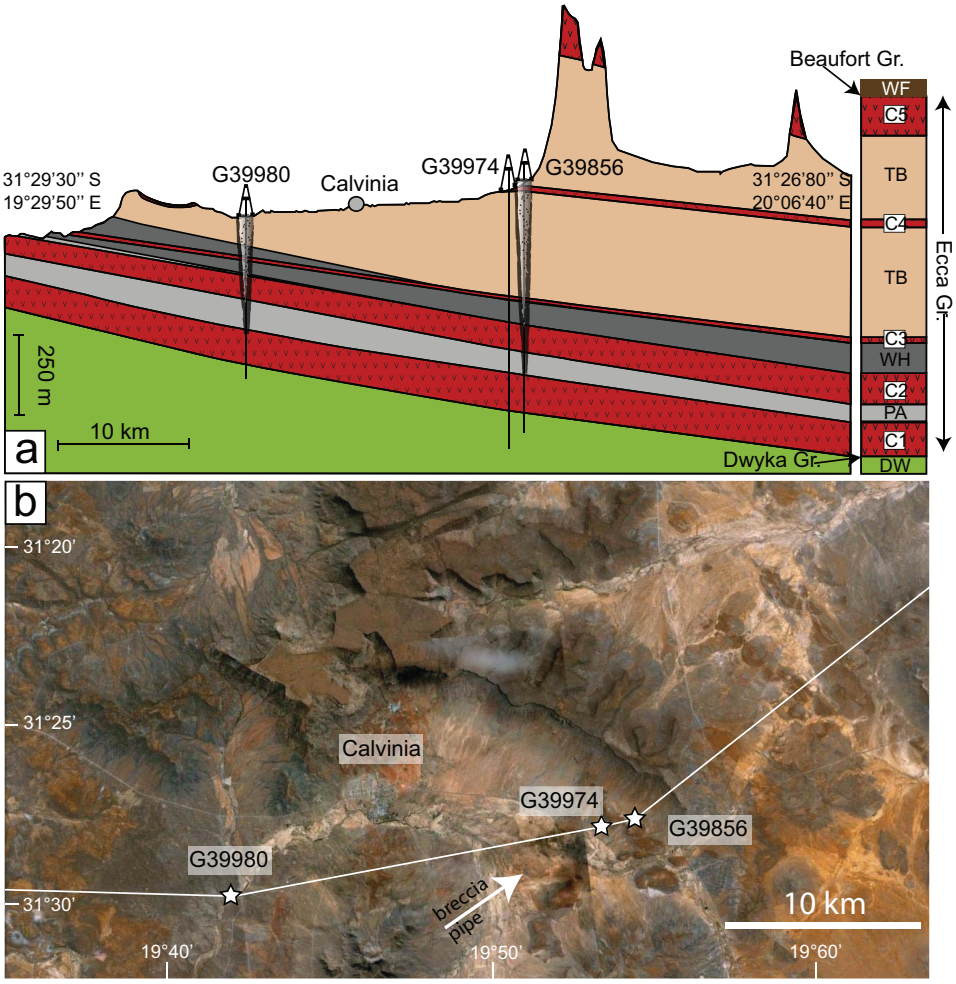

Figure 3.2: **(a)** Simplified cross-section based on three boreholes and outcropping geology. Two boreholes (G39980 and G39856) are drilled trough vent complexes. The stratigraphic logs are after Svensen *et al.* (2007). DW - Dwyka Group; PA - Prince Albert Fm.; WH - Whitehill Fm.; TB - Tierberg Fm.; WF - Waterford Fm. (from the Beaufort Group). C1 - 116 m thick sill; C2 - 85 m thick sill; C3 - 10 m thick sill, presented in detail in this study; C4 - 17 m thick sill; C5 - 100 meter thick sill, where the thickness is inferred from outcropping geology and elevation maps. Note that several sills follow the horizons between different formations. **(b)** Aerial photo from Google Earth showing the outcropping geology of the Calvinia location. The white line represents the cross-section in (a), the stars show the locations of the boreholes and the arrow points out another breccia pipe located in the area. The outcropping sills can be identified by the distinct reddish-brown color and by the sometimes sharp boundary with the sedimentary formations below.

3.4.2 Bulk chemical analysis

Total organic carbon (TOC) contents, Rock-Eval and vitrinite reflectance analyses were carried out on 12 powdered samples from G39974 and 43 samples from KL 1/78 and DP 1/78 using a Rock-Eval 6

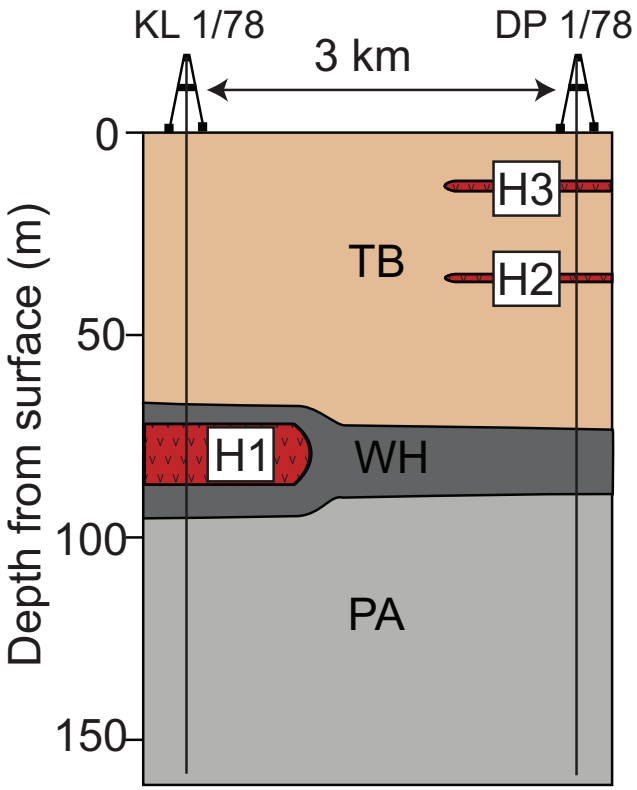

Figure 3.3: Simplified logs of the Hopetown location from DP 1/78 and KL 1/78. The boreholes are located 3 km apart. The 15.5 meter thick sill (H1) intruding the Whitehill Fm. in the KL 1/78 are not present in DL 1/78, The two sills of 1 m (H2) and 2 m (H3) intruding DP 1/78 are not present in KL 1/78. TB - Tierberg Fm.; WH - Whitehill Fm.; PA - Prince Albert Fm.

instrument at Applied Petroleum Technology (APT), Kjeller, Norway. The TOC and Rock-Eval analyses are performed at temperatures between 300 °C and 850 °C during 25 minutes. Mineral carbon is defined as CO_2 released after the CO signal in the IR-detector drops to zero. The TOC and total carbon (TC) were determined at the Department of Geosciences, University of Oslo, Norway, using a LECO CR-412 in order to get the amount of inorganic carbon in the samples, which subtracted from the mineral carbon measurements from APT gives the amount of graphite. The samples were heated to 1350 °C under constant oxygen supply in a CO_2-free environment. HCl was used to remove all inorganic carbon for the TOC measurements, after determining the TC.

The vitrinite reflectance was determined at APT from polished slabs analysed on a Zeiss Standard Universal research microscope-photometer (MPM01K) equipped with a tungsten-halogen lamp (12V, 100w) and an Epiplan-Neofluar 40/0.90 oil objective. Quality ratings reported in Table 3.1 are based on various important aspects which may affect the measurements, like abundance of vitrinite, uncertainties in the identification of indigenous vitrinite, type of vitrinite, particle size and particle surface quality.

3.4.3 Petrography

Thin sections were studied and analysed using a JEOL JSM 6460LV Scanning Electron Microscope (SEM) and a Cameca SX100 electron microprobe with integrated energy dispersive spectrometer and five wavelength-dispersive crystal spectrometers at the Department of Geosciences, University of Oslo. Standard polished thin-sections were carbon-coated for microprobe analyses, while carbon present in the samples was detected using uncoated thin sections and low vacuum SEM analysis. The microprobe analyses were carried out with an accelerating voltage of 15 kV and a beam current of 10 A. The detection limit is on average 0.08 wt. %. We analysed plagioclase, K-feldspar, chlorite, muscovite, biotite, epidote and titanite. Occurrences of quartz, carbonate, pyrite and titanium oxides were also confirmed using the microprobe.

3.4.4 Numerical modeling

We have adopted the numerical model presented in detail by Aarnes *et al.* (accepted) which solves the heat conduction equation with latent heat, coupled to organic and inorganic devolatilization reactions using the finite difference method. Organic maturation is solved by assuming a reaction rate following the Arrhenius equation with a set of parallel first order reactions (i), $k_i = A\exp(-E_i/RT)$, where A is the frequency factor, R is the gas constant and E_i is the activation energy for the reaction i (Tissot *et al.*, 1987; Ungerer & Pelet, 1987). We implement the Easy%Ro method developed by Sweeney & Burnham (1990) to obtain the vitrinite reflectance and organic cracking reactions, $\%\mathrm{Ro} = \exp(-1.6 + 3.7F)$, where F is the fraction of converted material. Values for E are taken from Sweeney & Burnham (1990).

The CH_4 yield (kg_{CH_4}/m^3 rock) is calculated from the relation (cf. Schmoker, 1994), $Q_{CH_4} = Q_t \times \tau \times M_f \times \rho_{hr}$, where Q_t is hydrocarbon yield ($g_{HC}/kg_{TOC}/1000$), τ is kg carbon per kg shale (wt. % TOC/100), M_f is conversion factor from C to CH_4 (1.34), and ρ_{hr} is density of the host-rock (2400 kg/m^3), which corresponds to an average density of sediments at $\sim$3 km depth in a basin (Storvoll *et al.*, 2005). This depth corresponds roughly to the stratigraphic position of the Ecca Group at about 31 ° South (i.e. Calvinia) in the Karoo Basin (Catuneanu *et al.*, 2005).

Mineral dehydration reactions are coupled to the thermal solver by assuming phase equilibria (Connolly, 2005). We use the bulk rock compositions of the Tierberg, Whitehill and Prince Albert formations from analyses given in Visser (1992) to calculate mineral equilibria (Fig. 3.4). The major dehydration reactions are related to breakdown of chlorite (Chl) and muscovite (Mus). The maximum H_2O content in the equilibrium mineral assemblage of the initial host-rock at a given temperature gives the amount of H_2O released as a free fluid phase. We fix the thermodynamic pressure at 100 MPa, which is the approximate lithostatic pressure at 3 to 4 km depth. However, the pressure dependence on the equilibrium H_2O contents is insignificant above $\sim$50 MPa.

Initial and boundary conditions

The initial conditions are chosen in order to match the Hopetown case study. We use an intrusion temperature of 1150 °C (Toplis & Carroll, 1995) and a host-rock temperature of 50 °C with a geothermal gradient of 25 °C /km (Brown *et al.*, 1994), which would place the top of the Ecca Group at about 2 km depth. At the latitude of Hopetown (29.4° S), the Ecca Group is inferred to be at about 1-2 km depth

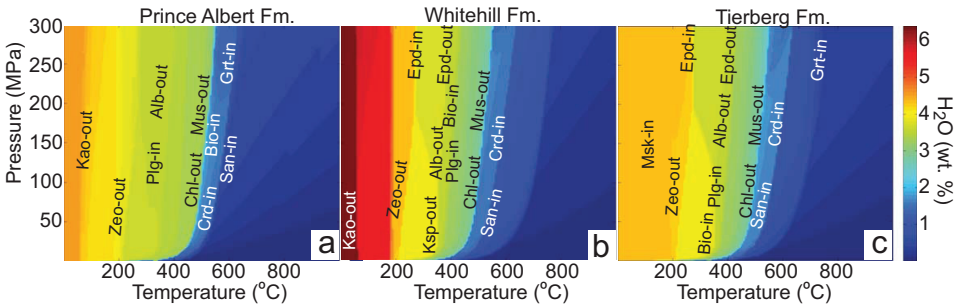

Figure 3.4: Calculated bulk H_2O contents for **(a)** the Prince Albert Fm. (max 4.53 wt. % H_2O), **(b)** the Whitehill Fm. (max 6.12 wt. % H_2O), and **(c)** the Tierberg Fm. (max 4.37 wt. % H_2O), as a function of pressure and temperature, based on mineral equilibrium calculations in Perple_X (Connolly, 2005). The bulk rock compositions are taken from Visser (1992). Mineral abbreviations with solid solution: Bio - biotite, Chl - chlorite, Epd - epidote, Crd - high cordierite, Ksp - alkali feldspar, Mus - muscovite, Plg - plagioclase (ordered structure), San - alkali feldspar (ordered structure), and Zeo - zeolite. Without solid solution: Alb - albite, and Kao - kaolinite.

(Catuneanu *et al.*, 1998). As an initial condition before emplacing the intrusion, we ran the model until the calculated background vitrinite reflectance fitted the vitrinite reflectance data of DP 1/78. The initial amount of TOC is found from interpolation of the TOC data from DL 1/78. The thermal diffusivities used are 1.0×10^{-6} m^2s^{-1} for the shales and 9.8×10^{-7} m^2s^{-1} for the dolerite (Aarnes *et al.*, accepted, and references therein).

Model assumptions

We focus on quantifying the effect of conductive heating with latent heat of crystallization and mineral reactions as a first approximation. Therefore heat advection is not considered. This can be justified since the advective heat transported with the fluids out of the aureole is commonly considered a second order effect (Peacock, 1987; Connolly & Thompson, 1989; Ferry & Dipple, 1991; Podladchikov & Wickham, 1994). Moreover, modelling of heat advection is associated with several unconstrained parameters, such as transient permeabilities and reaction induced pressure gradients. A thorough quantification of feedback of advective heating on reaction progress is hence outside the scope of this study.

We assume that all hydrocarbons are converted into methane (CH_4) as a first approximation, since the kinetic conditions for transformation of organic matter at high temperatures promote gaseous products over liquid petroleum (e.g. Reverdatto & Melenevskii, 1983; Tissot & Welte, 1984; Schenk *et al.*, 1997; Karlsen & Skeie, 2006).

Loss on ignition (LOI) values are reported in weight percent to be 5.66 in the Prince Albert Fm., 10.2 in the Whitehill Fm., and 4.85 in the Tierberg Fm. (Visser, 1992). However, it is likely that the content of pure H_2O is less than what is reported from LOI, because unknown amounts of other components, such as CO_2, make up the total LOI. Because the LOI values should be a function of the organic matter content in the samples, we reduced LOI by a factor related to the reported carbon, which are respectively 2, 4 and 1 wt. % for the Prince Albert, Whitehill and Tierberg formations. The reductions resulted in

4.53 wt. % H_2O for the Prince Albert Fm. (20% less than the LOI value), 6.12 wt. % H_2O for the Whitehill Fm. (40% less) and 4.37 wt. % H_2O for the Tierberg Fm. (10% less). These H_2O contents are similar to average low-grade pelitic shales (4.34 wt. %; Shaw, 1956), and the reduction is done in order to have reliable estimates of water production in the aureoles.

We consider dehydration reactions occurring at thermodynamic equilibrium conditions. This assumption is based on studies reporting that the overstepping temperatures relative to equilibrium are rarely more than a few degrees for most dehydration reactions (Walther & Wood, 1984). This would only lead to a minor shift towards higher temperatures in the calculated equilibrium reactions (Fig. 3.4).

3.5 Results

3.5.1 Thermal alteration of organic matter

We have investigated the thermal alteration of organic matter around the 10 meter thick sill C3 in borehole G39974 (Calvinia location and Figure 3.2). This borehole is particularly interesting for our study, as it consists of multiple intrusions of variable thickness. We include data from the entire borehole section in order to constrain the numerical modelling. Selected data of TOC (wt. %) and %Ro is plotted in Figure 3.5, and additional data is presented in Table 3.1. The contact metamorphic Tierberg Fm. above the C3 sill is a consolidated, dark grey shale with occasional layers of poorly cemented volcanic ash that is better cemented close to the intrusion. Subvertical veins filled with minerals like titanite, chlorite and plagioclase are constrained to within 1 meter of the upper contact of the sill. The highest vein frequency coincides with the highest TOC loss for the shale. The TOC loss is reflected in the rock color, which progressively darkens from pale grey hornfels at the contact to dark grey shale about 2 meters away from the contact (Fig. 3.5b).

The influence of contact metamorphism on the Whitehill Fm. black shale is seen by the lack of gypsum precipitation on the core surface, which occurs due to the interaction of the shales with water in the atmosphere (Fig. 3.5c). The shales are overall well compacted, with very high vitrinite reflectance values (1.2-4.7 %Ro) and low TOC values (Fig. 3.5a). Vitrinite in the samples is dominated by inertinite and reworked vitrinite, which makes reliable vitrinite measurements difficult. All samples in the borehole have very low yields of S1 (hydrocarbons in the sample), S2 (hydrocarbons generated upon pyrolysis) and S3 (CO_2 generated upon pyrolysis). The only significant occurrences of graphite (above 5 wt. %) are in the two Whitehill Fm. samples at the lower contact with the C3 sill (sample G39974-07-344.11 m and sample G39974-07-346.00 m).

At the Hopetown location we have data from both a reference borehole (DP 1/78) and the contact-metamorphic equivalent (KL 1/78) intruded by a 15.5 meter thick sill (H1; Fig. 3). This provides a unique data set to constrain our numerical modelling. The samples from DP 1/78 are good source rocks for oil and gas, while the metamorphosed sections in KL1/78 and G39974 are virtually barren (Fig. 3.6a). The reference Whitehill Fm. (sample DP 1/78-81.85) is made up by up to 50 % dark bands of organic matter interlayered with fine-grained quartz, plagioclase and smectite (Fig. 3.6b). The remaining 50% is calcite. The contact metamorphosed equivalent of the Whitehill Fm. (KL 1/78-71.28) was sampled at the upper contact of the H1 sill. The sample consists of 90% well compacted calcite and

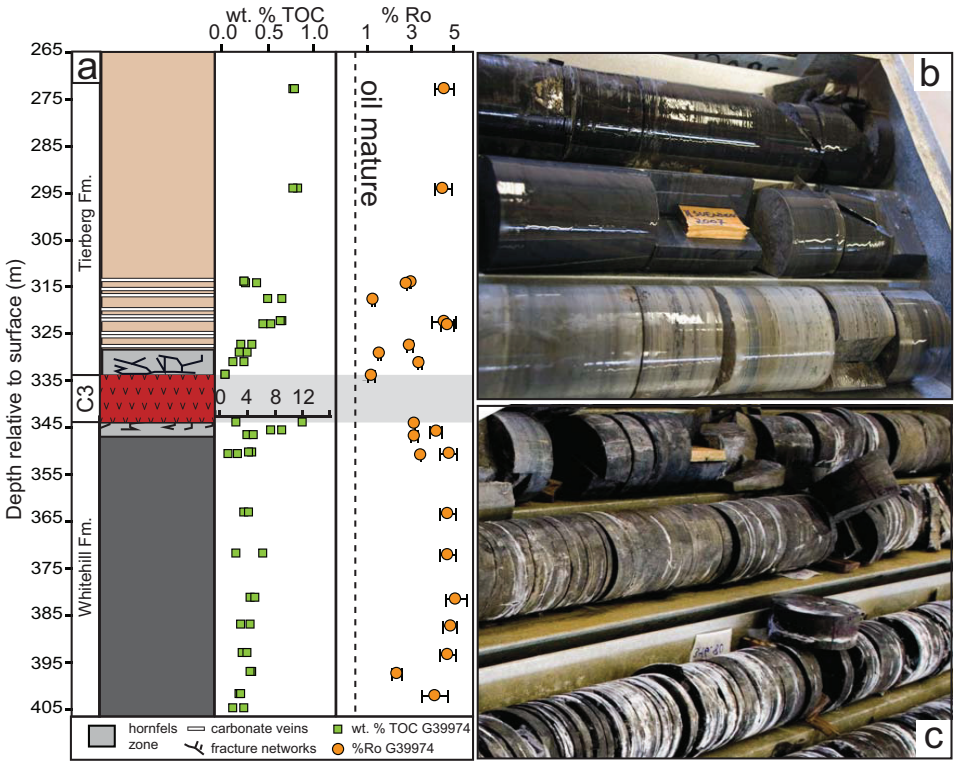

Figure 3.5: **(a)** Log of the borehole core G39974 around the 10 meter thick sill intrusion (C3) at the Calvinia location. Mineralized veins are occurring close to the sill contacts, while horizontal carbonate layers are found up to 20 meters above the upper contact. The TOC contents in the upper contact decrease towards the sill, while the TOC contents in the lower aureole show no trend towards the intrusion. Note the new TOC-scale for the Whitehill Fm. samples. The vitrinite reflectances have very high values and are all above oil maturity (0.5 %Ro; e.g. Hunt, 1996). The data are scattered, and there is little trend in the data towards the intrusion. **(b)** Borehole section of the Tierberg Fm. in the upper aureole. The loss of TOC can be seen as a progressive bleaching of the Tierberg Fm. shale towards the contact. **(c)** Core from the Whitehill Fm. below the sill. The lower sill contact is located at the upper left corner of the image. The degree of contact metamorphism is traced by the progressive loss of gypsum precipitation (white surface) towards the contact.

about 10% Mg-chlorite. Almost all the organic matter is gone from the sample (Fig. 3.6c). Only minor traces (μm) of organic carbon remain in the veins together with pyrite, apatite and calcite.

3.5.2 Mineralogy and petrography

Selected mineral analyses are presented from the Tierberg and Whitehill formations sampled at the upper and lower contact of the C3 sill at the Calvinia. We present the two contact samples, G39974-334.18 from the Tierberg Fm. (Table 3.2) and G39974-344.11 from the Whitehill Fm. (Table 3.3), since they represent the samples that experienced the highest degree of metamorphism. The analyses are used

Table 3.1: Data from Rock-Eval and organic analyses for the borehole G39974 at the Calvinia location.

Well	depth	TOC*	Min.C*	TOC **	TC**	Graph.				Overall	S1	S2	S3	Tmax	HI	OI	
sample	(m)	(wt%)	(wt%)	(wt%)	(wt%)	(wt%)	%Ro	std%	#	quality	(mg/g)	(mg/g)	(mg/g)	(°C)	(mg/g)	(mg/g)	FM
G39974/04-	203.15	1.01	0.20	0.95	1.11	0.04	4.14	0.34	20	M/G	0.02	0.06	0.23	477	6	23	TB
G39974/04-	238.30	0.65	0.20	0.77	0.85	0.12	4.34	0.30	20	M	0.02	0.03	0.13	490	5	20	TB
G39974/04-	273.22	0.79	0.20	0.81	0.93	0.08	4.53	0.43	22	M/G	0.01	0.05	0.08	513	7	10	TB
G39974/04-	294.42	0.85	0.10	0.79	0.84	0.05	4.52	0.40	21	M	0.02	0.03	0.09	506	3	11	TB
G39974-07-	314.20	0.26	0.10	0.26	0.30	0.06	3.01	0.05	6	M	0.01	0.07	0.24	343	27	92	TB
G39974-07-	314.66	0.28	0.30	0.40	0.57	0.13	2.79	0.00	1	P	0.01	0.06	0.18	408	21	64	TB
G39974-07-	317.86	0.52	0.11	0.67	0.72	0.06	1.28	0.05	1	G	0.01	0.08	0.25	343	15	48	TB
G39974/04-	322.50	0.67	0.10	0.65	0.67	0.08	4.53	0.52	21	M/G	0.01	0.03	0.11	438	5	16	TB
G39974-07-	323.23	0.47	0.10	0.55	0.53	0.10	4.68	0.28	6	M	0.01	0.06	0.18	369	13	38	TB
G39974-07-	327.58	0.23	0.17	0.35	0.39	0.13	2.95	0.15	3	P	0.01	0.05	0.18	441	22	78	TB
G39974-07-	329.33	0.29	0.50	0.21	0.69	0.02	1.56	0.06	7	M/G	0.01	0.06	0.35	337	21	121	TB
G39974-07-	331.56	0.14	0.13	0.26	0.24	0.13	3.43	0.13	2	P	0.01	0.07	0.22	342	50	157	TB
G39974-07-	334.18	0.05	0.10	0.06	0.02	0.10	1.21	0.16	3	P	0.01	0.06	0.17	384	120	330	TB
Sill C3																	
G39974-07-	344.11	2.62	6.92	12.23	12.52	6.63	3.14	0.00	1	P	0.03	0.23	0.26	582	9	10	WH
G39974-07-	346.00	7.55	5.22	9.25	9.28	5.19	4.12	0.25	7	M	0.13	0.50	0.38	334	7	5	WH
G39974-07-	346.80	4.17	0.39	5.14	5.16	0.37	3.11	0.14	9	M	0.04	0.10	0.27	337	2	6	WH
G39974/04-	350.45	4.73	0.30	4.46	4.39	0.30	4.69	0.40	20	G/M	0.04	0.02	0.12	347	0	3	WH
G39974-07-	351.10	1.46	8.78	2.81	10.90	0.69	3.45	0.00	1	P	0.02	0.06	0.42	340	4	29	WH
G39974/04-	363.40	3.75	0.70	4.29	4.24	0.70	4.61	0.36	20	G/M	0.03	0.03	0.16	348	1	4	WH
G39974/04-	372.00	2.43	0.40	6.50	6.40	0.50	4.65	0.34	22	M	0.02	0.05	0.09	517	2	4	WH
G39974/04-	381.39	4.53	0.70	5.22	5.19	0.70	5.03	0.45	20	G/M	0.09	0.05	0.08	307	1	2	WH
G39974/04-	387.36	3.10	1.50	4.58	4.61	1.47	4.77	0.32	19	G/M	0.10	0.09	0.11	298	3	4	WH
G39974/04-	393.26	3.37	1.10	4.07	4.06	1.10	4.64	0.38	20	M/G	0.05	0.17	0.42	376	5	12	WH
G39974/04-	397.43	4.85	0.80	4.62	4.68	0.74	2.36	0.19	4	P	0.03	0.09	0.16	433	2	3	WH
G39974/04-	402.11	3.08	0.80	3.21	3.23	0.78	4.08	0.56	21	M	0.04	0.18	0.09	364	6	3	WH
G39974/04-	405.13	2.12	1.60	3.70	3.75	1.55	barren	-	0	P	0.01	0.03	0.00	542	1	-	WH
G39974/04-	409.66	1.11	1.80	2.89	2.88	1.80	7.39	0.67	12	M	0.01	0.03	0.00	360	3	-	WH
G39974/04-	412.67	0.03	0.60	8.87	13.54	0.00	7.77	0.75	3	P	0.00	0.01	0.28	336	47	933	WH
G39974/04-	415.70	0.02	0.00	0.00	0.00	0.00	7.90	0.49	15	P	0.01	0.05	0.03	600	230	150	WH
Sill C2																	
G39974/04-	502.60	0.01	0.00	0.00	0.02	0.00	barren	-	0	-	0.00	0.02	0.13	355	200	1300	PA
G39974/04-	512.81	0.02	0.00	0.00	0.00	0.00	4.87	0.46	4	P	0.00	0.03	0.15	520	130	750	PA
G39974/04-	520.20	0.03	0.00	0.00	0.00	0.00	8.19	0.43	10	M/G	0.01	0.02	0.03	468	67	100	PA
G39974/04-	534.40	0.01	0.00	0.00	0.00	0.00	7.58	0.66	23	M/G	0.00	0.03	0.03	502	310	300	PA
G39974/04-	558.08	0.04	0.30	0.34	0.38	0.26	7.60	0.53	21	M/G	0.00	0.01	0.00	509	20	-	PA
Sill C1																	
G39974/04-	705.42	0.03	0.00	0.00	0.00	0.00	barren	-	0	-	0.00	0.01	0.00	336	40	-	DW
G39974/04-	727.80	0.07	0.20	0.00	0.00	0.20	6.96	0.47	6	P	0.01	0.01	0.00	341	11	-	DW
G39974/04-	777.90	0.05	0.10	0.01	0.07	0.04	2.69	0.51	5	P	0.00	0.04	0.13	444	70	260	DW
G39974/04-	798.28	0.02	0.30	0.00	0.08	0.22	3.11	0.35	11	P	0.00	0.02	0.16	445	90	800	DW
G39974/04-	821.77	0.08	0.10	0.03	0.20	0.00	2.93	0.28	17	M	0.01	0.02	0.03	509	24	38	DW

= Number of measurements; Min. C. = Mineral carbon; G = Good, M = Moderate, P = Poor; *Applied Petroleum Technology;
**University of Oslo; FM = Sedimentary formations; TB = Tierberg; WH = Whitehill; PA = Prince Albert; DW = Dwyka;

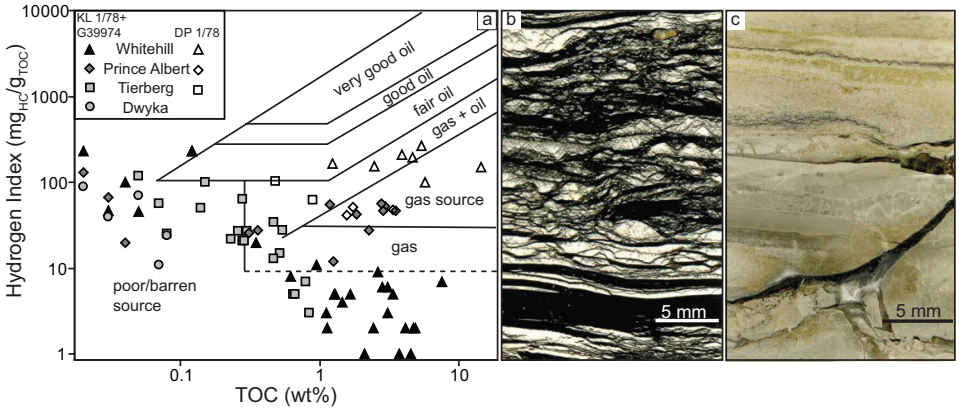

Figure 3.6: **(a)** Source rock richness plot of all samples from the Calvinia and Hopetown locations as a function of Hydrogen Index (HI) and wt% TOC (Table 3.1 and Polteau *et al.*, in prep.). The unmetamorphosed samples (open symbols) indicate a fairly good potential for oil and gas particularly for the Whitehill formation, while the metamorphosed equivalents (filled symbols) are to a large degree barren. Modified after Akande *et al.* (1998). **(b)** Thin section image of the low-grade metamorphosed sample DL 1/78-81.85 from the Whitehill Fm. A fine-grained mineral network intermixed with carbon is making up most of the sample, making it a good source for hydrocarbons. The off-white areas are calcite-carbonate. **(c)** Thin section image of the metamorphosed equivalent of the Whitehill Fm. at the very contact in sample KL 1/78-71.28. The sample is basically barren, except for a carbon remnant in the vein. The sample is mostly calcite with some Mg-rich chlorite.

to infer peak metamorphic conditions, and to provide information about the mineral reactions during metamorphism.

The Tierberg Fm. sample (G39974-334.18) is a hornfels with a 2D porosity of about 6 % and several sub-vertical and horizontal veins (Fig. 3.7). The main mineral phases are quartz (Qtz), alkali feldspar (Ksp), albitic plagioclase (Alb), muscovite (Mus) and chlorite (Chl), with accessory titanite (Ttn), epidote (Epd), calcium-carbonate (Car) and rare apatite (Apt). Some of the epidotes are interpreted as REE-epidote (allanite) due to the low total oxide sum in the analyses (Tables 3.2 and 3.3). There are two main domains in the sample, one muscovite-dominated (Fig. 3.7b) and one quartz-dominated domain (Fig. 3.7c). This is likely a result of depositional differences with mainly detrital muscovite and quartz, respectively. Most of the vertical veins terminate against the muscovite dominated lithology, where the fluid-pathway is dominated by an interconnected micro-porosity (Fig. 3.7b). The quartz-dominated lithology in the sample G39974-334.18 has pores up to 50 μm in diameter, in addition to some micro-porosity. Although the pores are relatively large, they appear to have low interconnectivity based on the 2D BSE image (Fig. 3.7c).

Metamorphic muscovite and chlorite are growing within the pores, commonly as needles or fans. There are no significant chemical differences between the same mineral phases occurring in the matrix compared to those occurring in the veins. Epidote and titanite only occur in veins and nodules. The nodules are circular mineral domains interpreted to be formed as a response to metamorphic mineral growth.

The Tierberg Fm. samples up to ∼20 meters above the contact (i.e. at 314.20 m) are dominated by chlorite, plagioclase, quartz and K-feldspar, with accessory pyrite and carbonate. There are no clay-minerals within ∼2 meters from the contact, while clay-minerals are present in the samples above ∼2 meters.

The Whitehill Fm. sample (G39974-344.11) represents a metamorphic black shale, with some vertical and horizontal veins. The main mineral phases in the Whitehill Fm. are quartz, plagioclase and biotite (Bio) with minor muscovite, alkali feldspar, rutile, titanite, pyrite, calcite and epidote. The biotite is partly retrograded to chlorite, which is evident from the low oxide sums and low potassium (K) contents.

The mineral assemblage in the Whitehill Fm. sample differs from the Tierberg Fm. sample by containing metamorphic biotite, but not metamorphic chlorite as is common in the Tierberg Fm. sample. The Whitehill Fm. sample has both plagioclase and albite, while the Tierberg Fm. sample only contains albite. Furthermore, metamorphic epidote is part of the mineral matrix, and not restricted to veins, as is the case in the Tierberg Fm. sample. The muscovite analyses show higher iron and magnesium contents in the Whitehill Fm. compared to the Tierberg Fm..

There are less veins in the Whitehill Fm. as a whole compared to the Tierberg Fm.. A few veins in the Whitehill Fm. are containing solid bitumen that was once liquid petroleum. The mineral assemblages in Whitehill Fm. down to ∼10 meters (sample G39974-351.10) away from the bottom contact resemble the contact sample, although the carbonate contents vary locally.

3.5.3 Modeling organic maturation and gas generation

The effect of a single sill

From the boreholes at the Hopetown location (DP 1/78 and KL 1/78) it is possible to calculate the difference between the formations that were affected by a 15.5 meter thick dolerite sill (H1) and the unaffected reference hole. In order to make a coherent quantification of the organic maturation and gas generation in the aureoles we apply our numerical model to this case study as mainly a calibration study. In order to plot the two boreholes on the same log, we have adjusted the original borehole depth of the core DP 1/78 to account for the H1 sill.

Figure 8 shows the modelling results compared to the borehole data. The calculated TOC after the intrusive event fits well with the data from KL 1/78 (Fig. 3.8a). All vitrinite populations are plotted, as it is difficult to define the true population in the high grade samples (Fig. 3.8b). Two vitrinite reflectance samples of about 8 %Ro at the upper and lower contact are omitted from the graphical representation due to the model limitations of Easy%Ro to maximum 4.6 %Ro. Despite the wide scatter of the data, the general trend of increasing vitrinite reflectance towards the sill contact relative to the background values is captured.

The fluid yields represent the amounts generated within the rock volume of a unit column. Summing up the total yields in this column above and below the sill results in a total amount of 1700 kg/m^2 of CH_4 and 1200 kg/m^2 of H_2O (Fig. 3.8c). The calculated amount of methane is comparable to the 1671 kg/m^2 CH_4 estimated by Polteau *et al.* (in prep.) from the same data. The maximum temperature calculated is 590 °C within 10 cm from the contacts, and above 150 °C for the rest of the plotted section (Fig. 3.8d).

Table 3.2: Selected mineral analyses from the contact metamorphic Tierberg Fm. sample G39974 - 334.18.

sample	334.18	334.18	334.18	334.18	334.18	334.18	334.18	334.18	334.18	334.18	334.18	334.18	334.18	334.18	334.18	334.18	334.18	334.18	334.18
comment	*nodule QD*	*vein QD*	*matrix QD*	*vein MD*	*matrix MD*	*matrix QD*	*vein QD*	*matrix MD*	*vein QD*	*matrix QD*	*nodule QD*	*matrix MD*	*matrix MD*	*vein QD*	*matrix QD*	*vein QD*	*vein QD*	*vein QD*	*nodule QD*
mineral	Chl	Chl	Chl	Chl	Chl	Mus	Mus	Mus	Alb	Alb	Alb	Alb	Ksp	Ksp	Ksp	Epd	Epd	Ttn	Ttn
SiO_2	24.08	24.66	25.37	25.12	25.83	48.00	47.83	49.72	65.93	66.04	67.49	66.03	61.54	63.13	64.52	32.61	36.07	30.56	30.29
Al_2O_3	20.25	20.45	20.85	21.23	20.61	32.91	32.66	34.88	20.57	20.70	20.22	20.42	21.66	18.45	19.14	21.17	25.13	6.19	4.29
TiO_2	-	-	-	0.05	-	0.14	0.15	0.10	0.07	0.06	-	-	0.06	0.14	-	0.03	0.11	32.33	34.54
Cr_2O_3	-	-	-	0.02	-	0.01	-	-	-	0.06	-	0.02	-	0.06	-	-	-	-	0.07
FeO	29.53	29.02	30.54	29.15	28.27	2.99	3.00	0.63	0.27	0.11	-	0.04	0.42	0.20	0.07	7.81	6.86	0.11	0.16
MnO	0.87	0.93	0.87	0.70	0.89	0.07	0.01	0.02	-	0.02	0.01	0.01	-	-	0.01	0.16	0.10	0.04	-
MgO	10.81	10.80	10.00	10.91	10.27	1.52	2.00	0.96	-	0.03	-	0.01	0.24	-	0.01	0.74	0.61	-	0.05
CaO	-	-	-	0.05	-	0.04	0.05	0.24	1.69	1.68	0.93	1.20	0.29	0.14	0.05	15.13	18.88	29.30	29.35
Na_2O	0.01	0.01	0.02	0.02	-	0.16	0.16	0.22	10.80	10.79	11.01	10.49	0.72	0.26	0.47	0.03	-	0.02	-
K_2O	0.02	-	0.12	0.04	0.25	8.04	7.82	8.40	0.07	0.08	0.10	0.18	12.94	13.98	11.80	-	0.01	0.03	-
Total	85.55	85.87	87.77	87.29	86.11	93.89	93.67	95.17	99.40	99.55	99.75	98.39	97.87	96.36	96.07	77.68	87.77	98.58	98.75
	Structural formula based on Si+Al = 4.000 and 14 oxygen					Si+Al=4.000 and 11 oxygen					Si+Al =4.000 and 8 oxygen					12 oxygen		5 oxygen	
Si	2.686	2.726	2.755	2.722	2.824	3.159	3.153	3.184	2.916	2.914	2.959	2.938	2.872	2.995	3.018	3.089	3.012	1.004	0.997
Al	2.662	2.665	2.669	2.711	2.656	2.553	2.538	2.633	1.084	1.086	1.041	1.062	1.128	1.005	0.982	2.363	2.473	0.240	0.166
Ti	-	-	-	0.004	-	0.007	0.008	0.005	0.002	0.002	-	-	0.002	0.005	-	0.002	0.007	0.799	0.855
Cr	-	-	-	0.002	-	-	-	-	-	0.002	-	0.001	0.000	0.002	-	-	-	-	0.002
Fe^{2+}tot	2.754	2.683	2.774	2.642	2.586	0.165	0.165	0.034	0.010	0.004	-	0.001	0.016	0.008	0.003	0.619	0.479	0.003	0.004
Mn	0.082	0.087	0.080	0.065	0.082	0.004	0.001	0.001	-	0.001	-	-	-	-	-	0.013	0.007	0.001	0.000
Mg	1.797	1.779	1.619	1.762	1.673	0.149	0.196	0.092	-	0.002	-	-	0.016	0.000	0.001	0.105	0.076	-	0.003
Ca	-	-	-	0.006	-	0.003	0.003	0.017	0.080	0.079	0.044	0.057	0.015	0.007	0.003	1.535	1.689	1.031	1.035
Na	0.001	0.001	0.002	0.002	-	0.012	0.011	0.015	0.926	0.923	0.936	0.905	0.065	0.024	0.042	0.006	-	0.001	-
K	0.004	-	0.025	0.008	0.053	1.026	1.000	1.044	0.001	0.002	0.002	0.003	0.771	0.846	0.704	-	0.001	0.001	-
Sum	9.986	9.942	9.924	9.918	9.874	7.070	7.068	7.019	5.020	5.014	4.985	4.974	4.883	4.885	4.753	7.606	7.738	2.833	2.888
	X_{Fe}	X_{Fe}	X_{Fe}	X_{Fe}	X_{Fe}	X_{Al}	X_{Al}	X_{Al}	X_{ab}	X_{ab}	X_{ab}	X_{ab}	X_K	X_K	X_K	X_{Al}	X_{Al}	X_{Ti}	X_{Ti}
	0.61	0.60	0.63	0.60	0.61	0.89	0.88	0.95	0.92	0.92	0.96	0.94	0.98	0.99	1.00	0.77	0.82	0.44	0.45

QD - Quartz-domain; MD - Muscovite-domain; X_{Fe}=Fe/Fe+Mg; X_{Al}=Al/Al+Fe+Mg; X_{ab}=Na/Na+Ca; X_K=K/K+Na; X_{Ti}=Ti/Ti+Ca

Table 3.3: Selected mineral analyses from the contact metamorphic Whitehill Fm. sample G39974 - 344.11.

sample	344.11	344.11	344.11	344.11	344.11	344.11	344.11	344.11	344.11	344.11	344.11	344.11	344.11	344.11	344.11	344.11	344.11
comment	matrix	matrix	matrix	nodule	matrix	matrix	matrix	matrix	matrix	matrix	nodule	nodule	matrix	vein	matrix	matrix	nodule
mineral	Mus	Mus	Bio*	Bio*	Bio*	Bio*	Plg	Plg	Plg	Plg	Alb	Alb	Ksp	Ksp	Epd	Epd	Ttn
SiO_2	49.25	50.79	39.61	39.09	38.33	38.92	52.89	57.34	59.69	63.69	65.67	68.53	65.25	62.85	33.14	33.85	30.03
Al_2O_3	33.91	32.68	20.68	18.00	18.12	20.22	29.23	26.66	25.10	22.95	21.16	19.38	18.88	19.10	19.11	22.19	4.18
TiO_2	0.05	-	0.29	0.30	0.89	0.23	-	-	-	-	-	-	0.01	0.01	0.08	0.25	34.52
Cr_2O_3	0.05	-	-	0.04	0.02	0.04	0.04	-	-	-	-	-	0.05	-	-	-	0.05
FeO	1.62	1.33	16.80	16.78	17.52	15.08	0.03	0.04	0.15	0.10	0.12	0.27	0.02	0.20	8.61	7.19	0.46
MnO	0.05	0.03	0.45	0.34	0.28	0.32	0.03	0.03	-	0.01	-	-	0.11	0.02	0.97	0.35	0.02
MgO	1.64	0.55	9.53	12.04	9.89	9.26	0.02	-	-	0.03	0.03	-	-	0.04	0.16	0.11	-
CaO	0.09	0.75	0.03	0.12	0.06	0.02	12.60	9.36	6.72	3.81	2.32	0.23	0.31	-	13.42	18.12	28.27
Na_2O	0.15	1.93	0.04	-	0.01	0.07	4.30	5.94	7.89	8.16	10.52	11.80	3.24	0.30	0.11	-	-
K_2O	7.08	7.47	6.38	4.87	5.30	6.71	0.26	0.43	0.35	1.54	0.21	0.06	11.81	13.20	0.05	-	0.10
Total	93.87	95.51	93.81	91.57	90.43	90.86	99.39	99.81	99.91	100.29	100.03	100.26	99.68	95.73	75.64	82.07	97.62
	Structural formula based on Si+Al = 4 and 11 oxygen								Si+Al=4.000 and 8 oxygen						12 oxygen		5 oxygen
Si	3.197	3.279	2.883	2.913	2.910	2.908	2.412	2.578	2.668	2.814	2.891	2.991	2.982	2.985	3.234	3.049	1.000
Al	2.595	2.487	1.775	1.581	1.621	1.781	1.588	1.422	1.332	1.186	1.109	1.009	1.017	1.069	2.199	2.356	0.164
Ti	0.002	0.000	0.016	0.017	0.051	0.013	0.000	0.000	0.000	0.000	0.000	0.000	0.000	0.000	0.006	0.017	0.864
Cr	0.002	0.000	0.000	0.002	0.001	0.002	0.001	0.000	0.000	0.000	0.000	0.000	0.002	0.000	0.000	0.000	0.001
Fe**	0.088	0.072	1.023	1.046	1.113	0.943	0.001	0.002	0.006	0.004	0.004	0.010	0.001	0.008	0.702	0.541	0.013
Mn	0.003	0.001	0.027	0.021	0.018	0.020	0.001	0.001	0.000	0.000	0.000	0.000	0.004	0.001	0.080	0.027	0.001
Mg	0.159	0.053	1.034	1.338	1.120	1.031	0.002	0.000	0.000	0.002	0.002	0.000	0.000	0.003	0.023	0.015	0.000
Ca	0.006	0.052	0.003	0.010	0.005	0.001	0.616	0.451	0.322	0.181	0.109	0.011	0.015	0.000	1.403	1.750	1.009
Na	0.010	0.133	0.003	0.000	0.001	0.006	0.380	0.518	0.684	0.699	0.898	0.999	0.287	0.028	0.021	0.000	0.000
K	0.891	0.935	0.901	0.703	0.780	0.972	0.015	0.025	0.020	0.087	0.012	0.003	0.688	0.800	0.006	0.000	0.004
Sum	6.950	7.012	7.649	7.614	7.569	7.664	5.014	4.996	5.032	4.972	5.025	5.022	4.990	4.882	7.668	7.738	2.873
	X_{Al}	X_{Al}	X_{Fe}	X_{Fe}	X_{Fe}	X_{Fe}	X_{ab}	X_{ab}	X_{ab}	X_{ab}	X_{ab}	X_{ab}	X_K	X_K	X_{Al}	X_{Al}	X_{Ti}
	0.91	0.95	0.50	0.44	0.50	0.48	0.38	0.53	0.68	0.79	0.89	0.99	0.71	0.97	0.75	0.81	0.46

X_{Fe}=Fe/Fe+Mg; X_{Al}=Al/Al+Fe+Mg; X_{ab}=Na/Na+Ca; X_K=K/K+Na; X_{Ti}=Ti/Ti+Ca. *Partly retrograded to chlorite. **Total Fe given as Fe^{2+}

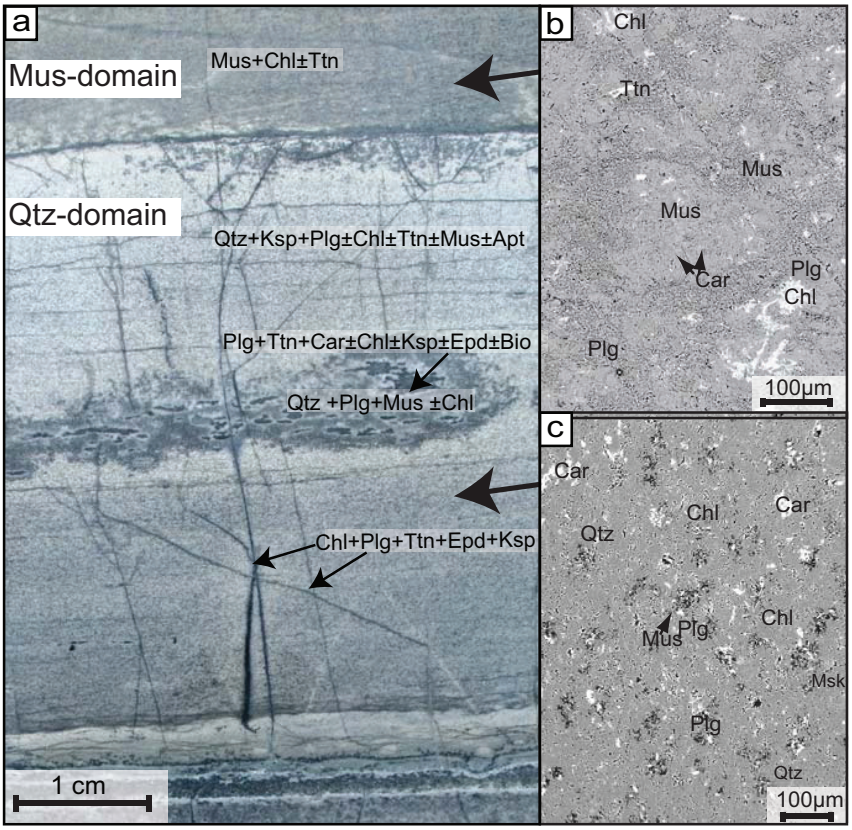

Figure 3.7: Sample G39974-334.18 from the Tierberg Fm. close to the upper contact. **(a)** A hand-specimen image of the extensive fracture network crosscutting the sample.**(b)** Backscatter electron (BSE) image of the matrix in the muscovite-rich domain shows interconnected micropores through the solid matrix. **(c)** A BSE image of the matrix in the quartz-rich domain reveal relatively large, isolated pore spaces, making up about ∼6% of the surface. Mineral abbreviations are the same as in Figure 3.4.

We can assume that this 15.5 meter thick sill is present within the Whitehill Formation in a larger area. If we assume that the sill thickness and host-rock lithology is maintained, we can extrapolate the amount of generated hydrocarbons as a function of sill size. Upscaling to a sill of 50×50 km, which is geologically plausible, results in a hydrocarbon generation of 4.3 gigatons (Gt) CH_4 (Fig. 3.9).

The effect of vertical separation between two sill intrusions

Modelling of the 15.5 meter sill showed that the thermal influence of a single sill is not enough to reproduce elevated vitrinite reflectances significantly more than 20 meters above and below, although the vitrinite data show elevated reflectances up to 30 meters away from the contacts (Fig. 3.8b). Because multiple intrusions-levels are very common in the Karoo Basin, it is possible that the thermal profile was influenced by more than one sill.

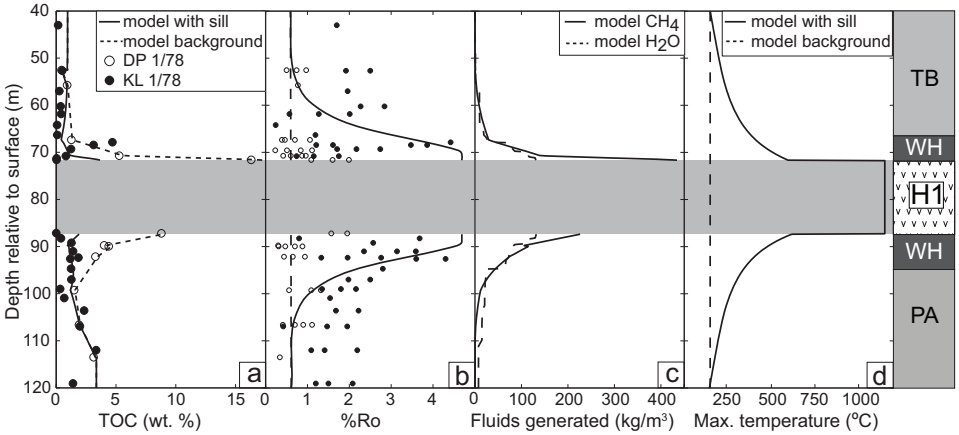

Figure 3.8: Modelling of the 15.5 meter thick sill (H1) near Hopetown based on the reference borehole DP 1/78 (open circles) and the intruded borehole KL 1/78 (filled circles). **(a)** Modelling of organic cracking (TOC). Dashed line is the inferred background TOC based on the data from DP 1/78, and the solid line is the calculated TOC compared to the KL 1/78 data. **(b)** Calculated vitrinite maturation (%Ro). The level of background maturation is determined from the mean through the open circles (DP 1/78). All populations of the vitrinite reflectances are plotted, which result in a large scatter in the data (KL 1/78). **(c)** Calculated CH_4 and H_2O generation. **(d)** Recorded maximum temperature in the aureole from the model. The borehole depth of DP 1/78 was corrected for the missing sill by adjusting the level of the 5 uppermost samples 10 meters up and the 7 lowermost samples 5 meters down.

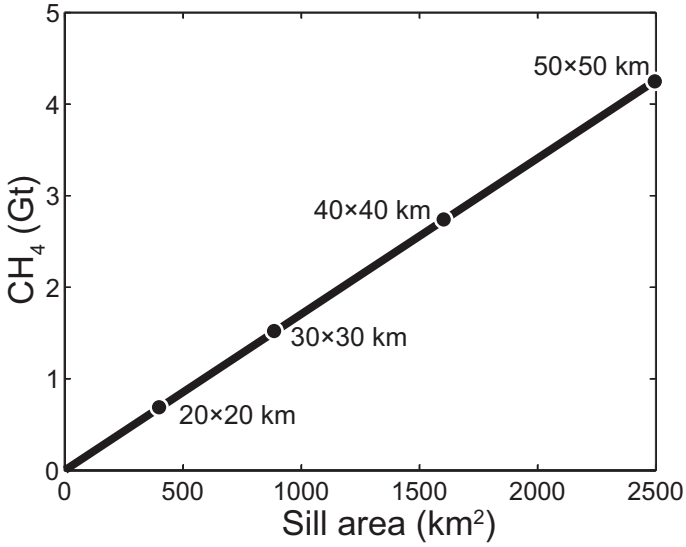

Figure 3.9: Calculated methane generation around the 15 meter thick sill intruding into the Whitehill formation as a function sill area. For a sill of 50 by 50 km the estimated total generation is 4.3 Gt of CH_4.

We evaluated numerically the total methane production as a function of vertical distance between the H1 sill and an assumed sill of the same thickness (15.5 m) simultaneously emplaced below the H1-sill with a vertical distance of 0 to 150 meters. Zero distance is the same as one merged sill of 31 m. The result of 150 1D-model runs shows that there is a critical distance at which the thermal aureoles of the two sills start to interact in the host-rock between the two sills (Fig. 3.10a). This occurs at a vertical distance of 110 meters ($\sim$7 times the sill thickness). The interaction becomes stronger as the two sills move closer. At the same time the volume of rock available for devolatilization reactions decreases between the sills.

The result in (Fig. 3.10b) shows the total gas generation when the two sills are emplaced in the Hopetown location (solid line), and when the two sills are emplaced in host-rock with a fixed TOC (dashed line) in order to avoid the influence of local variations. Figure 3.10 reveals that there is an ideal spacing for maximum gas generation of about 5 ton/m^2 when the two sills are about 60 meters apart (i.e. 4 sill thicknesses). This is due to an optimal balance between the strength of the thermal interaction compared to the total rock volume that is affected. The interaction of two sills results in about 35% higher methane production than the two separate sills of 15.5 meters ($\sim$4 ton/m^2). When there are no differences in initial TOC values (dashed line), we find that one thick sill gives a higher gas yield than two isolated sills.

A model run with two 100 meter thick sills results in the same pattern as shown in Figure 3.10. The main differences compared to the modelling of the 15.5 meter sills are that the thermal interaction occurs when the sills are 10 times the sill thickness apart, and the maximum gas production occurs when the two sills are 5 sill thicknesses apart. Also from the runs of 100 meter thick sills, two sills closer than 10 sill thicknesses apart creates up to $\sim$30% higher gas production than the two separate sills.

The effect of multiple sill intrusions

Data and stratigraphy from the Calvinia area (Fig. 3.2) are used to model the full sedimentary succession of the Ecca Group in the Karoo Basin. From Figure 3.2 we implement a cross-section going from the topmost sill (C5) covering the Tierberg Fm. down to the basal Dwyka Group. The modelling results are presented in Figure 3.11. The borehole depth and the data are taken from G39974, thus negative depth corresponds to lithologies more elevated than the starting point of the borehole. The physical properties are equal to those used to model the Hopetown location. We repeated an initial heating similar to the Hopetown model before emplacing the sills. Initial TOC values (dashed line, (Fig. 3.11a) are chosen to best fit the final data, and are comparable to the values from the reference borehole (DP 1/78).

If all sills are intruded simultaneously, the calculated TOC-profile greatly overestimates the metamorphic grade indicated by the TOC data around the three lowest sills (C1-C3) because of the close distance between the sills (Fig. 3.10). There are no real constraints about the timing of sill emplacement available for the Karoo Basin. We therefore conducted several runs applying different emplacement intervals, and found that an emplacement interval of 20 000 years between each sill gave a reasonably good fit to the TOC data (Fig. 3.11)a. An interval of 30 000 years did not change the profile significantly; while an interval of 10 000 years resulted in a slight overestimation of the calculated TOC compared to the TOC data within the Whitehill Fm..

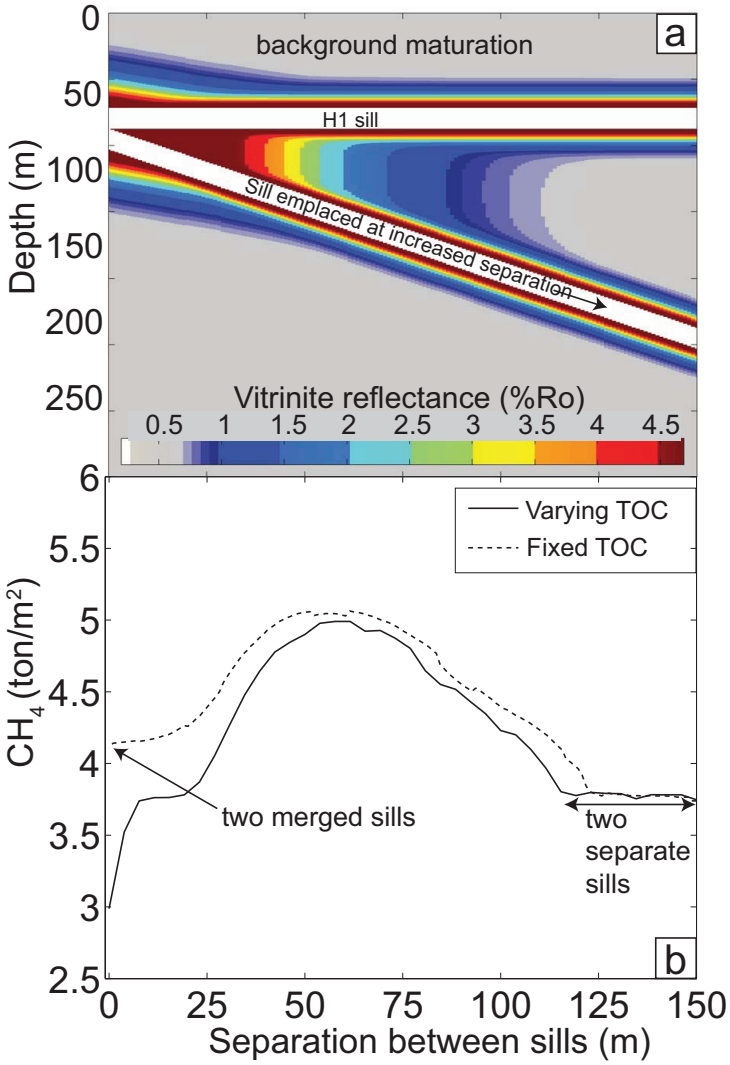

Figure 3.10: (a) The result of several 1D model runs with increasing vertical distance between two sills of 15.5 meters emplaced in the Hopetown location, where the upper sill corresponds to H1 and second sill is emplaced below with a distance varying from 0 to 150 meters. The plot shows elevated vitrinite reflectance relative to the background maturation, and reveals that there is a critical distance ($\sim$110 meters) where the thermal profiles of the two sills start to interact. **(b)** Calculated methane generation in a vertical column of the Hopetown location (solid line) and an idealized setting with fixed initial TOC (dashed line) as a function of vertical distance between the two sills. As the sills are moved closer, the degree of the interaction increases up to about 60 meters, where the volume of rock that is affected decreases and thus the total methane production decreases.

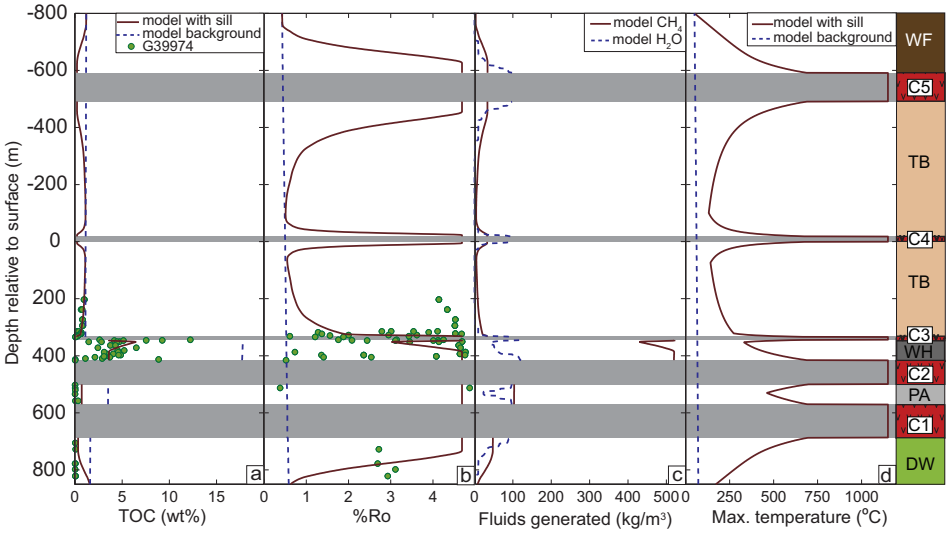

Figure 3.11: Modelling results from borehole G39974 at the Calvinia location of **(a)** TOC evolution, **(b)** vitrinite reflectance, **(c)** fluids generated and **(d)** maximum temperature in a stratigraphic sequence influenced by five intrusions. The stratigraphy is based on logs by Svensen *et al.* (2007) and the cross section in Figure 3.2. The sills are emplaced with an interval of 20 000 years, starting with the lowermost sill. The uppermost sill is emplaced 80 000 years after the bottom sill.

The fit with vitrinite reflectance is difficult, both due to the large scatter and the lower maximum value of the Easy%Ro-implementation than the measured ones (Fig. 3.11b). We did not plot the measured reflectance values above 5 %Ro, as they most likely arise from other organic macerals than vitrinite.

The calculated amount of fluids generated reveal that H_2O is the dominating fluid released in the low TOC shales, whereas CH_4 dominates in the high TOC shale (Fig. 3.11c). The total amount of carbon released from a vertical column of the cumulative Ecca Gr. formations is ∼60 ton CH_4/m2-column. To summarize, the most important modelling results are that multiple sill intrusions result in elevated background maturation and large scale gas generation throughout the organic-rich formations, and that the maximum calculated temperature reaches above as much as 150 °C throughout the modelled cross-section (Fig. 3.11d).

3.6 Discussion

3.6.1 Mineral dehydration

The presence of metamorphic minerals such as biotite, epidote and plagioclase in the Whitehill Fm. sample indicates that the duration of the thermal pulse from the 10 meter thick sill was long enough for mineral reactions to occur as a response to contact metamorphism. Occurrence of biotite suggests that dehydration due to break-down of chlorite occurred, and that the temperature reached at least

∼350 °C , as calculated from thermodynamic equilibrium (Fig. 3.4). This reaction corresponds to a major liberation of mineral-bound water. In the Tierberg Fm., the lack of clay minerals within 2 meters above the C3 sill strongly suggests water liberation from breakdown of hydrous clay phases during contact metamorphism.

The metamorphic minerals of the Whitehill Fm. (e.g. biotite, epidote and plagioclase) indicate a higher metamorphic grade than the metamorphic minerals in the Tierberg Fm. (e.g. chlorite and albite). This can be related to the more extensive fracture network in the Tierberg Fm., indicating active fluid-flow through the fractures and pores for some time before mineral precipitation. At the time when the fluids have sealed the fractures through precipitation, the temperature has also cooled down and the minerals will record a corresponding lower metamorphic grade. Conversely, in the Whitehill Fm. where fractures and hence fluid flow are limited, the metamorphic minerals can form at peak metamorphic conditions.

This is supported by similar mineral compositions in the veins and matrix in the Tierberg Fm. (Table 3.2), which suggests that the metamorphic minerals precipitated from a fluid going through both the pores and veins. Furthermore, the epidote-minerals in the veins of the Tierberg Fm. suggests that the temperature of the fluid was above 200 °C at the time of crystallization (Figure 3.4; Bird and Spieler (2004)). This implies that the veins were acting as active transport channels during the contact metamorphic event. They were however sealed before the contact temperature decreased to 200 °C , which from modelling suggests precipitation within 10 years after emplacement.

3.6.2 Fate of the organic carbon

Our modelling suggests that hydrocarbons will be formed primarily as methane, as high maximum temperatures (∼590-150 °C) were reached in the models of both the Hopetown and Calvinia locations, and oil is converted into gas above ∼120 °C (Hunt, 1996). Moreover, the overall high vitrinite reflectances above 1.3 %Ro are equivalent of being in the metagenetic stage where all the oil has converted to gas through secondary cracking (Bostick, 1979). Bitumen-filled veins in the Whitehill Fm. demonstrate the presence of some liquid hydrocarbons trapped below the C3 sill from Calvinia. However, vertical migration of liquid hydrocarbons from metamorphic sediments below cannot be excluded. We therefore infer that both oil and gas will be liberated in the basin as a whole, while the hydrocarbon products will be mostly gaseous in the contact aureoles.

The high-grade contact zone in the Tierberg Fm. above the C3 sill contains no organic carbon, although residual carbon is expected from the conversion of kerogen to hydrocarbons (Tissot *et al.*, 1987). The total loss of graphite indicates a process where residual carbon is dissolved by supercritical H_2O-dominated fluids. It has been shown that graphite can react with water to produce carbon gas above ∼250 °C following the reaction $2C_{graphite}+2H_2O = CH_4+CO_2$ (Connolly & Cesare, 1993; Pattison, 2006). Pattison (2006) showed that significant amounts of residual graphite can be dissolved by fluids released during mineral dehydration reactions in shales. This reaction favours gaseous products with increasing temperature (Barker *et al.*, 1998). If we in addition to mineral dehydration account for pre-existing pore-waters heated by the intrusion, the conversion of solid graphite to carbon gases provides an efficient way of transport residual carbon away from at least the inner part of the aureoles. The complete

loss of TOC will result in rock compaction (cf. Yoshinobu & Girty, 1999). A compaction of the reacted host-rock is supported by the stratigraphic thickness of the metamorphosed Whitehill Fm. from KL 1/78 being about 2 meter (∼20%) thinner than the thickness of the reference Whitehill Fm. in DL 1/78 (Polteau *et al.*, in prep.).

In order for the gigatons of carbon gas generated in the aureole to have an impact on the global carbon cycle, they need to be released rapidly to the surface. This large-scale fluid transport from the aureoles to the atmospheric cycle is interpreted to occur through the abundant breccia pipes associated with the Ecca Group in the Karoo Basin (Svensen *et al.*, 2004, 2006, 2007, 2008, 2009). Numerous horizontal fractures are compatible with a large lateral component in the fluid flux (Ferry & Gerdes, 1998), possibly feeding the vertical pipe-structures.

There are at least 5 more breccia pipes present near the Calvinia area, and more than 400 breccia pipes associated with metamorphism of the Prince Albert and Whitehill Fm. in the Loriesfontein area ∼50 km further north (Svensen *et al.*, 2007). Figure 3.2 shows that the vent complexes are rooted in the Prince Albert Fm. where the predicted fluid generation is the highest (Fig. 3.11). Assuming that the top sill acts as an effectively impermeable layer, the generated fluids will create a massive pressure build-up (Aarnes *et al.*, in prep.). This pressure can be released through vent formation (Jamtveit *et al.*, 2004; Svensen *et al.*, 2006; Aarnes *et al.*, in prep.).

The inferred compaction in the Hopetown accompanying the devolatilization in the low-permeable shales will promote the development of porosity waves, which provide enhanced fluid-flux out of the aureole (Connolly & Podladchikov, 2000; Appold & Nunn, 2002; Connolly & Podladchikov, 2007).

3.6.3 Effect of multiple intrusions in the basin

The high maximum-temperatures reached during the model runs (>150 °C) predict that the whole Ecca Group experienced sill-induced maturation of organic material. This is consistent with the study of Brown *et al.* (1994), suggesting that the thermal history of the Karoo Basin was strongly influenced by the intrusive event. For comparison, cracking of organic matter to hydrocarbons is thought to initiate at about 85 °C (Tissot & Welte, 1984; Killops & Killops, 1993). The overall high vitrinite reflectance and the low TOC content in the borehole G39974 support such a high level of organic maturation. Moreover, the low gas yields (S1, S2 and S3; Table 3.1) from the organic pyrolysis show that the Calvinia section has been subjected to extensive metamorphism of organic material throughout the core.

The TOC data fits well to the calculated values from the combined thermal evolution of the multiple sills, emplaced at 20 000 years interval (Fig. 3.11). This choice of interval is based on several modelling runs varying from syn-emplacement to an interval of 30 000 years, where 20 000 years gave a good fit between modelling and data for our choice of initial model conditions. We did not pursue the effect of timing on other parameters in this study, and can therefore not exclude that with different initial conditions another interval would be more appropriate. However, the modelling results suggest that the thermal maturation around a set of three closely emplaced sills is insensitive to emplacement intervals on a time-resolution lower than 10 000 years.

The lack of clear trends in the vitrinite reflectances towards the C3 sill (Fig. 3.5) can be explained by the overall high metamorphic grade due to the influence of the larger sills below. Also, modelling of

the H1 sill could not reproduce the high levels of vitrinite reflectance in borehole KL 1/78 up to more than 20 meters away from the sill, although the reflectance data show elevated vitrinite reflectances at least up to 30 meters away. This suggests a thermal influence from other sills also in the Hopetown location. Due to the predicted elevated maturation throughout the Ecca Group, the samples of the reference-hole (DP1/78) have most likely experienced some degree of metamorphism in addition to burial metamorphism, even though we have evidence of only two minor sills in this borehole (H2 and H3). This is supported both by the occurrence of bitumen veins also in the DP 1/78 (Polteau *et al.*, in prep.), and by a background vitrinite reflectance above 0.5 %Ro in most of the DL 1/78 samples corresponding to the level of active hydrocarbon generation (Dow, 1977). However, based on the large scatter in vitrinite reflectances, the lack of non-recycled vitrinite macerals, the poor overall quality of the measurements, and the potential dissolution of organic matter by hot fluids, we have to be careful when using the vitrinite data as an absolute maturation index related to the contact metamorphic events in the Calvinia and Hopetown case studies.

Aarnes *et al.* (accepted) showed how aureole thicknesses are directly controlled by background temperature of the intruded host-rock. Thus in a volcanic basin, previous intrusions will raise the background temperature for thousands of years and create favourable conditions for hydrocarbon formation. This is because higher background temperatures require less added heat before organic cracking initiates, and because higher background temperatures make intrusive cooling slower due to less steep thermal gradients between the sill and the host-rock. The main implications of the elevated metamorphic grade due to multiple intrusions are:

1. The elevated heat flow resulting from multiple sills emplaced throughout the basin will influence the maturation level several hundred meters away from the intrusions. This is important when interpreting maturation levels and burial depths in volcanic basins.

2. Gas generation is not limited to the aureoles, but will occur in the whole basin as a result of the intrusive activity. Thus the total hydrocarbon yield in a volcanic basin is potentially many times larger than what can be estimated by assuming separate intrusions.

3.7 Conclusions

Based on an integration of numerical modelling with organic and inorganic geochemistry, we are able to constrain and quantify the effect of single and multiple sills on the intruded shales. The major conclusions can be summarized:

- Field data show that the key consequences of intrusive heating are major loss of organic carbon, increased maturity, metamorphic mineral reactions and generation of overpressure and fluid flow out of the aureoles.

- One single, thin (15 m) sill intruded into the organic-rich Whitehill Fm. can generate several gigatons of CH_4, depending on the lateral extent of the sill.

- When two 15 meter thick sills are simultaneously emplaced with a vertical separation of less than about 7 sill thicknesses, they induce elevated organic maturation and gas generation relative to

two isolated sills emplaced further apart. There is an optimal vertical distance of about 4 sill thicknesses where the total gas generation increases by 35%, relative to two separate sills. For two 100 meter thick sills the thermal interaction initiates at ∼10 sill thicknesses, with a maximum generation at ∼5 sill thicknesses of vertical separation.The total gas generation increases by 30% relative to two separate sills.

- Numerical modelling of 5 sills of variable thicknesses intruded into the Ecca Group in the Calvinia area shows that hydrocarbon production is occurring throughout the entire sedimentary section, and is not restricted to the aureoles.
- Since multiple intrusion levels are common in the Karoo Basin, our study strongly supports large-scale and basin-wide generation of hydrocarbons in the Early Jurassic.

Acknowledgements

This study was supported by Grant 169457/S30 from the Norwegian Research Council. We would like to thank Yuri Podladchikov, Jamie Connolly and Bjørn Jamtveit for important contributions to this project. Muriel Erambert and Berit Løken Berg is thanked for assistance during EMP and SEM analyses. Maarten Aerts is thanked for discussions and improving the manuscript.

REFERENCES

AARNES I., PODLADCHIKOV Y.Y. & SVENSEN H. (in prep.) Overpressure generated from devolatilization reactions during metamorphism: implications for breccia pipe formation. .

AARNES I., SVENSEN H., CONNOLLY J.A.D. & PODLADCHIKOV Y.Y. (accepted) How contact metamorphism can trigger global climate changes: Modeling gas generation around igneous sills in sedimentary basins. *Geochimica Et Cosmochimica Acta*, **Accepted**.

AKANDE S.O., OJO O.J., ERDTMANN B.D. & HETENYI M. (1998) Paleoenvironments, source rock potential and thermal maturity of the Upper Benue rift basins, Nigeria: implications for hydrocarbon exploration. *Organic Geochemistry*, **29**, 531–542.

APPOLD M.S. & NUNN J.A. (2002) Numerical models of petroleum migration via buoyancy-driven porosity waves in viscously deformable sediments. *Geofluids*, **2**, 233–247.

BARKER C.E., BONE Y. & LEWAN M.D. (1998) Fluid inclusion and vitrinite-reflectance geothermometry compared to heat-flow models of maximum paleotemperature next to dikes, western onshore Gippsland Basin, Australia. *International Journal of Coal Geology*, **37**, 73–111.

BOSTICK N.H. (1979) Microscopic measurement of the level of catagenesis of solid organic matter in sedimentary rocks to aid exploration for petroleum and to determine former burial temperatures – a review. In: *Aspects of Diagenesis, S.E.P.M Special Publication* (Ed. P.A. Scholle & P.R. Schluger), vol. 26, 17–43.

BROWN R., GALLAGHER K. & DUANE M. (1994) A quantitative assessment of the effects of magmatism on the thermal history of the Karoo sedimentary sequence. *Journal of African Earth Sciences*, **18**, 227–243.

CATUNEANU O., HANCOX P.J. & RUBIDGE B.S. (1998) Reciprocal flexural behaviour and contrasting stratigraphies: a new basin development model for the Karoo retroarc foreland system, South Africa. *Basin Research*, **10**, 417–439.

CATUNEANU O., WOPFNER H., ERIKSSON P.G., CAIRNCROSS B., RUBIDGE B.S., SMITH R.M.H. & HANCOX P.J. (2005) The Karoo basins of south-central Africa. *Journal of African Earth Sciences*, **43**, 211–253.

CHEVALLIER L. & WOODFORD A. (1999) Morpho-tectonics and mechanism of emplacement of the dolerite rings and sills of the Western Karoo, South Africa. *South African Journal of Geology*, **102**, 43–54.

CLAYTON J.L. & BOSTICK N.H. (1986) Temperature effects on kerogen and on molecular and isotopic composition of organic matter in Pierre Shale near an igneous dike. *Organic Geochemistry*, **10**, 135–143.

COLE D.I. (1992) Evolution and Development of the Karoo Basin. *Inversion Tectonics of the Cape Fold Belt, Karoo and Cretaceous Basins of Southern Africa*, 87–99.

CONNOLLY J.A.D. (2005) Computation of phase equilibria by linear programming: A tool for geodynamic modeling and its application to subduction zone decarbonation. *Earth and Planetary Science Letters*, **236**, 524–541.

CONNOLLY J.A.D. & CESARE B. (1993) C-O-H-S Fluid Composition and Oxygen Fugacity in Graphitic Metapelites. *Journal of Metamorphic Geology*, **11**, 379–388.

CONNOLLY J.A.D. & PODLADCHIKOV Y.Y. (2000) Temperature-dependent viscoelastic compaction and compartmentalization in sedimentary basins. *Tectonophysics*, **324**, 137–168.

CONNOLLY J.A.D. & PODLADCHIKOV Y.Y. (2007) Decompaction weakening and channeling instability in ductile porous media: Implications for asthenospheric melt segregation. *Journal of Geophysical Research-Solid Earth*, **112**.

CONNOLLY J.A.D. & THOMPSON A.B. (1989) Fluid and enthalpy production during regional metamorphism. *Contributions to Mineralogy and Petrology*, **102**, 347–366.

COURTILLOT V.E. & RENNE P.R. (2003) On the ages of flood basalt events. *Comptes Rendus Geosciences*, **335**, 113–140.

DICKENS G.R., CASTILLO M.M. & WALKER J.C.G. (1997) A blast of gas in the latest Paleocene: Simulating first-order effects of massive dissociation of oceanic methane hydrate. *Geology*, **25**, 259–262.

DOW W.G. (1977) Kerogen studies and geological interpretations. *Journal of Geochemical Exploration*, **7**, 79–99.

DU TOIT A.L. (1920) The Karoo dolerites of South Africa: a study in hypabyssal injection. *Transactions of the Geological Society of South Africa*, **23**, 1–42.

DUNCAN R., HOOPER P., REHACEK J., MARSH J. & DUNCAN A. (1997) The timing and duration of the Karoo igneous event, southern Gondwana. *Journal of Geophysical Research*, **102, B8**, 18127–18138.

FAURE K. & COLE D. (1999) Geochemical evidence for lacustrine microbial blooms in the vast Permian Main Karoo, Parana, Falkland Islands and Huab basins of southwestern Gondwana. *Palaeogeography Palaeoclimatology Palaeoecology*, **152**, 189–213.

FERRY J.M. & DIPPLE G.M. (1991) Fluid flow, mineral reactions, and metasomatism. *Geology*, **19**, 211–214.

FERRY J.M. & GERDES M.L. (1998) Chemically reactive fluid flow during metamorphism. *Annual Review of Earth and Planetary Sciences*, **26**, 255–287.

GALERNE C.Y., NEUMANN E.R. & PLANKE S. (2008) Emplacement mechanisms of sill complexes: Information from the geochemical architecture of the Golden Valley Sill Complex, South Africa. *Journal of Volcanology and Geothermal Research*, **177**, 425–440.

GANINO C. & ARNDT N.T. (2009) Climate changes caused by degassing of sediments during the emplacement of large igneous provinces. *Geology*, **37**, 323–326.

HANSON R.B. & BARTON M.D. (1989) Thermal Development of Low-Pressure Metamorphic Belts - Results from Two-Dimensional Numerical-Models. *Journal of Geophysical Research-Solid Earth and Planets*, **94**, 10363–10377.

HESSELBO S.P., GROCKE D.R., JENKYNS H.C., BJERRUM C.J., FARRIMOND P., BELL H.S.M. & GREEN O.R. (2000) Massive dissociation of gas hydrate during a Jurassic oceanic anoxic event. *Nature*, **406**, 392–395.

HUNT J.M. (1996) *Petroleum Geochemistry and Geology (Second Edition)*. W.H. Freeman and Company, 2nd edn.

JAMTVEIT B., SVENSEN H. & PODLADCHIKOV Y.Y. (2004) Hydrothermal vent complexes associated with sill intrusions in sedimentary basins. In: *Physical Geology of High-Level Magmatic Systems* (Ed. C. Breitkreuz & N. Petford), vol. 234. Geological Society, London, Special Publications.

JENKYNS H.C. & CLAYTON C.J. (1997) Lower Jurassic epicontinental carbonates and mudstones from England and Wales: chemostratigraphic signals and the early Toarcian anoxic event. *Sedimentology*, **44**, 687–706.

KARLSEN D.A. & SKEIE J.E. (2006) Petroleum migration, faults and overpressure, Part I: Calibrating basin modelling using petroleum in traps - A review. *Journal of Petroleum Geology*, **29**, 227–255.

KEMP D.B., COE A.L., COHEN A.S. & SCHWARK L. (2005) Astronomical pacing of methane release in the Early Jurassic period. *Nature*, **437**, 396–399.

KILLOPS S.D. & KILLOPS V.J. (1993) *An introduction to organic geochemistry*. J. Wiley and Sons Inc., New York.

LOCK B.E. (1980) Flat-Plate Subduction and the Cape Fold Belt of South-Africa. *Geology*, **8**, 35–39.

MARSH J., HOOPER P., REHACEK J., DUNCAN R. & DUNCAN A. (1997) Stratigraphy and age of Karoo basalts of Lesotho and implications for correlations within the Karoo igneous province. In: *Large Provinces: continental, oceanic and planetary flood volcanism* (Ed. J. Mahoney & M. Coffin), vol. 100, 247–272. Geophysical Monograph.

MCELWAIN J.C., WADE-MURPHY J. & HESSELBO S.P. (2005) Changes in carbon dioxide during an oceanic anoxic event linked to intrusion into Gondwana coals. *Nature*, **435**, 479–482.

PALFY J. & SMITH P.L. (2000) Synchrony between Early Jurassic extinction, oceanic anoxic event, and the Karoo-Ferrar flood basalt volcanism. *Geology*, **28**, 747–750.

PATTISON D.R.M. (2006) The fate of graphite in prograde metamorphism of pelites: An example from the Ballachulish aureole, Scotland. *Lithos*, **88**, 85–99.

PEACOCK S.M. (1987) Thermal effects of metamorphic fluids in subduction zones. *Geology*, **15**, 1057–1060.

PERREGAARD J. & SCHIENER E.J. (1979) Thermal alteration of sedimentary organic matter by a basalt intrusive (Kimmeridgian Shales, Milne Land, East Greenland). *Chemical Geology*, **26**, 331–343.

PODLADCHIKOV Y.Y. & WICKHAM S.M. (1994) Crystallization of Hydrous Magmas - Calculation of Associated Thermal Effects, Volatile Fluxes, and Isotopic Alteration. *Journal of Geology*, **102**, 25–45.

POLTEAU S., FERRE E.C., PLANKE S., NEUMANN E.R. & CHEVALLIER L. (2008) How are saucer-shaped sills emplaced? Constraints from the Golden Valley Sill, South Africa. *Journal of Geophysical Research-Solid Earth*, **113, B12**, B12104.

POLTEAU S., SVENSEN H., PLANKE S. & AARNES I. (in prep.) Geochemistry of contact metamorphic black shale around sill intrusions in the Karoo Basin and the implication for the Toarcian carbon isotope excursion.

PRICE L.C. (1983) Geologic time as a parameter in organic metamorphism and vitrinite reflectance as an absolute paleogeothermometer. *Journal of Petroleum Geology*, **6**, 5–37.

RAMPINO M.R. & STOTHERS R.B. (1988) Flood-Basalt Volcanism During the Past 250 Million Years. *Science*, **241**, 663–668.

RAYMOND A.C. & MURCHISON D.G. (1988) Development of Organic Maturation in the Thermal Aureoles of Sills and Its Relation to Sediment Compaction. *Fuel*, **67**, 1599–1608.

REVERDATTO V.V. & MELENEVSKII V.N. (1983) Magmatic heat as a factor in generation of hydrocarbons: the case of basalt sills. *Geologiya i Geofizika*, **24**, 15–23.

SCHENK H.J., DIPRIMIO R. & HORSFIELD B. (1997) The conversion of oil into gas in petroleum reservoirs .1. Comparative kinetic investigation of gas generation from crude oils of lacustrine, marine and fluviodeltaic origin by programmed-temperature closed-system pyrolysis. *Organic Geochemistry*, **26**, 467–481.

SCHMOKER J.W. (1994) Volumetric calculation of hydrocarbons generated. In: *The petroleum system - from source to trap: AAPG Memoir 60* (Ed. L.B. Magoon & W.G. Dow), 323–326.

SIMONEIT B.R.T., BRENNER S., PETERS K.E. & KAPLAN I.R. (1978) Thermal Alteration of Cretaceous Black Shale by Basaltic Intrusions in Eastern Atlantic. *Nature*, **273**, 501–504.

SMITH R.M.H. (1990) A review of stratigraphy and sedimentary environments of the Karoo Basin of South Africa. *Journal of African Earth Sciences*, **10**, 117–137.

STORVOLL V., BJORLYKKE K. & MONDOL N.H. (2005) Velocity-depth trends in mesozoic and cenozoic sediments from the Norwegian shelf. *AAPG Bulletin*, **89**, 359–381.

SUAN G., PITTET B., BOUR I., MATTIOLI E., DUARTE L.V. & MAILLIOT S. (2008) Duration of the Early Toarcian carbon isotope excursion deduced from spectral analysis: Consequence for its possible causes. *Earth and Planetary Science Letters*, **267**, 666–679.

SVENSEN H., BEBOUT G., KRONZ A., LI L., PLANKE S., CHEVALLIER L. & JAMTVEIT B. (2008) Nitrogen geochemistry as a tracer of fluid flow in a hydrothermal vent complex in the Karoo Basin, South Africa. *Geochimica et Cosmochimica Acta*, **72**, 4929–4947.

SVENSEN H., JAMTVEIT B., PLANKE S. & CHEVALLIER L. (2006) Structure and evolution of hydrothermal vent complexes in the Karoo Basin, South Africa. *Journal of the Geological Society*, **163**, 671–682.

SVENSEN H., PLANKE S., CHEVALLIER L., MALTHE-SØRENSSEN A., CORFU F. & JAMTVEIT B. (2007) Hydrothermal venting of greenhouse gases triggering Early Jurassic global warming. *Earth and Planetary Science Letters*, **256**, 554–566.

SVENSEN H., PLANKE S., MALTHE-SORENSSEN A., JAMTVEIT B., MYKLEBUST R., EIDEM T.R. & REY S.S. (2004) Release of methane from a volcanic basin as a mechanism for initial Eocene global warming. *Nature*, **429**, 542–545.

SVENSEN H., PLANKE S., POLOZOV A.G., SCHMIDBAUER N., CORFU F., PODLADCHIKOV Y.Y. & JAMTVEIT B. (2009) Siberian gas venting and the end-Permian environmental crisis. *Earth and Planetary Science Letters*, **277**, 490–500.

SWEENEY J. & BURNHAM .K. (1990) Evaluation of a simple model of vitrinite reflectance based on chemical kinetics. *AAPG Bulletin*, **74**, 1559–1570.

TISSOT B. & WELTE D.H. (1984) *Petroleum Formation and Occurrence*. Springer Verlag, Berlin, 2nd edn.

TISSOT B.P., PELET R. & UNGERER P. (1987) Thermal History of Sedimentary Basins, Maturation Indexes, and Kinetics of Oil and Gas Generation. *AAPG Bulletin*, **71**, 1445–1466.

TOPLIS M. & CARROLL M. (1995) An Experimental Study of the Influence of Oxygen Fugacity on Fe-Ti Oxide Stability, Phase Relations, and Mineral–Melt Equilibria in Ferro-Basaltic Systems. *Journal of Petrology*, **36**, 1137–1179.

UNGERER P. & PELET R. (1987) Extrapolation of the Kinetics of Oil and Gas-Formation from Laboratory Experiments to Sedimentary Basins. *Nature*, **327**, 52–54.

VISSER J.N.J. (1992) Deposition of the Early to Late Permian Whitehill Formation during a sea-level highstand in a juvenile foreland basin. *South African Journal of Geology*, **95**, 181–193.

WALKER F. & POLDERVAART A. (1949) Karroo dolerites of the Union of South Africa. *Geological Society of America Bulletin*, **60**, 591–706.

WALTHER J.V. & WOOD B.J. (1984) Rate and Mechanism in Prograde Metamorphism. *Contributions to Mineralogy and Petrology*, **88**, 246–259.

WIGNALL P.B. (2001) Large igneous provinces and mass extinctions. *Earth-Science Reviews*, **53**, 1–33.

YOSHINOBU A.S. & GIRTY G.H. (1999) Measuring host rock volume changes during magma emplacement. *Journal of Structural Geology*, **21**, 111–116.

Chapter 4

Fluid overpressure and rate of devolatilization during metamorphism

by Ingrid Aarnes*, Yuri Y. Podladchikov* and Henrik Svensen*
Manuscript prepared for Journal of Geophysical Research - Solid Earth

4.1 Abstract

Exact and numerical solutions to reaction induced fluid overpressure coupled to temperature and fluid flow are derived. The model is derived from basic principles of conservation of mass, energy and momentum, and is thermodynamically consistent. Devolatilization reactions leading to overpressure are particularly important during contact metamorphism where high thermal fluxes cause large volumes of fluids to be rapidly generated. We employ a model of conductive heat transfer around a magmatic intrusion with latent heat of crystallization, coupled to overpressure buildup resulting from fluid generation and diffusive fluid flux. We can identify three key factors involved in the pressure build-up: 1) The efficiency of flow relative to the thermal reaction front, 2) the reaction temperature relative to the available heat in the system, and 3) the feedback of overpressure on the reaction temperature as a function of the Clapeyron-slope. If the fluid production is more efficient than the fluid transport out from the front, the solution simplifies to an isochoric system controlled by the effective volume change of the reaction. Fluid flow reduces the pressure at the reaction front by dispersing it over a larger area. Still, overpressures above 10 MPa can develop in the presence of fluid flow. If the devolatilization reaction is pressure dependent, the fluid pressure build-up from the reaction will shift the equilibrium conditions for the dehydration reaction towards higher temperatures, which in turn will impede the reaction rate. We use the model to deduce the criteria for fracturing and breccia-pipe formation. The formation of breccia-pipes is important as they provide efficient transport channels for aureole fluids to the atmosphere, with a potential impact on the global climate. The analytical solutions are however general, and can be applied to quantify a number of geological processes related to dehydration-reactions during prograde metamorphism. Moreover, the solutions presented in this study can be used for verification and development of reactive transport models.

*Physics of Geological Processes, University of Oslo, P.box 1048 Blindern, 0316 Oslo, Norway.

4.2 Introduction

Devolatilization of sedimentary rocks is a key process during progressive metamorphism. Commonly, the positive change in fluid volume released upon devolatilization is larger than the corresponding decrease in solid volume, causing a net volume increase of the reaction. If the sudden increase in volume of the reaction cannot be accommodated by the host-rock, the fluid pressure will build up (Hanshaw & Bredehoeft, 1968; Thompson, 1987; Walther, 1990). By definition, fluid overpressure is present when the fluid pressure exceeds the hydrostatic pressure. Understanding processes related to devolatilization of carbon-fluids, such as CH_4 and CO_2 is important also in a broader perspective due to the potential influence on the global carbon cycle (e.g. Bickle, 1996; Svensen *et al.*, 2004).

Contact metamorphism is of particular relevance due to the rapid heat transfer causing efficient devolatilization of the intruded sediments (e.g. Simoneit *et al.*, 1978; Jamtveit *et al.*, 1992; Lasaga & Rye, 1993; Bishop & Abbott, 1995; Cooper *et al.*, 2007; Nabelek, 2007; Aarnes *et al.*, in review). Overpressure during contact metamorphism can be generated by several volume changing processes, such as boiling and thermal expansion of pore fluids, buoyancy effects, release of magmatic fluids and fluid generation within the contact aureole (e.g. Furlong *et al.*, 1991; Hanson, 1992; Nabelek & Labotka, 1993; Hanson, 1995; Osborne & Swarbrick, 1997). Overpressures resulting from boiling and thermal expansion of pore-fluids is well documented, especially around large plutons (Knapp & Knight, 1977; Norton & Knight, 1977; Einsele *et al.*, 1980; Delaney, 1982; Manning & Bird, 1991; Cathles *et al.*, 1997; Cui *et al.*, 2001). Similarly, phase transitions related to secondary cracking of oil to gas can cause a significant fluid pressure increase (Barker, 1990; Luo & Vasseur, 1996; Carcione & Gangi, 2000). Buoyancy forces are on the contrary considered to be minor (Cathles, 1977).

Depending on the permeability of the host-rock in front of the reacting interface, the efficiency of fluid generation (pressure buildup) can be comparable to the efficiency of fluid flow (pressure relaxation). Typical devolatilization reactions related to pressure-anomalies are water liberation from hydrous minerals such as sheet silicates (Walther & Orville, 1982; Connolly, 1997), decarbonation of calcite and dolomite (Balashov & Yardley, 1998), and cracking of organic matter to hydrocarbon fluids and CO_2 (Osborne & Swarbrick, 1997; Burrus, 1998; Berg & Gangi, 1999; Wangen, 2001; Hansom & Lee, 2005; Rodriguez Monreal *et al.*, 2009). The fluid-pressure anomalies depend on the efficiency of the reaction and the magnitude of the volume changes (e.g. Ague *et al.*, 1998).

Dehydration reactions are mainly temperature dependent, hence pressure is generally considered a minor factor in prograde dehydration reactions. However, a recent study suggests that pressure can have a critical influence on the dehydration conditions in the Southern Alps, New Zealand (Vry *et al.*, 2010). Vry and co-workers provide evidence for major dehydration upon decompression and uplift at temperature conditions below 500 °C , rather than at the deepest parts of the mountain chain. The full implications of this study requires a larger understanding of the influence of pressure on the reaction dynamics (Wannamaker, 2010).

Due to the relatively high permeabilities estimated in the upper 5 km of the crust (Ingebritsen & Manning, 2002), overpressures are commonly assumed negligible in this regime. However, evidences of significant overpressure generation during contact metamorphism comes from development of fracture networks (e.g. Nishiyama, 1989; Manning & Bird, 1991; Nabelek & Labotka, 1993; Aarnes *et al.*, in

review), fluidization of the host sediment (Delaney, 1982; Kokelaar, 1982), formation of sandstone dykes (Walton & O'Sullivan, 1950; Svensen *et al.*, in press) and hydrothermal vent complexes and breccia pipes from within the aureoles (Jamtveit *et al.*, 2004; Skinner & Marsh, 2004; Svensen *et al.*, 2004; Planke *et al.*, 2005; Oliver *et al.*, 2006; Svensen *et al.*, 2006, 2007; Aarnes *et al.*, in review). Breccia pipes and hydrothermal vent complexes are vertical cylindrical structures that cut vertically through sedimentary strata (Fig. 4.1). Hydrothermal vent complexes are related to boiling and expansion of pore-fluids due to the intrusive heat in the upper $\sim$1 km (Jamtveit *et al.*, 2004).

Breccia pipes are rooted deeper (2-3 km) than where boiling of pure water can occur ($\sim$1 km), and are suggested to form by large-scale devolatilization of intruded shales (Svensen *et al.*, 2007). From theoretical approximations with order of magnitude estimates, Jamtveit *et al.* (2004) recognized that the amount of fluid overpressure depends to a large degree on the relative rates of heat and fluid transport. The development of vent complexes is particularly important for the fluid budget of contact aureoles, as they provide efficient transport channels of fluids from the aureole to the atmosphere. The large scale release of carbon gases generated in the aureole may have global climatic consequences (e.g. Svensen *et al.*, 2004, 2007, 2009; Aarnes *et al.*, accepted).

Implications for fluid flow, fracturing and brecciation of the host-rock require a better model quantifying the fluid pressure buildup in a devolatilizing, partly drained system. Reactive transport models in porous media coupling mass transport, heat, fluid flow and chemical reactions in various geological systems are well documented in the literature (e.g. Lichtner, 1985; Ortoleva *et al.*, 1987; Lichtner, 1988; Baumgartner & Ferry, 1991; Steefel & Lasaga, 1994; Kelemen *et al.*, 1995; Le Gallo *et al.*, 1998; Xu & Pruess, 2001; Gaus *et al.*, 2005). A key topic in these models is fluid-rock interactions (Steefel & Maher, 2009, , and references therein). Such reaction models, however, do not usually provide an understanding of the hydrologic driving forces for the fluid flow while deriving the fluid flux from the conservation of the fluid mass under simplifying steady-state conditions and other assumptions, such as a steady-state flow regime in response to thermal expansion (Furlong *et al.*, 1991; Ferry & Gerdes, 1998).

In this study we continue the work initiated by Jamtveit *et al.* (2004), by adding exact solutions for a thermally driven reaction front coupled to overpressure generation, and accounting for pressure relaxation by fluid flow. The solutions are based on conservation laws of energy, mass and momentum, and are thermodynamically consistent. We focus on the first order processes related to contact metamorphism, such as conductive heat transfer with latent heat of crystallization, velocity of the reaction front, Darcian fluid flow, and feedback of pressure on the reaction rate. The reactions are represented by a source-term and can therefore be substituted by any reaction with a net volume change. The basic setup allows us to investigate the main processes determining the overpressure generation. The model is solved for contact metamorphism specifically, but the results are also relevant for regional prograde metamorphism, and other areas with high heat flow, such as crustal shear zones and zones with magmatic activity during crustal thickening (e.g. Peacock, 1989; Leloup *et al.*, 1999; Baxter *et al.*, 2002; Ague & Baxter, 2007; Weinberg *et al.*, 2009).

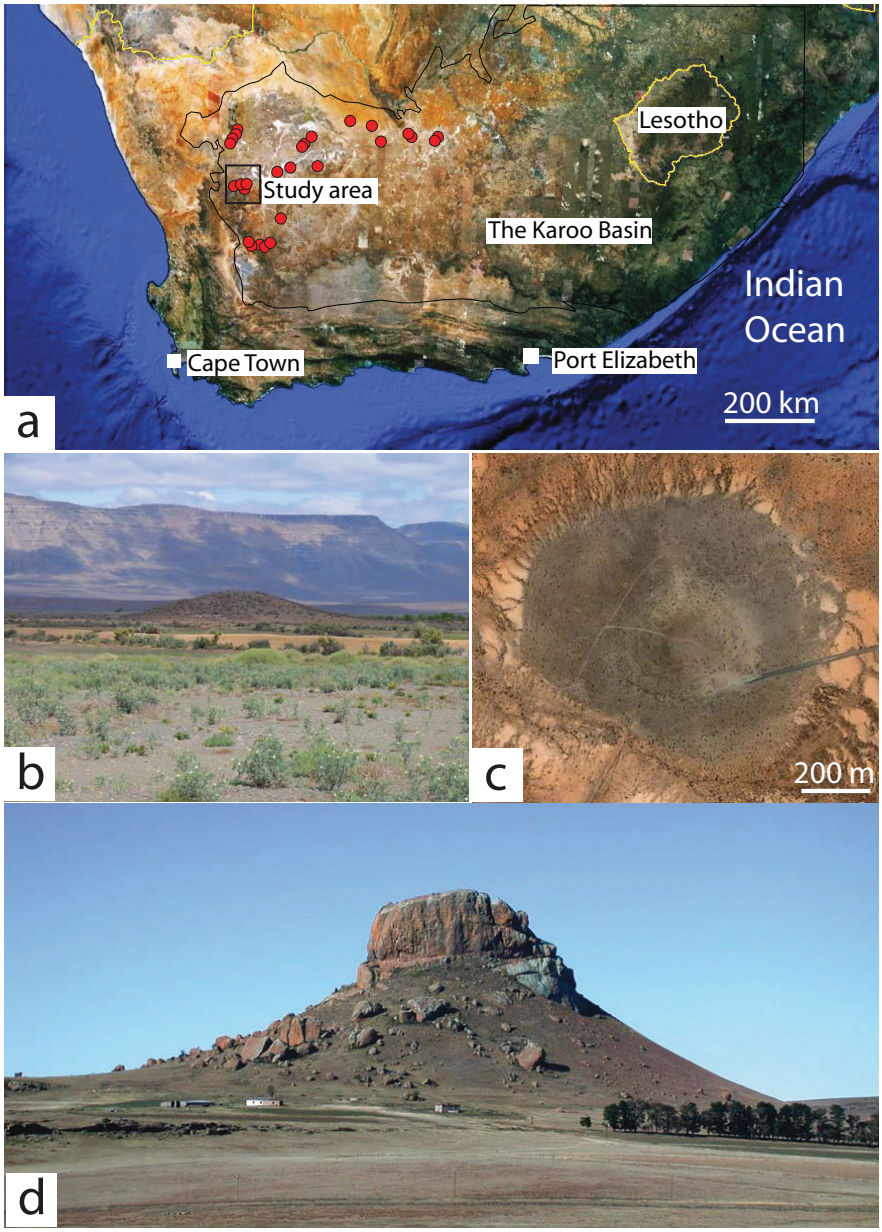

Figure 4.1: **(a)** Satellite image of the Karoo Basin, South Africa, from Google Earth. Red dots represent clusters of breccia pipes associated with the stratigraphically deepest shale formations in the Karoo Basin. **(b)** A photograph of a breccia pipe located at the study area marked in (a). **(c)** A satellite image from Google Earth of the same breccia pipe as (b). **(d)** A photo of the Mackay's Kop hydrothermal vent complex, located in the Eastern Cape, South Africa.

Table 4.1: Symbols and typical values used in this paper.

Symbol	Description	Unit	Typical value
z	Vertical direction	m	
z_m, z_r	Position of crystallization and reaction fronts	m	
t	Time	s	
T_m, T_{hr}	Melt and host-rock temperatures	K	1100-1200; 20-100
T_r, T_c	Reaction and contact temperatures	K	100-500; 500-600
T_L, T_S	Liquidus and solidus temperatures	K	1200; 900-1000
P_f, P_{hr}	Fluid pressure; background hydrostatic fluid pressure	Pa	
P_r, ΔP_r	Fluid pressure and overpressure $(P_r - P_{hr})$ at the front	Pa	
P_V	Isochoric overpressure	Pa	
P_c	'Dummy' constant for fluid pressure at the intrusive contact	Pa	
h, Δh	Specific enthalpy; latent heat of crystallization $\left(h_f - h_s\right)$	kJ/kg	; 320-400
s_f, s_s	Specific entropy; fluid and solid	J/K/m^3	
ρ_f, ρ_s	Density; fluid and solid	kg/m^3	200-1000; 2400
u_f, u_s	Specific internal energy; fluid and solid	J/ m^3	
v_f, v_s	Velocity; fluid and solid	m/s	
ϕ, $(1-\phi)$	Porosity; fluid and solid	m^3/m^3	
q_S	Entropy flux	J/K/kg/m^2/s	
q_ρ	Mass flux	kg/m^2/s	
q_E	Energy flux	J/kg/m^2/s	
q_v	Momentum flux	m/s/kg/m^2/s	
$Q_{S,f}$, $Q_{S,s}$	Entropy source; fluid, solid	J/K/kg/m^2/s	
Q_S^{total}	Total entropy source $\left(Q_{S,f} - Q_{S,s}\right)$	J/K/kg/m^2/s	
$Q_{\rho,f}$, $Q_{\rho,s}$	Mass source; fluid and solid	kg/m^2/s	
$Q_{E,f}$, $Q_{E,s}$	Energy source; fluid and solid	J/kg/m^2/s	
$Q_{v,f}$, $Q_{v,s}$	Momentum source; fluid and solid	m/s/kg/m^2/s	
Q_f^{total}	Total fluid generated at the reaction front	kg/m^3	20-120
λ	Heat conduction coefficient	J/K/s/m	1-3
Cp	Specific heat capacity	J/kg/K	700-1000
κ_T	Thermal diffusivity coefficient, $\lambda/\rho/Cp$	m^2/s	10^{-6}; 10^{-3}-10^{-7}
k	Permeability of the host-rock	m^2	10^{-12}-10^{-20}
μ_f,μ_s	Viscosity; fluid and solid	Pas	
β_f	Effective isothermal compressibility of the fluid	1/Pa	10^{-8}-10^{-10}
η	Bulk viscosity	Pas	
κ_H	Hydraulic diffusivity coefficient, $\left(k/\mu_f/\beta_f/\phi\right)$	m^2/s	10^{-6}; 10^{-3}-10^{-7}
α_f	Isobaric thermal expansion of the fluid	1/K	
ξ_T, ξ_P	Non-dimensional coordinates; temperature and pressure	-	
ξ_T^m	Rate of the crystallization front (non-dimensional)$(z_m/2\kappa_T t)$	-	
ξ_T^r	Rate of the reaction front (non-dimensional)$(z_r/2\kappa_T t)$	-	
Ri	Efficiency of reaction versus fluid flow, $\xi_T^r \kappa_T/\kappa_H$	-	
Rc	Degree of overpressure effects on reaction-closure (non-dimensional)	-	
ΔT_{oh}	Degree of thermal overheating of the host-rock (non-dimensional)	-	
Ste, L^*	Degree of latent heat effects (analytical, numerical) (non-dimensional)	-	

4.3 Theoretical background and methods

4.3.1 Temperature of a cooling sill

Conductive heat transfer

A description of all symbols used in the following sections are given in Table 4.1. In our model we use conductive heat transfer from the intrusion to the host-rock with latent heat of crystallization released within the intrusion, as they contribute to the first order temperature changes in a contact metamorphic setting (cf. Appendix 4.C). The heat conduction equation is derived in Appendix 4.A-4.C, and can be written

$$\frac{\partial T}{\partial t} = \kappa_T \frac{\partial^2 T}{\partial z^2} \tag{4.3.1}$$

(1) where z is the vertical direction, t is time, T is temperature, $\kappa_T = \lambda/\rho/Cp$ is the thermal diffusivity, and Cp is the specific heat capacity, ρ is density and λ is the thermal conductivity.

Latent heat of crystallization

Specific latent heat, Δh, is given in J/kg and is the amount of energy released upon the phase transition from melt to crystals in a cooling magma. There are different methods to treat this non-linearity in the temperature equation. We use the effective heat capacity method for the numerical solution, and apply conservation of energy at the crystallization front for the analytical solution.

The effective heat capacity method is conveniently implemented in the numerical solution. Specific heat capacity (Cp) is defined as the specific enthalpy (h) change as a function of temperature change at constant pressure, $Cp = (\partial h/\partial T)_P$. A higher effective value for the heat capacity is therefore equivalent of releasing excess enthalpy (i.e. energy) over the crystallization interval without changing the temperature. A melt consists of several phases with different crystallization temperatures, so that the heat capacity can be approximated as a linear function over the crystallization interval between the solidus (T_S) and liquidus (T_L) temperatures. The effective heat capacity becomes,

$$\begin{aligned} Cp^{\text{eff}} &= Cp\,(1+L^*) \quad \text{for } T_S < T < T_L \\ Cp^{\text{eff}} &= Cp \qquad\qquad\quad \text{for } T \leq T_S \text{ and } T \geq T_L, \end{aligned} \tag{4.3.2}$$

where the degree of the latent heat effect is determined by

$$L^* = \frac{\Delta h}{Cp\,(T_L - T_S)},$$

and $\Delta h = (h_f - h_s)$

In the analytical solution, the latent heat release is more conveniently treated by a heat balance at the crystallization front in the limit where T_S is close to T_L. Conservation of energy requires that the rate of latent heat release at the crystallization front equals the rate of heat conducted away from the interface

(Turcotte & Schubert, 2002),

$$\rho\Delta h\left(\frac{dz_m}{dt}\right)=\lambda\left(\frac{\partial T}{\partial z}\right)_{z=z_m}. \tag{4.3.3}$$

The left-hand side expresses the rate of the latent heat release at the crystallization front and the right-hand side expresses the rate of heat conduction away from the crystallization front following Fourier's law. In this manner the latent heat is incorporated into the thermal budget. Although looking different from the effective heat capacity method, this is simply two ways of treating the same physics.

4.3.2 Fluid pressure during prograde metamorphism

Fluid pressure evolution

The fluid pressure equation is derived on the basis of the conservation laws in the Appendices 4.A-4.C, and can be written,

$$\frac{\partial P_f}{\partial t}=\kappa_H\frac{\partial^2 P_f}{\partial z^2}, \tag{4.3.4}$$

where P_f is the fluid pressure, $\kappa_H = k/(\phi\beta_f\mu_f)$ is the hydraulic diffusivity coefficient, k is the permeability, μ_f is the fluid viscosity, ϕ is porosity, and β_f the effective fluid compressibility assuming spatially homogeneous permeability and viscosity. The pressure evolution by diffusive fluid flux is identical in structure to the thermal equation.

Reaction induced pressure

The pressure at the reaction front P_r is coupled to temperature through a devolatilizing reaction-front z_r following a reaction-temperature isograd T_r (Fig. 4.2). The position of this reaction-front is controlled by the efficiency of heat diffusion into the host-rock. If the generated fluids stagnate at the reaction-front, the overpressure is controlled by the effective volume change of the reaction, i.e. the isochoric pressure buildup. If the fluids are allowed to flow away from the reaction-front the overpressure at the front is reduced by distributing the pressure further out into the host-rock (Fig. 4.2).

There is conceptually no difference between the source of pressure due to devolatilization-reactions and the source of heat due to crystallization-reactions. For the numerical simulation of pressure it is convenient to introduce the devolatilization-reaction as a separate source-term in Eq. 4.3.4, cf. Appendix 4.C,

$$\frac{\partial P_f}{\partial t}=\kappa_H\frac{\partial^2 P_f}{\partial z^2}+\left(\frac{1}{\rho_f}-\frac{1}{\rho_s}\right)\frac{Q_{\rho,f}}{\phi\beta_f}, \tag{4.3.5}$$

where $1/\rho_f - 1/\rho_s$ is the net volume change of the reaction, ρ_f is the fluid density ($\mathrm{kg}_{fluid}/\mathrm{m}^3_{fluid}$),$\rho_s$ is the solid density ($\mathrm{kg}_{rock}/\mathrm{m}^3_{rock}$), and $Q_{\rho,f}$ is the rate of fluid mass production per unit volume of rock ($\mathrm{kg}_{fluid}/\mathrm{m}^3_{rock}/\mathrm{s}$). The source term $Q_{\rho,f}$ ($\mathrm{kg}_{fluid}/\mathrm{m}^3_{fluid}$) encompass all devolatilization reactions occurring at the reaction front. Eq. 4.3.5 shows that the fluid pressure evolves through time due to the imbalance between the reduction of pressure through Darcy flux and the increase of pressure through the source-term. Although we focus on devolatilization, the source term can describe any volume-changing process such as melting and expansion of pore-fluids. For example if the reaction related to a phase change occurs in an isochoric system , Eq. 4.3.5 has a source term where $Q_{\rho,f} = \alpha_f dT/dt$ and α_f is

thermal expansion of the fluid (e.g. Domenico & Palciauskas, 1979; Manning & Bird, 1991; Corbet & Bethke, 1992; Aarnes *et al.*, 2008)

By analogy with the energy balance for latent heat released at the crystallization front (Eq. 4.3.3), the pressure source is readily incorporated into the analytical solution by introducing a mass balance relation at the reaction front. Due to the low storage capacity for excess fluid in the host-rock, conservation of mass requires that the fluid production rate at the reaction front equals the fluid expulsion rate away from the reaction front,

$$\left(\frac{1}{\rho_f}-\frac{1}{\rho_s}\right) Q_f^{total}\frac{dz_r}{dt} = -\frac{k}{\mu_f}\left(\frac{\partial \Delta P_f}{\partial z}\right)_{z=z_r}, \tag{4.3.6}$$

where Q_f^{total} is the total amount of fluids generated at the front ($\mathrm{kg}_{fluid}/\mathrm{m}^3_{rock}$) and $\Delta P_f = P_f - P_{hr}$ is the fluid overpressure, i.e. the fluid pressure relative to the background hydrostatic pressure (P_{hr}) prior to any devolatilization-reaction. The left-hand side of Eq. 4.3.6 describes the fluid production rate at the reaction front, and the right-hand side of Eq. 4.3.6 describes the expulsion rate out of the front following Darcian flux down the pressure gradient. This balance assumes a steady state fluid flux away from the reaction front and further into the host-rock.

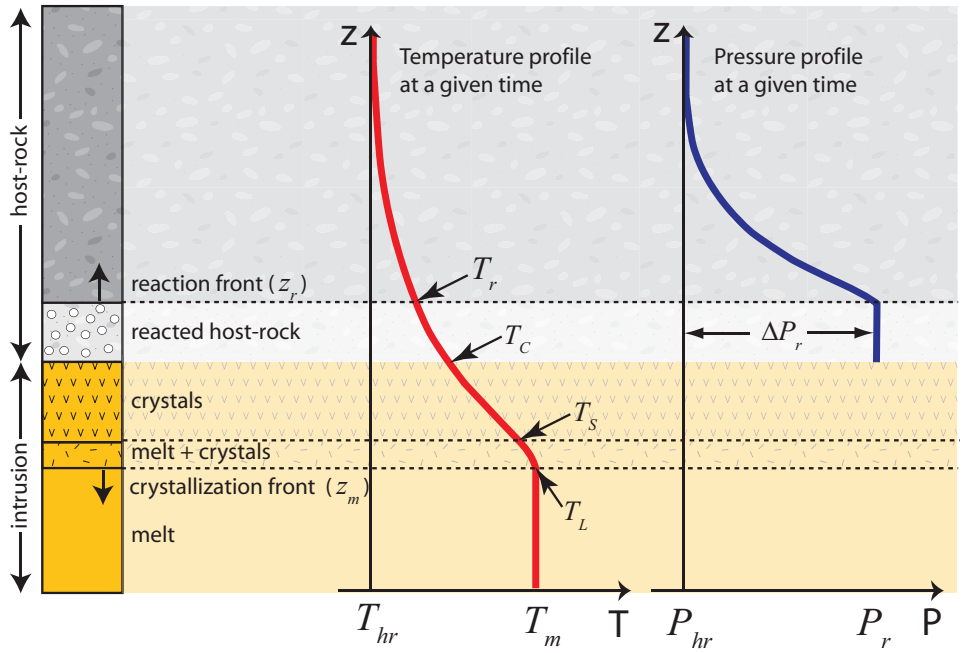

Figure 4.2: A schematic drawing of temperature and pressure profiles at a certain time after sill emplacement. There are two moving fronts; the crystallization front (z_m) and the reaction front (z_r). The crystallization front marks the interface between melt and crystals, and moves towards the center of the intrusion with time. Latent heat is released upon crystallization in the zone where melt and crystals exist. The reaction front follows the reaction temperature isograd (T_r), and marks the interface between the devolatilization reactions and the un-reacted host-rock. The release of fluids at the reaction front builds up an overpressure ΔP_r (P_r relative to background hydrostatic pressure P_{hr}).

4.4 Formulation of analytical solutions

4.4.1 Temperature

One method to find the analytical solution to a partial differential equation on the form $T = T(t,z)$ with variables t and z, is to transform the equation into an ordinary differential equation where temperature is a function of only one variable $T = T(\xi_T)$, and $\xi_T = \xi_T(t,z)$. This transformation can be achieved through dimensional analysis, and is presented in detail in Appendix 4.D.

The transformation of Eq. 4.3.1 gives the following equation (Eq. 4.D.7 from Appendix 4.D),

$$\frac{dT^*}{d\xi_T} = -\frac{1}{2\xi_T}\frac{d^2T^*}{d{\xi_T}^2}$$

where we from the dimensional analysis have defined the new variable as $\xi_T = z/(2\sqrt{\kappa_T t})$ (Eq. 4.D.2a, Appendix 4.D), and the non-dimensional temperature as $T^* = (T - T_{hr})/(T_m - T_{hr})$ (Eq. 4.D.1, Appendix 4.D). T_{hr} is the initial host-rock temperature and T_m is the initial melt temperature. The non-dimensional temperature is not a necessity, but is introduced to simplify the solution in order to reduce the number of controlling parameters.

We define our system to be half of a contact metamorphic setting. Thus, the solution starts at the crystallization front (ξ_T^m), where the temperature is equal to the melt temperature, $T^*(\xi_T^m) = T_m^* = 1$, and ends infinitely far into the host-rock (ξ_T^∞), where the temperature equals the background host-rock temperature, $T^*(\xi_T^\infty) = T_{hr}^* = 0$. The differential equation for temperature is solved by advanced integration of the Eq. 4.D.7 using these boundary conditions. The final analytical solution to the thermal equation is

$$T^*(\xi_T) = \frac{\operatorname{erfc}(\xi_T)}{1 + \operatorname{erf}(\xi_T^m)} \tag{4.4.1}$$

as derived in Appendix 4.D. The error function is by definition

$$\operatorname{erf}(\xi) = \frac{2}{\sqrt{\pi}}\int_0^\xi e^{-\tau^2} d\tau$$

, and $\operatorname{erfc}(\xi) = 1 - \operatorname{erf}(\xi)$, given as the classical solutions to the linear second order ordinary differential equations in a semi-infinite half-space (e.g. Carslaw & Jaeger, 1959; Crank, 1979; Turcotte & Schubert, 2002; Philpotts & Ague, 2009). The error function has the properties that $\operatorname{erf}(0) = 0$ and $\operatorname{erf}(\infty) = 1$.

Of key interest in geological systems is the solution for the dimensional temperature $T(t,z)$, which is achieved by substitution of the non-dimensional expressions for ξ_T (Eq. 4.D.2a) and T^* (Eq. 4.D.1) into Eq. 4.4.1:

$$T(t,z) = T_{hr} + \frac{(T_m - T_{hr})\operatorname{erfc}\left(\frac{z}{2\sqrt{\kappa_T t}}\right)}{1 + \operatorname{erf}(\xi_T^m)}. \tag{4.4.2}$$

Figure 4.3 illustrates the relationship between the dimensional and non-dimensional coordinate systems. The temperature is conducted out into the aureole with time in the dimensional coordinate system of z (Fig. 3a). If we divide each of the thermal profiles in Fig. 3a by $2\sqrt{\kappa_T t}$ for their respective times, they collapse to the exact same profile in the non-dimensional coordinate system of ξ_T (Fig. 3b). This

profile stays constant for all times until the intrusion has crystallized completely, because time is already included as a parameter in the horizontal axis. This implies that the parameter ξ_T^m has a constant value which represents the position of the crystallization front in the non-dimensional coordinate system, i.e. at -0.5 in Fig. 3b. The crystallization front has a negative value because the intrusion is located at $-d < z < 0$, where d is the half thickness of the intrusion, and $z_c = 0$ at the contact between the host-rock and the intrusion (Fig. 4.2).

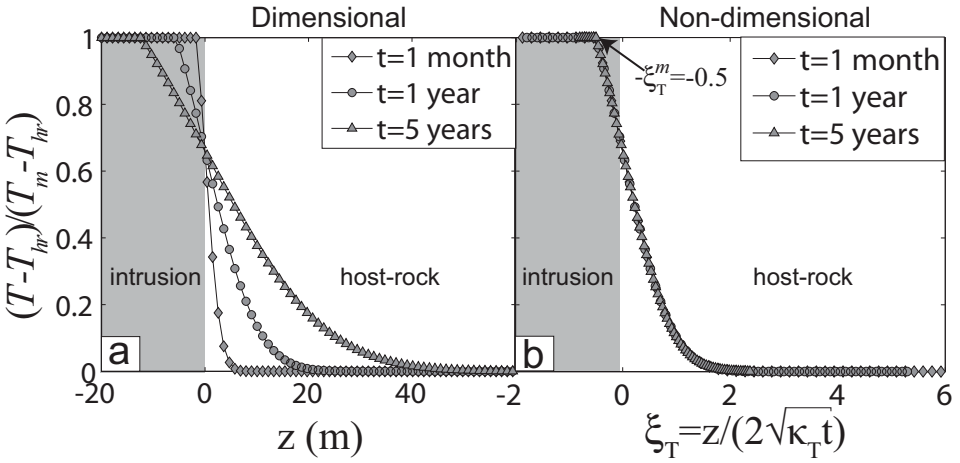

Figure 4.3: (a) The analytical solution for thermal profiles for three different times in the dimensional coordinate system for an intrusion with a half-thickness of 20 meters using Eq. 4.4.2. The heat is conducted further into the host-rock with time as the crystallization of the intrusion continues. **(b)** When the thermal profiles are normalized by the square root of the thermal diffusivity and their respective times the solutions collapse to one single profile in the non-dimensional coordinate system (Eq. 4.4.1). The parameters are set to $\kappa_T = 10^{-6}$ m^2/s and $-\xi_T^m = -0.5$.

The crystallization front

While κ_T is a well constrained parameter for most rocks, the position of the crystallization front ξ_T^m is still an unknown quantity. This position depends on the initial thermal gradients between the host-rock and the intrusion, and on the latent heat released during crystallization. The parameter ξ_T^m describes the rate of crystallization, i.e. how fast the crystallization front reaches a given position, or how far it reaches for a given time. We find the location of this boundary in the dimensional coordinate system by rearranging Eq. 4.D.2a and solving it at the crystallization front z_m,

$$z_m = -2\xi_T^m \sqrt{\kappa_T t}. \tag{4.4.3}$$

This relation shows that ξ_T^m can be interpreted as a constant controlling the position of the crystallization front in the dimensional coordinate system.

The value for ξ_T^m is determined by evaluating the heat balance relation at the crystallization front (Eq. 4.3.3). The rate of the crystallization front is found by differentiating Eq. 4.4.3 with respect to

time,

$$\frac{dz_m}{dt} = \xi_T^m \sqrt{\frac{\kappa_T}{t}}. \tag{4.4.4}$$

The temperature gradient at $z = z_m$ is found from taking the gradient of T from Eq. 4.4.2 and using the chain rule of differentiation,

$$\left(\frac{\partial T}{\partial z}\right)_{z=z_m} = (T_m - T_{hr}) \left(\frac{\partial T^*}{\partial \xi_T}\right)_{\xi_T=\xi_T^m} \left(\frac{\partial \xi_T}{\partial z}\right) = -\frac{\exp\left(-\xi_T^{m2}\right)(T_m - T_{hr})}{\sqrt{\pi \kappa_T t}\left(1+\mathrm{erf}\left(\xi_T^m\right)\right)}. \tag{4.4.5}$$

Substitution of Eq. 4.4.4 and Eq. 4.4.5 into Eq. 4.3.3, and including the definition of κ_T, gives an equation for calculating ξ_T^m,

$$Ste = \frac{\Delta h}{Cp\,(T_m - T_{hr})} = \frac{\exp\left(-\xi_T^{m2}\right)}{\sqrt{\pi}\xi_T^m\left(1+\mathrm{erf}\left(\xi_T^m\right)\right)}, \tag{4.4.6}$$

where the left hand side is called the Stefan number (Ste). The equation defines an unique correspondence between *Ste* and ξ_T^m that can be demonstrated by computing the *Ste* number using the above explicit equation as a function of varying ξ_T^m and graphically visualizing it on ξ_T^m-*Ste* diagram at the desired range of the *Ste* numbers (Fig. 4.4a). The data used to plo this figure can be used as a lookup table to infer ξ_T^m as a function of *Ste* number. A Stefan number of zero is equivalent of no latent heat released upon crystallization.

When the crystallization front is calculated for the system of interest, we can solve the corresponding temperature analytically from Eqs. 4.4.1 or 4.4.2. For illustration, two temperature profiles are plotted as a function of ξ_T for Stefan numbers of 1.2 and 0.2 (Fig. 4.4b). A higher Stefan number is equivalent of the release of more latent heat, and corresponds to a less extensive crystallization front (i.e. smaller ξ_T^m).

The contact temperature T_c^* is depending on the Stefan number, where a higher Stefan number gives a higher contact temperature ($T_c^* = 0.74$ for $Ste = 1.2$) (Fig. 4.4c). For a lower Stefan number, the contact temperature is just above half between the initial melt (T_m) and host-rock (T_{hr}) temperatures ($T_c^* = 0.58$ for $Ste = 0.2$). The non-dimensional contact temperature can be found from $T_c = T_c^* T_m + (1 - T_c^*)\,T_{hr}$.

4.5 Pressure

The pressure equation is solved in an identical way as the temperature by the three main steps; 1) transformation of the partial differential equation through dimensional analysis of the fluid pressure equation (Eq. 4.3.4) presented in Appendix 4.D; 2) specification of the boundary conditions and solving the equation; 3) treating the pressure source at the reaction front (Eq. 4.3.6).

From the dimensional analysis we transformed the partial differential equation of pressure into an ordinary differential equation (Eq. 4.D.8, Appendix 4.D),

$$\frac{d\Delta P_f(\xi_P)}{d\xi_P} = -\frac{1}{2\xi_P}\frac{d^2\Delta P_f(\xi_P)}{d{\xi_P}^2}$$

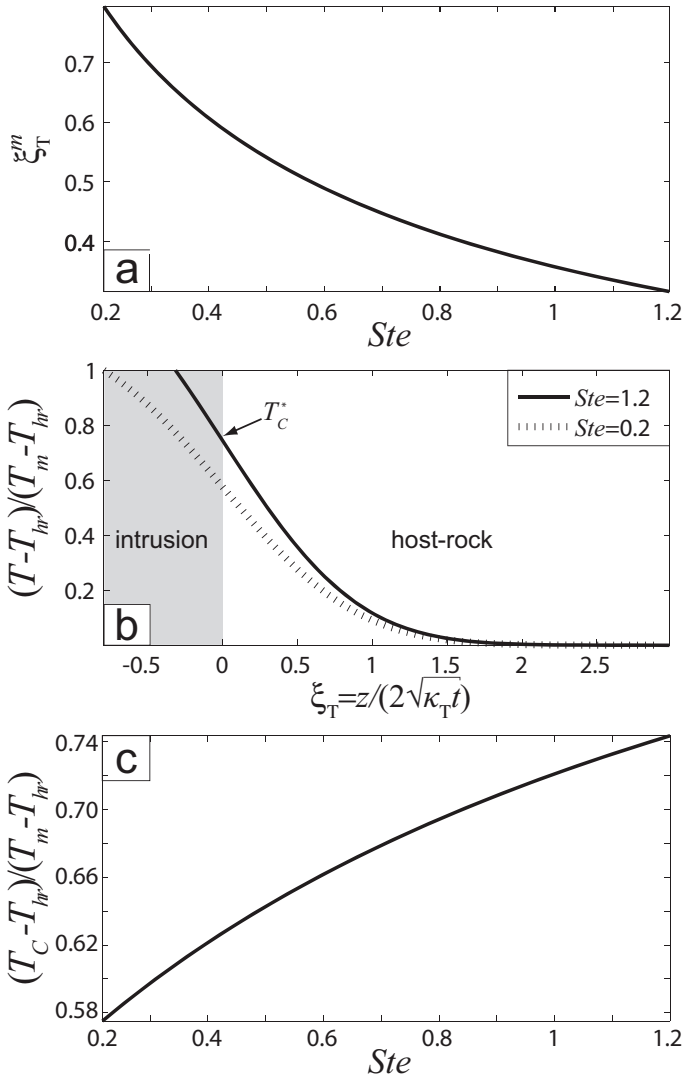

Figure 4.4: Calculations of different relationships between the crystallization front (ξ_T^m), Stefan numbers (Ste) and contact temperatures (T_c). **(a)** Plotted solutions to Eq. 4.4.6 as a function of the Stefan number. Higher Stefan numbers inhibit the movement of the crystallization front, i.e. smaller values of ξ_T^m. **(b)** Analytical solutions to temperature profiles of a cooling intrusion for two different Stefan numbers (Eq. 4.4.1). At higher Stefan numbers (1.2) the release of more latent heat is slowing down the crystallization, and causing a higher contact temperature than at small Stefan numbers (0.2). **(c)** Plotted solutions of contact temperature as a function of varying Stefan numbers. More latent heat release results in a higher contact temperature.

where the fluid overpressure is a function of a single parameter, $\Delta P_f = f(\xi_P)$. The new non-dimensional parameter is defined as $\xi_P = z/2\sqrt{\kappa_H t}$ (Eq. 4.D.2b, Appendix 4.D). As boundary conditions we set the

overpressure infinitely far from the reaction front to zero, $\Delta P_f(\xi_P^{\infty}) = 0$, and the fluid overpressure at the contact to a constant contact pressure, $\Delta P_f(0) = P_c$. The analytical solution for overpressure (Eq. 4.D.10, Appendix 4.D) becomes

$$\Delta P_f(\xi_P) = \operatorname{erfc}(\xi_P) P_c.$$

In the dimensional coordinate system this can be written as

$$\Delta P_f(z,t) = \operatorname{erfc}\left(\frac{z}{\sqrt{\kappa_H t}}\right) P_c. \tag{4.5.1}$$

An expression for P_c is an unknown constant representing pressure at the contact is derived in the following section.

The contact pressure

The expression for the unknown contact pressure P_c is found from solving the conservation of mass relation (Eq. 4.3.6) at the reaction front. The spatial position of the reaction front z_r is controlled by the temperature evolution (Eq. 4.D.2a),

$$z_r = 2\xi_T^r \sqrt{\kappa_T t}, \tag{4.5.2}$$

where ξ_T^r is the position of the reaction front (i.e. the isograd of the reaction temperature) in the non-dimensional coordinate system. ξ_T^r can be interpreted as a factor that controlling the extent of the reaction in the aureole; for a large value of ξ_T^r the reaction front will be located further away from the contact at a certain time compared to a smaller value. Similarly, the time required for the reaction to reach a fixed position in z-space is proportional to $(\xi_T^r)^{-2}$, which implies that a higher value results in a shorter time. It thus plays a similar role as the ξ_T^m does for determining the efficiency of the crystallization front.

The rate of the reaction front (left-hand side of Eq. 4.3.6) is solved by taking the time derivative of Eq. 4.5.2 with respect to time,

$$\frac{dz_r}{dt} = \xi_T^r \sqrt{\frac{\kappa_T}{t}}. \tag{4.5.3}$$

The fluid-pressure gradient at the front is found from taking the gradient of Eq. 4.5.1 at $z = z_r$,

$$\left(\frac{\partial \Delta P_f}{\partial z}\right)_{z=z_r} = -\frac{P_c}{\sqrt{\pi \kappa_H t}} \exp\left(-\frac{(\xi_T^r)^2 \kappa_T}{\kappa_H}\right). \tag{4.5.4}$$

Substituting Eqs. 4.5.3 and 4.5.4 into Eq. 4.3.6 and solving the expression for P_c yields:

$$P_c = \left(\frac{1}{\rho_f} - \frac{1}{\rho_s}\right) \frac{Q_f^{total}}{\phi \beta_f} \sqrt{\pi} \left(\xi_T^r \sqrt{\frac{\kappa_T}{\kappa_H}}\right) \exp\left({\xi_T^r}^2 \frac{\kappa_T}{\kappa_H}\right). \tag{4.5.5}$$

The time parameter is cancelled, which implies that the contact pressure is not a function of time. This is consistent with our assumption of a constant in time contact pressure as our boundary condition of our solution (Eq. 4.5.1) to the pressure equation.

Since we have obtained an expression for the pressure at the contact, we can substitute this into Eq.

4.5.1 (or Eq. 4.5.2) to obtain the analytical solution to the overpressure,

$$\Delta P_f(\xi_P) = \operatorname{erfc}(\xi_P)\left(\frac{1}{\rho_f}-\frac{1}{\rho_s}\right)\frac{Q_f^{total}}{\phi\beta_f}\sqrt{\pi}\left(\xi_T^r\sqrt{\frac{\kappa_T}{\kappa_H}}\right)\exp\left(\xi_T^{r\,2}\frac{\kappa_T}{\kappa_H}\right). \tag{4.5.6}$$

This expression appears complicated, but by looking closer at the terms, we recognize that the ratio κ_T/κ_H times the square of ξ_T^r reappears in all the terms. We assign this term to a non-dimensional parameter,

$$Ri = (\xi_T^r)^2\frac{\kappa_T}{\kappa_H}, \tag{4.5.7}$$

which describes the competition between the velocity of reaction front propagation and the efficiency of the hydraulic diffusion. A large value for Ri is equivalent to a high reaction intensity, with efficient reaction rate and heat diffusion relative to the fluid flow.

We also recognize that the ratio of constants in Eq. 4.5.6 defines the over-pressure generated at constant volume P_V, i.e. at isochoric conditions,

$$P_V = \left(\frac{1}{\rho_f}-\frac{1}{\rho_s}\right)\frac{Q_f^{total}}{\phi\beta_f}. \tag{4.5.8}$$

By taking the rate of Q_f^{total} we can recover the source term in the pressure equation used for the numerical solution (Eq. 4.3.5).

Introducing the new notations, the analytical solution to pressure (Eq. 4.5.7) reduces to

$$P^* = \operatorname{erfc}(\xi_P)\sqrt{\pi Ri}\exp(Ri), \tag{4.5.9}$$

where $P^* = \Delta P_f/P_V$ is the non-dimensional overpressure. At isochoric conditions the host-rock does not release any overpressure by fluid flow to accommodate the effective volume change of the reaction determined by P_V. Thus, the isochoric condition defines the maximum overpressure that can be generated. ξ_P can be substituted by Eq. 4.D.2b from Appendix 4.D to obtain dimensional coordinates.

4.5.1 Resolving overpressure at the reaction front

Eq. 4.5.9 provides a solution to the fluid pressure profile in space and time. Using this expression we can obtain an exact solution to the overpressure at the reaction front, ΔP_r, by substituting $z = z_r$ from Eq. 4.5.2 into Eq. 4.5.9, which gives

$$P_r^* = \frac{\Delta P_r}{P_V} = \sqrt{\pi Ri}\exp(Ri)\operatorname{erfc}\left(\sqrt{Ri}\right). \tag{4.5.10}$$

This equation quantifies the over-pressure instantly generated at the front upon fluid production, while at the same time the overpressure is relaxed through fluids diffusing away from the front. Time is not a separate parameter in this solution, which implies that a system with a constant diffusivity ratio generates a constant value for the overpressure at the reaction front with time. The spatial position of the front (z_r) will of course move through time, with a rate depending on the value of the reaction extent parameter ξ_T^r and the efficiency of heat conduction. The solution to Eq. 4.5.10 is plotted in Figure 4.5 for different

theoretical values of *Ri*.

For large values of $Ri\,(>1)$, the reaction rate is much larger than the hydraulic diffusivity, and the fluids are stagnant relative to the reaction front. As a result the over-pressure approaches isochoric conditions, and Eq. 4.5.10 reduces to $P^* \approx 1$. This relation can be found from Taylor expansion of Eq. 4.5.10 around $Ri = \infty$. In the opposite case when *Ri* is small ($\ll 1$), Eq. 4.5.10 reduces to $P^* \approx \sqrt{\pi Ri}$. This can be found from series expansion of Eq. 4.5.10 around $Ri = 0$. This expression provides a simple approximation to the overpressure generated at the front allowing for fluid flow, revealing the key parameters controlling the overpressure (κ_T, κ_H and ξ_T^r).

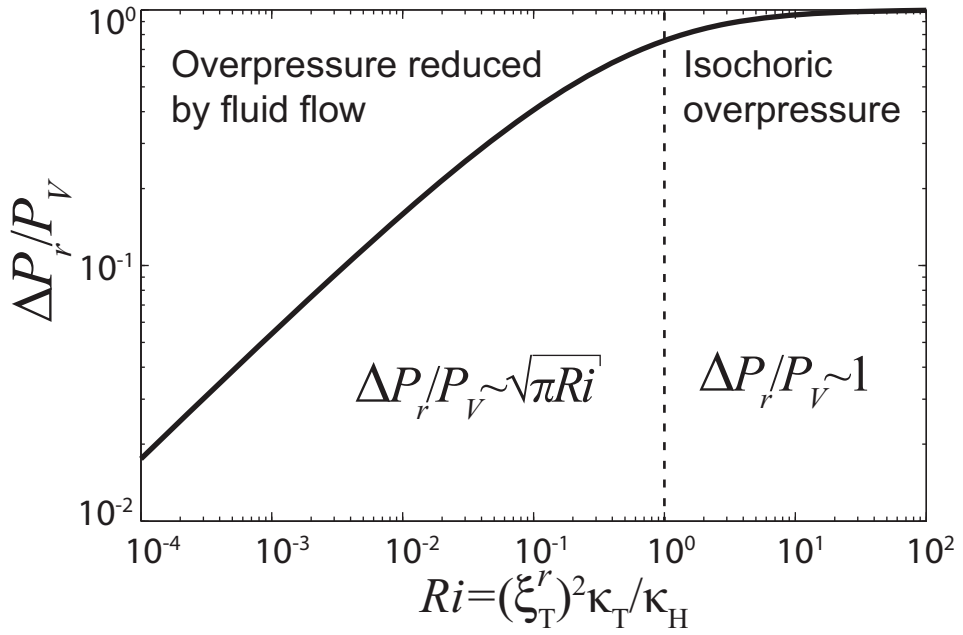

Figure 4.5: The solution to pressure at the front (Eq. 4.5.10) as a function of the parameter *Ri* (Eq. 4.5.7). When the reaction front driven by heat conduction is much larger than the fluid flux ($Ri > 1$), the over-pressure approaches the volume-change of the reaction (P_V), i.e. isochoric pressure build-up. Fluid flux out of the dehydration front reduces the over-pressure. The reduction is proportional to a factor $\sqrt{\pi Ri}$.

4.5.2 Reaction front controlled by temperature

Figure 4.5 shows theoretical values of *Ri* which needs to be substituted by real numbers in order to solve the overpressure analytically. The thermal and hydraulic diffusivities are assumed to be known model parameters. However, the ξ_T^r at the reaction front is still an unknown integration constant that needs to be calculated. In case of purely temperature controlled reactions, we can calculate the reaction front by substituting the temperature defining the reaction front T_r into the analytical solution of temperature

(Eq. 4.4.1).

$$\frac{T_r - T_{hr}}{T_c - T_{hr}} = \mathrm{erfc}\left(\xi_T^r\right). \tag{4.5.11}$$

Eq. 4.5.11 is normalized by contact temperature instead of melt temperature due to substitution of $1+\mathrm{erf}\left(\xi_T^m\right)$ with $(T_m - T_{hr})/(T_c - T_{hr})$.

We have solved Eq. 4.5.11 for different reaction and contact temperatures (Fig. 4.6). Large values for ξ_T^r represent scenarios where the temperature defining the reaction front (T_r) is close to the initial host-rock temperature (T_{hr}). The reaction front progresses efficiently because the amount of additional host-rock heating needed for the reaction to occur is low. Oppositely, small values for ξ_T^r represent high reaction temperatures close to the maximum temperatures that can be obtained by heating from the intrusion, i.e. the contact temperature. In this scenario the host-rock sediments require significant heating before the devolatilization reaction initiates. The reaction rate is correspondingly limited.

The generated overpressure has thus an implicit dependency on the reaction temperature. Figure 4.7 illustrates this dependence of overpressure on both fluid flow and reaction temperature. The fluid flow is primarily controlled by the permeability of the host-rock in front of the reaction interface, and higher permeability implies higher flow and thus reduction of the overpressure. The values for the fixed parameters are given in the caption of Figure 4.7.

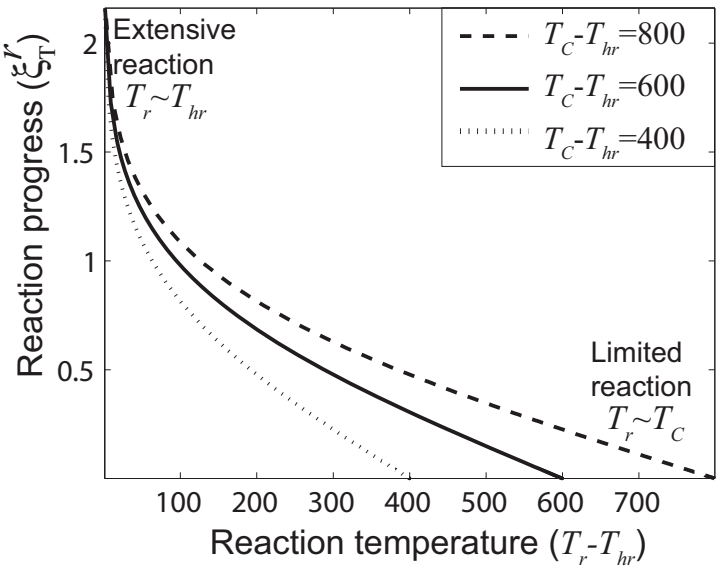

Figure 4.6: Calculated reaction extents as a function of reaction temperatures. The tree curves show the reaction extent for different contact temperatures. The reaction front is efficient when the reaction temperature is close to the host-rock temperature, while it becomes limited as the reaction temperature gets closer to the contact temperature. All reaction temperatures are given relative to host-rock temperature.

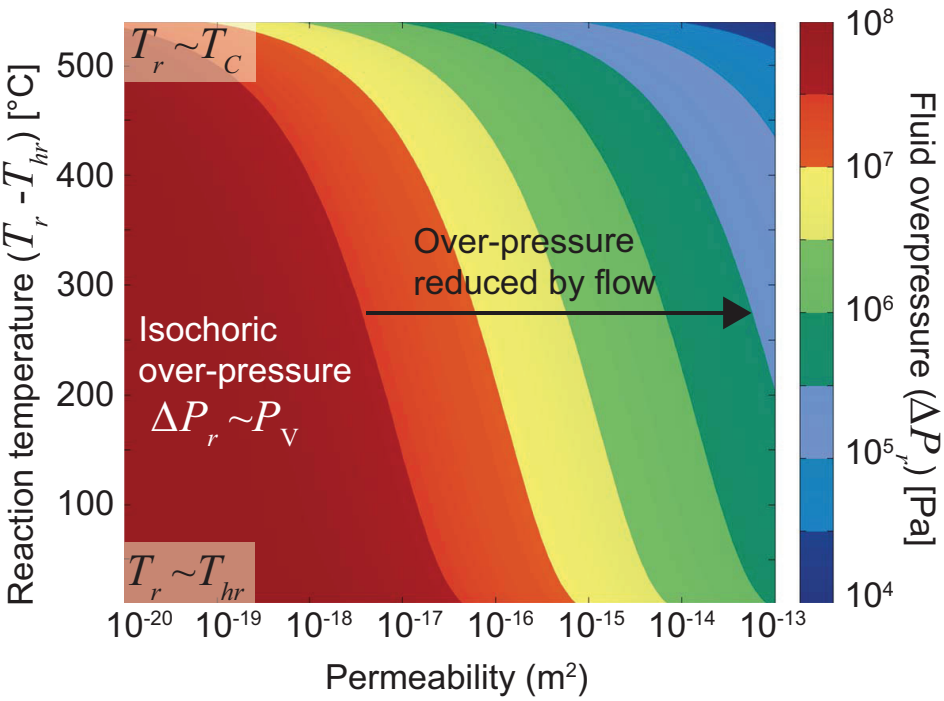

Figure 4.7: One solution to fluid overpressure (ΔP_r) as a function of both the reaction temperature and the degree of fluid flow, i.e. mainly permeability. A low reaction temperature will promote efficient movement of the reaction front, and fluids will be liberated faster than they are able to flow out, hence increasing the pressure. We have fixed the other parameters to the following values: T_c-T_{hr}=550 °C and *Ste*=0.5, corresponding to a T_c-T_{hr}= 1100 °C ; $\kappa_T = 10^{-6}$m^2/s, which is the typical heat diffusivity for most rocks (Delaney, 1982); $\mu_f \phi \beta_f = 10^{-12}$ s corresponding to a H_2O or CH_4 fluid (Ague et al., 1998; Wangen, 2001), and an isochoric pressure P_V of 10^8 Pa (Aarnes et al., 2008). Note that at relatively high permeabilities (10^{-16}-10^{-15} m^2), the generated overpressure can be significant (>10 MPa).

4.5.3 Validation by numerical solution

We have compared our derived analytical solutions to the equivalent numerical solutions in order to validate the model. It is easier to compare temperature and pressure through the dimensional coordinates (z,t) than in the non-dimensional coordinate system (ξ_T and ξ_P). The following solution is therefore a representation of one out of several possible contact metamorphic systems. As an initial setup the intrusion temperature equals the initial melt temperature, and the host-rock temperature equals the background temperature. The initial condition for overpressure is zero throughout the domain, i.e. pressure equals hydrostatic pressure.

The comparison shows that the analytical solution to the temperature evolution with latent heat (Eq. 4.4.2) plots on top of the numerical solution to Eq. 4.3.1, with the use of Eq. 4.3.2 for the latent heat of crystallization (Fig. 4.8a). Due to the different ways of treating the latent heat, the two solutions differ slightly in the crystallization interval. When solving the analytical expression we include

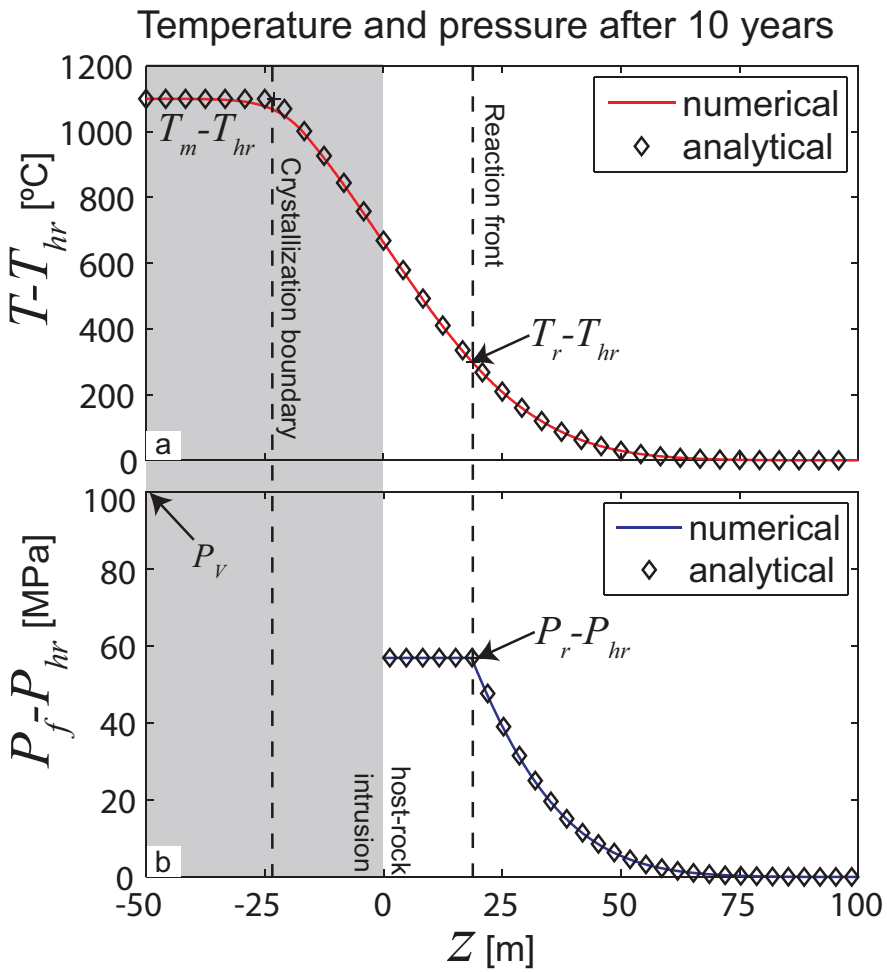

Figure 4.8: Model result showing numerical and analytical solutions to temperature (Eqs. 1 and 8) and pressure (Eqs. 3 and 16) for a sill with a half-thickness of 50 meters after 10 years. **(a)** Temperature relative to host-rock temperature, with a latent heat of 320 kJ/kg; $T_m - T_{hr} = 1100$; $T_r - T_{hr} = 300$; and $\kappa_T = 10^{-6}\text{m}^2/\text{s}$. **(b)** Overpressure relative to background host-rock pressure, with a P_V of 10^8 Pa (100 MPa) and $\kappa_H = 10^{-6}$ m^2/s.

a condition specifying that $\xi_T < -\xi_T^m = -\xi_T^m$, to extend the validity range of the analytical solution from the crystallization front to the intrusion center.

The analytical solution to the fluid pressure in the aureole (Eq. 4.5.9) plots exactly on top of the numerical solution to Eq. 4.3.5 (Fig. 4.8b). The analytical solution has boundaries from the reaction front and infinitely far into the host-rock due to the choice of boundary conditions. We extend the validity range by adding the condition $P(0 < z < z_r) = P_r$, assuming no flow of fluids into the intrusion. The extent of the reaction front, ξ_T^r, is found from solving Eq. 4.5.11 for thermal values given in the

caption of Figure 4.8. Implementation of the reaction source-term at an interface in the numerical model with a finite resolution is done by chain rule of differentiation at the front, $Q_{\rho,f} = (dz_r/dt)\left(Q_{\rho,f}/dz\right)$, where dz is the length of one grid point defined by the numerical resolution.

4.6 Reaction closure by fluid overpressure

4.6.1 A pressure sensitive reaction rate

When the fluid-pressure increases as a result of dehydration, the equilibrium conditions for the reaction are simultaneously shifted along the reaction curve in the $P-T$ space. Figure 4.9 shows three theoretical reaction curves with different Clapeyron-slopes: 1) temperature controlled, 2) intermediate, and 3) pressure controlled. When the reaction initiates, the temperature is equal to reaction temperature (T_r) and pressure is equal to the background host-rock pressure (P_{hr}). As the fluids are liberated, the overpressure increases with a magnitude ΔP_r. This creates a new $P-T$-condition for the reaction to proceed depending on the Clapeyron-slope of the reaction. A gentle slope gives a higher effective reaction temperature, slowing down the reaction due to the additional heating required for the reaction to continue. If the reaction is very pressure sensitive (line 3 in Fig. 4.9) this may even terminate the reaction.

We therefore correct Eq. 4.5.11 for the influence of the overpressure and Clapeyron-slope of the reaction by adding the effective temperature increase. From geometrical constraints we find that the effective reaction temperature is $T_r^{\text{eff}} = T_{r0} + (dT/dP)\,\Delta P_r$, where T_{r0} is the initial reaction temperature. Substitution of T_r^{eff} into Eq. 4.5.11 gives a pressure-dependent reaction rate,

$$\left(\frac{dT}{dP}\frac{\Delta P_r}{T_c - T_{hr}}\right) + \left(\frac{T_{r0} - T_{hr}}{T_c - T_{hr}}\right) = \operatorname{erfc}\left(\xi_T^r\right). \tag{4.6.1}$$

Although it is most common to represent the Clapeyron-slope as dP/dT, we use the opposite relation dT/dP, as it is the form appearing in Eq. 4.6.1.

4.6.2 Data collapse

The aim of the following analysis is to show the three dependencies of ξ_T^r, i.e. reaction front temperature, fluid flow and Clapeyron-slope in a simple 2D representation. First we substitute $\Delta P_r = P_r^* P_V$ into Eq. 4.6.1 and use the approximation $P_r^* \approx \sqrt{\pi}\xi_T^r\sqrt{\kappa_T/\kappa_H}$ from the fluid flow regime ($Ri \ll 1$; Fig. 4.5). Secondly, for small values of the reaction rate ($\xi_T^r < 0.1$) we can approximate $\operatorname{erfc}\left(\xi_T^r\right) \approx 1$. This approximation is good for predicting closure of the reaction, as ξ_T^r will be correspondingly small. Applying these approximations we can equate ξ_T^r to the relevant parameters from Eq. 4.6.1:

$$\xi_T^r \approx \frac{1}{\Delta T_{oh} Rc} \tag{4.6.2}$$

where the non-dimensional parameter group Rc represents the parameters influencing reaction closure by fluid overpressure,

$$Rc = \frac{dT}{dP_V}\frac{\Delta P_r}{(T_c - T_{hr})}\sqrt{\pi\frac{\kappa_T}{\kappa_H}}, \tag{4.6.3}$$

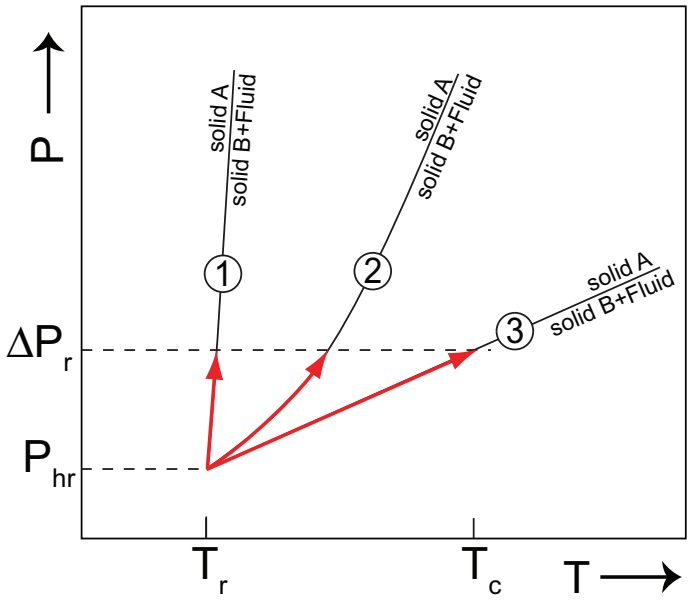

Figure 4.9: Three schematic end-member reaction lines drawn in a $P-T$ diagram for **(1)** a temperature controlled reaction, **(2)** an intermediate and **(3)** a pressure controlled reaction. When the temperature has reached the reaction curve at T_r at a background pressure of P_{hr}, the reaction has three possibilities: (1) The reaction curve is temperature controlled, and an increase in pressure (ΔP_r) will simply move the reaction-condition along the curve up-pressure without changing T_r. (2) The reaction curve depends both on temperature and pressure, and an increase in pressure will shift the reaction-conditions to higher temperatures. (3) The reaction curve is pressure dependent, and a little change in pressure will require a large change in the temperature at which reaction takes place.

and ΔT_{oh} represents the parameters determining the degree of thermal overheating of the host-rock,

$$\Delta T_{oh} = \frac{T_c - T_{hr}}{T_c - T_r}. \tag{4.6.4}$$

Figure 4.10 shows the approximated value for ξ_T^r as a function of Rc and ΔT_{oh}. Red colours represent efficient reaction rate, and blue colours represent reaction closure. We identify two domains, one where the reaction rate (ξ_T^r) is temperature controlled (vertical lines) and one where the reaction rate is influenced by temperature and pressure (inclined lines). In the temperature domain $(Rc < 1)$ the solution for ξ_T^r is governed by Eq. 4.5.11, and the reaction rate is only dependent on of the degree of thermal overheating, i.e. the amount of heating required for the host-rock to reach the reaction temperature. A large value of ΔT_{oh} is equivalent of a large degree of host-rock heating before the reaction temperature is reached $(T_r \sim T_c)$, slowing down the reaction front.

In the pressure domain $(Rc \gg 1)$ the solution for ξ_T^r is governed by both overpressure and temperature. Depending on the magnitude of the overpressure determined from the volume change of the reaction (P_V), and the amount of overpressure reduced by flow $\left(\sqrt{\kappa_T/\kappa_H}\right)$, variations in the

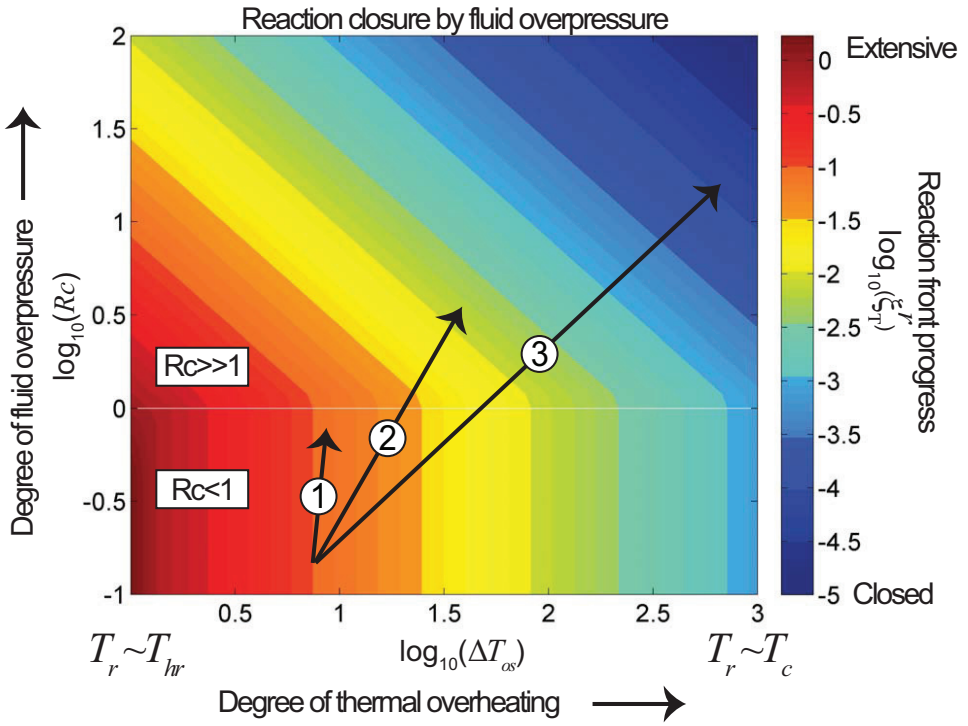

Figure 4.10: The solution of Eq. 4.6.2 for ξ_T^r as a function of the non-dimensional parameter *Rc* (Eq. 4.6.3) and degree of thermal overheating (Eq. 4.6.4). When *Rc* is larger than 1, then the reaction proceeds according to the temperature conditions. However, if *Rc* is much larger than 1, then the overpressure generated due to the reaction will work to inhibit the movement of the reaction front, and hence closing the reaction. The black lines (1,2 and 3) represent theoretical scenarios for reactions with different Clapeyron-slopes, i.e. the curves 1,2 and 3 from Figure 4.9. Steep slopes (curve 1) have limited influence of the generated overpressure and are thermally controlled, while reactions with gentle slopes (curve 3) will be strongly influenced by the reaction induced overpressure, and will require more heating for the reaction to proceed. We have fixed the contact temperature to $T_c - T_{hr} = 680$ °C as an intermediate choice, and changes in this value have negligible influence on the diagram.

Clapeyron-slopes (dT/dP) will influence the reaction rate.

In the case of a steep reaction curve, i.e. a small value of dT/dP (curve 1, Figs. 4.9 and 4.10), the change in reaction temperature with increasing pressure is negligible, and the reaction will rate as constrained by the initial reaction temperature only. Larger dT/dP of the dehydration reactions (curve 2, Figs. 4.9 and 4.10) reduces the movement of the reaction front by requiring a higher effective reaction temperature. In the case of gentle Clapeyron-slopes (curve 3, Figs. 4.9 and 4.10), the overpressures created can be large enough to terminate the reaction due to the very high effective reaction temperatures. When this is the case, the reaction can continue if the overpressure is reduced by for example fracturing of the host-rock. This is equivalent of reducing the value of *Rc*, and thus moving downwards in the diagram to the conditions where a more efficient reaction rate is expected.

4.6.3 Feedback mechanism of fluid overpressure

Figure 4.11 illustrates two solutions to overpressure generated at the reaction front as a function of the Clapeyron-slope of the reaction (pressure dependence) and permeability of the host-rock (degree of fluid flow) by using the full equation for the reaction rate Eq. 4.6.1. For illustration purposes we use isochoric pressures P_V of 10^8 Pa (a,c) and 10^9 Pa (b,d). The other parameters are given in the figure caption.

Isochoric pressure conditions are predicted for permeabilities lower than 10^{-17} m^2 for both cases in the thermally controlled regime (i.e. red areas in (Fig. 4.11c,d). A higher permeability requires a more gentle dT/dP-slope to have any effect of pressure. Furthermore, there is a large difference between P_V of 10^8 Pa and 10^9 Pa, where in the latter case the feedback of overpressure on the reaction rate becomes relevant already at slopes about 10^{-6} °C /Pa (i.e. 10^6 Pa/ °C or 10 bar/ °C). Even more gentle slopes of 10^{-5} °C /Pa (1 bar/ °C) have the potential to impede reaction rate, and as a consequence reduce the overpressure by two orders of magnitude.

4.7 Geological examples

4.7.1 Aureole fracturing

Fracturing of host-rocks in contact with magmatic intrusions provide evidence for overpressure on the scale of tensile strength. Figure 4.12 shows fracturing in shales intruded by a 10 meter thick horizontal sheet intrusion in the Karoo Basin, South Africa. There is a clear relation between fracturing and loss of total organic carbon (TOC) and hydrous minerals in the contact aureole (Aarnes *et al.*, in review).

In shales, permeabilities are generally very low, i.e. $<10^{-18}$ m^2 (Brace, 1980). It is therefore likely that the overpressure generated is close to the isochoric overpressure before fracturing occurs (Fig. 4.11). Figure 4.13 illustrates the isochoric pressures calculated as a function of different wt. % of fluid released during metamorphism, $Q_f^{total} = wt.\%/100 \times \rho_{hr}$, and different fluid densities. Due to the simple relationship in Eq. 4.5.8, decreasing the compressibility with one magnitude increases the overpressure with one magnitude.

A fluid pressure greater than ∼30 MPa above the lithostatic pressure is sufficient to cause brittle failure of most host-rocks (Philpotts & Ague, 2009). This implies that at ∼2-3 km depth, the tensile strength of the host-rocks is about 100 MPa. Hence, cracking of >1 wt. % TOC to methane is sufficient to cause fracturing. This is supported by host-rock fracturing close to the contact zones (Fig. 4.12), where the fluid generation is most extensive (Aarnes *et al.*, in review).

4.7.2 Breccia pipe formation and venting

We utilize the exact solution to overpressure at the front (Eq. 4.5.10) to estimate when the generation of methane in the contact aureoles can cause fracturing and venting through breccia pipes (Fig. 4.1). Figure 4.14 shows expected venting conditions as a function of depth and permeability using a tensile strength of 10 MPa above the lithostatic pressure. The case study represent a shale with 5 wt. % TOC or a P_V of 3×10^8 Pa. Lower (1 wt. %) and higher (10 wt%) TOC cases are also indicated. For shales with initially ∼5 wt. % TOC content, venting is expected at permeabilities lower than $\sim 10^{-17}$ m^2 at 2-3 km

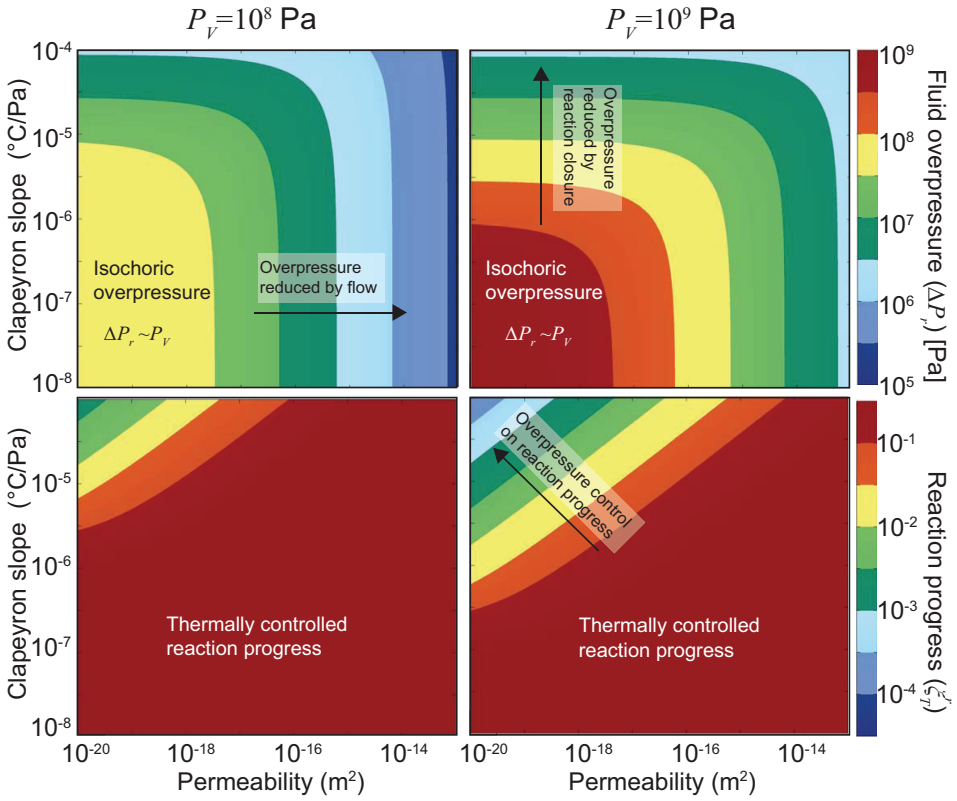

Figure 4.11: Calculated overpressure (a,b) and reaction rate (c,d) as a function of permeability and Clapeyron-slope of the reaction, calculated from Eq. 4.6.1. The fluid overpressure can decrease up to four magnitudes both due to fluid flow out of the reaction front and due to overpressure inhibiting the reaction rate. **(a)** Fluid overpressure calculated with $P_V = 10^8$ Pa. Yellow area shows isochoric conditions. **(b)** Fluid overpressure calculated with $P_V = 10^9$ Pa. Red area shows isochoric conditions. **(c)** Reaction rate calculated with $P_V = 10^8$ Pa. The red area shows where the reaction is temperature controlled. The multi-coloured area indicates where the reaction rate is affected by overpressure. **(d)** Reaction rate calculated with $P_V = 10^9$ Pa. The red area shows where the reaction is temperature controlled. The multi-coloured area indicates where the reaction rate is affected by overpressure. The other parameters in the equation were set to: T_c-T_{hr} = 600 °C ; T_r-T_{hr} = 300 °C ; $\kappa_T = 10^{-6}$ m²/s; $\mu_f \phi \beta_f = 10^{-12}$ Pas/Pa.

depth, corresponding to the paleodepth of the shale formations in the Karoo Basin in the study area (Fig. 4.1a) (Catuneanu *et al.*, 1998). These low permeabilities are consistent with for example unfractured shale or crystallized igneous intrusions (Brace, 1980). For shales with initially ∼10 wt. % TOC, venting is expected at permeabilities lower than $\sim 10^{-16}$ m² at 2-3 km depth. At 1 km the permeability can be as high as $\sim 10^{-15}$ m² and still cause venting in this high TOC-case. However, for shales with initially ∼1 wt. % TOC, permeabilities lower than 10^{-18} m² is required for venting to occur. Note that the diagram in Figure 4.14 assumes certain properties of the system such as reaction temperature, gas compressibility

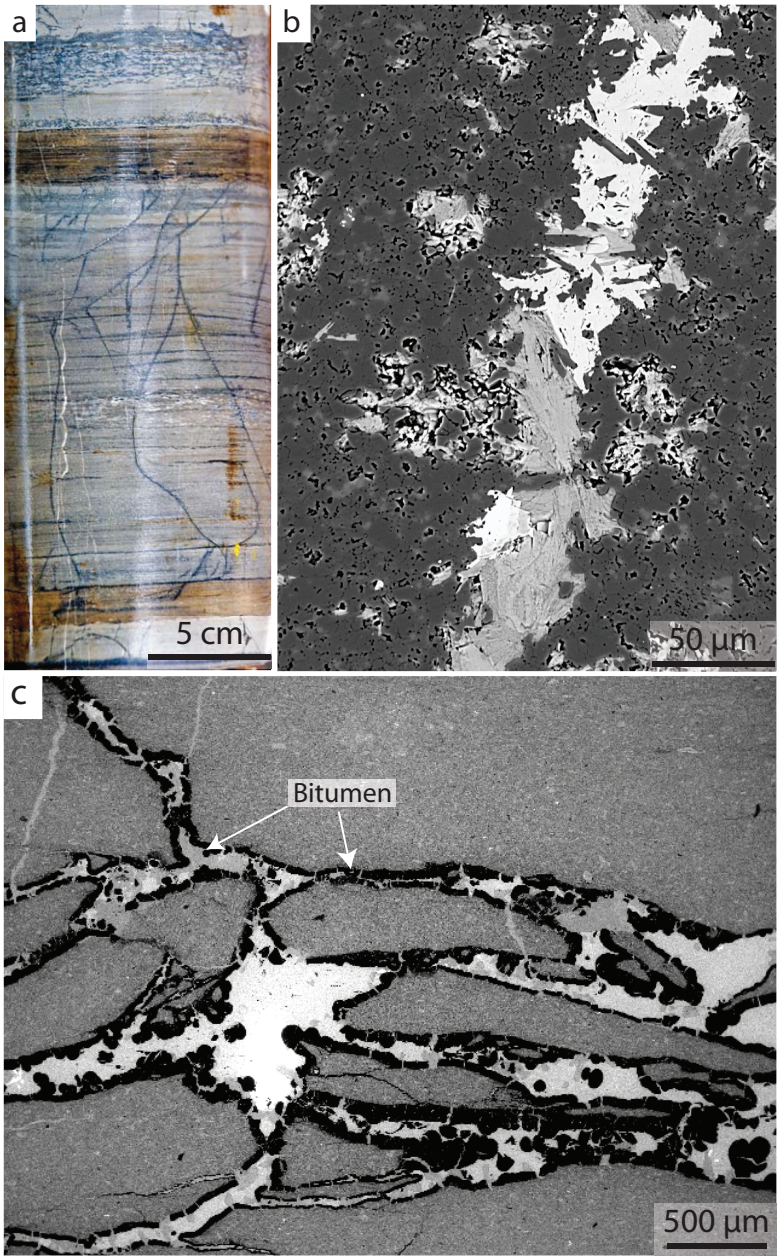

Figure 4.12: Examples of fracturing in shales in the contact aureole around a 10 m thick sheet intrusion in the Karoo Basin. **(a)** Hand specimen of a borehole sample with initial ∼1 wt. % TOC. **(b)** Backscatter Electron (BSE) image of the mineralized veins in (a). **(c)** BSE image of bitumen filled veins in a borehole sample with initial >5 wt. % TOC

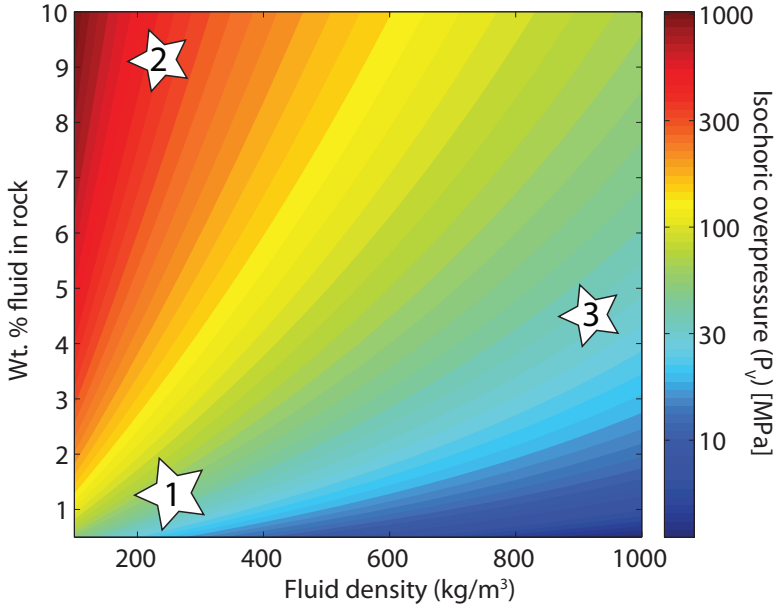

Figure 4.13: Isochoric overpressure (P_V) as a function of fluid density and weight % fluid in the rock before devolatilization occurs (wt. % H_2O or TOC). Using a methane density of 200-300 kg/m^3 ($T = 100 - 350$ °C and $P = 100$ MPa) (Setzmann and Wagner, 1991) we get: **(1)** P_V ∼60-160 MPa in shales with low wt. % TOC and release of methane. **(2)** P_V ∼500-900 MPa in shales with high wt. % TOC upon release of methane. **(3)** P_V ∼50-80 MPa in average shales upon release of a H_2O-fluid with a density of 850-950 kg/m^3 (Wagner and Pruss, 2002). We use $\rho_{hr} = 2400$ kg/m^3 and $\phi\beta_f = 10^{-9}$ Pa^{-1}.

and tensile strength of the rocks given in the caption, and must be interpreted on the basis of these assumptions.

4.8 Discussion

4.8.1 The model

Our model of significant overpressure generation during prograde contact metamorphism is in contrast to other contact metamorphic models assuming no pressure variations, or minor fluid pressure gradients (Baumgartner & Ferry, 1991; Léger & Ferry, 1993). The model is based on basic physical principles with only few assumptions about our system. The coupling of physical and chemical processes is important for the development of models describing complex geological systems (Steefel *et al.*, 2005). The coupled analytical solutions provide a good basis for further development of such models, but can also be used successfully to explain a number of phenomena, among others fracturing and reaction closure. The analytical solutions are validated by numerical modeling, and shows that the equations are indifferent to the choice of method used for treating the source-terms.

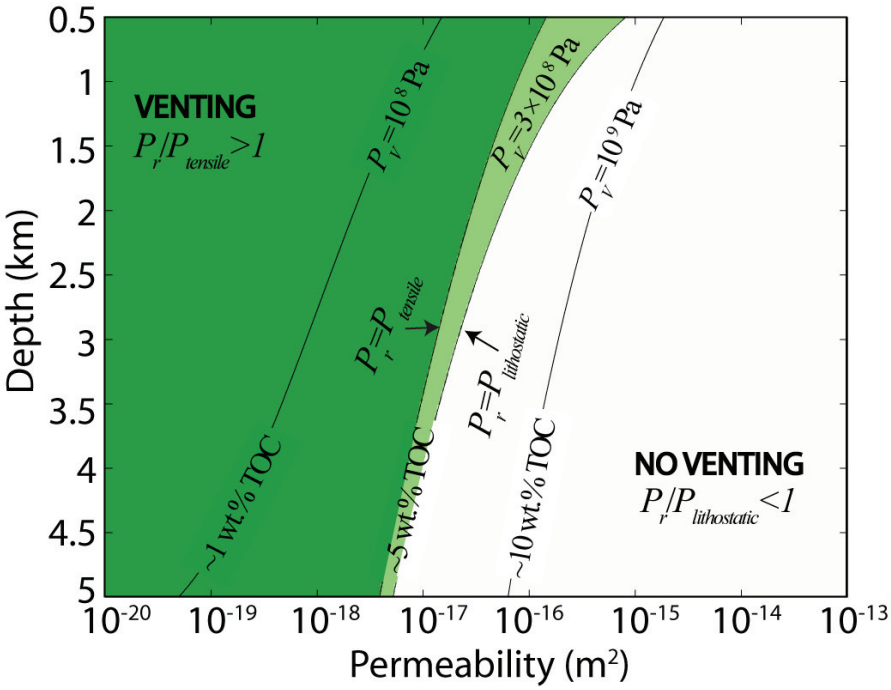

Figure 4.14: Depth of intrusion versus log of permeability based on Eq. 4.5.10. For a $P_V = 3 \times 10^8$ Pa corresponding to 5 wt. % TOC venting will occur when the permeability is lower than about 10^{-17} m^2. In the region to the right, the pressure will be reduced by fluid flow before any venting occurs. We also indicate the tensile strength curves for $P_V = 10^8$ Pa and $P_V = 10^9$ Pa. The other parameters are set to $P_{hydrostatic} = \rho_f gZ$,$P_{lithostatic} = \rho_{hr} gZ$ and $P_{tensile} = \rho_{hr} gZ + 10$ MPa, where $g = 9.81$ m/s^2, host-rock density is a linear function of $\rho_{hr} = 2200 - 2600$ kg/m^3 for Z= 0.5-5 km, $\rho_f = 250$ kg/m^3 for 100 meters (i.e. the generated CH_4) and $\rho_f = 1000$ kg/m^3 (i.e. pore-fluid H_2O) for the rest of the hydrostatic column. The other values are given in the caption of Figure 4.11.

In this paper we focus on the case of low permeability, where the thermal and hydraulic diffusivities are comparable (cf. Appendix 4.C). In the case of a high permeability the fluid flow is more effective than the thermal reaction front, and a steady state hydraulic gradient will develop from the dehydrating reaction front. The analytical solutions to this high-permeability case is presented by Litvinovski *et al.* (1990) who showed that the total fluid pressures ($P_{H_2O} = P_{tot}$) at the dehydrating reaction front reached 200-400 MPa for intrusions at 1-2 km depth.

We did not consider the thermal feed-back of fluid flow, i.e. heat advection, in the solution. Podladchikov & Wickham (1994) present analytical solutions to heat and material transport, including the advective terms. They showed that for systems with less than 10 wt. % released as a free fluid phase, the advection of heat is negligible. This is consistent with the conclusions of Peacock (1987) and Thompson & Connolly (1992) for pervasive fluid flow. However, if fluid is focused into widely spaced channels with extensive fluid flow over a significant period of time, advection of heat may become an

important factor (Peacock, 1989). Thus advection may affect the thermal regime within vent complexes.

The pressure equation (Eq. 4.3.5) can be expanded with several individual source terms, each defining a separate process that affects the pressure, such as compaction (e.g. Connolly, 1997), thermal stresses (e.g. Aarnes *et al.*, 2008), or an array of different reactions involving a net volume change. The value chosen for permeability encompass a porosity dependence on flow properties, where the permeability commonly varies with approximately the cube of porosity (e.g. Zhang *et al.*, 1994; Connolly, 1997). The fluid density is dependent on the thermal expansion (α_f), which can be incorporated by a temperature dependent density $\rho_f = \rho_f^0(1-\alpha_f dT)$.

The effect of gravitational flow due to buoyancy is incorporated through solving for pressures in excess of the background hydrostatic pressures. The long-term influence on flow and overpressure by host-rock compaction (e.g. Walder & Nur, 1984; Connolly, 1997) is negligible due to the relatively brief scale of contact metamorphism (cf. Appendix 4.C). The full pressure equation including porosity changes is derived in the Appendix 4.B (Eq. 4.B.12), and can be used for solving systems where host-rock compaction is an important factor, but this is not treated explicitly here.

In the solution, we have considered that a major fluid-release are occurring at one temperature, for example at 300 °C above the background (Fig. 4.11). In an aureole this reaction temperature isograde comprises a variety of minerals and organic matter that release fluids. A high temperature for the reaction front can incorporate a thermal overstep of the equilibrium conditions of devolatilization and ensure a fast reaction rate (e.g. Lasaga, 1989; Ague *et al.*, 1998). For example the decomposition of organic matter to hydrocarbons initiates is about ∼85 °C (Tissot & Welte, 1984), so for a temperature of 350 °C , the cracking will basically be instantaneous (e.g. Ungerer *et al.*, 1988). Dehydration reactions are usually occurring at larger temperature intervals, and major dehydration is associated with breakdown of among others the hydrous mineral chlorite at about 350 °C to less hydrous phases such as biotite. If only sparse devolatilization reactions occur, it is equivalent of having a smaller initial P_V, due to a smaller Q_f^{total}-source term.

For the reaction closure we have assumed that the dehydration reactions occur at local thermodynamic equilibrium (Fig. 4.9). There is however no conflict between this assumption and the introduction of minor thermal overstepping of the equilibrium condition, which is assumed to be the case for most dehydration reactions (Walther & Wood, 1984).

4.8.2 Overpressure reduction by fluid flow

Permeability is the key parameter controlling the efficiency of fluid flow, and has thus a major control on the magnitude of overpressure. It is unfortunately a relatively difficult parameter to constrain for a full geological system, as it can vary several orders of magnitudes (Ingebritsen & Manning, 2002). However, unfractured shales and crystalline rocks are measured to have very low permeabilities about 10^{-21}-10^{-16} m^2 (Brace, 1980; Hanson, 1995), which makes significant overpressure generation in intruded shale-systems likely. Laboratory experiments show that dehydration of gypsum can generate excess pore pressures on the scale of 150 MPa during isochoric conditions (Wang & Wong, 2003). This corresponds well with our estimates (Fig. 4.13).

One main result from our model is that devolatilizing systems with active fluid flow out of the

reaction front can still create significant overpressures, although reduced relative to the isochoric systems (Figs. 4.7 and 4.11). Even for relatively high-permeable devolatilizing systems ($\sim 10^{-15}$ m^2), fluid overpressures of 10 MPa can be expected. This is supported by dehydration experiments with the hydrous mineral gypsum giving pore pressures up to 93 MPa when allowing for flow out of the dehydrating sample (Olgaard *et al.*, 1995; Wong *et al.*, 1997).

Although we predict that these overpressures are generated instantly at the front, the hydraulic conductivity is of major importance for the maintenance of the overpressure (e.g. Bredehoeft & Hanshaw, 1968; Ko *et al.*, 1997). For high permeabilities the pressure buildup will only be transient, and diffuse efficiently away after the devolatilization reaction has seized (e.g. Wong *et al.*, 1997).

4.8.3 Reaction closure by fluid overpressure

A potentially important implication of increased fluid pressure is the feedback on the reaction rate for pressure-dependent reactions (Colten-Bradley, 1987; Osborne & Swarbrick, 1997; Miller *et al.*, 2003; Wang & Wong, 2003). Dehydration of gypsum yields a relevant example of how elevated pore-pressures inhibits the reaction rate until fluid flow relaxes the overpressure (Wang & Wong, 2003).

The dehydration-reaction of the clay mineral smectite to illite and water has a relatively shallow Clapeyron-slope ($\sim 10^{-5}$ °C/Pa), and it has been shown that this reaction can terminate when the pressure increases (Colten-Bradley, 1987). This is consistent with the results in Figure 4.10 and Figure 4.11. Similarly, brucite ($Mg(OH)_2$) to periclase (MgO) and H_2O has a dT/dP of $\sim 10^{-6}$ °C /Pa (Barnes & Ernst, 1963), which for an overpressure of 10^8 Pa is equivalent of a 100 °C increase in the effective reaction temperature. Also the decarbonation reaction of calcite + quartz to produce wollastonite and CO_2 can have a dT/dP of $\sim 4 \times 10^{-6}$ °C /Pa, depending on the CO_2 content in the fluid (Philpotts & Ague, 2009). The effect of pressure on organic cracking is minor, although there is a tendency that above a certain pressure ($\sim$60 MPa), the gas yield from cracking decreases with increasing pressure (Hill *et al.*, 1996).

Most devolatilization-reactions are mainly temperature-dependent with typical Clapeyron-slopes of $\sim 10^{-7}$ °C /Pa, at least at pressures above $\sim$50 MPa as calculated from thermodynamic phase equilibria (Connolly, 2005, 2009). The influence of pressure on the effective reaction temperature is thus on the order of 10-100 °C for P_V of 10^8-10^9 Pa. From the two solutions in Figure 4.11 we see that the effect of pressure has limited influence on the rate of most dehydration reactions, unless the tensile strength of the rocks is high and the system permeability is lower than $\sim 10^{-17}$ m^2. We can speculate that such conditions could occur at great depths ($\sim$30-40 km) and thus be relevant for the limited dehydration reactions at lithostatic pressures of 800-1000 MPa, as suggested for the Southern Alps, New Zealand (Vry *et al.*, 2010). In any case the study by Vry *et al.* (2010) reveals the importance of considering the pressure for dehydration reactions occurring below 500 °C, i.e. at contact metamorphic temperatures.

There are some cases of negative dT/dP where the reaction temperature decreases with increasing pressure at higher pressures. Examples of such reactions are dehydration of kaolinite at thermodynamic pressures above 10^9 Pa (1 GPa) and 350 °C (Chatterjee *et al.*, 1984), and biotite + quartz + cordierite which react to garnet + K-feldspar + H_2O (Thompson, 1976). This is because the fluids at such pressures are so compressible that they occupy less space as a fluid phase than in the mineral phase, i.e. a total

negative volume change of the reaction, and would result in an underpressure (e.g. Delany & Helgeson, 1978). In the case of lowering the pressure on a negative Clapeyron slope, it would also require a shift towards higher temperatures in the $P-T$ diagram.

4.8.4 Fracturing and venting

The maximum overpressure that can be generated in a host-rock also depends on the tensile strength of the rock. Hydraulic fracturing will therefore put an upper bound to the amount of overpressure generated (e.g. Walther & Orville, 1982; Nishiyama, 1989; Guéguen & Palciauskas, 1994). Fracturing of the host-rock when the overpressure exceeds the tensile strength of the rock is equivalent of increasing the effective permeability of the rock, depending on the extent of fracturation. An increased permeability will in turn act to reduce the maximum overpressure at the front by increased flow, as can be seen from the Figures 4.7 and 4.11. If the permeability varies spatially in the system it is important to include it in the derivative of Eq. 4.3.5.

Higher overpressures can by definition be sustained where the difference between the hydrostatic pressure and the tensile strength can reach several hundred MPa. This can be seen from the slopes of the tensile strength curves in Figure 4.14. In general, shales have low permeabilities and are therefore subject to fracturing. This is consistent with the fractured aureoles found in the Karoo Basin, South Africa (Fig. 4.12). It is likely to assume that venting occurs in shale formations intruded by thick, horizontal intrusions ($>$100 m), where the reaction front can sweep over a larger volume of sediments than for example around a 10 meter thick intrusion. Although the tensile strength can be reached in the aureoles of thinner intrusions ($\sim$10 meters) the affected volume will most likely not be enough for the fracturing to localize into breccia pipes.

The interaction of several sills can be important for vent formation. In a volcanic basin like the Karoo, multiple levels of magmatic intrusions into sedimentary rocks are common (e.g. Marsh *et al.*, 1997; Chevallier & Woodford, 1999; Galerne *et al.*, 2008; Polteau *et al.*, 2008). Two 100 meter thick intrusions enveloping a $\sim$100 meter thick shale-formation will ensure large-scale fluid generation throughout the formation due to heating from both above and below (Aarnes *et al.*, in review). Furhtermore, the upper intrusion can act as a low-permeable seal, thus increasing the chance of venting and breccia pipe formation (Fig. 4.14). This is consistent with the occurrence of several thousand breccia pipes originating in shale formations intruded by multiple sills in the Karoo Basin (Fig. 4.1).

4.9 Conclusions

In this study we provide analytical and numerical solutions to reactive transport involving temperature, pressure, fluid flow and devolatilization reactions. The main conclusions about devolatilization induced overpressure and the implications for reaction rate and aureole fracturing are summarized:

- The overpressure is determined by the ratio of thermal and hydraulic diffusion and the rate of the reaction front.

- In the limit when the fluid flow is stagnant relative to the rate of the front, the maximum

overpressure is dictated by the amount of fluids liberated, the net volume change of the reaction, porosity and the effective fluid compressibility.

- When fluid flow is more efficient than the reaction front, the isochoric overpressure can be reduced by several orders of magnitude, depending on the effective permeability.
- The rate of the reaction front is controlled by the temperature at which the reaction occurs. A reaction temperature close to the host-rock temperature requires less overheating of the sediments for the reaction to rate, and the reaction front is efficiently moving through the aureole.
- In the case of pressure dependent reactions, the generated overpressure will shift the equilibrium conditions towards higher pressures and temperatures. The effectively higher reaction temperatures will slow down the reaction, and may even terminate it completely.
- The analytical solutions to overpressure constrain the conditions for fracturing and breccia-pipe formation from fluid generation in contact aureoles. Low permeabilities ($<10^{-17}$ m^2) and high content of organic material in the sediments (>5 wt%) are favourable conditions for aureole fracturing and venting.

To conclude, this model provides a theoretical basis for several geological processes related to prograde metamorphism, and the analytical solutions can be used for verification and further development of reactive transport models.

Acknowledgement

This study was supported by Grant 169457/S30 from the Norwegian Research Council. We would like to thank Magnus B. Løberg and Viktoriya M. Yarushina for important discussions and help to improve the manuscript. Acknowledgements go to all the participants in the Wednesday Club for year-long discussions on the matter.

Appendix 4.A Derivation of fluxes and sources

4.A.1 Local equilibrium thermodynamics

The main goal of the following appendices is to derive a closed system of thermodynamically consistent equations using balance of mass, energy and momentum. The starting point for the derivations is a combination of the 1^{st} and 2^{nd} laws of thermodynamics,

$$du = Tds - Pd(1/\rho) \tag{4.A.1}$$

where u is specific internal energy, s is specific entropy, $1/\rho$ is specific volume and ρ is density. The term 'specific' refers to the standard extensive thermodynamic variables normalized by mass of the system, i.e. volume, entropy and internal energy per unit mass. The advantage of this division is that all variables used in the following derivations are intensive quantities.

Eq. 4.A.1 is valid for spatially homogeneous systems evolving sufficiently slow to allow the quasi-static approximation. However, in a geological system such as around a magmatic intrusion there are large spatial gradients in for example temperature and pressure, and the system as a whole is out of equilibrium. Following the recipe of classical non-equilibrium thermodynamics, we avoid this problem by assuming that every infinitesimal part of the system can be approximated as being in local thermodynamic equilibrium (e.g. Lichtner, 1988; Steefel and Lasaga, 1994; Ferry and Gerdes, 1998; Xu and Pruess, 2001). We can write Eq. 4.A.1 in a weaker form consistent with this assumption, which states that for non-equilibrium processes we can divide our system into infinitesimal parts changing with time in agreement with equilibrium thermodynamics (Eq. 4.A.1),

$$\frac{du}{dt} = T\frac{ds}{dt} + \frac{P}{\rho^2}\frac{d\rho}{dt} \tag{4.A.2}$$

where $\frac{d}{dt}$ is the full material time derivative to keep track of the spatial movement of the infinitesimal parts of our system. The second law of thermodynamics states that the change in entropy of isolated systems is zero for equilibrium processes and positive for irreversible processes, $ds \geq 0$. The following sections are based on a simple recipe where the main goal is to make sure that we obey this second law.

4.A.2 The balance laws

Getting an expression for entropy production

The general form of a balance law for any quantity M can be written

$$\frac{\partial}{\partial t}(M\rho\phi) + \frac{\partial}{\partial z}(M\rho\phi v) = -\frac{\partial}{\partial z}q_M + Q_M \tag{4.A.3}$$

where ϕ is the volume fraction of a phase (e.g. porosity) and v is velocity (e.g. de Groot and Mazur, 1984). This quantity M changes with the difference of fluxes in and out from neighboring regions, q_M, and the rate of production or elimination of the quantity M in a unit volume, Q_M. In our system, M is substituted by entropy, energy, mass and momentum. We recover the mass balance equation if we substitute $M = 1$ into Eq. 4.A.3,

$$\frac{\partial}{\partial t}(\rho\phi) + \frac{\partial}{\partial z}(\rho\phi v) = Q_\rho \tag{4.A.4}$$

where Q_ρ is the rate of mass production (kg/m^3/s) due to phase transitions. We choose our system velocities to be from the center of mass, implying that there will be no mass flux of fluid within the fluid mass, and solid flux within the solid mass, i.e. $\frac{\partial}{\partial z}q_\rho = 0$. The balance law on the form of Eq. 4.A.3 requires several repetitions of the product rule to single out an expression for the change of M with time. For convenient substitution of the balance laws into the thermodynamic equation (Eq. 4.A.2) we utilize a mathematically equivalent (for sufficiently smooth functions) form of the balance law (Eq. 4.A.3) that can be obtained using the mass balance equation Eq. 4.A.4 and the product rule of differentiation,

$$\frac{dM}{dt} = -\frac{1}{\rho\phi}\left(\frac{\partial}{\partial z}q_M - Q_M + MQ_\rho\right). \tag{4.A.5}$$

To get the entropy balance, we simply insert $M = s$ into Eq. 4.A.5,

$$\frac{ds}{dt} = -\frac{1}{\rho\phi}\left(\frac{\partial}{\partial z}q_S - Q_S + sQ_\rho\right). \tag{4.A.6}$$

The change in entropy ds can be attributed to both a spatial difference in the flux q_S and a local source Q_S. When the second law of thermodynamics demand ds of the isolated system to be non-negative it is equivalent of requiring non-negativity of the entropy source Q_S. We use Eq. 4.A.2 to substitute for ds/dt in Eq. 4.A.6, using the assumption of local equilibrium. Solving for Q_S gives

$$Q_S = \frac{\rho\phi}{T}\frac{du}{dt} - \frac{\phi P}{T\rho}\frac{d\rho}{dt} + \frac{\partial q_S}{\partial z} + sQ_\rho. \tag{4.A.7}$$

The following sections will have the governing aim of ensuring non-negativity of this expression.

Elimination of time derivatives

The time derivatives of internal energy (u) and mass (ρ) make it difficult to ensure the non-negativity of entropy production, because the time derivative of a variable can be both positive and negative, e.g. density can increase and decrease with time. This problem is avoided by substitution of the time derivatives by balance laws for mass, total energy (kinetic and internal) and specific momentum (v). The momentum balance is required for further elimination of specific kinetic energy $\left(v^2/2\right)$ from the energy balance.

Substitution for M into Eq. 4.A.5 gives the balance equations for total energy (E) and momentum (v):

$$\frac{du}{dt} = -\frac{1}{\rho\phi}\left(\frac{\partial}{\partial z}q_E - Q_E + \left(u + \frac{v^2}{2}\right)Q_\rho\right) - v\frac{dv}{dt} \tag{4.A.8}$$

$$\frac{dv}{dt} = -\frac{1}{\rho\phi}\left(\frac{\partial}{\partial z}q_v - Q_v + vQ_\rho\right). \tag{4.A.9}$$

The mass balance is already implicit in Eq. 4.A.5 which makes that expression unsuitable to find an equation for $d\rho/dt$. We instead continue to apply the product rule on Eq. 4.A.4 to single out ρ,

$$\frac{d\rho}{dt} = \frac{1}{\phi}\left(Q_\rho - \rho\frac{d\phi}{dt} - \rho\phi\frac{\partial v}{\partial z}\right). \tag{4.A.10}$$

Substitution of all the balance laws (Eqs. 4.A.8 - 4.A.10) into Eq. 4.A.7, for the corresponding material derivatives gives after some rearrangement

$$Q_S = \frac{1}{T}\left(-\frac{\partial q_E}{\partial z} + v\frac{\partial q_v}{\partial z} + \frac{\partial q_S}{\partial z} + \phi P\frac{\partial v}{\partial z} + P\frac{d\phi}{dt} + Q_E - vQ_v + \left(-u + \frac{v^2}{2} - \frac{P}{\rho} + Ts\right)Q_\rho\right). \tag{4.A.11}$$

Elimination of spatial derivatives

By analogy with the time derivatives, it is difficult to define the fluxes (q) that guarantee non-negativity of their spatial derivatives and $Q_S \geq 0$. This problem can be avoided by applying the product rule 'backwards',

$$v\frac{\partial q_v}{\partial z} = \frac{\partial q_v v}{\partial z} - q_v\frac{\partial v}{\partial z} \tag{4.A.12}$$

$$T\frac{\partial q_s}{\partial z} = \frac{\partial q_s T}{\partial z} - q_s\frac{\partial T}{\partial z} \tag{4.A.13}$$

where we made the first step to remove the derivatives from the fluxes. Substitution of Eqs. 4.A.12 and 4.A.13 into Eq. 4.A.11 and rearranging gives,

$$\begin{aligned} Q_S = \frac{1}{T}\frac{\partial}{\partial z}\left(-q_E + vq_v + Tq_s\right) - \frac{q_s}{T}\frac{\partial T}{\partial z} + \left(\phi P - q_v\right)\frac{1}{T}\frac{\partial v}{\partial z} \\ + \frac{P}{T}\left(\frac{\partial \phi}{\partial t} + v\frac{\partial \phi}{\partial z}\right) + \frac{Q_E}{T} - \frac{vQ_v}{T} + \left(-\frac{P}{\rho} + Ts - u + \frac{v^2}{2}\right)\frac{Q_\rho}{T}. \end{aligned} \tag{4.A.14}$$

From this expression for the entropy production we can find thermodynamically admissible fluxes and sources.

4.A.3 Processes within one phase

Fluxes represent changes of a quantity in a volume through its surface and are related to changes within one phase. Because the equations are identical for fluid and solid we treat the following equations without specifying the phase. When we determine the fluxes, we want to choose them in such way that they conveniently assure non-negativity of Q_S. This can most simply be accomplished by making the expression associated with a flux to be always square (i.e. always positive) irreversible processes or by eliminating it from the entropy source equation Eq. 4.A.14 (i.e. zero) for reversible processes.

We start by evaluating the expression associated with the entropy flux q_s in Eq. 4.A.14, $-\frac{q_s}{T}\frac{\partial T}{\partial z} \geq 0$, where a simple solution for this term is to make it square by choosing

$$q_s = -\frac{\lambda}{T}\frac{\partial T}{\partial z}, \tag{4.A.15}$$

where λ is a positive proportionality constant with the physical meaning of thermal conductivity (J/s/K/m). It is divided by temperature (K) to make the correct dimensions of q_s (J/K/m^2). The positive contribution to Q_S is consistent with heat transfer being an irreversible process.

Similarly, we evaluate the term associated with momentum flux q_v in Eq. 4.A.14, $\frac{1}{T}\left(\phi P - q_v\right)\frac{\partial v}{\partial z} \geq 0$. An easy way to make the whole term zero is to choose

$$q_v = \phi P \tag{4.A.16}$$

. This expression implies no entropy production due to the momentum flux, i.e. a choice of an elastic rheology by definition.

The expression related to q_E is inside a derivative, which makes a choice for the flux inconvenient.

However, by evaluating the expression $\frac{1}{T}\frac{\partial}{\partial z}\left(-q_E + v q_v + T q_s\right) \geq 0$, we see that we can avoid the problem of potential non-negative entropy source by choosing

$$q_E = v q_v + T q_s \tag{4.A.17}$$

which sets the whole expression to zero and gives no contribution of energy flux to the entropy production.

Substitution of these fluxes (Eqs. 4.A.15 - 4.A.17) into Eq. 4.A.14 gives

$$Q_S = \frac{\lambda}{T^2}\left(\frac{\partial T}{\partial z}\right)^2 + \left(\frac{P}{T}\left(\frac{\partial \phi}{\partial t} + v\frac{\partial \phi}{\partial z}\right) + \frac{Q_E}{T} - \frac{v Q_v}{T} + \left(-\frac{P}{\rho} + Ts - u + \frac{v^2}{2}\right)\frac{Q_\rho}{T}\right), \tag{4.A.18}$$

where the terms with no contribution to the entropy source are removed from the equation, and the terms contributing to the entropy production are always positive.

4.A.4 Interaction between two phases

Total entropy production

So far we have been evaluating processes related to within a phase only, and it was sufficient to require that Q_S for that phase should be always positive for those terms. However, the sources (Q) contribute to entropy production arising from the interaction between phases, for example fluid ('f') and solid ('s') in our system. Any exchange process between two phases must be associated with the total entropy production that is either positive or zero $Q_S^{total} \geq 0$. In order to find the total entropy exchange we specify the entropy production equation (Eq. 4.A.18) for fluid and solid, and then sum up.

Furthermore we ensure that our system of fluid and solid as a whole does satisfy fundamental laws of nature:

$$Q_{E,s} = -Q_{E,f} \quad \text{-} \quad \text{Conservation of energy} \tag{4.A.19a}$$

$$Q_{v,s} = -Q_{v,f} \quad \text{-} \quad \text{Conservation of momentum} \tag{4.A.19b}$$

$$Q_{\rho,s} = -Q_{\rho,f} \quad \text{-} \quad \text{Conservation of mass} \tag{4.A.19c}$$

For fluid and solid Eq. 4.A.18 becomes:

$$Q_{S,f} = \frac{\lambda_f}{T_f^2}\left(\frac{\partial T_f}{\partial z}\right)^2 + \frac{P_f}{T_f}\frac{d_f \phi_f}{dt} + \frac{Q_{E,f}}{T_f} - \frac{v_f Q_{v,f}}{T_f} + \left(-\frac{P_f}{\rho_f} + T_f s_f - u_f + \frac{{v_f}^2}{2}\right)\frac{Q_{\rho,f}}{T_f} \tag{4.A.20a}$$

$$Q_{S,s} = \frac{\lambda_s}{T_s^2}\left(\frac{\partial T_s}{\partial z}\right)^2 + \frac{P_s}{T_s}\frac{d_s \phi_s}{dt} + \frac{Q_{E,s}}{T_s} - \frac{v_s Q_{v,s}}{T_s} + \left(-\frac{P_s}{\rho_s} + T_s s_s - u_s + \frac{{v_s}^2}{2}\right)\frac{Q_{\rho,s}}{T_s} \tag{4.A.20b}$$

where the material derivatives for fluid and solid are

$$\frac{d_f}{dt} = \frac{\partial}{\partial t} + v_f\frac{\partial}{\partial z} \quad \text{and} \quad \frac{d_s}{dt} = \frac{\partial}{\partial t} + v_s\frac{\partial}{\partial z}.$$

For a two phase media $\phi_f = \phi$; $\phi_s = 1 - \phi$ and $\frac{d_s \phi_s}{dt} = -\frac{d_s \phi}{dt}$.

Reversible equilibrium processes

We first consider equilibrium, reversible processes, where the total entropy production becomes zero. In other words, because we assume local equilibrium between the fluid and the solid, we can set up two conditions that come as a natural consequence:

$$T_s = T_f \quad - \quad \text{Thermal equilibrium} \tag{4.A.21a}$$

$$g_s = g_f \quad - \quad \text{Phase equilibrium} \tag{4.A.21b}$$

where g is specific Gibbs energy.

The terms in front of the source of mass can be equated to the specific Gibbs free energy between the solid and the fluid phases,

$$\Delta g = \left(\frac{P_s}{\rho_s} - \frac{P_f}{\rho_f}\right) - T\left(s_s - s_f\right) + \left(u_s - u_f\right) + \frac{\Delta v^2}{2}.$$

According to Eq. 4.A.21b, $\Delta g = 0$ at equilibrium. Similarly, conservation of energy (Eq. 4.A.19a) requires that there are no entropy production at equilibrium, and the energy source of fluid and solid cancels.

Applying the relations in Eqs. 4.A.21-4.A.19 and summing up Eqs. 4.A.20a and 4.A.20b gives,

$$Q_S^{total} = \left(\frac{\lambda_f + \lambda_s}{T^2}\right)\left(\frac{\partial T}{\partial z}\right)^2 + \frac{\left(P_f - P_s\right)}{T}\frac{d_s\phi}{dt} + \frac{\Delta v}{T}\left(P_f\frac{\partial \phi}{\partial z} - Q_{v,f}\right) \tag{4.A.22}$$

where Q_S^{total} is the total entropy production.

Irreversible non-equilibrium processes

As a minimum requirement to generate fluid flow, we consider momentum exchange between the fluid and solid as a non-equilibrium process. By evaluating the expression related to the momentum source, $\frac{\Delta v}{T}\left(P_f\frac{\partial \phi}{\partial z} - Q_{v,f}\right) \geq 0$, we find that a first obvious choice of momentum source is $Q_{v,f} = P_f \partial\phi/\partial z$, which ensures a zero contribution of momentum to the entropy production. However, relative motion between solid and fluid can contribute to entropy production or loss of energy. Therefore we capture more processes by choosing the momentum source as

$$Q_{v,f} = P_f\frac{\partial \phi}{\partial z} - \theta T \Delta v \tag{4.A.23}$$

where θ is a positive constant of proportionality, with the physical meaning of $\theta = \phi^2\mu_f/k$ for Darcian flow, where μ_f/k is the fluid viscosity divided by permeability.

The last term remaining is the one related to total change in porosity. By evaluating the term associated with porosity $\frac{\left(P_f - P_s\right)}{T}\frac{d_s\phi}{dt} \geq 0$, we can get thermodynamically applicable porosity evolution,

$$\frac{d_s\phi}{dt} = \frac{1}{\eta}\left(P_f - P_s\right) \tag{4.A.24}$$

where η is a positive constant representing the resistance to compaction, or bulk viscosity. By substitution of these equations (Eqs. 4.A.23 and 4.A.24) into Eq. 4.A.22, the final expression for entropy production becomes:

$$Q_S^{total} = \left(\frac{\lambda_f + \lambda_s}{T^2}\right)\left(\frac{\partial T}{\partial z}\right)^2 + \frac{1}{\eta T}(P_f - P_s)^2 + \frac{\mu_f}{kT}(\phi \Delta v)^2 \tag{4.A.25}$$

where we have successfully satisfied our goal of non-negative entropy production.

Appendix 4.B Derivation of the system of equations

4.B.1 The temperature equation

For the derivation of the thermal equation we use the entropy balance (Eq. 4.A.6) for solid and fluid, and sum them up:

$$\rho_f \phi \frac{d_f s_f}{dt} + \rho_s (1-\phi)\frac{d_s s_s}{dt} = -\frac{\partial}{\partial z} q_{S,f} - \frac{\partial}{\partial z} q_{S,s} + Q_S^{total} + (s_s - s_f)\, Q_{\rho,f}. \tag{4.B.1}$$

Specific heat capacity is defined as the amount of heat released over a temperature interval, $Cp = \Delta Q / \Delta T = T ds/dT$. Hence we can write the material time derivative of entropy as

$$\frac{ds}{dt} = \frac{ds}{dT}\frac{dT}{dt} = \frac{Cp}{T}\frac{dT}{dt}. \tag{4.B.2}$$

We eliminate the fluid velocity from the equation by using

$$v_f = (v_f - v_s) + v_s = \Delta v + v_s. \tag{4.B.3}$$

The equation for entropy flux is derived in Appendix 4.A (Eq. 4.A.15),

$$\frac{\partial}{\partial z} q_s = -\frac{\partial}{\partial z}\left(\frac{\lambda}{T}\frac{\partial T}{\partial z}\right) = \frac{\lambda}{T^2}\left(\frac{\partial T}{\partial z}\right)^2 - \frac{\lambda}{T}\frac{\partial^2 T}{\partial z^2}. \tag{4.B.4}$$

Substitution of Eqs. 4.B.2 - 4.B.4 into Eq. 4.B.1 and rearranging gives:

$$(\rho_f \phi C p_f + \rho_s (1-\phi) C p_s)\left(\frac{\partial T}{\partial t} + v_s \frac{\partial T}{\partial z}\right) + \rho_f \phi C p_f \Delta v \frac{\partial T}{\partial z} = (\lambda_f + \lambda_s)\frac{\partial^2 T}{\partial z^2} + T\,(s_s - s_f)\, Q_{\rho,f} + \frac{1}{\eta}(P_f - P_s)^2 + \frac{\mu_f}{k}(\phi \Delta v)^2. \tag{4.B.5}$$

The difference in solid and fluid entropy in front of the source of mass, $(T s_s - T s_f)\, Q_{\rho,f}$, can be equated to specific enthalpy h in the unit J/kg,

$$T_f s_f - T_s s_s = \left(u_f + P_f \frac{1}{\rho_f}\right) - \left(u_s + P_s \frac{1}{\rho_s}\right) = h_f - h_s. \tag{4.B.6}$$

Introducing the notations $\rho Cp = (\rho_f \phi Cp_f + \rho_s (1-\phi) Cp_s)$ and $\lambda = (\lambda_s + \lambda_f)$, and substituting the total entropy production Q_S^{total} (Eq. 4.A.25) and the enthalpy (Eq. 4.B.6) gives the full thermal equation:

$$\rho Cp \frac{d_s T}{dt} + \rho_f Cp_f \phi \Delta v \frac{\partial T}{\partial z} = \lambda \frac{\partial^2 T}{\partial z^2} + \Delta h Q_{\rho,f} + \frac{1}{\eta}(P_f - P_s)^2 + \frac{\mu_f}{k}(\phi \Delta v)^2. \tag{4.B.7}$$

4.B.2 The fluid equation of motion

The difference in fluid and solid velocities times porosity $\phi\Delta v$ in Eq. 4.B.7 can be related to Darcy's law. We derive the full fluid flow equation from general force balance of fluid (Eq. 4.A.9):

$$\rho_f \phi \left(\frac{\partial}{\partial t} v_f + v_f \frac{\partial}{\partial z} v_f \right) = -\frac{\partial}{\partial z} q_{v,f} + Q_{v,f} - v_f Q_{\rho,f} \tag{4.B.8}$$

where $q_{v,f} = \phi P_f$ (Eq. 4.A.16) and $Q_{v,f} = P_f \frac{\partial \phi}{\partial z} - \frac{\mu_f \phi}{k} \phi \Delta v$ (Eq. 4.A.23) (Appendix 4.A). Applying the product rule, $-\frac{\partial (\phi P_f)}{\partial z} + P_f \frac{\partial \phi}{\partial z} = -\phi \frac{\partial P_f}{\partial z}$ and substituting the momentum flux and source yields

$$\rho_f \phi \frac{d_f v_f}{dt} = -\phi \frac{\partial P_f}{\partial z} - \frac{\mu_f \phi}{k} \phi \Delta v - v_f Q_{\rho,f}, \tag{4.B.9}$$

which is the full equation for porous fluid flow.

4.B.3 The pressure equation

We represent our host-rock by a two-phase medium consisting of fluid and solid, with subscripts f and s respectively. The pressure equation is derived from the mass balance law Eq. 4.A.4 specified for fluid and solid (Eq. 4.A.4). Applying the product rule to these equation yields

$$\phi \frac{\partial \rho_f}{\partial t} + \rho_f \frac{\partial \phi}{\partial t} + \phi v_f \frac{\partial \rho_f}{\partial z} + \rho_f v_f \frac{\partial \phi}{\partial z} + \rho_f \phi \frac{\partial v_f}{\partial z} = Q_{\rho,f} \tag{4.B.10}$$

$$(1-\phi) \frac{\partial \rho_s}{\partial t} - \rho_s \frac{\partial \phi}{\partial t} + (1-\phi) v_s \frac{\partial \rho_s}{\partial z} - \rho_s v_s \frac{\partial \phi}{\partial z} + \rho_s (1-\phi) \frac{\partial v_s}{\partial z} = Q_{\rho,s} \tag{4.B.11}$$

where we from conservation of mass we have that $Q_{\rho,s} = -Q_{\rho,f}$ (Eq. 4.A.19c). The total mass conservation equation is obtained by summing up the fluid and solid equations. Using Eq. 4.B.3 we eliminate v_f from the divergence of velocity terms. In order to have similar coefficients in front of the divergence terms, the fluid equation is multiplied with $\rho_s(1-\phi)$ and the solid equation with $-\rho_f \phi$. After summation the equation is divided by $\rho_f \phi_f \rho_s \phi_s$ for nicer coefficients, resulting in the following

$$\frac{\phi}{\rho_f} \frac{d_f \rho_f}{dt} - \frac{\phi}{\rho_s} \frac{d_s \rho_s}{dt} + \frac{1}{(1-\phi)} \frac{d_s \phi}{dt} + \frac{\partial \phi \Delta v}{\partial z} = \left(\frac{1}{\rho_f} + \frac{\phi}{\rho_s (1-\phi)} \right) Q_{\rho,f}. \tag{4.B.12}$$

Fluid density can be related to fluid pressure evolution using the definition of isothermal compressibility, (e.g. Turcotte and Schubert, 2002),

$$\beta = \frac{1}{\rho} \frac{d\rho}{dP}, \tag{4.B.13}$$

which after applying the chain rule and rearranging becomes:

$$\frac{1}{\rho_f}\frac{d_f\rho_f}{dt} = \beta_f \frac{d_f P_f}{dt} \tag{4.B.14}$$

By assuming an incompressible solid, we get

$$\frac{1}{\rho_s}\frac{d_s\rho_s}{dt} = 0$$

.

Furthermore, we can substitute the porosity evolution by considering mass balance of the solid (Eq. 4.A.4), i.e.

$$\frac{\partial(\rho_s(1-\phi))}{\partial t} + v_s\frac{\partial(\rho_s(1-\phi))}{\partial z} + \rho_s(1-\phi)\frac{\partial v_s}{\partial z} = -Q_{\rho,f} \tag{4.B.15}$$

which after applying the product rule and rearranging gives,

$$\frac{d_s\phi}{dt} = \frac{1}{\rho_s}Q_{\rho,f} + (1-\phi)\frac{\partial v_s}{\partial z} + \frac{(1-\phi)}{\rho_s}\frac{d_s\rho_s}{dt}. \tag{4.B.16}$$

Substitution of Eq. 4.B.14 and Eq. 4.B.16 into Eq. 4.B.12 gives,

$$\phi\beta_f\frac{d_f P_f}{dt} = -\frac{\partial\phi\Delta v}{\partial z} + \left(\frac{1}{\rho_f} - \frac{1}{\rho_s}\right)Q_{\rho,f} - \frac{\partial v_s}{\partial z} \tag{4.B.17}$$

where $1/\rho_f - 1/\rho_s$ is the net volume change of the reaction.

Appendix 4.C Dimensional analysis of the system equations

From the derivation of the equations of temperature, fluid flow and pressure we discover that there are several terms that in the best cases are remotely familiar to the standard equations usually solved in geological systems. One good method to evaluate the relative importance of these terms is to non-dimensionalize the equations and perform order of magnitude estimates.

We introduce a set of characteristic scales: z_C for length, t_C for time, T_C for temperature and P_C for pressure and replace all variables by its dimensionless analogue denoted by '$\sim$': $z = \tilde{z}\times z_C$; $t = \tilde{t}\times t_C$; $T = \tilde{T}\times T_C$; $P = \tilde{P}\times P_C$. The non-dimensional parameters will have the scale of one, thus all coefficients that are much smaller than 1 will have negligible influence, and can be removed from the equation. This can simplify the equations significantly.

4.C.1 Temperature

Substitution of the dimensional parameters in the temperature equation (Eq. 4.B.7) with the non-dimensional expressions and rearranging, gives the following expression:

$$\left(\frac{\partial \tilde{T}}{\partial \tilde{t}} + \frac{P_C t_C}{\eta}\tilde{v}_s \frac{\partial \tilde{T}}{\partial \tilde{z}}\right) + \frac{\rho_f C p_f}{\rho C p}\frac{\kappa_H}{\kappa_T}\phi\beta_f P_C \phi \Delta\tilde{v}\frac{\partial \tilde{T}}{\partial \tilde{z}} = \frac{\partial^2 \tilde{T}}{\partial \tilde{z}^2} + \frac{\Delta h}{\rho C p}Q_{\rho,f} + \frac{{P_C}^2 t_C}{\eta \rho C p T_C}\left(\tilde{P}_f - \tilde{P}_s\right)^2 + \frac{\kappa_H \phi\beta_f {P_C}^2 \phi^2}{\kappa_T \rho C p T_C}(\Delta\tilde{v})^2 \quad (4.C.1)$$

We choose characteristic values compatible with a contact metamorphic setting: $T_C = T_m - T_{hr} \sim 500$ °C ; $t_C \sim 10^9$ s (∼100 years) which is approximate crystallization time for a 100 meter thick intrusion; $z_C = \sqrt{\kappa_T t_C}$, which is the thermal diffusion length. Using $\kappa_T \sim 10^{-6}$ m^2/s we get a critical length scale of $z_C \sim 30$ m. We consider a low permeability case, as justified from permeabilities of unfractured shales $k \sim 10^{-18}$ m^2 (Brace, 1980). In this case, the critical pressure scale will be high. In the opposite case, with higher permeabilities, the characteristic pressure scale would have been correspondingly lower. Hence we choose, $P_C = P_V \sim 10^8$ Pa (isochoric pressure). For the characteristic fluid velocity we use the scale of Darcy law, $v_C^f = kP_C/\mu_f z_C$. For the characteristic solid velocity we use the compaction scale, $v_C^s = \frac{P_C z_C}{\eta}$. The value of the different material properties are chosen as $\mu_f \sim 10^{-4}$ Pas, $\eta \sim 10^{20}$ Pas, $\rho Cp \sim 10^6$ J/K/m^3, $\rho_f \sim 10^2$ kg/m^3, $\rho_s \sim 10^3$kg/m^3, $\phi\beta_f \tilde{} 10^{-9}$ 1/Pa, $\phi \sim 10^{-2}$ and $\kappa_H \sim 10^{-5}$ m^2/s.

Applying all of these order of magnitude estimates to the parameters in Eq. 4.C.1 using the low permeability case, we get the following relations,

$$\frac{P_C t_C}{\eta} \sim 10^{-3},\ \frac{\rho_f C p_f}{\rho C p}\frac{\kappa_H}{\kappa_T}\phi\beta_f P_C \phi \sim 10^{-3},\ \frac{{P_C}^2 t_C}{\eta \rho C p T_C} \sim 10^{-4} \text{ and } \frac{\kappa_H \phi\beta_f {P_C}^2 \phi^2}{\kappa_T \rho C p T_C} \sim 10^{-5},$$

which are all very small relative to 1. For the latent heat effects we get

$$\frac{\Delta h}{\rho C p}Q_{\rho,f} \sim 1$$

for $\Delta h Q_{\rho,f} \sim 10^6$ J/m^3/s, which is considerable. The equation for temperature (Eq. 4.C.1) thus reduces to,

$$\frac{\partial \tilde{T}}{\partial \tilde{t}} = \frac{\partial^2 \tilde{T}}{\partial \tilde{z}^2} + \frac{t_C}{\rho C p T_C}\Delta h Q_{\rho,f} \quad (4.C.2)$$

with the first order terms contributing to temperature changes being conduction and latent heat of crystallization. Substituted back into the dimensional form the temperature equation becomes

$$\frac{\partial T}{\partial t} = \kappa_T \frac{\partial^2 T}{\partial x^2} + \frac{\Delta h}{\rho C p}Q_{\rho,f} \quad (4.C.3)$$

In our model we treat latent heat of crystallization $\left(\frac{\Delta h}{\rho C p}Q_{\rho,f}\right)$ not as a source term, but rather by effective heat capacity (numerically) and conservation of energy (analytically). The form of the temperature

equation used in the to get these solutions thus becomes,

$$\frac{\partial T}{\partial t} = \kappa_T \frac{\partial^2 T}{\partial x^2}. \tag{4.C.4}$$

4.C.2 Fluid flow

Using the characteristic scales found from the temperature equation gives the following result for the fluid flow equation (Eq. 4.B.9):

$$\phi \Delta \tilde{v} = -\frac{\partial \tilde{P}}{\partial \tilde{z}} - \frac{\kappa_H \phi \beta_f Q_{\rho,f}}{\phi} \tilde{v}_f - \frac{\rho_f \kappa_H \phi \beta_f}{t_C} \frac{\partial \tilde{v}_f}{\partial \tilde{t}} - \frac{\rho_f P_C (\kappa_H \phi \beta_f)^2}{\kappa_T t_C} \tilde{v}_f \frac{\partial \tilde{v}_f}{\partial \tilde{z}}. \tag{4.C.5}$$

Evaluating the coefficient-groups for the same values as for temperature for the low permeability case gives:

$$\frac{\rho_f \kappa_H \phi \beta_f}{t_C} \sim 10^{-21} \text{ and } \frac{\rho_f P_C (\kappa_H \phi \beta_f)^2}{\kappa_T t_C} \sim 10^{-21}.$$

With a fluid source on the order of $Q_{\rho,f} \sim 10^{-4}$ kg/m^3/s, we get

$$\frac{\kappa_H \phi \beta_f Q_{\rho,f}}{\phi} \sim 10^{-15}.$$

These terms are all very negligible for the system we consider, thus the equation Eq. 4.C.5 reduces to

$$\phi \Delta \tilde{v} = -\frac{\partial \tilde{P}}{\partial \tilde{z}} \tag{4.C.6}$$

which in the dimensional form becomes:

$$\phi \Delta v = -\frac{k}{\mu_f} \frac{\partial P_f}{\partial z}. \tag{4.C.7}$$

This is also known as the Darcy law for quasi-static fluid flow in a porous media.

4.C.3 Pressure

Non-dimensionalization of the pressure equation and substituting the Darcy flux (Eq. 4.C.7) for $\phi \Delta v$ gives:

$$\frac{\partial \tilde{P}_f}{\partial \tilde{t}} + \phi \beta_f P_C \tilde{v}_f \frac{\partial \tilde{P}_f}{\partial \tilde{z}} = -\frac{\partial^2 \tilde{P}_f}{\partial \tilde{z}^2} + \frac{t_C Q_{\rho,f}}{\phi \beta_f P_C \rho_C} \left(\frac{1}{\tilde{\rho}_f} - \frac{1}{\tilde{\rho}_s} \right) - \frac{t_C}{\phi \beta_f \eta} \frac{\partial \tilde{v}_s}{\partial \tilde{z}}. \tag{4.C.8}$$

Evaluation of the terms gives

$$\phi \beta_f P_C \sim 0.1 \text{ and } \frac{t_C}{\phi \beta_f \eta} \sim 10^{-2},$$

which are both small relative to 1. On the other hand,

$$\frac{t_C Q_{\rho,f}}{\phi \beta_f P_C \rho_C} > 1.$$

The final equation of pressure thus reduces to

$$\phi \frac{\partial \tilde{P}_f}{\partial \tilde{t}} = \frac{\kappa_H}{\kappa_T} \frac{\partial^2 \tilde{P}_f}{\partial \tilde{z}^2} + \frac{t_C}{\phi \beta_f P_C} \left(\frac{1}{\rho_f} - \frac{1}{\rho_s} \right) Q_{\rho,f} \tag{4.C.9}$$

which converted back to dimensional form becomes:

$$\frac{\partial P_f}{\partial t} = \kappa_H \frac{\partial^2 P_f}{\partial z^2} + \left(\frac{1}{\rho_f} - \frac{1}{\rho_s} \right) \frac{Q_{\rho,f}}{\phi \beta_f}. \tag{4.C.10}$$

Appendix 4.D Solving the system of equations

4.D.1 Dimensional analysis

Another recipe of dimensional analysis is used to convert the partial differential equations to ordinary differential equations. The first step is to make a list of parameters that determine the temperature and pressure: $T = f(t, \kappa_T, z, T_{hr}, T_m, L^*)$, $P_f = f(t, \kappa_H, z, P_{hr})$, where T_{hr} is the host-rock temperature, T_m is the melt temperature and P_{hr} is the initial host-rock fluid pressure. The basic units of these parameters are: $t = [\mathrm{s}]$; $\kappa_T = [\mathrm{m^2/s}]$; $z = [\mathrm{m}]$; $T = [\mathrm{K}]$; $L^* = [-]$; $\kappa_H = [\mathrm{m^2/s}]$; $P_f = [\mathrm{Pa}]$.. The next step is to go through the list to find independent and dependent units. t is the first occurrence of seconds and is the independent time-scale for both cases. κ_T and κ_H are the first occurrence of square meters per seconds of both systems, and are the independent diffusion-scales. z has the dimension meter, and meter can also be expressed by the square root of time and diffusivity, $\sqrt{\mathrm{m^2/s \times s}} = \mathrm{m}$. Thus, z is a dependent length scale. In the thermal case we select the characteristic length scale as $\sqrt{\kappa_T t}$. In the hydraulic case we select $\sqrt{\kappa_H t}$ as the characteristic length scale. L^* is already non-dimensionalized, and is the independent scale of latent heat effects.

T, T_{hr} and T_m are all expressed in Kelvin. We can eliminate the host-rock temperature T_{hr}, by subtracting all temperatures by T_{hr}. We choose $T_m - T_{hr}$ as our independent temperature scale, which implies that $T - T_{hr}$ is the dependent temperature scale. Similarly we can subtract the background fluid pressure from the total fluid pressure, and only solve for the fluid overpressure, $\Delta P_f = P_f - P_{hr}$.

The next step is to divide all parameters by their respective new independent scales:

$$\frac{(T - T_{hr})}{(T_m - T_{hr})} = f\left(\frac{t}{t}, \frac{\kappa_T}{\kappa_T}, \frac{z}{\sqrt{\kappa_T t}}, \frac{T_{hr} - T_{hr}}{T_m - T_{hr}}, \frac{T_m - T_{hr}}{T_m - T_{hr}}, \frac{L^*}{L^*} \right)$$
$$\Delta P_f = f\left(\frac{t}{t}, \frac{\kappa_H}{\kappa_H}, \frac{z}{\sqrt{\kappa_H t}} \right).$$

All the non-dimensional independent parameters become 1 (constant), and the non-dimensional host-rock temperature becomes 0. The only dependency left is the non-dimensionalized length scale, $T^* = f(z/\sqrt{\kappa_T t})$ and $\Delta P_f = f(z/\sqrt{\kappa_H t})$, where the non-dimensional temperature is defined as

$$T^* = (T - T_{hr}) / (T_m - T_{hr}). \tag{4.D.1}$$

The new non-dimensional parameters are:

$$\xi_T = z/2\sqrt{\kappa_T t} \tag{4.D.2a}$$

$$\xi_P = z/2\sqrt{\kappa_H t} \tag{4.D.2b}$$

where the factor 1/2 is introduced to simplify the final analytical answer. It is perfectly fine to avoid this factor, but then the alternative, twice larger ξ_T will be divided by a factor 2 everywhere in the final answer. We therefore 'cheat' and introduce 1/2 already at this stage for this cosmetic reason.

4.D.2 Analytical solutions

We have identified that $T^* = T^*(\xi_T)$ and $\Delta P_f = \Delta P_f(\xi_P)$, where $\xi_T = \xi_T(t,z)$ and $\xi_P = \xi_P(t,z)$. We are now ready to transform the partial differential equations (Eq. 4.3.1 and Eq. 4.3.4) on the form $T(t,z)$ and $P_f(t,z)$ into the new variables. The following procedure is identical for pressure and temperature, and we present the transformation of temperature only.

First, we apply the chain rule of differentiation to the left hand side of Eq. 4.3.1,

$$\frac{\partial}{\partial t}T(t,z) = \frac{\partial}{\partial \xi_T}T^*(\xi_T)\frac{\partial}{\partial t}\xi_T, \tag{4.D.3}$$

where we from derivation of Eq. 4.D.2a with respect to t get that

$$\frac{\partial}{\partial t}\xi_T = -z/4t\sqrt{\kappa_T t}. \tag{4.D.4}$$

On the right hand side of Eq. 4.3.1, the chain rule is a bit trickier due to the double derivative,

$$\kappa_T \frac{\partial^2}{\partial z^2}T(t,z) = \kappa_T \frac{\partial^2}{\partial {\xi_T}^2}T(t,z)\left(\frac{\partial}{\partial z}\xi_T\right)^2 \tag{4.D.5}$$

where we from derivation of Eq. 4.D.2a with respect to z get

$$\left(\frac{\partial}{\partial z}\xi_T\right)^2 = 1/4\kappa_T t. \tag{4.D.6}$$

Substituting Eq. 4.D.3 to 4.D.6 into Eq. 4.3.1 gives a new form of the thermal equation:

$$\frac{d}{d\xi_T}T^*(\xi_T) = -\frac{1}{2\xi_T}\frac{d^2}{d{\xi_T}^2}T^*(\xi_T). \tag{4.D.7}$$

For pressure the transformed equation becomes

$$\frac{d}{d\xi_P}\Delta P_f(\xi_P) = -\frac{1}{2\xi_P}\frac{d^2}{d{\xi_P}^2}\Delta P_f(\xi_P). \tag{4.D.8}$$

Time t appears on both sides of the equation and cancels out.

To solve Eq. 4.D.7 we specify the boundary conditions. We define our system domain to start at the center of the intrusion and end infinitely far into the host-rock, i.e. half of a contact metamorphic setting.

Because temperature is differentiated twice, we need two boundary conditions: 1) The temperature at the crystallization front (ξ_T^m) is equal to the melt temperature, $T^*\left(\xi_T^m\right) = T_m^* = 1$, and 2) the temperature infinitely far away from the intrusion (ξ_T^∞) equals the background host-rock temperature, $T^*\left(\xi_T^\infty\right) = T_{hr}^* = 0$. The differential equation for temperature is solved by integration of the Eq. 4.D.7, and applying boundary conditions to solve for the integration constants. The final analytical solution to the thermal equation is

$$T^*\left(\xi_T\right) = \frac{\operatorname{erfc}\left(\xi_T\right)}{1+\operatorname{erf}\left(\xi_T^m\right)} \tag{4.D.9}$$

where the error function is by definition $\operatorname{erf}\left(\xi\right) = \frac{2}{\sqrt{\pi}} \int_0^\xi e^{-\tau^2} d\tau$ and $\operatorname{erfc}\left(\xi\right) = 1 - \operatorname{erf}\left(\xi\right)$. The equation for pressure (Eq. 4.D.8) is solved in a similar manner. As boundary conditions we set the overpressure infinitely far from the reaction front $\xi_P^\infty$is zero, i.e. $\Delta P_f(\xi_P^\infty) = 0$. The fluid overpressure at the contact is set to a constant contact pressure $\Delta P_f(0) = P_C$. The analytical solution for overpressure becomes

$$\Delta P_f\left(\xi_P\right) = \operatorname{erfc}\left(\xi_P\right) P_C. \tag{4.D.10}$$

REFERENCES

AARNES I., PODLADCHIKOV Y.Y. & NEUMANN E.R. (2008) Post-emplacement melt flow induced by thermal stresses: Implications for differentiation in sills. *Earth and Planetary Science Letters*, **276**, 152–166.

AARNES I., SVENSEN H., CONNOLLY J.A.D. & PODLADCHIKOV Y.Y. (accepted) How contact metamorphism can trigger global climate changes: Modeling gas generation around igneous sills in sedimentary basins. *Geochimica Et Cosmochimica Acta*, **Accepted**.

AARNES I., SVENSEN H., POLTEAU S. & PLANKE S. (in review) Contact metamorphic devolatilization of shales in the Karoo Basin, South Africa, and the effects of multiple sill intrusions . *Chemical Geology*, **In review**.

AGUE J.J. & BAXTER E.F. (2007) Brief thermal pulses during mountain building recorded by Sr diffusion in apatite and multicomponent diffusion in garnet. *Earth and Planetary Science Letters*, **261**, 500–516.

AGUE J.J., PARK J. & RYE D.M. (1998) Regional Metamorphic Dehydration and Seismic Hazard. *Geophysical Research Letters*, **25**.

BALASHOV V.N. & YARDLEY B.W.D. (1998) Modeling metamorphic fluid flow with reaction-compaction-permeability feedbacks. *American Journal of Science*, **298**, 441–470.

BARKER C. (1990) Calculated volume and pressure changes during the thermal cracking of oil to gas in reservoirs. *AAPG Bulletin*, **74**, 1254–1261.

BARNES H.L. & ERNST W.G. (1963) Ideality and Ionization in Hydrothermal Fluids - System MgO-H_2O-NaOH. *American Journal of Science*, **261**, 129–&.

BAUMGARTNER L.P. & FERRY J.M. (1991) A Model for Coupled Fluid-Flow and Mixed-Volatile Mineral Reactions with Applications to Regional Metamorphism. *Contributions to Mineralogy and Petrology*, **106**, 273–285.

BAXTER E.F., AGUE J.J. & DEPAOLO D.J. (2002) Prograde temperature-time evolution in the Barrovian type-locality constrained by Sm/Nd garnet ages from Glen Clova, Scotland. *Journal of the Geological Society*, **159**, 71–82.

BERG R.R. & GANGI A.F. (1999) Primary migration by oil-generation microfracturing in low-permeability source rocks: Application to the Austin Chalk, Texas. *AAPG Bulletin*, **83**, 727–756.

BICKLE M.J. (1996) Metamorphic decarbonation, silicate weathering and the long-term carbon cycle. *Terra Nova*, **8**, 270–276.

BISHOP A.N. & ABBOTT G.D. (1995) Vitrinite Reflectance and Molecular Geochemistry of Jurassic Sediments - the Influence of Heating by Tertiary Dykes (Northwest Scotland). *Organic Geochemistry*, **22**, 165–177.

BRACE W.F. (1980) Permeability of crystalline and argillaceous rocks. *International Journal of Rock Mechanics and Mining Sciences & Geomechanics Abstracts*, **17**, 241–251.

BREDEHOEFT J.D. & HANSHAW B.B. (1968) On Maintenance of Anomalous Fluid Pressures: I. Thick Sedimentary Sequences. *Geological Society of America Bulletin*, **79**, 1097–&.

BURRUS J. (1998) Overpressure models for clastic rocks, their relation to hydrocarbon expulsion: A critical reevaluation. *Abnormal Pressures in Hydrocarbon Environments*, **70**, 35–63.

CARCIONE J.M. & GANGI A.F. (2000) Gas generation and overpressure: Effects on seismic attributes. *Geophysics*, **65**, 1769–1779.

CARSLAW H.S. & JAEGER J.C. (1959) *Conduction of heat in solids*. Clarendon Press, Oxford, 2nd edn.

CATHLES L.M. (1977) Analysis of Cooling of Intrusives by Groundwater Convection Which Includes Boiling. *Economic Geology*, **72**, 804–826.

CATHLES L.M., ERENDI A.H.J. & BARRIE T. (1997) How long can a hydrothermal system be sustained by a single intrusive event? *Economic Geology and the Bulletin of the Society of Economic Geologists*, **92**, 766–771.

CATUNEANU O., HANCOX P.J. & RUBIDGE B.S. (1998) Reciprocal flexural behaviour and contrasting stratigraphies: a new basin development model for the Karoo retroarc foreland system, South Africa. *Basin Research*, **10**, 417–439.

CHATTERJEE N.D., JOHANNES W. & LEISTNER H. (1984) The System CaO-Al_2O_3-SiO_2-H_2O - New Phase-Equilibria Data, Some Calculated Phase-Relations, and Their Petrological Applications. *Contributions to Mineralogy and Petrology*, **88**, 1–13.

CHEVALLIER L. & WOODFORD A. (1999) Morpho-tectonics and mechanism of emplacement of the dolerite rings and sills of the Western Karoo, South Africa. *South African Journal of Geology*, **102**, 43–54.

COLTEN-BRADLEY V.A. (1987) Role of Pressure in Smectite Dehydration - Effects on Geopressure and Smectite-to-Illite Transformation. *AAPG Bulletin*, **71**, 1414–1427.

CONNOLLY J.A.D. (1997) Devolatilization-generated fluid pressure and deformation-propagated fluid flow during prograde regional metamorphism. *Journal of Geophysical Research-Solid Earth*, **102**, 18149–18173.

CONNOLLY J.A.D. (2005) Computation of phase equilibria by linear programming: A tool for geodynamic modeling and its application to subduction zone decarbonation. *Earth and Planetary Science Letters*, **236**, 524–541.

CONNOLLY J.A.D. (2009) The geodynamic equation of state: What and how. *Geochemistry Geophysics Geosystems*, **10**.

COOPER J.R., CRELLING J.C., RIMMER S.M. & WHITTINGTON A.G. (2007) Coal metamorphism by igneous intrusion in the Raton Basin, CO and NM: Implications for generation of volatiles. *International Journal of Coal Geology*, **71**, 15–27.

CORBET T.F. & BETHKE C.M. (1992) Disequilibrium Fluid Pressures and Groundwater Flow in the Western Canada Sedimentary Basin. *Journal of Geophysical Research-Solid Earth*, **97**, 7203–7217.

CRANK J. (1979) *The mathematics of diffusion*. Oxford University Press, USA.

CUI X.J., NABELEK P.I. & LIU M. (2001) Heat and fluid flow in contact metamorphic aureoles with layered and transient permeability, with application to the Notch Peak aureole, Utah. *Journal of Geophysical Research-Solid Earth*, **106**, 6477–6491.

DELANEY P.T. (1982) Rapid Intrusion of Magma into Wet Rock - Groundwater-Flow Due to Pore Pressure Increases. *Journal of Geophysical Research*, **87**, 7739–756.

DELANY J.M. & HELGESON H.C. (1978) Calculation of the thermodynamic consequences of dehydration in subducting oceanic crust to 100 kb and ¿ 800 degrees C. *American Journal of Science*, **278**, 638–686.

DOMENICO P.A. & PALCIAUSKAS V.V. (1979) Thermal-Expansion of Fluids and Fracture Initiation in Compacting Sediments - Summary. *Geological Society of America Bulletin*, **90**, 518–520.

EINSELE G., GIESKES J.M., CURRAY J., MOORE D.M., AGUAYO E., AUBRY M.P., FORNARI D., GUERRERO J., KASTNER M., KELTS K., LYLE M., MATOBA Y., MOLINACRUZ A., NIEMITZ J., RUEDA J., SAUNDERS A., SCHRADER H., SIMONEIT B. & VACQUIER V. (1980) Intrusion of Basaltic Sills into Highly Porous Sediments, and Resulting Hydrothermal Activity. *Nature*, **283**, 441–445.

FERRY J.M. & GERDES M.L. (1998) Chemically reactive fluid flow during metamorphism. *Annual Review of Earth and Planetary Sciences*, **26**, 255–287.

FURLONG K.P., HANSON R.B. & BOWERS J.R. (1991) Modeling thermal regimes. In: *Reviews in Mineralogy and Geochemistry*, vol. 26, 437.

GALERNE C.Y., NEUMANN E.R. & PLANKE S. (2008) Emplacement mechanisms of sill complexes: Information from the geochemical architecture of the Golden Valley Sill Complex, South Africa. *Journal of Volcanology and Geothermal Research*, **177**, 425–440.

GAUS I., AZAROUAL M. & CZERNICHOWSKI-LAURIOL I. (2005) Reactive transport modelling of the impact of CO2 injection on the clayey cap rock at Sleipner (North Sea). *Chemical Geology*, **217**, 319–337.

GUÉGUEN Y. & PALCIAUSKAS V. (1994) *Introduction to the Physics of Rocks*. Princeton University Press.

HANSHAW B.B. & BREDEHOEFT J.D. (1968) On the Maintenance of Anomalous Fluid Pressures: II. Source Layer at Depth. *Geological Society of America Bulletin*, **79**, 1107–1122.

HANSOM J. & LEE M.K. (2005) Effects of hydrocarbon generation, basal heat flow and sediment compaction on overpressure development: a numerical study. *Petroleum Geoscience*, **11**, 353–360.

HANSON R.B. (1992) Effects of Fluid Production on Fluid-Flow During Regional and Contact-Metamorphism. *Journal of Metamorphic Geology*, **10**, 87–97.

HANSON R.B. (1995) The hydrodynamics of contact-metamorphism. *Geological Society of America Bulletin*, **107**, 595–611.

HILL R.J., TANG Y.C., KAPLAN I.R. & JENDEN P.D. (1996) The influence of pressure on the thermal cracking of oil. *Energy & Fuels*, **10**, 873–882.

INGEBRITSEN S.E. & MANNING C.E. (2002) Diffuse fluid flux through orogenic belts: Implications for the world ocean. *Proceedings of the National Academy of Sciences of the United States of America*, **99**, 9113–9116.

JAMTVEIT B., GRORUD H.F. & BUCHER-NURMINEN K. (1992) Contact metamorphism of layered carbonate-shale sequences in the Oslo Rift. II: Migration of isotopic and reaction fronts around cooling plutons. *Earth and Planetary Science Letters*, **114**, 131–148.

JAMTVEIT B., SVENSEN H. & PODLADCHIKOV Y.Y. (2004) Hydrothermal vent complexes associated with sill intrusions in sedimentary basins. In: *Physical Geology of High-Level Magmatic Systems* (Ed. C. Breitkreuz & N. Petford), vol. 234. Geological Society, London, Special Publications.

KELEMEN P.B., WHITEHEAD J.A., AHARONOV E. & JORDAHL K.A. (1995) Experiments on Flow Focusing in Soluble Porous-Media, with Applications to Melt Extraction from the Mantle. *Journal of Geophysical Research-Solid Earth*, **100**, 475–496.

KNAPP R.B. & KNIGHT J.E. (1977) Differential Thermal-Expansion of Pore Fluids - Fracture Propagation and Microearthquake Production in Hot Pluton Environments. *Journal of Geophysical Research*, **82**, 2515–2522.

KO S.C., OLGAARD D.L. & WONG T.F. (1997) Generation and maintenance of pore pressure excess in a dehydrating system .1. Experimental and microstructural observations. *Journal of Geophysical Research-Solid Earth*, **102**, 825–839.

KOKELAAR B.P. (1982) Fluidization of Wet Sediments During the Emplacement and Cooling of Various Igneous Bodies. *Journal of the Geological Society*, **139**, 21–33.

LASAGA A.C. (1989) Fluid flow and chemical reaction kinetics in metamorphic systems: a new simple model. *Earth and Planetary Science Letters*, **94**, 417–424.

LASAGA A.C. & RYE D.M. (1993) Fluid-Flow and Chemical-Reaction Kinetics in Metamorphic Systems. *American Journal of Science*, **293**, 361–404.

LE GALLO Y., BILDSTEIN O. & BROSSE E. (1998) Coupled reaction-flow modeling of diagenetic changes in reservoir permeability, porosity and mineral compositions. *Journal of Hydrology*, **209**, 366–388.

LELOUP P.H., RICARD Y., BATTAGLIA J. & LACASSIN R. (1999) Shear heating in continental strike-slip shear zones: model and field examples. *Geophysical Journal International*, **136**, 19–40.

LÉGER A. & FERRY J.M. (1993) Fluid Infiltration and Regional Metamorphism of the Waits River Formation, North-East Vermont, USA. *Journal of Metamorphic Geology*, **11**, 3–29.

LICHTNER P.C. (1985) Continuum model for simultaneous chemical reactions and mass transport in hydrothermal systems. *Geochimica et Cosmochimica Acta*, **49**, 779–800.

LICHTNER P.C. (1988) The quasi-stationary state approximation to coupled mass transport and fluid-rock interaction in a porous medium. *Geochimica et Cosmochimica Acta*, **52**, 143–165.

LITVINOVSKI B.A., PODLADCHIKOV Y.Y., ZANVILEVITCH A.N. & DUNITCHEV V.M. (1990) On the melting of acidic volcanites in the contact of basic magma at shallow depth. *Geochimya*, **6**, 807–814.

LUO X. & VASSEUR G. (1996) Geopressuring Mechanism of Organic Matter Cracking: Numerical Modeling, journal = AAPG Bulletin . **80**, 856–874.

MANNING C.E. & BIRD D.K. (1991) Porosity Evolution and Fluid-Flow in the Basalts of the Skaergaard Magma-Hydrothermal System, East Greenland. *American Journal of Science*, **291**, 201–257.

MARSH J., HOOPER P., REHACEK J., DUNCAN R. & DUNCAN A. (1997) Stratigraphy and age of Karoo basalts of Lesotho and implications for correlations within the Karoo igneous province. In: *Large Provinces: continental, oceanic and planetary flood volcanism* (Ed. J. Mahoney & M. Coffin), vol. 100, 247–272. Geophysical Monograph.

MILLER S.A., VAN DER ZEE W., OLGAARD D.L. & CONNOLLY J.A.D. (2003) A fluid-pressure feedback model of dehydration reactions: experiments, modelling, and application to subduction zones. *Tectonophysics*, **370**, 241–251.

NABELEK P.I. (2007) Fluid evolution and kinetics of metamorphic reactions in calc-silicate contact aureoles - From H_2O to CO_2 and back. *Geology*, **35**, 927–930.

NABELEK P.I. & LABOTKA T.C. (1993) Implications of geochemical fronts in the Notch Peak contact-metamorphic aureole, Utah, USA. *Earth and Planetary Science Letters*, **119**, 539–559.

NISHIYAMA T. (1989) Kinetics of Hydrofracturing and Metamorphic Veining. *Geology*, **17**, 1068–1071.

NORTON D. & KNIGHT J.E. (1977) Transport phenomena in hydrothermal systems; cooling plutons. *American Journal of Science*, **277**, 937–981.

OLGAARD D.L., KO S.C. & WONG T.F. (1995) Deformation and Pore Pressure in Dehydrating Gypsum under Transiently Drained Conditions. *Tectonophysics*, **245**, 237–248.

OLIVER N.H.S., RUBENACH M.J., FU B., BAKER T., BLENKINSOP T.G., CLEVERLEY J.S., MARSHALL L.J. & RIDD P.J. (2006) Granite-related overpressure and volatile release in the mid crust: fluidized breccias from the Cloncurry District, Australia. *Geofluids*, **6**, 346–358.

ORTOLEVA P., MERINO E., MOORE C. & CHADAM J. (1987) Geochemical Self-Organization .1. Reaction-Transport Feedbacks and Modeling Approach. *American Journal of Science*, **287**, 979–1007.

OSBORNE M.J. & SWARBRICK R.E. (1997) Mechanisms for generating overpressure in sedimentary basins: A reevaluation. *AAPG Bulletin*, **81**, 1023–1041.

PEACOCK S.M. (1987) Thermal effects of metamorphic fluids in subduction zones. *Geology*, **15**, 1057–1060.

PEACOCK S.M. (1989) Numerical Constraints on Rates of Metamorphism, Fluid Production, and Fluid Flux During Regional Metamorphism. *Geological Society of America Bulletin*, **101**, 476–485.

PHILPOTTS A.R. & AGUE J.J. (2009) *Principles of igneous and metamorphic petrology*. Cambridge University Press, 2nd edn.

PLANKE S., RASMUSSEN T., REY S.S. & MYKLEBUST R. (2005) Seismic characteristics and distribution of volcanic intrusions and hydrothermal vent complexes in the Vøring and Møre basins. In: *Petroleum Geology: North-West Europe and Global Perspectives & Proceedings of the 6th Petroleum Geology Conference. Geological Society, London*, 833–844.

PODLADCHIKOV Y.Y. & WICKHAM S.M. (1994) Crystallization of Hydrous Magmas - Calculation of Associated Thermal Effects, Volatile Fluxes, and Isotopic Alteration. *Journal of Geology*, **102**, 25–45.

POLTEAU S., MAZZINI A., GALLAND O., PLANKE S. & MALTHE-SØRENSSEN A. (2008) Saucer-shaped intrusions: Occurrences, emplacement and implications. *Earth and Planetary Science Letters*, **266**, 195–204.

RODRIGUEZ MONREAL F., VILLAR H.J., BAUDINO R., DELPINO D. & ZENCICH S. (2009) Modeling an atypical petroleum system: A case study of hydrocarbon generation, migration and accumulation related to igneous intrusions in the Neuquen Basin, Argentina. *Marine and Petroleum Geology*, **26**, 590–605.

SIMONEIT B.R.T., BRENNER S., PETERS K.E. & KAPLAN I.R. (1978) Thermal Alteration of Cretaceous Black Shale by Basaltic Intrusions in Eastern Atlantic. *Nature*, **273**, 501–504.

SKINNER E.M.W. & MARSH J.S. (2004) Distinct kimberlite pipe classes with contrasting eruption processes. *Lithos*, **76**, 183–200.

STEEFEL C.I., DEPAOLO D.J. & LICHTNER P.C. (2005) Reactive transport modeling: An essential tool and a new research approach for the Earth sciences. *Earth and Planetary Science Letters*, **240**, 539–558.

STEEFEL C.I. & LASAGA A.C. (1994) A Coupled Model for Transport of Multiple Chemical-Species and Kinetic Precipitation Dissolution Reactions with Application to Reactive Flow in Single-Phase Hydrothermal Systems. *American Journal of Science*, **294**, 529–592.

STEEFEL C.I. & MAHER K. (2009) Fluid-Rock Interaction: A Reactive Transport Approach. In: *Thermodynamics and Kinetics of Water-Rock Interaction* (Ed. E.H. Oelkers & J. Schott), vol. 70 of *Reviews in Mineralogy and Geochemistry*, 485–532.

SVENSEN H., AARNES I., PODLADCHIKOV Y.Y., JETTESTUEN E., HARSTAD C.H. & PLANKE S. (in press) Sandstone dikes in dolerite sills: Evidence for high pressure gradients and sediment mobilization during solidification of magmatic sheet intrusions in sedimentary basins. *Geosphere*, **In press**.

SVENSEN H., JAMTVEIT B., PLANKE S. & CHEVALLIER L. (2006) Structure and evolution of hydrothermal vent complexes in the Karoo Basin, South Africa. *Journal of the Geological Society*, **163**, 671–682.

SVENSEN H., PLANKE S., CHEVALLIER L., MALTHE-SØRENSSEN A., CORFU F. & JAMTVEIT B. (2007) Hydrothermal venting of greenhouse gases triggering Early Jurassic global warming. *Earth and Planetary Science Letters*, **256**, 554–566.

SVENSEN H., PLANKE S., MALTHE-SORENSSEN A., JAMTVEIT B., MYKLEBUST R., EIDEM T.R. & REY S.S. (2004) Release of methane from a volcanic basin as a mechanism for initial Eocene global warming. *Nature*, **429**, 542–545.

SVENSEN H., PLANKE S., POLOZOV A.G., SCHMIDBAUER N., CORFU F., PODLADCHIKOV Y.Y. & JAMTVEIT B. (2009) Siberian gas venting and the end-Permian environmental crisis. *Earth and Planetary Science Letters*, **277**, 490–500.

THOMPSON A.B. (1976) Mineral reactions in pelitic rocks; I, Prediction of P-T-X(Fe-Mg) phase relations. *American Journal of Science*, **276**, 401–424.

THOMPSON A.B. (1987) Some aspects of fluid motion during metamorphism. *Journal of the Geological Society*, **144**, 309–312.

THOMPSON A.B. & CONNOLLY J.A.D. (1992) Migration of Metamorphic Fluid - Some Aspects of Mass and Heat-Transfer. *Earth-Science Reviews*, **32**, 107–121.

TISSOT B. & WELTE D.H. (1984) *Petroleum Formation and Occurrence*. Springer Verlag, Berlin, 2nd edn.

TURCOTTE D.L. & SCHUBERT G. (2002) *Geodynamics*. Cambridge, 2nd edn.

UNGERER P., BEHAR F., VILLALBA M., HEUM O.R. & AUDIBERT A. (1988) Kinetic modelling of oil cracking. *Organic Geochemistry*, **13**, 857–868.

VRY J., POWELL R., GOLDEN K.M. & PETERSEN K. (2010) The role of exhumation in metamorphic dehydration and fluid production. *Nature Geoscience*, **3**, 31–35.

WALDER J. & NUR A. (1984) Porosity Reduction and Crustal Pore Pressure Development. *Journal of Geophysical Research*, **89**, 1539–1548.

WALTHER J.V. (1990) Fluid dynamics during progressive regional metamorphism. In: *The Role of Fluids in Crustal Processes* (Ed. J.D. Bredehoeft & D. Norton), 64–71. National Academy Press, Washington, DC.

WALTHER J.V. & ORVILLE P.M. (1982) Volatile Production and Transport in Regional Metamorphism. *Contributions to Mineralogy and Petrology*, **79**, 252–257.

WALTHER J.V. & WOOD B.J. (1984) Rate and Mechanism in Prograde Metamorphism. *Contributions to Mineralogy and Petrology*, **88**, 246–259.

WALTON M.S. & O'SULLIVAN R.B. (1950) The intrusive mechanics of a clastic dike (Connecticut). *American Journal of Science*, **248**, 1–21.

WANG W.H. & WONG T.F. (2003) Effects of reaction kinetics and fluid drainage on the development of pore pressure excess in a dehydrating system. *Tectonophysics*, **370**, 227–239.

WANGEN M. (2001) A quantitative comparison of some mechanisms generating overpressure in sedimentary basins. *Tectonophysics*, **334**, 211–234.

WANNAMAKER P.E. (2010) Metamorphism: Water from stone. *Nature Geoscience*, **3**, 10–11.

WEINBERG R.F., MARK G. & REICHARDT H. (2009) Magma ponding in the Karakoram shear zone, Ladakh, NW India. *Geological Society of America Bulletin*, **121**, 278–285.

WONG T.F., KO S.C. & OLGAARD D.L. (1997) Generation and maintenance of pore pressure excess in a dehydrating system .2. Theoretical analysis. *Journal of Geophysical Research-Solid Earth*, **102**, 841–852.

XU T.F. & PRUESS K. (2001) Modeling multiphase non-isothermal fluid flow and reactive geochemical transport in variably saturated fractured rocks: 1. Methodology. *American Journal of Science*, **301**, 16–33.

ZHANG S.Q., PATERSON M.S. & COX S.F. (1994) Porosity and Permeability Evolution During Hot Isostatic Pressing of Calcite Aggregates. *Journal of Geophysical Research-Solid Earth*, **99**, 15741–15760.

Chapter 5

Sandstone dikes in dolerite sills: Evidence for high pressure gradients and sediment mobilization during solidification of magmatic sheet intrusions in sedimentary basins

by
Henrik Svensen[*], Ingrid Aarnes[*], Yuri Y. Podladchikov[*], Espen Jettestuen[*†], Camilla H. Harstad[‡] and Sverre Planke[*§]
Manuscript in press in *Geosphere*

[*]Physics of Geological Processes, University of Oslo, P.box 1048 Blindern, 0316 Oslo, Norway.
[†]International Research Institute of Stavanger (IRIS), Prof. Olav Hanssensvei 15, 4068 Stavanger, Norway.
[‡]GR Group, Karenslyst allè 4, 0278 Oslo, Norway.
[§]Volcanic Basin Petroleum Research (VBPR), Oslo, Norway.

5.1 Abstract

Sediment dikes are common within dolerite sill intrusions in the Karoo Basin in South Africa. The dikes are sub-vertical and up to 2 meters wide, sometimes with abundant fragments of sedimentary rocks and dolerite. The matrix consists of contact metamorphic sandstone. There is no petrographic evidence for melting within the sediment dikes. The maximum temperature during heating is restricted to the plagioclase and biotite stability field, or above c. 350 °C. Thermal modeling of a sandstone dike in a dolerite sill shows that a temperature of 350-450 °C is reached in the dike after a few hundred years of sill cooling. The calculated pressure history of a cooling sill and its contact aureole shows that substantial fluid pressure anomalies develop on a short timescale (1-15 years) and are maintained for more than 100 years. Calculated pressure anomalies in the sill (-7 to -22 MPa) and the aureole (4-22 MPa) are significant and may explain sill fracturing and sediment mobilization from the aureole into the sill. We conclude that sediment dikes represent common features of sedimentary basins with sill intrusions in which fluid pressure gradient have been high. Sediment dikes thus signify that pore fluids may escape from the aureoles on a short timescale, representing an intermediate situation between fluid loss during formation of micro-fractures and fluid loss during violent vent formation.

5.2 Introduction

Subsurface sediment mobilization and fluidization has been recognized from many geological settings, ranging from overpressured clastic reservoirs (Nichols *et al.*, 1994; Jolly & Lonergan, 2002; Mazzini *et al.*, 2003) to contact metamorphism around magmatic sill intrusions (Jamtveit *et al.*, 2004; Svensen *et al.*, 2006). In sedimentary basins affected by magmatic sill intrusions (i.e., volcanic basins), like the Karoo Basin in South Africa, sediment dikes are reported from within doleritic sills (Van Biljon & Smitter, 1956). Interestingly, these dikes comprise metamorphic sandstone, demonstrating that the sand intruded the dolerite while the sills were still hot. The importance of these observations is that they form direct evidence for high pore fluid pressure during sill emplacement and subsequent contact metamorphism.

In a classic study by Walton & O'Sullivan (1950), it was suggested that pressure drop during sill cooling and fracturing (i.e., thermal contraction) led to boiling of aureole pore fluids that ultimately led to sediment fluidization. That study was based on field examples from a sill emplaced in sediments during formation of the Central Atlantic Magmatic Province. The role of pore fluid boiling in causing high aureole pressures and subsequent fluid movement was explored in more detail by Delaney (1982) and more recently by e.g. Jamtveit *et al.* (2004).

Understanding sediment mobilization from contact aureoles may put important constraints on pressure evolution of aureoles. The last decade has seen an increasing interest in degassing of volatiles from sedimentary basins with magmatic intrusions, where high pore fluid pressure plays a key role (Svensen *et al.*, 2004; McElwain *et al.*, 2005; Svensen *et al.*, 2007; Retallack & Jahren, 2008; Ganino & Arndt, 2009; Svensen *et al.*, 2009). Gas venting triggered by overpressure in contact aureoles within shale has been proposed to cause global climate changes in the end-Permian, in the Early Jurassic (Toarcian), and at the Paleocene-Eocene boundary (Svensen *et al.*, 2004, 2007, 2009).

The aim of this study is to understand the formation of sandstone intrusions in dolerite sills. We present several case studies of sediment dikes and sediment breccias within sills in the Karoo Basin. However, the results can be applied to other sedimentary basins where sediments have been injected into magmatic sheet intrusions, including the Vøring Basin offshore Norway, the Tunguska Basin of East Siberia, and the Amazonas Basin in Brazil. The process of sediment injections is addressed by adopting a new theoretical model for sill pressure evolution during cooling and crystallization (Aarnes *et al.*, 2008).

5.3 Geological setting

The Karoo Basin (Fig. 5.1) covers more than half of South Africa. The basin is bounded by the Cape Fold Belt along its southern margin and comprises up to 6 km of clastic sedimentary strata capped by at least 1.4 km of basaltic lava (e.g. Smith, 1990; Johnson *et al.*, 1997). The sediments were deposited from the Late Carboniferous to the Middle Jurassic, in an environment ranging from dominantly marine (the Dwyka and Ecca groups) to fluvial (the Beaufort Group and parts of the Stormberg Group) and aeolian (upper part of the Stormberg Group) (Veevers *et al.*, 1994; Catuneanu *et al.*, 1998). The Beaufort Group is a thick sequence of dominantly sandstones. The overlying Stormberg Group includes the Molteno Formation (coarse sandstone, shale, and coal), the Elliot Formation (sandstone, shale; "red beds"), and the Clarens Formation (sandstone with occasional siltstone horizons).

Both southern Africa and Antarctica experienced extensive volcanic activity in early Jurassic times, starting at about 182.5 Ma. Dolerites and lavas of the Karoo-Ferrar Large Igneous Province were emplaced within a relatively short time span. The main phase of flood volcanism lasted less than 1 m.y. (Duncan *et al.*, 1997; Jourdan *et al.*, 2005), although volcanism in southern Africa continued for several million years (Jourdan *et al.*, 2005). Sills and dikes are present throughout the sedimentary succession in the Karoo Basin (Fig. 5.1) (Chevallier & Woodford, 1999; Polteau *et al.*, 2008b), where they locally comprise up to 70 % of the stratigraphy (Rowsell & De Swardt, 1976).

5.4 Methods

5.4.1 Sampling and petrography

Sediment dikes are common within thick (70-120 meter) dolerite sills within the Beaufort Group sediments. The depth of magma emplacement is estimated to 600-1000 meters below the paleo-surface based on present day stratigraphic levels. We have done detailed studies of three localities with sediment dikes in dolerites, 1) the Waterdown Dam area, 2) the Elandsberg road cut (the Nico Malan Pass), and 3) the Golden Valley (Fig. 5.1). Many more localities with sediment dikes have been discovered during our fieldwork in the Karoo Basin during the last decade e.g., south of Cathcart), but the chosen localities are representative. One of the sediment dikes from the Waterdown Dam locality contains numerous fragments of sediments and dolerite. It was mapped in detail by covering it with transparent A4 plastic sheets and tracing individual clasts by hand. This method was preferred over photo analysis due to better accuracy and the benefit of doing on-site interpretations on clast type and clast outline. The resulting

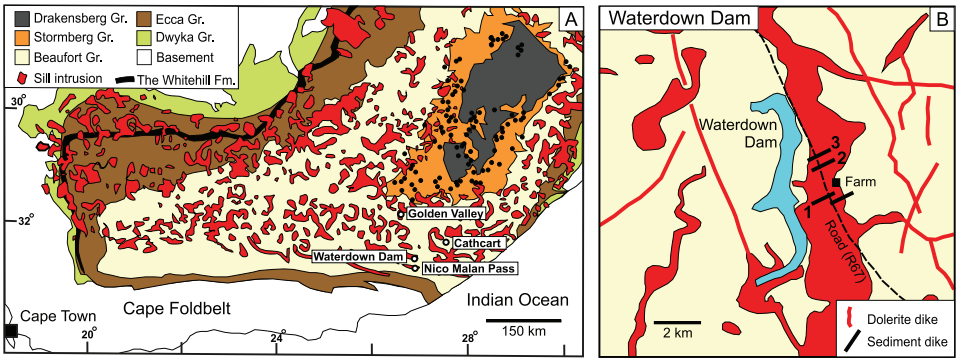

Figure 5.1: **(A)** Simplified geological map of the Karoo Basin in South Africa with sill intrusions and hydrothermal vent complexes as black dots. The three study localities are shown. One more locality with sediment dikes in sills is shown (Cathcart) but not included in this study. **(B)** Geological map of the Waterdown Dam area based on the 1:250 000 geological map of Council for Geoscience, South Africa. Note that there is one locality with dikes that have not been included in this study.

map represents a 2D slice through the dike. We then used image analysis techniques and a Matlab code to quantify the clast content (i.e., area). Probability densities were calculated using a smoothening procedure, where data was binned in either ten consecutive areas (for sediment clasts) or five consecutive areas (for dolerite clasts). The aspect ratio between the long and short axes of the fragments was also calculated. Since our mapping analyses are done in 2D, and the fact that we only have one slice through the dike, the results should be regarded as approximate.

Thin sections of collected samples were studied by optical and electron microscopes (SEM) at the Department of Geology, University of Oslo. The SEM is a JEOL JSM 840, and was also utilized for cathodoluminescence imaging.

5.4.2 Phase stability calculations

We have used Perple_X (Connolly, 2005) to compute phase diagrams for rocks with a pelite composition to predict the temperature stability of the mineral assemblages identified in the sandstone dykes. The calculated phase diagram is projected from an average pelite composition (Caddick & Thompson, 2008), with SiO_2=59.8, Al_2O_3=16.6, FeO=5.8, MgO=2.6, CaO=1.1, Na_2O=1.7, K_2O=3.53, TiO_2=0.75, H_2O=5.0 (all in wt. %). We have calculated the reaction using quartz-saturation which means that the phase assemblages obtained are not dependent upon the bulk content of quartz. Hence the phase diagram is valid for sandstones as well as pelites as long as the ratios of the other oxides do not change significantly.

5.4.3 Numerical modeling

We have developed a numerical model using the Finite Element Method (FEM) in Matlab. We couple standard heat conduction to pressure (or hydraulic) diffusion using the equation for thermal stress similar to that of Aarnes *et al.* (2008). We calculate the pressure anomalies arising from pore fluid expansion of

pure water in the contact aureole, and the pressure changes related to phase transitions (melt to crystal) in the sill. The pressure-anomalies diffuse over time according to the Darcy law. The equations are solved on a 2D square grid with a resolution of 25 by 200 elements. Initial conditions for the thermal solver is a host-rock temperature T_{hr} of 35 °C , and a sill temperature, T_m, of 1200 °C . For temperature boundary conditions we fixed both the upper and lower boundaries at initial host-rock temperature, as the geothermal gradient is negligible on the scale of a few hundred meters. We assume a hydrostatic pressure gradient with a fluid density of 1000 kg/m^3 as initial conditions for pressure. The upper and lower boundaries are fixed according to initial hydrostatic pressure. The boundaries do not influence the calculations.

Model assumptions

We have developed a numerical model to quantify the first order effects associated with sill cooling and pressure evolution. The model is conceptual and does not attempt to describe the full system. We assume an instant emplacement model of the sill because sediment dikes are related to post-emplacement processes occurring at sub-solidus conditions. The thermal diffusivities are equal for the sill and the sedimentary host rock, as differences in thermal properties are negligible (see Table 5.1). However, the hydraulic diffusion coefficients of melts and pore fluids differ by approximately one order of magnitude in our model. We assume no heat advection by fluids either in the sill or the contact aureole. This is justified from studies showing that heat advection by fluids is a second-order effect (Podladchikov & Wickham, 1994; Connolly, 1997). Apart from the sandstone dikes, there are little evidence of high fluid circulation in the intruded sediments, which makes heat advection within the intrusion negligible (cf. Norton *et al.*, 1984).

The major assumption concerning the equation of thermal stresses is that expansion of pore fluids and contraction of melt due to crystallization are prevented either by the sediment matrix or the crystal network. This assumption is valid until the expanding fluids break the sediment matrix and reduce the overpressure either by fluidization or by pervasive flow along the overpressure-gradient. We account for fracturing of the host-rock by resetting pressures that exceed the tensile strength of the host-rock to hydrostatic pressure. We assume the tensile strength of our model sandstone host-rock to be on average 35 MPa (Ai & Ahrens, 2004). We expect a drop in overpressure gradients with time, depending on how freely the mobilized sediments can move and re-equilibrate the overpressure anomalies. For the underpressure, we expect the assumption of prevented volume change to be valid for the intrusion until the thermal contraction produces fracturing of the sill. Tensile strength of gabbroic rocks is above 125 MPa (Ai & Ahrens, 2004). Such underpressure is not achieved in our model, which suggests that we are using conservative values. The main equations used for the modeling are shown in Appendix 5.A.

Table 5.1: Symbols and values used in the numerical model.

Symbol	Description	Initial value	Unit	Ref
Z	vertical system size	500	m	1
d	sill thickness	100	m	1
T_m	initial temperature of melt	1200 + 273	K	1
T_{hr}	initial temperature of host-rock	35 + 273	K	1
T_L	liquidus temperature of melt	1200 + 273	K	1
T_S	solidus temperature of melt	900 + 273	K	1
K_T	thermal diffusivity of melt ($k/C_P/\rho$)	10^{-6}	m^2s^{-1}	2
K_{Hm}	hydraulic diffusivity of melt ($\chi_{sill}/\mu_m/\beta_m$)	2.3×10^{-3}	m^2s^{-1}	2/3
K_{Hhr}	hydraulic diffusivity of host-rock ($\chi_{hr}/\mu_f/\beta_f$)	3.7×10^{-2}	m^2s^{-1}	2/4
β	isothermal compressibility (fluid/water)	4.3×10^{-10}	Pa^{-1}	2
α	thermal expansion coefficient (water)	4.1×10^{-4}	K^{-1}	2
L	latent heat of crystallzation	320000	Jkg^{-1}	4
Ste	stefan number	0.27		1/4
P	hydrostatic pressure	$1000 \times g \times Z$	Pa	1
g	standard gravity	9.81	ms^{-2}	
t	time	0	s	1

1) This study; 2) Delaney (1982); 3) Hersum *et al.* (2005); 4) Turcotte & Schubert (2002).

5.5 Results

5.5.1 Sediment dikes in dolerite sills

Waterdown Dam

Several sediment dikes within dolerite sills are located in road cuts along the Waterdown Dam north of the Elandsberg area in South Africa (Fig. 5.1). The main sites are numbered 1-3 in Figure 5.1B, where thick sediment dikes are exposed close to the lower contact of a transgressive dolerite sill. The intruded sediments are mainly sandstones, all from the Permian and Triassic Beaufort Group. An overview of the locality is given in Figure 5.2A. At all sites, the field evidence suggests upward movement of sediment, based on the presence of dolerite bridges. The maximum upward penetration is not known, but is estimated to 10-15 % of the sill thickness based on the exposed dike heights and sill thickness.

At site 1 (S32°18.2', E26°52.6'), a sediment breccia dike can be traced for about 150 meters westwards from the main road, cutting vertically through at least 15 vertical meters of dolerite. The strike is 80° east, and it pinches out in both directions. The maximum thickness is 0.5 meters and it splits in two branches towards the west. Up to 40 cm long sediment and dolerite fragments are common, and bridge-like portions of dolerite are present locally (Fig. 5.2E). The latter suggests an eastwards direction of emplacement.

Several thin sandstone dikes crop out at site 2 (Fig. 5.2B). The maximum width is 0.5 meter, the strike is 84° east, and their vertical extension can be traced for 10-15 meters in the road cut. A few pieces of fresh dolerite are located within the dikes. These represent fragments of wall rock dolerite

broken off during dike emplacement, as also seen at site 1.

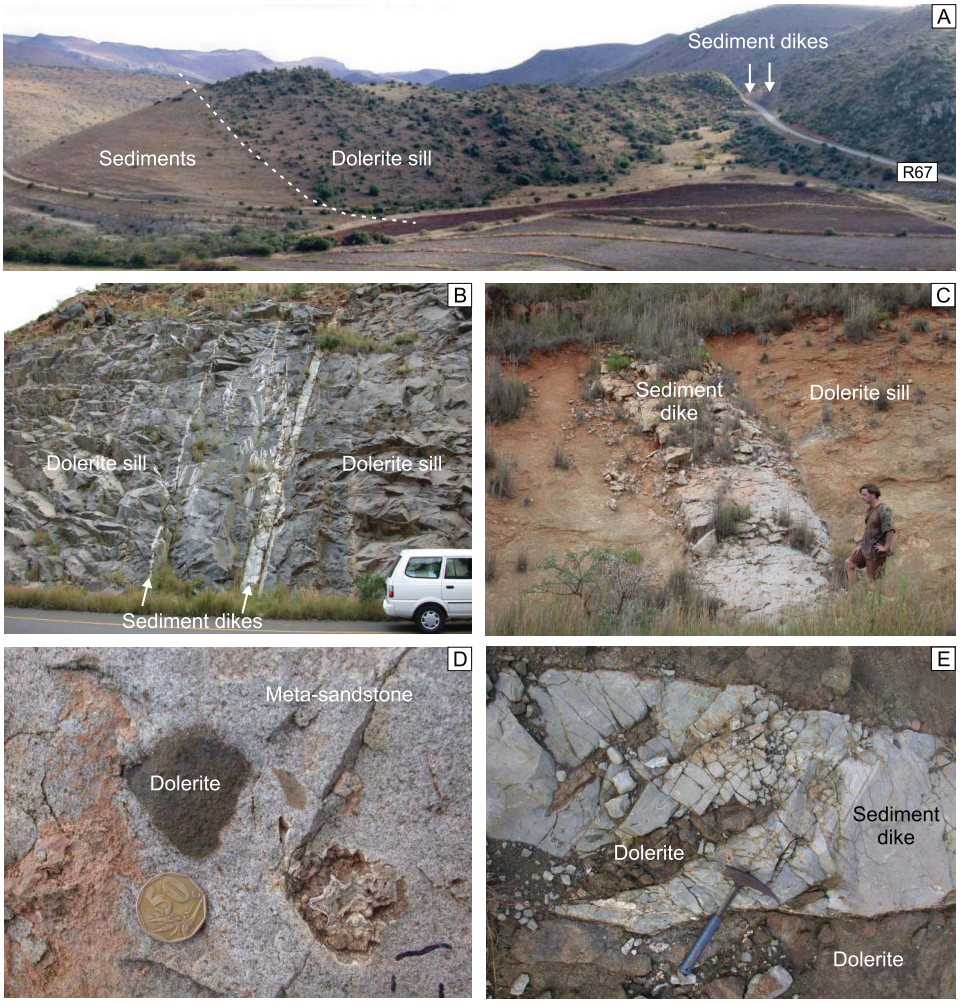

Figure 5.2: The Waterdown Dam locality. **(A)** Overview of the locality, showing the transgressive dolerite sill and the road cut along R67 with sediment dike localities. **(B)** Site 2, with sediment dikes that can be traced 10-15 vertical meters. **(C)** Site 3, with the >2 meter thick breccia dike within the dolerite. **(D)** Close-up of the dike at site 3, showing a dolerite fragment within the baked sandstone. Note the irregular fragment in the lower right, possibly representing altered magmatic material. Coin for scale. **(E)** The sediment dike at site 1. Note the sediment fragments and the dolerite "bridge" extending from the walls and into the dike. Hammer for scale.

At site 3, a vertical dike up to 2.2 meter in thickness crops out along the road (Fig. 5.2C), striking 78° east. This is, to our knowledge, the thickest sediment dike ever found in a sill intrusion. The contact with the dolerite is sharp, although weathered, and it comprises a breccia with sedimentary fragments up to 40 cm long. Some of the fragments show sedimentary layering. The lateral extension of the dike

is unknown due to poor exposures, but the dike is located some 10 meters above the dolerite-sediment contact cropping out to the west. In addition to the sedimentary clasts, the dike contains numerous fragments of dolerite (Fig. 5.2D). The dike has been mapped in detail, and the results are presented in Figure 5.3A. The area percentage occupied by clasts and their size distribution has been quantified (Fig. 5.3B). The results show that the sandstone matrix (including clasts less than 0.5 cm) comprises 86.4 % of the area, sediment fragments occupy 10.6 % (320 clasts) and dolerite fragments comprise 3.0 % (70 clasts). There is a four order of magnitude variation in clast size for the sedimentary fragments, but a lesser variation for the dolerite fragments. Note that the probability versus size relationship is similar for both sediment and dolerite clasts. The aspect ratio of the clasts length and width is calculated and shown in Figure 5.3C. Interestingly, the aspect ratio is independent of the clast size. The sediment clasts are more elongated compared to the dolerite clasts (aspect ratios of 2.51 and 1.95, respectively), which is also evident from Figure 5.3A.

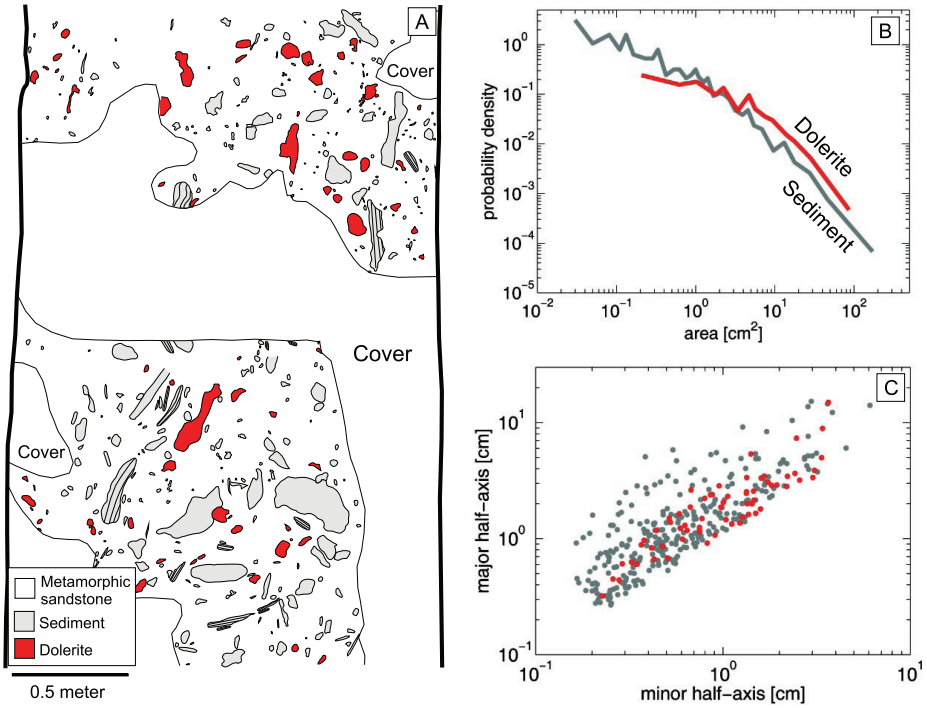

Figure 5.3: **(A)** Graphical representation of the rock fragments in the sediment breccia dike at site 3. The dike content was drawn on transparent plastic sheets (1:1 scale), scanned and re-drawn. Note the abundant dolerite fragments and sedimentary fragments with preserved sedimentary layering. **(B)** Image analysis shows that the rock fragments constitute 13.6 % of the dike area. **(C)** The figure shows a scatter plot of the minor and major half-axis for ellipses fitted to the fragments with dolerite in red and sediment in gray. The plot suggests a linear trend between the minor and major half-axis, hence the aspect ratio is independent of the fragment size. The mean aspect ratios for dolerite and sediment fragments are 1.95 and 2.51 respectively. Very small fragments (less than 0.1 cm^2 (ie. 10 pixels)) are disregarded.

The Elandsberg road cut (the Nico Malan Pass)

The locality is located in the great escarpment defined by thick sill intrusions in the Beaufort Group sediments. A sediment dike was found intruding into the lower contact of the upper sill encountered when driving north towards the Nico Malan Pass along the R67 (S32°30.2', E26°50.2'). The dike has penetrated 2.3 meters into the inclined dolerite sill, and has a slightly curved and irregular shape (Fig. 5.4A). The maximum width is about 20 cm, and the dike pinches out upwards. No dolerite fragments were found in the dike, and the sandstone texture was marked differently at the tip of the dike compared to the surrounding contact aureole sandstone, becoming increasingly recrystallized. No flow structures were observed in the sediment beds below the dike or within in the dike itself.

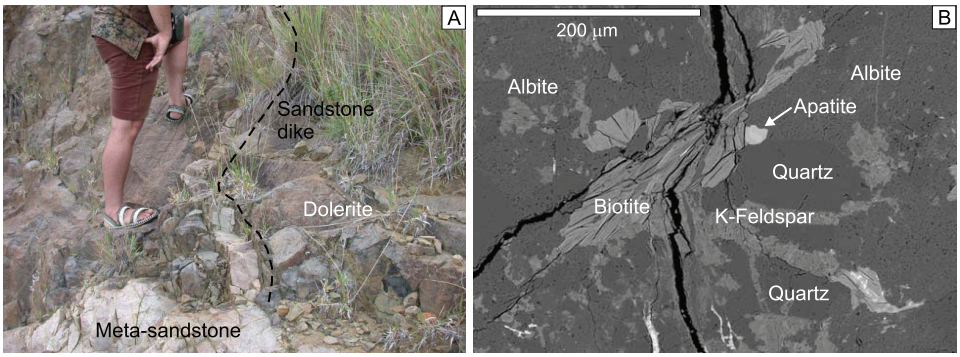

Figure 5.4: The Elandsberg road cut (The Nico Malan Pass). **(A)** Sandstone dike extending about 2.5 vertical meters from the base of a ∼100 meters thick dolerite sill. **(B)** SEM picture showing metamorphic biotite, chlorite, and feldspar in the meta-sandstone from 2.3 meters into the dike.

Golden Valley

The Golden Valley sill complex (Galerne *et al.*, 2008; Polteau *et al.*, 2008a,b) is characterized by a flat inner sill that is partly exposed along a small river in the southern end. Here (S31°58.4', E26°16.4'), a well-exposed part of the sill-roof hosts several small (<30 cm wide) sandstone intrusions (Fig. 5.5A). Note that the sediment source is located above the sill contact, demonstrating downward sediment movement. Note that in general, downward sediment movement is not unique for this location (e.g. Vitanage, 1954; Harms, 1965; Peterson, 1968). The dikes are irregularly shaped, and are characterized by a network-like pattern. Brownish alteration haloes are common around the dikes. The intruded sediments are Beaufort Group sandstones and shales, where the sandstones contain abundant nodules with radial fracture patterns (Fig. 5.5B). These nodules were originally composed of carbonate, but were modified during metamorphism.

5.5.2 Sediment petrography and petrology

We have studied thin sections of sediment dikes from the Waterdown Dam (site 3), the Nico Malan Pass, and Golden Valley. The main aims were to identify metamorphic minerals, characterize the texture, and

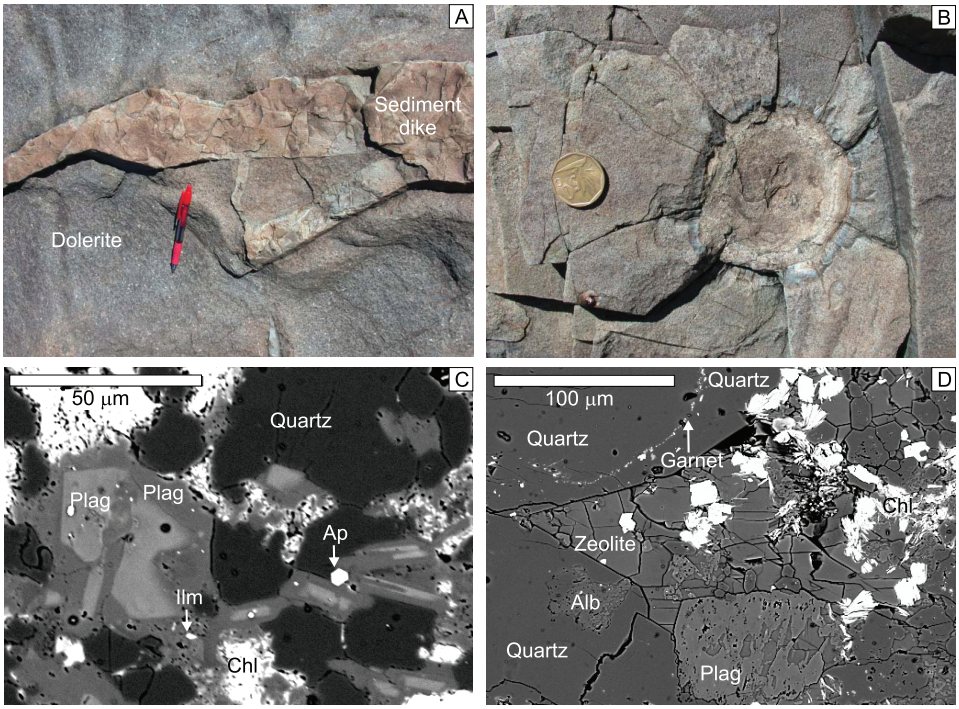

Figure 5.5: The Golden Valley locality. **(A)** Network of sandstone dikes within the upper meter of a sill in the floor of the Golden Valley saucer. (B) Reaction nodule in sandstone from 1-2 meters above the contact with the sill. **(C)** SEM picture showing metamorphic plagioclase, chlorite, and apatite in a sample from the thickest dike shown in (A). **(D)** SEM picture showing authigenic garnet, zeolite, quartz, and chlorite in the nodule in (B).

to characterize the metamorphic conditions. The diagenesis of non-metamorphic sandstones located far from sill intrusions in the Karoo Basin are characterized by authigenic minerals stable at relatively shallow burial (clay minerals, K-feldspar, calcite, albite, and quartz) (e.g. Turner, 1972; Rowsell & De Swardt, 1976; Svensen *et al.*, 2008). Typically, detrital grains (like quartz and K-feldspar) get coated and overgrown by authigenic minerals during burial without affecting the composition or texture of the grain interiors. At one kilometer of burial in the Karoo Basin, the original sandstone porosity could have been in the order of 10-25 %, presumably filled with low salinity pore fluids. During contact metamorphism of sandstone within the sediment dikes, detrital quartz grains are still easily recognized whereas feldspars (plagioclase and K-feldspar) are recrystallized in mosaic patterns. Moreover, the porosity is negligible, and chlorite and biotite are commonly present. Further details of the effects of contact metamorphism of sandstone from the examined localities are given below.

The sediment dike at Waterdown Dam contains metamorphic sandstone. Former grains and grain boundaries, representing the original sedimentary components, are easily recognized (Fig. 5.6A). This is confirmed by cathode luminescence imaging of quartz (Fig. 5.6B). Besides quartz, the dominant minerals that recrystallized in the dike are K-feldspar, plagioclase, and chlorite. Detrital feldspar

grains are recrystallized and contain a mosaic of K-feldspar and plagioclase. Based on the grey scale variations on SEM backscatter images, the plagioclase is characterized by several different compositions, apparently in textural equilibrium (Fig. 5.6C), and thus recrystallized during high temperature metamorphic conditions. Biotite was not identified in the studied sample, but abundant chlorite could possibly be a product of biotite retrogression. The altered dolerite fragments in the dike are dominated by chlorite.

The Elandsberg sandstone dike contains identifiable detrital sand grains with quartz overgrowths. A sample from 2.3 meters into the dike was studied using SEM, where cathode luminescence imaging revealed detrital quartz cores. Of importance is the presence of metamorphic epidote and biotite. The biotite is partly altered to chlorite, although the dominating mode of chlorite occurrence is in fresh patches unrelated to alteration. Feldspar grains are recrystallized and comprise mixtures of K-feldspar, albite, and plagioclase. Generally, the textures within the dike sample are tight and typical hornfels-like.

The sandstone dikes from Golden Valley have the same mineral content as the one at Waterdown Dam. Quartz, plagioclase, and chlorite are the main minerals. One difference, however, is the plagioclase textures. In Golden Valley, the detrital plagioclase is apparently completely recrystallized and zoned, present as tabular crystals (Fig. 5.5C). Ilmenite and apatite are minor minerals. The chlorite is locally present as tabular crystals, possibly suggesting biotite replacement. We have compared this mineral assemblage with the assemblage within a former carbonate nodule with sandstone from the same locality. The sample (Fig. 5.5B) is located about 2-3 meters above the contact with the dolerite sill, and is characterized by radial fractures extending out from a zoned nodule. In thin section, the main minerals are quartz (with detrital cores and overgrowths), feldspar, chlorite, and zeolite (Fig. 5.5D). The boundaries between detrital cores and metamorphic quartz are marked by rims of metamorphic garnet. The plagioclase is partly dissolved, and the pores filled by zeolite. Chlorite is common within the zeolite.

To conclude, the studied textures from the examined localities show that the sandstone dikes experienced medium-temperature metamorphism following injection. Original quartz grain boundaries and grain cores are still preserved and document that the sediment dikes did not undergo partial melting after emplacement. This is consistent with the absence of macroscopic melt patches in the dikes. Diagnostic peak metamorphic minerals are sparse in meta-sandstones due to the low iron and magnesium content. Recrystallization of quartz and feldspar grains is the dominant mode of mineralogical transformation. However, the occurrence of minerals like chlorite, biotite, plagioclase, and epidote is typical for greenschist facies conditions. Based on the general presence of these phases in the sediment dikes, we can use phase petrology to constrain the peak metamorphic conditions. We have made a phase diagram projected from a pelite composition, and compared the calculated phase assemblages with those identified in the rocks in order to determine the temperature during dike emplacement (Fig. 5.7).

5.5.3 Fluid pressure evolution during sill cooling

We have developed a numerical model in order to calculate the pressure gradients developing between an igneous sill and the surrounding sedimentary rocks as a function of temperature. Here we present snapshots of the temperature and pressure state during sill cooling. The modeling is based on the

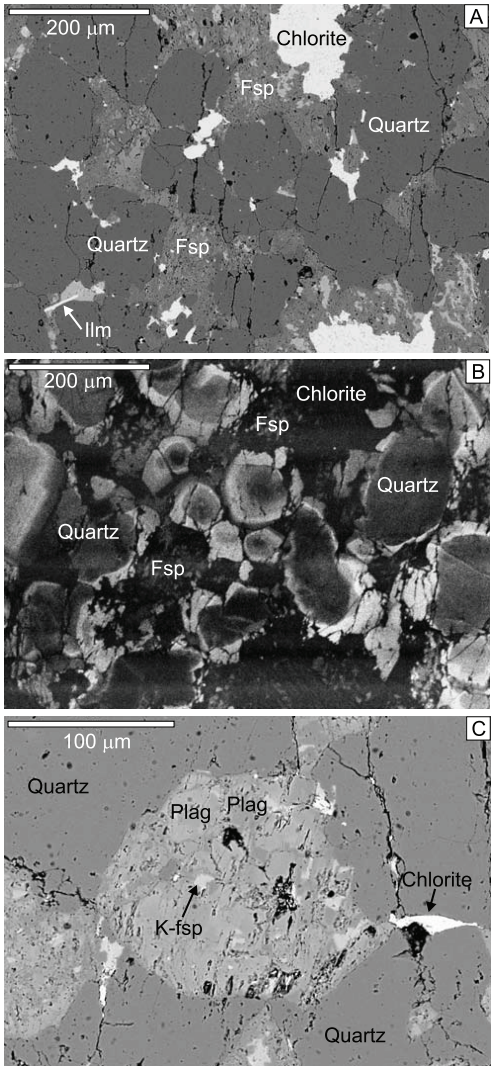

Figure 5.6: SEM petrography from the sediment dike at Waterdown Dam, site 3. The sandstone matrix shows well defined quartz grains **(A)** that have survived metamorphism. The cathode luminescence imaging **(B)** demonstrates further that melting never took place, as the quartz grains have retained their detrital core. The feldspar grains are however pervasively recrystallized, present as mosaics of K-feldspar and plagioclase with various compositions **(C)**.

parameters listed in Table 5.1.

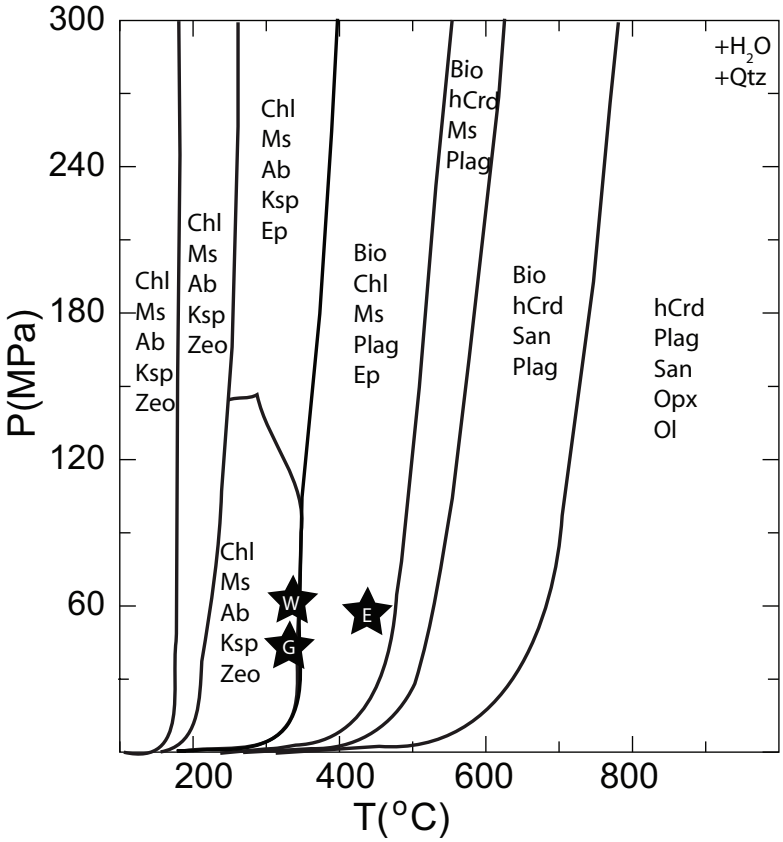

Figure 5.7: Phase diagram calculated using Perple_X for a rock with a pelite composition. The mineral assemblages are shown in between the black lines (dehydration reactions), and the position of the sediment dike samples are indicated by star symbols (W: Waterdown Dam, G: Golden Valley, E: Elandsberg).

Fifteen years after emplacement

At the time of instantaneous emplacement, the 100 meter thick sill is hot (1200 °C) with a sharp thermal boundary to the cold host-rock (35 °C) (Fig. 5.8A). Note that the gradient will be similar even if the sill is emplaced by continuous infilling and inflation. After fifteen years the temperature increases rapidly in the host-rock causing thermal expansion of the pore fluids, which results in overpressure of ∼22 MPa relative to the hydrostatic pressure gradient (∼7-8 MPa) (Figures 8A and 8B). A fracture pressure of 35 MPa is indicated by a red dashed line in Figure 5.8B. The sill is in a state of underpressure due to cooling and crystallization of interstitial melt in a solid crystal network. The major mechanism of underpressure within the sill (-22 MPa relative to the hydrostatic pressure gradient) is due to a density change when interstitial melt (2600 kg/m^3) is crystallizing (2900 kg/m^3) within a confining crystal network during cooling. Note that the tensile strength of a gabbroic rock is above 125 MPa (Ai & Ahrens, 2004).

Hundred years after emplacement

After 100 years, the sill has solidified and the temperature gradients become less steep (Fig. 5.8C). Correspondingly, the pressure gradient anomalies are reduced through diffusive fluid flow. The internal gradient within the sill is dispersed, and the main gradient is now from the host-rock and into the sill (Fig. 5.8D). The difference between the maximum overpressure ($\sim$4 MPa) in the host-rock and underpressure in the sill ($\sim$-7 MPa) is on the order of $\sim$10 MPa, relative to hydrostatic pressure.

5.5.4 Fluid pressure evolution during sediment heating

The fluid pressure in the aureole is increasing after sill emplacement due to the density change associated with heating of the H_2O pore fluid. Assuming a pore fluid pressure of 25 MPa at $\sim$1 km depth, H_2O experiences a density reduction from 1004 kg/m^3 to 162 kg/m^3 when heated from 35 °C to 400 °C (Wagner and Pruss, 2002). The thermal expansion of the sediment matrix for the same temperature interval is negligible relative to the phase transition in the fluid (i.e. boiling). The over-pressure is released through diffusive flow, with rates depending on the permeability of the host-rock. Similarly, the underpressure within the sill is created during cooling and crystallization. The thermal contraction associated with the melt to crystal transition is several magnitudes larger than the thermal contraction of the surrounding network for the same temperature interval. Hence, an underpressure will develop as a response to the density change of interstitial melt (>55% crystals Marsh, 1996; Philpotts & Carroll, 1996). This underpressure can be relaxed through internal melt flow from the molten to the crystallizing regions of the sill. When the sill is 100% crystals, the thermal stresses will continue to develop as long as the thermal contraction is larger than what can be accommodated by volume change. The stresses can be released through brittle fracturing of the rocks, which in turn can be filled in by for example fluids, interior melt, or fluidized sediments (e.g. Norton *et al.*, 1984).

When estimating the thermal expansion of pore fluids in the aureole, we use a conservative coefficient value of 4.1×10^{-4} (Delaney, 1982), resulting in pressure anomalies of up to $\sim$25 MPa. Using the definition of thermal expansion coefficient ,

$$\alpha = \frac{1}{v}\left(\frac{\partial v}{\partial T}\right)_P$$

where v is specific volume (pr unit mass, $1/\rho$; ρ is density), the expansion coefficient for pore-fluid is $2.3 \times 10^{-2}\mathrm{K}^{-1}$ where boiling occurs, and for melt-to-crystal transition it is 3.5×10^{-4} K^{-1}. The maximum pressure anomaly by boiling and expansion of pore fluids may thus be up to two magnitudes larger than our estimates.

5.5.5 Thermal modeling of sediment dikes

We have made a thermal model with a realistic sediment dike geometry to estimate the maximum temperature attained within the dike at a given sill temperature. We emplace a 20 meter tall and 2 meter thick sandstone dike with an initial temperature of 35 °C into a 100 meter thick sill with sill temperatures between 1100 and 1200 °C (Fig. 5.9). As expected, the dike rapidly reaches peak temperature (i.e., within a year). Hence, the initial temperature of the sandstone dike is not important for the final

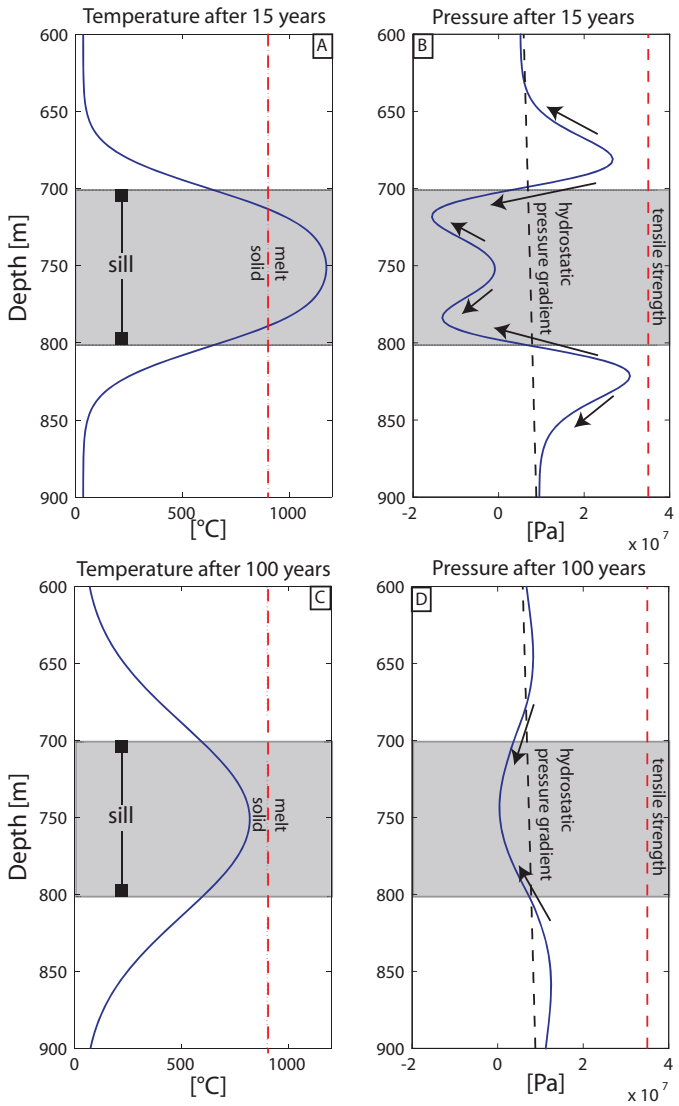

Figure 5.8: **(A)** Pressure gradients developed after 15 years of sill cooling. The sill is still close to 100 % molten (see vertical dashed line). **(B)** There is a strong pressure gradient between the sill margins and the aureole, where the aureole pressure is generated by thermal expansion of pore water. The arrows indicate pressure gradients along which melt and fluids are expected flow. The tensile strength of dolerite is indicated. **(C)** The sill is solidified after 100 years of cooling. The sill is now solidified. **(D)** Note that there is still a strong gradient going from the underpressure at the margins to the overpressure in the aureole, but most of the overpressure that was generated previously has diffused away.

maximum temperature recorded in the sill. If the dike is injected fifteen years after sill emplacement, the sediment dike reaches a temperature of ∼850 °C . Injection at the time of sill solidification (i.e., at

∼100 years), the peak temperature in the dike is ∼650-675 °C . For the sandstone dike to be heated to a maximum of ∼450 °C (cf. Elandsberg), injection after 300 years of sill cooling is indicated. After 600 years the sill has cooled to such an extent that the temperature in the sediment dike never exceeds 350 °C (cf. Golden Valley and Waterdown Dam).

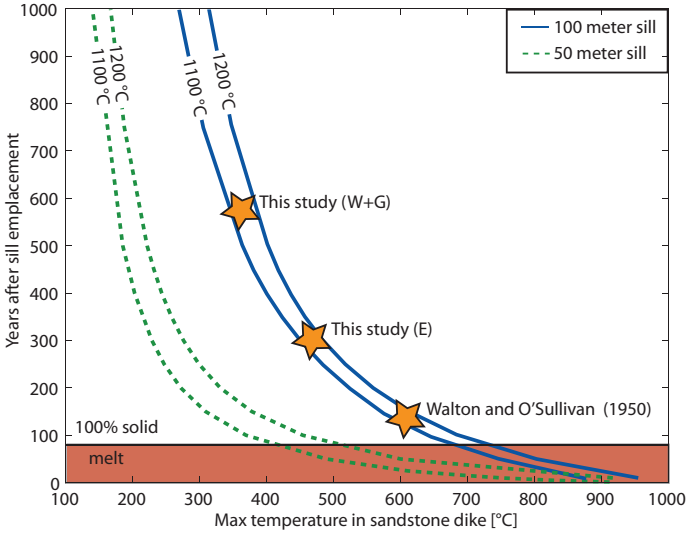

Figure 5.9: Calculated maximum temperature of a 2×20 meter sediment dike injected into a 100 meter (solid lines) and a 1×10 meter sediment dike injected into a 50 meter (dashed lines) sill for intrusion temperatures of 1100-1200 °C as a function of injection time after sill emplacement. The grey area indicates when the sill is still molten. By knowing the maximum temperature of the sandstone dike we can infer that the injection time was ∼300 years after sill emplacement for the Elandsberg dike and ∼600 years for the Golden Valley and Waterdown Dam dikes. For comparison the calculated injection time of the dikes from Walton and O'Sullivan occurred closely after sill solidification (∼150 years).

5.6 Discussion

5.6.1 Contact metamorphism in sedimentary basins

In contrast to the 30-70 m.y. time scale of fluid production and pressure buildup during regional metamorphism and orogenesis (e.g. Walther & Orville, 1982; Connolly & Thompson, 1989), contact metamorphism around igneous sill intrusions in sedimentary basins have dramatic and short term effects on fluid flow. This is particularly important in basins with rapidly cooling sill intrusions compared to settings with >100 k.y. contact metamorphism around plutons (e.g. Hanson, 1992, 1995). When sedimentary host rocks are heated around sills, pore fluid expansion and boiling occur on timescale of years, dominating the fluid production compared to devolatilization reactions (e.g. Delaney, 1982; Hanson, 1995; Jamtveit *et al.*, 2004). Overpressure related to boiling and pore fluid expansion may

ultimately lead to hydrofracturing and the formation of hydrothermal vent complexes in the upper kilometer in the basin (e.g. Jamtveit *et al.*, 2004). In the Karoo Basin, the hydrothermal vent complexes commonly crop out in the Stormberg Group sediments. In addition, numerous breccia pipes are rooted in contact aureoles of black shale, demonstrating that high pore fluid pressures developed during rapid cracking of organic matter to methane (Svensen *et al.*, 2007). Thus contact metamorphism around sill intrusions is a process that causes rapid pressure build-up and drives fluid flow on a very short timescale. In this setting, sediment dikes represent direct evidence for the rapid release of aureole pressure and fluids.

5.6.2 The pressure evolution of a cooling sill

Recently, it was shown that sill cooling and crystallization result in an underpressure within the sill (Aarnes *et al.*, 2008). The reason for underpressure generation is the following. At the earlier stages of the sill cooling, a solid crystal network (>55% crystals) with interstitial melt will form (Marsh, 1988, 1996; Philpotts & Carroll, 1996). With further cooling the interstitial melt experiences a significant density change due to the melt-to-crystal transition. However, a strong crystal network prevents a volume change and causes a large underpressure to develop. It is shown through experiments that a crystal network have considerable strength already at 35 % crystals, and effectively behaves as a solid even with large amounts of interstitial melts (Philpotts & Carroll, 1996). Such an underpressure may induce melt flow, have consequences for the chemistry of the magmatic system, and induce sediment injections into the sill (Aarnes *et al.*, 2008).

During the initial stages of sill cooling, the pore water in the aureole sediments will expand and flow either away from the sill or into the sill depending on the pressure gradients. Melt may also flow within the sill along the pressure gradient towards the cooling margins (c.f. Figure 5.8). The fluid flow is a result of the developed pressure anomalies and will act to even out the pressure anomalies with time. After 100 years the pressure gradient within the sill is reversed, going from the margins to the center (Fig. 5.8B). However, the melt is now unable to flow as solidification is complete. At this time, the pressure in the sedimentary host rock has effectively been diffused by fluid flow. Thus, the main pressure gradient is now from the host rock towards the sill, both above and below the intrusion. At this stage, heated pore fluids will flow into the sill if permeability allows the fluids to enter, i.e., if fractures develop.

5.6.3 Aureole overpressure and sediment injections into sills

Fluidization due to heating of water-rich sedimentary rocks is most likely to occur at depths where pressure is less than the pressure corresponding to the critical point of water (Kokelaar, 1982; Jamtveit *et al.*, 2004). The paleo-depth of the study areas with sediment dikes in dolerites is ∼600-900 meters, thus shallower than the critical depth. In some geological settings overpressure can cause horizontal fracturing through fluids seeping away from the overpressurized source (e.g. Mourgues & Cobbold, 2003; Cobbold & Rodrigues, 2007), while in the case of boiling and very high overpressures, modeling has demonstrated that the gas release may localize vertically and eventually reach the atmosphere (e.g. Jamtveit *et al.*, 2004; Rozhko *et al.*, 2007). The key requirements for pressure-

induced sediment mobilization in the aureole are low permeabilities, high porosities and high thermal diffusivities (Delaney, 1982; Jamtveit *et al.*, 2004). In the case of high permeabilities in shallow sandstones, the rate of heating must exceed the rate of pressure loss by fluid flow in order to build up significant over-pressure. When the host-rock experience extensive pressure-buildup the sedimentary rock may ultimately loose all cohesive strength and become fluidized and result in substantial sediment displacement (e.g. Vitanage, 1954; Harms, 1965; Kokelaar, 1982; Ross & White, 2005). The sandstones of the Beaufort Group in the Karoo Basin were still in the early to intermediate stages of diagenesis (i.e., reached quartz cementation) at the time of sill emplacement. Thus the conditions were right for fluidization to occur, at least where clay minerals limit relaxation of pressures through fluid flow (Jolly & Lonergan, 2002), or as mentioned, if heating was rapid compared to pressure drop by fluid flow (Jamtveit *et al.*, 2004).

Heat-induced overpressure and subsequent fluidization of sediments in the contact aureole is here suggested to be the main formation mechanism of sandstone dikes in magmatic intrusion. We show that there is an additional strong gradient from the aureole into the intrusion, and that this gradient makes sediment mobilization more likely to happen compared to injections driven by pore fluid boiling and fracturing during thermal contraction. Still, we argue that fracturing during thermal contraction is of lesser importance, as sediment dikes are not present in a hexagonal network even in areas with abundant fractures developed during thermal contraction (e.g., the Golden Valley locality). The overpressure scenario is schematically presented in Figure 5.10. Our results show pressure anomalies of up to 10^8 Pa after solidification of the sill, which are in agreement with the magnitude 10^7 Pa overpressure commonly found for several rock types due to expansion of pore fluids from magmatic intrusion (Delaney, 1982). Importantly, the high pressure is sufficient to break the tensile strength of sandstones above $\sim$1 km depth (e.g. Kokelaar, 1982), thus fluids can potentially flow from the aureole and into the sill.

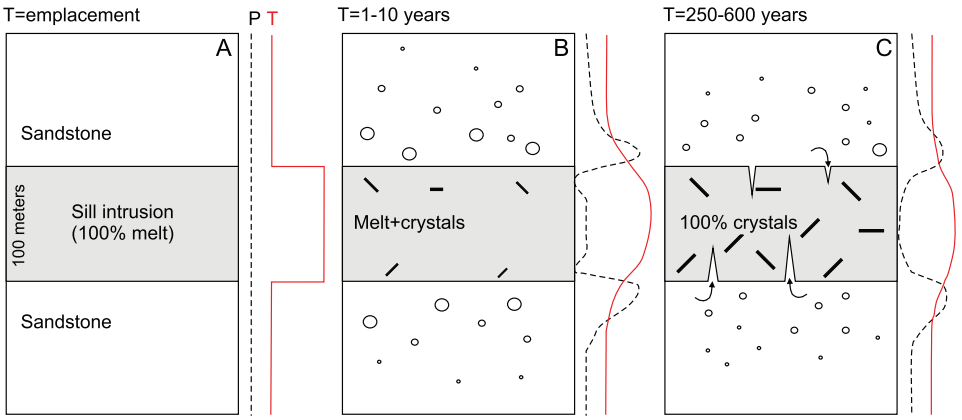

Figure 5.10: Schematic evolution of a sill-aureole system with sediment injections. **(A)** Initial sill emplacement into cold sedimentary host rocks. **(B)** Contact metamorphism around the molten sill, and expansion of sedimentary pore fluids (symbolized by circles). **(C)** Crystallization of the sill followed by fracturing due to the huge pressure difference between sill and aureole. The sill is still hot enough to cause high temperature metamorphism of the injected sediments.

We therefore argue that sandstone dikes form as a result of the difference in pressure between the sill and the aureole (∼10 MPa) that develops during sill cooling and sediment contact metamorphism. The pressure gradient is sufficient for fracturing the sill (pressures beyond the lithostatic) and to act as ”sucking” force on the sediments from the moment the chilled margin of the sill fractures. Once initiated, the fracture will propagate as a result of the injected pore fluids and sediments, which also may lead to further tensile failure (c.f. Rubin, 1993). The fracturing process may be violent, as indicated by the high proportion of both sedimentary and doleritic rock fragments in the dikes at Waterdown Dam. Sediment fragments comprise 86 % of the dike surface at site 3, and the size distribution between sedimentary and dolerite clasts suggests that the same process was responsible for brecciation of both dolerite sill and aureole sediments. The four orders of magnitude variation in clast size (Fig. 5.3B) demonstrates that the brecciation was rapid and that bulk of the breccia was injected into the sill.

5.6.4 Sediment dike metamorphism and injection timing

The sediment dikes described in this study are all affected by contact metamorphism. Thus they were heated while the sill intrusions were still hot, either in situ in the contact aureole prior to injection, or within the sediment dike. Metamorphism of the sedimentary material is a common observation from all sediment dikes in magmatic sill intrusions (Walton & O'Sullivan, 1950; Van Biljon & Smitter, 1956). Based on the metamorphic minerals in the dikes and aureoles from the Karoo Basin (chlorite, biotite, plagioclase, and epidote, garnet), the metamorphic conditions were equivalent to those of the greenschist facies. Based on these minerals and the presented phase diagram (Fig. 5.7), a maximum temperature of about 450 °C is suggested.. There are no accurate thermometers that can be applied to the identified mineral assemblages, so the temperature is approximate. Comparing with active hydrothermal metamorphism of sandstone, biotite appears at ∼320 °C (e.g. Schiffman *et al.*, 1985), so our estimate is reasonable. The absence of minerals like cordierite, clinopyroxene, and muscovite furthermore suggests temperatures below ∼450 °C , although the potential for generating some of these minerals depends on the bulk rock composition. As the temperature of heated sedimentary rocks around a sill intrusion will never exceed about half the sill temperature, a doleritic sill (∼1200 °C) will commonly not be able to melt the host sediments and maximum temperatures should be close to 600-700 °C depending upon the host rock temperature at the time of emplacement. However, this situation may be different in other geological systems (e.g. Hersum *et al.*, 2007).

The temperature estimates from the mineralogy are of importance when assessing the timing of sediment dike emplacement. As we have shown, an early emplacement into a hot sill will result in high temperature metamorphism in the dike. Based on our thermal modeling, injection after 250-600 years of sill solidification will give 325-450 °C in the dike. Note that reaction kinetics or significant latent heat of vaporization may contribute to discrepancies between modeled heat from conduction and that of a natural system. Earlier timing of sediment injection is therefore possible. To summarize, our data suggest that the emplacement of the sediment dikes occurred after the sill was 100% crystallized, which puts a lower boundary to the timing of injection of about 100 years. This means that sediment injection into sills has only limited potential for contaminating the magma since the sill is 100% crystallized at the time of sandstone injection. For contamination to happen, the sediments would have to be injected

into a partly molten sill, which of we have no supporting observations.

Field evidence shows that sediment dikes can propagate tens of meters into dolerite sills from the lower contact. The vertical termination of dikes has however not been found in the field. However, since the metamorphic recrystallization led to very low permeabilities, the sediment dikes were prevented from becoming long-lasting fluid flow pathways.

Finally, we may outline under which basin settings sediment dikes within igneous sills are not likely to form: 1) when the overpressure difference between sill and aureole is small, as when the sill intrusion is thin or 2) the aureole has limited potential for generating overpressure during heating, like when the porosity is very low or the content of organic matter is negligible. Thus the presence of sediment injections in igneous systems may provide important constraints on the pressure evolution and fluid flow history in sedimentary basins with sill intrusions.

5.7 Conclusions

Sediment dikes have been discovered within dolerite sill intrusions at several localities in the Karoo Basin in South Africa. The sediment dikes contain metamorphic sandstone and clasts of sediments and dolerite. Field, petrographic, and numerical evidence suggests that:

- Both upward and downward movement of sediments into sill intrusions is common.
- The sediments intruded while the sills were hot, producing mineral assemblages typical for $>$300 °C metamorphism.
- Thermal modeling shows that the sediment dikes were injected more than 100 years after sill emplacement to account for the dike metamorphism, depending on sill thickness and the initial sill temperature.
- The presence of sediment dikes in sills is a result of the coupled pressure evolution of dolerite sills and contact aureoles. Negative pressure anomalies in the sill forms due to cooling, whereas high pressure develops in the aureole due to thermal expansion.
- The pressure generated is of the right order of magnitude required to explain fracturing of the solidified sill. The sediments were accordingly 'sucked' into the sill.

Acknowledgement

This study was supported by a PetroMaks grant from the Norwegian Research Council to H. Svensen. We thank Goonie Marsh and Luc Chevallier for discussions during our field trips to South Africa, in particular Goonie for showing us the Waterdown Dam locality, and Dirk Liss for the company and assistance during sampling of the sediment dykes. Else-Ragnhild Neumann and the "Golden Valley Study Group" at PGP contributed with valuable input to the project,, and Joe Cartwright, an anonymous referee, and a Geosphere editor, are all thanked for critical comments.

Appendix 5.A Equations

The cooling of the sill and heating of the host-rock follows the heat conduction equation,

$$\frac{\partial T}{\partial t} = K_T^{\text{eff}} \left\{ \frac{\partial^2 T}{\partial x^2} + \frac{\partial^2 T}{\partial z^2} \right\} \tag{5.A.1}$$

where T is the temperature, $K_T^{\text{eff}}$is thermal diffusivity coefficient, x is lateral direction and y is vertical direction. The effective thermal diffusivity accounts for the latent heat of fusion:

$$\begin{array}{ll} K_T^{\text{eff}} = \frac{K_T}{(1+Ste)} & for \quad (T_S < T < T_L) \\ K_T^{\text{eff}} = K_T & for \quad (T_S > T). \end{array} \tag{5.A.2}$$

Non-dimensional ratio quantifying the effect of the latent heat is the Stefan number, Ste, given by

$$Ste = \frac{L}{(T_L - T_S)C_P} \tag{5.A.3}$$

where C_P is heat capacity and L the latent heat of fusion per unit mass.

Equation 5.A.1 is coupled with pressure through thermal stresses,

$$dP = \frac{\alpha}{\beta} dT \tag{5.A.4}$$

as described by e.g. Turcotte and Schubert (2002), assuming isochoric conditions for crystallization. Taking the partial derivative of Equation 5.A.4 with respect to time, the hydraulic equation becomes

$$\frac{\partial P}{\partial t} = K_H \left\{ \frac{\partial^2 P}{\partial x^2} + \frac{\partial^2 P}{\partial z^2} \right\} + \frac{\alpha}{\beta} \frac{\partial T}{\partial t} \tag{5.A.5}$$

where P is pressure, α the volumetric coefficient of thermal expansion and β the isothermal compressibility. K_H is the hydraulic diffusivity, $K_H = \chi \setminus \mu \setminus \beta$ and χ is matrix permeability, μ is viscosity of fluid and β is compressibility. This modified hydraulic diffusion equation is similar to that of Delaney (1982). The first part on the right hand side of Equation 5.A.5 describes the pressure diffusion (similar to heat conduction Equation 5.A.1); the second part describes the development of pressure anomalies due to changes in temperature. The initial over-pressure is zero since the flow only depends on the evolving pressure anomalies.

REFERENCES

AARNES I., PODLADCHIKOV Y.Y. & NEUMANN E.R. (2008) Post-emplacement melt flow induced by thermal stresses: Implications for differentiation in sills. *Earth and Planetary Science Letters*, **276**, 152–166.

AI H.A. & AHRENS T.J. (2004) Dynamic tensile strength of terrestrial rocks and application to impact cratering. *Meteoritics and Planetary Science*, **39**, 233–246.

CADDICK M.J. & THOMPSON A.B. (2008) Quantifying the tectono-metamorphic evolution of pelitic rocks from a wide range of tectonic settings: mineral compositions in equilibrium. *Contributions to Mineralogy and Petrology*, **156**, 177–195.

CATUNEANU O., HANCOX P.J. & RUBIDGE B.S. (1998) Reciprocal flexural behaviour and contrasting stratigraphies: a new basin development model for the Karoo retroarc foreland system, South Africa. *Basin Research*, **10**, 417–439.

CHEVALLIER L. & WOODFORD A. (1999) Morpho-tectonics and mechanism of emplacement of the dolerite rings and sills of the Western Karoo, South Africa. *South African Journal of Geology*, **102**, 43–54.

COBBOLD P.R. & RODRIGUES N. (2007) Seepage forces, important factors in the formation of horizontal hydraulic fractures and bedding-parallel fibrous veins ('beef' and icone-in-cone). *Geofluids*, **7**, 313–322.

CONNOLLY J.A.D. (1997) Devolatilization-generated fluid pressure and deformation-propagated fluid flow during prograde regional metamorphism. *Journal of Geophysical Research-Solid Earth*, **102**, 18149–18173.

CONNOLLY J.A.D. (2005) Computation of phase equilibria by linear programming: A tool for geodynamic modeling and its application to subduction zone decarbonation. *Earth and Planetary Science Letters*, **236**, 524–541.

CONNOLLY J.A.D. & THOMPSON A.B. (1989) Fluid and enthalpy production during regional metamorphism. *Contributions to Mineralogy and Petrology*, **102**, 347–366.

DELANEY P.T. (1982) Rapid Intrusion of Magma into Wet Rock - Groundwater-Flow Due to Pore Pressure Increases. *Journal of Geophysical Research*, **87**, 7739–756.

DUNCAN R., HOOPER P., REHACEK J., MARSH J. & DUNCAN A. (1997) The timing and duration of the Karoo igneous event, southern Gondwana. *Journal of Geophysical Research*, **102, B8**, 18127–18138.

GALERNE C.Y., NEUMANN E.R. & PLANKE S. (2008) Emplacement mechanisms of sill complexes: Information from the geochemical architecture of the Golden Valley Sill Complex, South Africa. *Journal of Volcanology and Geothermal Research*, **177**, 425–440.

GANINO C. & ARNDT N.T. (2009) Climate changes caused by degassing of sediments during the emplacement of large igneous provinces. *Geology*, **37**, 323–326.

HANSON R.B. (1992) Effects of Fluid Production on Fluid-Flow During Regional and Contact-Metamorphism. *Journal of Metamorphic Geology*, **10**, 87–97.

HANSON R.B. (1995) The hydrodynamics of contact-metamorphism. *Geological Society of America Bulletin*, **107**, 595–611.

HARMS J.C. (1965) Sandstone Dikes in Relation to Laramide Faults and Stress Distribution in the Southern Front Range, Colorado. *Geological Society of America Bulletin*, **76**, 981–1002.

HERSUM T., HILPERT M. & MARSH B. (2005) Permeability and melt flow in simulated and natural partially molten basaltic magmas. *Earth and Planetary Science Letters*, **237**, 798–814.

HERSUM T.G., MARSH B.D. & SIMON A.C. (2007) Contact Partial Melting of Granitic Country Rock, Melt Segregation, and Re-injection as Dikes into Ferrar Dolerite Sills, McMurdo Dry Valleys, Antarctica. *Journal of Petrology*, **48**, 2125–2148.

JAMTVEIT B., SVENSEN H. & PODLADCHIKOV Y.Y. (2004) Hydrothermal vent complexes associated with sill intrusions in sedimentary basins. In: *Physical Geology of High-Level Magmatic Systems* (Ed. C. Breitkreuz & N. Petford), vol. 234. Geological Society, London, Special Publications.

JOHNSON M.R., VUUREN C.J.V., VISSER J.N.J., COLE D.I., WICKENS H.D.V., CHRISTIE A.D.M., ROBERTS D.L. & SELLEY R.C. (1997) Chapter 12 The foreland Karoo basin, South Africa. In: *Sedimentary Basins of the World*, vol. Volume 3, 269–317. Elsevier.

JOLLY R.J.H. & LONERGAN L. (2002) Mechanisms and controls on the formation of sand intrusions. *Journal of the Geological Society*, **159**, 605–617.

JOURDAN F., FERAUD G., BERTRAND H., KAMPUNZU A.B., TSHOSO G., WATKEYS M.K. & LE GALL B. (2005) Karoo large igneous province: Brevity, origin, and relation to mass extinction questioned by new Ar-40/Ar-39 age data. *Geology*, **33**, 745–748.

KOKELAAR B.P. (1982) Fluidization of Wet Sediments During the Emplacement and Cooling of Various Igneous Bodies. *Journal of the Geological Society*, **139**, 21–33.

MARSH B.D. (1988) Crystal capture, sorting, and retention in convecting magma. *Geological Society of America Bulletin*, **100**, 1720–1737.

MARSH B.D. (1996) Solidification fronts and magmatic evolution. *Mineralogical Magazine*, **60**, 5–40.

MAZZINI A., JONK R., DURANTI D., PARNELL J., CRONIN B.T. & HURST A. (2003) Fluid escape from reservoirs: implications from cold seeps, fractures and injected sands. Part I: the fluid flow system. *Journal of Geochemical Exploration*, **78**, 293–296.

MCELWAIN J.C., WADE-MURPHY J. & HESSELBO S.P. (2005) Changes in carbon dioxide during an oceanic anoxic event linked to intrusion into Gondwana coals. *Nature*, **435**, 479–482.

MOURGUES R. & COBBOLD P.R. (2003) Some tectonic consequences of fluid overpressures and seepage forces as demonstrated by sandbox modelling. *Tectonophysics*, **376**, 75–97.

NICHOLS G.T., WYLLIE P.J. & STERN C.R. (1994) Subduction zone melting of pelagic sediments constrained by melting experiments. *Nature*, **371**, 785–788.

NORTON D., TAYLOR H.P. & BIRD D.K. (1984) The Geometry and High-Temperature Brittle Deformation of the Skaergaard Intrusion. *Journal of Geophysical Research*, **89**, 178–192.

PETERSON G.L. (1968) Flow structures in sandstone dikes. *Sedimentary Geology*, **2**, 177–190.

PHILPOTTS A.R. & CARROLL M. (1996) Physical properties of partly melted tholeiitic basalt. *Geology*, **24**, 1029–1032.

PODLADCHIKOV Y.Y. & WICKHAM S.M. (1994) Crystallization of Hydrous Magmas - Calculation of Associated Thermal Effects, Volatile Fluxes, and Isotopic Alteration. *Journal of Geology*, **102**, 25–45.

POLTEAU S., FERRE E.C., PLANKE S., NEUMANN E.R. & CHEVALLIER L. (2008a) How are saucer-shaped sills emplaced? Constraints from the Golden Valley Sill, South Africa. *Journal of Geophysical Research-Solid Earth*, **113, B12**, B12104.

POLTEAU S., MAZZINI A., GALLAND O., PLANKE S. & MALTHE-SØRENSSEN A. (2008b) Saucer-shaped intrusions: Occurrences, emplacement and implications. *Earth and Planetary Science Letters*, **266**, 195–204.

RETALLACK G.J. & JAHREN A.H. (2008) Methane Release from Igneous Intrusion of Coal during Late Permian Extinction Events. *The Journal of Geology*, **116**, 1–20.

ROSS P.S. & WHITE J.D.L. (2005) Unusually large clastic dykes formed by elutriation of a poorly sorted, coarser-grained source. *Journal of the Geological Society*, **162**, 579–582.

ROWSELL D. & DE SWARDT A. (1976) Diagenesis in Cape and Karoo sediments, South Africa and its bearing on their hydrocarbon potential. *Transactions of the Geological Society of South Africa*, **79**, 81–145.

ROZHKO A.Y., PODLADCHIKOV Y.Y. & RENARD F. (2007) Failure patterns caused by localized rise in pore-fluid overpressure and effective strength of rocks. *Geophysical Research Letters*, **34**, L22304.

SCHIFFMAN P., BIRD D.K. & ELDERS W.A. (1985) Hydrothermal mineralogy of calcareous sandstones from the Colorado River delta in the Cerro Prieto geothermal system, Baja California, Mexico. *Mineralogical Magazine*, **49**, 435–449.

SMITH R.M.H. (1990) A review of stratigraphy and sedimentary environments of the Karoo Basin of South Africa. *Journal of African Earth Sciences*, **10**, 117–137.

SVENSEN H., BEBOUT G., KRONZ A., LI L., PLANKE S., CHEVALLIER L. & JAMTVEIT B. (2008) Nitrogen geochemistry as a tracer of fluid flow in a hydrothermal vent complex in the Karoo Basin, South Africa. *Geochimica et Cosmochimica Acta*, **72**, 4929–4947.

SVENSEN H., JAMTVEIT B., PLANKE S. & CHEVALLIER L. (2006) Structure and evolution of hydrothermal vent complexes in the Karoo Basin, South Africa. *Journal of the Geological Society*, **163**, 671–682.

SVENSEN H., PLANKE S., CHEVALLIER L., MALTHE-SØRENSSEN A., CORFU F. & JAMTVEIT B. (2007) Hydrothermal venting of greenhouse gases triggering Early Jurassic global warming. *Earth and Planetary Science Letters*, **256**, 554–566.

SVENSEN H., PLANKE S., MALTHE-SORENSSEN A., JAMTVEIT B., MYKLEBUST R., EIDEM T.R. & REY S.S. (2004) Release of methane from a volcanic basin as a mechanism for initial Eocene global warming. *Nature*, **429**, 542–545.

SVENSEN H., PLANKE S., POLOZOV A.G., SCHMIDBAUER N., CORFU F., PODLADCHIKOV Y.Y. & JAMTVEIT B. (2009) Siberian gas venting and the end-Permian environmental crisis. *Earth and Planetary Science Letters*, **277**, 490–500.

TURCOTTE D.L. & SCHUBERT G. (2002) *Geodynamics*. Cambridge, 2nd edn.

TURNER B. (1972) Silica diagenesis in the Molteno sandstone. *Transactions of the Geological Society of South Africa*, **75**, 55–66.

VAN BILJON W.J. & SMITTER Y.H. (1956) A note on the occurrence of two sandstone dykes in a Karoo dolerite sill near Devon, South-Eastern Transvaal. *Transactions of the Geological Society of South Africa*, **59**, 135–139.

VEEVERS J., COLE D. & COWAN E. (1994) *Southern Africa: Karoo Basin and Cape Fold Belt*, vol. 184 of *Geological Society of America, Memoir*. Geological Society of America.

VITANAGE P.W. (1954) Sandstone Dikes in the South Platte Area, Colorado. *Journal of Geology*, **62**, 493–&.

WALTHER J.V. & ORVILLE P.M. (1982) Volatile Production and Transport in Regional Metamorphism. *Contributions to Mineralogy and Petrology*, **79**, 252–257.

WALTON M.S. & O'SULLIVAN R.B. (1950) The intrusive mechanics of a clastic dike (Connecticut). *American Journal of Science*, **248**, 1–21.

Chapter 6

Post-emplacement melt flow induced by thermal stresses: Implications for differentiation in sills

The following pages are taken from:
Aarnes, I., Podladchikov, Y. Y. and Neumann, E.-R. (2008) Post-emplacement melt flow induced by thermal stresses: Implications for differentiation in sills. ***Earth and Planetary Science Letters*****, 276, 152-166.**

Appendix A: PhD activities

Publications

Presented in this thesis

Aarnes I., Podladchikov Y. Y., and Neumann E.-R. (2008) Post-emplacement melt flow induced by thermal stresses: Implications for differentiation in sills. *Earth and Planetary Science Letters* **276**(1-2), 152-166.

Aarnes I., Svensen H., Connolly J. A. D., and Podladchikov Y. Y. (accepted) How contact metamorphism can trigger global climate changes: Modeling gas generation around igneous sills in sedimentary basins. *Geochimica et Cosmochimica Acta.* **Accepted**.

Aarnes I., Svensen H., Polteau S., and Planke S. (subm.) Contact metamorphic devolatilization of shales in the Karoo Basin, South Africa, and the effects of multiple sill intrusions. *Chem. Geol.* **Submitted.**

Aarnes I., Podladchikov Y. Y., and Svensen H. (In prep.) Fluid overpressure and rate of devolatilization during metamorphism. **In preparation.**

Svensen H., **Aarnes I.**, Podladchikov Y. Y., Jettestuen E., Harstad C. H., and Planke S. (2010) Sandstone dikes in dolerite sills: Evidence for high pressure gradients and sediment mobilization during solidification of magmatic sheet intrusions in sedimentary basins. *Geosphere*. **In press**.

Other publications

Galerne C. Y., Neumann E.-R., **Aarnes I.**, and Planke S. (2010) Magmatic differentiation processes in saucer-shaped sills: Evidence from the Golden Valley Sill in the Karoo Basin, South Africa. *Geosphere*. **In press.**

Polteau S., Svensen H., Planke S., and **Aarnes I.** (subm.) Geochemistry of contact metamorphic black shale around sill intrusions in the Karoo Basin and the implication for the Toarcian carbon isotope excursion. **Submitted.**

Svensen, H., **Aarnes, I.**, Planke, S., Skogseid, J., Karlsen, D.A., Pedersen, T., and Jettestuen, E. (In prep.) Early Eocene contact metamorphism of Cretaceous mudstones in the Vøring Basin, offshore Norway, and the implications for hydrocarbon generation. **In preparation.**

Conference abstracts

EGU Assembly, Vienna, Austria 2010: Aarnes, Ingrid; Svensen, Henrik; Polteau, Stephane; Connolly, James A.D.; Podladchikov, Yuri Y.; Planke, Sverre. Large scale sediment degassing during contact metamorphism of shales in volcanic basins. (Talk)

Aarnes, Ingrid; Podladchikov, Yuri Y.; Svensen, Henrik; Overpressure generated from devolatilization reactions during metamorphism: Implications for breccia pipe formation. (Talk)

EGU Assembly, Vienna, Austria 2009: Aarnes, Ingrid; Podladchikov, Yuri Y.; Neumann, Else Ragnhild; Galerne, Christophe Y. Post-emplacement melt-flow as a feasible mechanism for reversed differentiation in tholeiitic sills. (Talk)

Aarnes, Ingrid; Svensen, Henrik; Polteau, Stephane; Connolly, James A.D.; Podladchikov, Yuri; Planke, Sverre. Contact metamorphism of black shales: global carbon cycle and climate perturbations.(Poster)

22nd Kongsberg seminar, Norway 2009: Aarnes, Ingrid; Svensen, Henrik; Polteau, Stephane; Connolly, J.A.D.; Podladchikov, Yuri; Planke, Sverre. The impact of large scale contact metamorphism on global climate. (Poster)

Goldschmidt, Davos Switzerland 2009: Aarnes, Ingrid; Svensen, Henrik; Polteau, Stephane; Connolly, James A.D.; Podladchikov, Yuri Y. The impact of large scale contact metamorphism on global climate. (Talk)

LASI III, Elba Island, Italy 2008: Aarnes, Ingrid; Svensen, Henrik. Gas formation in contact aureoles: Constraints from kinetic and thermal modeling. (Talk)

Aarnes, Ingrid; Podladchikov, Yuri Y.; Neumann, Else-Ragnhild. Post-emplacement melt-flow induced by thermal stresses as a feasible mechanism for reversed differentiation in tholeiitic sills. (Poster)

33rd International Geological Congress, Oslo, Norway 2008: Aarnes, Ingrid; Svensen, Henrik; Polteau, Stephane. Gas formation from black shale during contact metamorphism. 33rd International Geological Congress. (Talk)

Aarnes, Ingrid; Podladchikov, Yuri Y.; Neumann, Else-Ragnhild. Post-emplacement melt-flow induced by thermal stresses as a feasible mechanism for reversed differentiation in tholeiitic sills. (Poster)

Dave Yuen's international 60-birthday symposium, Elm, Switzerland 2008: Aarnes, Ingrid; Podladchikov, Yuri Y.; Neumann, Else-Ragnhild. Post-emplacement melt flow as possible differentiation mechanism in sills. (Poster)

20nd Kongsberg seminar, Norway 2007: Aarnes, Ingrid. Formation of D- and I-shaped profiles in tholeiitic sills due to post-emplacement melt-flow induced by thermal stresses. (Poster)

AGU Fall meeting, San Fransisco, USA 2007: Aarnes, Ingrid; Podladchikov, Yuri Y.; Neumann, Else-Ragnhild. Formation of D- and I-shaped geochemical profiles in mafic sills due to post-emplacement magma flow induced by thermal stresses. (Poster)

Summer School on Geodynamics and Magmatic Processes, Iceland 2007: Aarnes, Ingrid; Podladchikov, Yuri Y.; Neumann, Else-Ragnhild. Formation of D- and I-shaped profiles in basaltic sills due to post-emplacement melt-flow induced by thermal stresses. (Poster)

Courses

GEO9051SP	Advanced topics in thermodynamics (5 credits)
GEO9211	Petroleum systems (10 credits)
MNSES9100	Science, ethics and society (5 credits)
FYS9470	Flow in porous media. (10 credits)